UNIVERSITY OF SOUTHAMPTON

FACULTY OF NATURAL AND ENVIRONMENTAL SCIENCES

Chemistry

Catalysis for Sustainable Energy Conversion and Storage

by

Davide Ansovini

Thesis for the degree of Doctor of Philosophy

September 2016

UNIVERSITY OF SOUTHAMPTON

ABSTRACT

FACULTY OF NATURAL AND ENVIRONMENTAL SCIENCES

Chemistry

Thesis for the degree of Doctor of Philosophy

CATALYSIS FOR SUSTAINABLE ENERGY CONVERSION AND STORAGE

Davide Ansovini

Climate change, pollution, unprecedented population growth, geopolitical tensions and rapid technological development are intrinsically connected to the nature, level and availability of global energy, which shapes present and future aspects of human society. Particularly, in a society where global energetic demand is continuously rising and the awareness of the negative impact of fossil fuels on the environment is becoming widespread, the exploitation of renewable sources for the generation of sustainable energy is highly needed. In this regard one key requirement for an effective deployment and expansion of renewable energy in the global energy market is represented by its ability to conveniently convert and store the energy derived from intermittent sources, in order to guarantee a constant supply to the electric grid. The technologies for the energy conversion and storage present various degrees of maturity, each one having specific advantages and disadvantages depending on the type of application and energetic source.

This thesis aims to give a tiny contribution to the complex problem of energy conversion and storage, through the design, characterisation and testing of electrocatalytic materials for water electrolysis, photoelectrochemical water splitting and direct methanol fuel cell. It is expected that the first two processes will play an important role in the future as convenient technologies for the conversion of solar and wind power into chemical energy in the form of hydrogen. The third process is regarded as promising way to convert the renewable chemical energy in the form of methanol into electrical energy.

At the core of the research lies the design and development of electrocatalysts, which are directly responsible for lowering the reaction overpotentials and ultimately increasing the overall efficiency of the processes. As such, in this thesis three materials were synthesised using straightforward methodologies and evaluated as electrocatalysts for the alkaline hydrogen evolution, the photoelectrochemical oxygen evolution and the alkaline methanol oxidation. Their

performances were directly linked to the morphological and structural properties which in turn significantly affected the nature of active sites. For the first work reported in Chapter 3, a material based on a mixed cobalt nickel sulphide nanoparticles supported onto Ni foam showed high activity toward the hydrogen evolution reaction, with a required small overpotentials of 163 mV at a current density of 10 mA/cm^2 in 1.0 M KOH electrolyte. This value compares well with the best existing hydrogen evolution reaction electrocatalysts based on non-noble elements. Moreover the catalyst showed good durability which was tested under chronoamperometric conditions, maintaining an optimal performance for 72 hours. The origin of such high activity was attributed to the existence of an optimal nickel-cobalt sulphide ratio at the surface of the electrode, which was obtained by selecting the appropriate temperature and time of thermal annealing of the material. This optimal presence of the biphasic nickel-cobalt sulphide nanoparticles led to high electrochemically active surface area and small charge transfer resistance, as evidenced by the extensive characterisation analysis carried out on these materials. For the second work reported in Chapter 4, a WO_3/Co_3O_4 photoanode was successfully synthesised via a facile sol-gel method and tested for the photoelectrochemical oxygen evolution. It was found that the degree of crystallinity of the cocatalyst influenced heavily the photoelectrochemical activity towards the oxygen evolution. In particular, a poorly crystalline structure of Co_3O_4 led to an improvement of up to 40% in photocurrent generation compared to the bare WO_3. Interestingly, the highly crystalline Co_3O_4 significantly suppressed the photocurrent generation, as a result of the creation of an unfavourable band alignment, with a dramatic increase in the charge recombination at the interface. Finally, for the third and last work reported in Chapter 5, ultra-small Pt nanoparticles embedded on a 3D structure composed of CeO_2, NiO and Ni foam was synthesised and tested as electrocatalyst for the alkaline methanol oxidation reaction. The generated catalyst showed extremely high activity for the alkaline methanol oxidation, with mass and geometric current density values of 1160 mA/mgPt and 202 mA/cm^2, whose values are among the highest ever reported for Pt-based materials. It was demonstrated that the unique morphological architecture and existence of a synergistic effect between Pt and adjacent CeO_2 nanoparticles contributed decisively to the observed high performance. Particularly the presence of defective and poorly crystalline CeO_2 nanoparticles was beneficial to the efficient oxidative removal of the CO from the Pt active sites which resulted in a higher durability of the electrocatalyst. Moreover, the concomitant presence of the superficial $Ni(OH)_2$ was thought to contribute to the supply of OH species to the Pt, which act as reactants for the CO removal. The most active electrocatalyst was subjected to stability test, retaining 40 % of the initial geometric current density after 6 hours, and quite surprisingly the activity could be totally restored through straightforward CV scans in 1.0 M NaOH electrolyte.

Table of Contents

Table of Contents **i**

List of Tables v

List of Figures vii

DECLARATION OF AUTHORSHIP **xvii**

Acknowledgements **xix**

Definitions and Abbreviations **xxi**

Chapter 1: Introduction **1**

1.1 Renewable energy: current outlook and future perspectives 1

1.2 Renewable energy conversion and storage: current status and research trends 4

1.2.1 Water electrolysis for hydrogen production: fundamental analysis and overview of the different existing technologies 8

1.2.2 Photoelectrochemical water splitting as a direct way to convert solar energy into chemical energy: a general overview 14

1.2.3 Methanol as a means of renewable energy storage: insights into its synthetic preparation from renewable hydrogen and its utilisation as fuel in direct methanol fuel cells (DMFCs) 19

1.3 Electrocatalysis: the fundamental key toward making ever more efficient energy storage and conversion processes 25

1.3.1 Electrocatalysis for the hydrogen evolution reaction: a fundamental analysis 25

1.3.2 Role of electrocatalysts in the photoelectrochemical water splitting 30

1.3.3 Electrocatalysis for the methanol oxidation reaction: a fundamental analysis 33

1.4 References 35

Chapter 2: Experimental **39**

2.1 Characterisation techniques 39

2.1.1 X-ray Powder Diffraction (XRD) 39

2.1.2 Scanning Electron Microscopy (SEM) 42

2.1.3 Transmission Electron Microscopy (TEM) 45
2.1.4 Energy Dispersive X-ray Spectroscopy (EDX) 46
2.1.5 Selected Area Electron Diffraction (SAED) 47
2.1.6 Raman Spectroscopy 47
2.1.7 UV-Visible spectroscopy 49
2.1.8 X-ray Photoelectron Spectroscopy (XPS) 50
2.1.9 Electrochemical Impedance Spectroscopy (EIS) 52

Chapter 3: Design of active electrocatalyst based on cobalt-nickel sulphide composite electrode for the alkaline hydrogen evolution reaction 55

3.1 Introduction 56

3.1.1 Transition metal sulphides: a promising class of active electrocatalysts for the hydrogen evolution reaction 56
3.1.2 Objectives 60

3.2 Results and Discussion 61

3.2.1 Description of the synthetic methodology based on thermal decomposition of cobalt-thiourea molecular complex 61
3.2.2 Structural and morphological characterisation 62
3.2.3 Analysis of the hydrogen evolution reaction: understanding the links between structural and catalytic properties of the synthesised electrocatalysts 76

3.3 Conclusions 86
3.4 References 88
3.5 Appendix 91

3.5.1 Experimental methods 91

Chapter 4: Correlating the structural properties of Co_3O_4 cocatalyst to the photoelectrochemical activity of Co_3O_4/WO_3 photoanode 95

4.1 Introduction 96

4.1.1 Tungsten oxide as photoanode for the photoelectrochemical water splitting: description of the effect of synthetic methodology and presence of cocatalyst on its photocurrent generation 96

4.1.2 Objectives 100

4.2 Results and Discussion 101

4.2.1 Deposition of WO_3 and Co_3O_4 thin films using sol-gel method: an overview 101

4.2.2 Structural and morphological characterisation 103

4.2.3 Photoelectrochemical water oxidation analysis of Co_3O_4/WO_3 thin film: effect of the annealing temperature on the photocurrent generation 110

4.3 Conclusions 122

4.4 References 124

4.5 Appendix 126

4.5.1 Experimental methods 126

Chapter 5: Design of active and durable self-standing Pt-CeO_2-NiO-Ni foam electrocatalyst for the alkaline methanol oxidation 129

5.1 Role of metal oxide support in the catalytic activity of Pt-based electrocatalysts for the methanol oxidation reaction 130

5.1.1 Objectives 133

5.2 Results and Discussion 134

5.2.1 Analysis of the synthetic steps for the fabrication of Pt-CeO_2-NiO-Ni foam electrocatalyst 134

5.2.2 Structural and morphological characterisation 136

5.2.3 Methanol oxidation activity and stability: evaluation of the catalytic performance of the synthesised materials and investigation into the principal mechanisms of reaction involved 143

5.3 Conclusions 150

5.4 References 151

5.5 Appendix 154

5.5.1 Experimental methods 154

Chapter 6: Future prospects 157

List of Tables

Table 1.1 *Classification of the principal energy storage systems*..5

Table 1.2 *Specifications of the three current existing technologies for water electrolysis* 11

Table 1.3 *State-of-the-art of the best solar-driven water splitting devices demonstrated in laboratory scale*...18

Table 1.4 *Specifications of the three types of DMFC (the data were taken from ref* ^{51}*)*.........23

Table 1.5 *Summary of the reaction steps involved during the HER in acidic and alkaline electrolyte*...26

Table 2.1 *The seven categories of Bravais unit cells*...41

Table 3.1 *XPS quantitative analysis of the elemental composition on the surface of* Co_9S_8-Ni_xS_y*/Nif electrode for different synthetic conditions* 73

Table 3.2 *Summary of the electrochemical properties of the* Co_9S_8-Ni_xS_y*/Nif and* Ni_3S_2*/Nif electrodes for the HER in 1M KOH* 79

Table 3.3 *Comparison of the HER performance between selected electrocatalysts based on earth-abundant elements in alkaline media* 80

Table 3.4 *XPS quantitative analysis of the elemental composition on the surface of* Co_9S_8-Ni_xS_y*/Nif electrode before and after the stability test*................................85

Table 4.1 *Comparison of the PEC activity of some* WO_3*-based thin film photoanodes found in the literature*...111

Table 4.2 R_{Bulk}*,* CPE_{Bulk}*,* R_{CT}*,* CPE_{CT} *values as obtained from electrochemical impedance spectroscopy simulation fit*...115

Table 4.3 *Band energy values calculated for* WO_3 *and* Co_3O_4 *(the values are referred to the absolute electronic energy scale)*..119

Table 5.1 *Mass loading of Pt and* CeO_2 *calculated through ICP* 138

Table 5.2 *XPS quantitative analysis of the Pt^0 and Pt^{2+} oxidation states of the as-synthesised samples* 142

Table 5.3 *Comparison of the alkaline MOR performance between selected electrocatalysts in the literature* 145

Table 5.4 *Fitting parameters resulting from the modelling of EIS measurements at -0.6 and -0.3 V vs Ag/AgCl for Pt-CeO_2(350)/NiF, Pt-CeO_2(500)/NiF and Pt/NiF electrocatalysts* 147

List of Figures

Figure 1.1 *Share in global energy consumption in 2014 (taken from ref.* [4]*)*............................2

Figure 1.2 *Percentage of renewable energy by sector (taken from ref.*[5]*)* 2

Figure 1.3 *Projection of the world energy consumption in the transport sector based on energy source (adapted from ref.*[3]*)*..3

Figure 1.4 *(a) Percentage share of the energy storage systems accounting for 1% of the global storage capacity; (b) Maturity curve for some energy storage technologies (taken from ref.*[19]*)*..5

Figure 1.5 *Comparison of different energy storage systems as a function of storage capacity and discharge time (adapted from ref.*[20]*)*...6

Figure 1.6 *Different pathways and applications for hydrogen as renewable energy storage system*..7

Figure 1.7 *Theoretical cell voltage as function of temperature (taken from ref* [26]*)* 8

Figure 1.8 *Example of a polarization curve diagram showing the contribution of different losses on the overall cell performance (taken from ref* [28]*)*....................10

Figure 1.9 *Indicative system cost breakdowns for (a) alkaline and (b) PEM electrolysers; indicative stack cost breakdowns for (c) alkaline and (d) PEM electrolysers (adapted from ref* [33]*)*..12

Figure 1.10 *Two different routes for solar energy conversion into hydrogen: PV + water electrolysis versus PEC water splitting*..14

Figure 1.11 *(a) Band energy of a single absorber consisting of n-type photoanode and counter electrode; (b) Band energy of a dual absorber consisting of n-type photoanode and p-type photocathode (adapted from ref* [35,36]*)* 15

Figure 1.12 *Theoretical STH and photocurrent as a function of the semiconductor band gap (taken from ref* [35]*)*...16

Figure 1.13 *Simplified process flow diagram of the CAMERE (carbon dioxide hydrogenation to form methanol via reverse-water gas shift) process for the renewable methanol production (adapted from ref [42])* 19

Figure 1.14 *Comparison of gravimetric and volumetric energetic density for some selected fuels based on their lower heating value (taken from ref [45])* 20

Figure 1.15 *Comparison of energy storage density between batteries and fuel cells (assuming H_2 fuel cell efficiency 40% and DMFC efficiency 25%); (taken from ref [49])* 21

Figure 1.16 *Polarization curve for a generic DMFC, highlighting the principal sources of potential loss(taken from ref [52])* 22

Figure 1.17 *Schematic diagram of (a) proton exchange DMFC and (b) alkaline anion exchange DMFC (taken from ref [53,54])* 24

Figure 1.18 *Exchange current density as a function of the free energy of hydrogen adsorption in (a) acid and (b) alkaline media. (Fig. (a) and (b) are taken from [58] and [61])* 27

Figure 1.19 *(a) Linear sweep voltammetry of two theoretical catalysts possessing different Tafel slopes and same overpotentials required to reach a defined current density; (b) correspondent Tafel plot (taken from ref [58])* 28

Figure 1.20 *Comparison of a n-type semiconductor photoanode in (a) absence of OER catalyst and (b) presence of OER catalyst (adapted from ref [71])* 31

Figure 1.21 *Detailed schematic diagram of (a) n-type semiconductor photoanode and (b) p-type semiconductor photocathode fully covered by catalytic passivation layers (adapted from ref [71])* 32

Figure 1.22 *Trend in OER activity for some selected electrocatalysts (taken from ref [76])* 32

Figure 1.23 *Volcano plot representing the MOR overpotential as a function of the free energy of OH adsorption ΔG_{OH} and CO adsorption ΔG_{CO} (taken from ref [82])* 34

Figure 2.1 *Schematic representation of X-ray diffraction* 39

Figure 2.2 *Schematic representation of (a) transmission Debye-Scherrer geometry and (b) reflection Bragg-Brentano geometry* 40

Figure 2.3 *Schematic representation of the fourteen different types of Bravais unit cells* 42

Figure 2.4 *Illustration of the different signals generated by the electron beam-sample interaction during SEM as a function of the bulk penetration depth* 43

Figure 2.5 *Types of emission resulting from inelastic scattering of incident electrons; a) X-ray emission, b) Auger electron emission* 44

Figure 2.6 *Illustration of the different signals generated by the electron beam-sample interaction during TEM* 45

Figure 2.7 *Energy diagram of the three different states occurring during Raman analysis* 48

Figure 2.8 *Generation of electron-hole pair upon absorption of photons with energy equal to the band gap of the semiconductor* 49

Figure 2.9 *Scheme of the three different configurations normally found in UV-Vis spectrophotometers* 50

Figure 2.10 *Schematic representation of the atomic ionisation by interaction of a X-ray photon occurring during XPS* 51

Figure 2.11 *Effect of small excitation signal of potential E on the recorded current I* 52

Figure 2.12 *Example of a Nyquist plot* 53

Figure 3.1 *XRD patterns for* Co_9S_8-Ni_xS_y/*Nif different annealing temperatures and times (a) 400 °C 10 min, (b) 400°C 90 min; (c) 500°C 10 min, (d) 500°C 90 min* 64

Figure 3.2 *XRD patterns for the* Ni_3S_2/*Nif at different annealing temperatures and times (a) 400 °C 10 min, (b) 400°C 90 min, (c) 500°C 10 min, (d) 500°C 90 min* 64

Figure 3.3 *Raman spectra for* Co_9S_8-Ni_xS_y/*Nif at different annealing temperatures and times (a) 400 °C 10 min, (b) 400°C 90 min, (c) 500°C 10 min, (d) 500°C 90 min* 65

Figure 3.4 *Low- and high-magnification SEM images for Co_9S_8-Ni_xS_y/Nif at different annealing temperatures and times (a) 400 °C 10 min, (b) 400°C 90 min; (c) 500°C 10 min, (d) 500°C 90 min* 67

Figure 3.5 *Low- and high-magnification SEM images for Ni_3S_2/Nif at different annealing temperatures and times (a) 400 °C 10 min, (b) 400°C 90 min, (c) 500°C 10 min, (d) 500°C 90 min* 68

Figure 3.6 *TEM images for Co_9S_8-Ni_xS_y/Nif at different annealing temperatures and times (a) 400 °C 10 min, (b) 400°C 90 min; (c) 500°C 10 min, (d) 500°C 90 min. Selected area electron diffraction patterns for Co_9S_8-Ni_xS_y/Nif at (e) 500°C 10 min and (f) 500°C 90 min* 68

Figure 3.7 *EDX analysis for Co_9S_8-Ni_xS_y/Nif at different annealing temperatures and times* 70

Figure 3.8 *EDX analysis for Ni_3S_2/Nif at (a) 400 °C 90 min, (b) 500 °C 90 min* 71

Figure 3.9 *Ni2p XPS patterns for Co_9S_8-Ni_xS_y/Nif at different annealing temperatures and times (a) 400 °C 10 min, (b) 400°C 90 min, (c) 500°C 10 min, (d) 500°C 90 min* 74

Figure 3.10 *Co2p XPS patterns for Co_9S_8-Ni_xS_y/Nif at different annealing temperatures and times (a) 400 °C 10 min, (b) 400°C 90 min, (c) 500°C 10 min, (d) 500°C 90 min* 74

Figure 3.11 *S2p XPS patterns for Co_9S_8-Ni_xS_y/Nif at different annealing temperatures and times (a) 400 °C 10 min, (b) 400°C 90 min, (c) 500°C 10 min, (d) 500°C 90 min* 75

Figure 3.12 *Ni2p (left) and S2p (right) XPS patterns for Ni_3S_2/Nif at different annealing temperatures and times (a) 400 °C 10 min, (b) 400°C 90 min, (c) 500°C 10 min, (d) 500°C 90 min* 75

Figure 3.13 *IR-corrected polarization curves for (a) Co_9S_8-Ni_xS_y/Nif and (b) Ni_3S_2/Nif at different annealing temperatures and times in 1M KOH electrolyte* 77

Figure 3.14 *IR-corrected Tafel plots for (a) Co_9S_8-Ni_xS_y/Nif and (b) Ni_3S_2/Nif at different annealing temperatures and times in 1M KOH electrolyte* 77

Figure 3.15 *Nyquist plots of (a)-(b) Co_9S_8-Ni_xS_y/Nif, (c)-(d) Ni_3S_2/Nif recorded under potentiostatic mode at -0.230 V vs RHE in 1.0 M KOH. The fitting was performed using the simplified Randles circuit* 81

Figure 3.16 *Simplified Randles circuit used for the fitting of the EIS data; R_s, series resistance; R_{ct}, charge-transfer resistance; CPE, constant phase element* 82

Figure 3.17 *(a) Chronoamperometry test for Co_9S_8-Ni_xS_y/Nif annealed at 500°C 10 min at -0.161 V vs RHE in 1M KOH. (b) XRD spectrum, (c) Low- and high magnification SEM, (d) EDX chart of Co_9S_8-Ni_xS_y/Nif after 72 hours of stability test* 84

Figure 3.18 *XPS patterns for Co_9S_8-Ni_xS_y/Nif annealed at 500°C 10 min after chronoamperometry test for 72 hours* 85

Figure 4.1 *Simplified scheme of the chelating effect of acetylacetone on the W alkoxide by replacement of methanol molecules* 101

Figure 4.2 *XRD patterns of (a) WO_3 film on FTO glass annealed at 500 °C and (b) Co_3O_4 on silicon annealed at 500 °C* 103

Figure 4.3 *Evolution of XRD pattern of Co_3O_4 film on silicon at different annealing temperatures* 105

Figure 4.4 *XRD spectra of 1 layer Co_3O_4 (annealed at 500 °C) on FTO/WO_3. Due to the thin Co_3O_4 layer, only WO_3 and FTO layer is detected* 105

Figure 4.5 *(a) UV-Vis absorption spectra of FTO/WO_3 (black) and FTO/WO_3/Co_3O_4 (red) film, (b) Tauc plot and band gap determination of WO_3 film* 107

Figure 4.6 *Surface morphology of (a)FTO/WO_3 film, and (b) FTO/WO_3/Co_3O_4 film (Co_3O_4 was annealed at 500 °C). The arrows point to the short interconnecting rods between growth regions* 108

Figure 4.7 *Cross-Sectional view of FTO/WO_3/Co_3O_4 film* 108

Figure 4.8 *EDX analysis of FTO/WO_3/Co_3O_4 film* 108

Figure 4.9 *XPS spectra of Co 2p for Co_3O_4/WO_3 film with the cocatalyst annealed at 350 °C* 109

Figure 4.10 Photocurrent densities of bare FTO/WO_3 and FTO/WO_3/Co_3O_4 in 0.1 M Na_2SO_4 (pH 5.8) under a light intensity of 100 mW/cm^2(Co_3O_4, 1 layer annealed at 350 °C, blue), (Co_3O_4, 3 layers annealed at 350 °C, black)............. 111

Figure 4.11 Percentage change in photocurrent (with respect to bare WO_3) with cocatalyst annealing temperature for FTO/WO_3/Co_3O_4 films at 1.2 V vs Ag/AgCl in 0.1 M Na_2SO_4 (pH 5.8) under a light intensity of 100 mW/cm^2........ 112

Figure 4.12 XRD spectra of NiO_x film on silicon at different annealing temperatures......... 113

Figure 4.13 Percentage change in photocurrent (with respect to bare WO_3) with cocatalyst annealing temperature for NiO_x/WO_3 film at 1.2 V vs Ag/AgCl in 0.1 M Na_2SO_4 (pH 5.8) under a light intensity of 100 mW/cm^2.......................... 113

Figure 4.14 a) Nyquist plot of electrochemical impedance spectroscopy data for WO_3 and Co_3O_4/WO_3 film annealed at 350 °C at 1.2V vs Ag/AgCl. (b) Equivalent circuit used for modelling the electrochemical cell. All capacitances are modelled using constant phase element (CPE) to achieve a good fitting. R_{Bulk} and CPE_{Bulk} refer to the resistance and capacitance across the bulk semiconductor while R_{CT} and CPE_{CT} correspond to the charge transfer interfacial layer between the electrode and the electrolyte 114

Figure 4.15 Correlation between the circuit element values and the measured photocurrent percentage with respect to the bare FTO/WO_3 sample taken as reference; a) R_{CT}, b) CPE_{CT}, c) R_{Bulk}, d) CPE_{Bulk}... 117

Figure 4.16 Band diagram of a semiconductor with energy band levels. The vacuum level is taken as the zero energy reference... 118

Figure 4.17 Energy band diagram of the n-WO_3/p-Co_3O_4 heterojunction 120

Figure 4.18 Hydrogen evolution under light illumination of (a) Co_3O_4/WO_3 and (b) WO_3; Oxygen evolution under light illumination of (c) Co_3O_4/WO_3 and (d) WO_3. The gases were measured by in-line GC... 121

Figure 5.1 Scheme of the reaction mechanism occurring during the reduction of Pt^{4+} due to the OH-terminated group of PVP 135

Figure 5.2 XRD patterns of the as-synthesized Pt-CeO_2(350)/NiF (green), Pt-CeO_2(500)/NiF (blue) and Pt/NiF (red).. 136

Figure 5.3 *Low- and high-magnification SEM images of (a)-(b) Pt-CeO_2(350)/NiF and (c)-(d) Pt-CeO_2(500)/NiF* 137

Figure 5.4 *Low- and high-magnification SEM images of Pt/NiF* 137

Figure 5.5 *Low- and high-magnification SEM images of (a)-(b) CeO_2(350)/NiF and (c)-(d) CeO_2(500)/NiF* 138

Figure 5.6 *(a)-(b) TEM and HRTEM (insets) images of the Pt-CeO_2(350)/NiF sample. (c) Pt NPs size distribution of Pt-CeO_2(350)/NiF sample. (d)-(e)-(f) TEM and HRTEM (insets) images of the Pt-CeO_2(500)/NiF sample* 139

Figure 5.7 *TEM and HRTEM (inset) images of the Pt/NiF sample* 140

Figure 5.8 *XPS patterns of the as-synthesised Pt-CeO_2(350)/NiF* 140

Figure 5.9 *XPS patterns of the as-synthesised Pt-CeO_2(500)/NiF* 141

Figure 5.10 *XPS patterns of the as-synthesised Pt/NiF* 141

Figure 5.11 *(a) Cyclic voltammetry (CV) curves of Pt-CeO_2(350)/NiF (green), Pt-CeO_2(500)/NiF (blue) and Pt/NiF (red) electrodes in N_2-saturated 1 M NaOH at a scan rate of 50 mV/s; (b)-(c) iR-corrected CV curves of the three electrodes in 0.5 M methanol/1 M NaOH at a scan rate of 50 mV/s; (d) short-term chronoamperometry test of the three electrodes at -0.3 V vs Ag/AgCl in 0.5 M methanol/1 M NaOH. In (b) and (c), the recorded electric currents are divided by the geometric area of the electrodes and the mass loading of Pt, respectively* 144

Figure 5.12 *(a) Nyquist plot for Pt-CeO_2(350)/NiF (green), Pt-CeO_2(500)/NiF (blue) and Pt/NiF (red) electrodes under potentiostatic mode at -0.6 V vs Ag/AgCl in 0.5 M methanol/1 M NaOH and (b) correspondent fitting equivalent circuit. (c) Nyquist plot for the same electrodes at -0.3 V vs Ag/AgCl in 0.5 M methanol/1 M NaOH and (d) correspondent fitting equivalent circuit* 147

Figure 5.13 *(a) Cumulative long-term chronoamperometry test of Pt-CeO_2(350)/NiF electrocatalyst at -0.3 V vs Ag/AgCl in 0.5 M methanol/ 1 M NaOH; (b) Pt4f XPS pattern, (c) TEM and (d) Pt NPs size distribution of the catalyst after 18 hours of chronoamperometry* 149

Figure 5.14 *Low- and high-magnification SEM images of the Pt-*CeO_2*(350)/NiF after long-term chronoamperometry test* 149

DECLARATION OF AUTHORSHIP

I, Davide Ansovini

declare that this thesis and the work presented in it are my own and has been generated by me as the result of my own original research.

Catalysis for Sustainable Energy Conversion and Storage

I confirm that:

1. This work was done wholly or mainly while in candidature for a research degree at this University;
2. Where any part of this thesis has previously been submitted for a degree or any other qualification at this University or any other institution, this has been clearly stated;
3. Where I have consulted the published work of others, this is always clearly attributed;
4. Where I have quoted from the work of others, the source is always given. With the exception of such quotations, this thesis is entirely my own work;
5. I have acknowledged all main sources of help;
6. Where the thesis is based on work done by myself jointly with others, I have made clear exactly what was done by others and what I have contributed myself;
7. Parts of this work have been published as
    - C. S. Chua, D. Ansovini, C. J. J. Lee, Y. T. Teng, L. T. Ong, D. Chi, T. S. A. Hor, R. Raja and Y.-F. Lim, Phys.Chem.Chem.Phys., **2016**, 18, 5172.
    - D. Ansovini, C. J. J. Lee, C. S. Chua, L. T. Ong, H. R. Tan, W. R. Webb, R. Raja and Y.-F. Lim, J. Mater. Chem. A, **2016**, 4, 9744.

Signed: ....

Date:..

Acknowledgements

First of all I would to express my sincere gratitude to Prof. Robert Raja, my supervisor at the University of Southampton for the support received in these four years of PhD. His enthusiasm in embracing new ideas and encouraging his group to think out of the box has greatly influenced my research. Most importantly, he taught me how to be self-independent in research, which is perhaps one of the most difficult and rewarding things to achieve. I also will be always grateful to him for giving me the opportunity to conduct my PhD in two countries, UK and Singapore as part of the A*STAR scholarship.

For my time in Southampton, I would like to thank all the past and present members of the Raja group, with a special mention to Christopher Hinde, Arran Gill and William Mothersole. With them I had the pleasure to share many important experiences throughout my PhD journey, inside and outside work. A big thanks goes to William Webb, who has promptly helped me to carry out some experiments which have added value to my research.

During the two years spent in Singapore I had the privilege to expose myself to a new stimulating environment, which truly broadened my horizon from a professional and cultural point of view. I would like to thank Dr. Yee-Fun Lim, my co-supervisor at IMRE, for welcoming me in his group and helping me in my research. He introduced me to new exciting areas of materials science, and I will be always grateful to him for that. I also would like to thank my group colleagues Dr. Chin Sheng Chua and Coryl Lee, for their important practical support provided to my work. To Weng Heng Liew, my fellow work colleague, I will not forget our stimulating discussions during my days in the lab which kept us motivated and hopeful despite some tough times.

Outside of work, my heartfelt gratitude goes to my sister, mum and dad for their unconditional love and encouragement. They have always stood by my side in every circumstance, and without them I would not have been the person that I am today.

Finally, I would like to express my deepest gratitude to my beloved wife Serena, who is my greatest source of inspiration, my confidant, my pillar of strength, my lifelong companion. She has always motivated me to go beyond my limits and realise my goals with love and enthusiasm. For all these reasons this thesis is dedicated to her.

Definitions and Abbreviations

AC: Alternating current

Ag/AgCl: Silver/silver chloride electrode

AM 1.5: Air Mass coefficient

AMOR: Alkaline Methanol Oxidation Reaction

CAMERE: Carbon dioxide hydrogenation via reverse-water gas shift

CPE: Constant Phase Element

CV: Cyclic Voltammetry

DFT: Density Functional Theory

DMFC: Direct Methanol Fuel Cell

ECSA: Electrochemical Active Surface Area

EDX: Energy Dispersive X-ray Spectroscopy

EIS: Electrochemical Impedance Spectroscopy

EU: European Union

FTO: Fluorine-doped Tin Oxide

FWHM: Full Width at Half Maximum

HAADF: High-Angle Annular Dark Field

HER: Hydrogen Evolution Reaction

HES: Hydrogen Energy Storage

HRTEM: High-Resolution Transmission Electron Microscopy

ICP: Inductively Coupled Plasma

IEA: International Energy Agency

IREA: International Renewable Energy Agency

JCPDS: Joint Committee on Powder Diffraction Standards

LSV: Linear Sweep Voltammetry

MHE: Material Handling Equipment

MOR: Methanol Oxidation Reaction

NHE: Normal Hydrogen Electrode

NP: Nanoparticle

OER: Oxygen Evolution Reaction

ORR: Oxygen Reduction Reaction

PBEC: Photovoltaic-Biased Electrosynthetic Cell

PBPC: Photovoltaic-Biased Photoelectrosynthetic Cell

PC: Photoelectrosynthetic Cell

PEC: Photoelectrochemical water splitting

PEG: Polyethylene Glycol

PEM: Polymer Electrolyte Membrane

PHS: Pumped Hydro Storage technology

PV: Photovoltaic

PVP: Poly(vinyl pyrrolidone)

RDS: Rate-Determining Step

RHE: Reversible Hydrogen Electrode

SAED: Selected Area Electron Diffraction

SCE: Saturated Calomel Electrode

SCLJ: Semiconductor-Liquid Junction

SEM: Scanning Electron Microscopy

SOE: Solid Oxide Electrolysis

STH: Solar-To-Hydrogen efficiency

TEM: Transmission Electron Microscopy

TMS: Transition Metal Sulphide

UN: United Nations

XPS: X-ray Photoelectron Spectroscopy

XRD: X-ray Powder Diffraction

Chapter 1: Introduction

1.1 Renewable energy: current outlook and future perspectives

Undoubtedly fossil fuels based on oil, coal and natural gas have played a fundamental role behind the unprecedented technological, economic and social development witnessed over the past two centuries. They provided immense amount of cheap and readily available high quality energy which fuelled the expansion of almost every industrial sector. This, in turn, led to a rapid exponential growth of the world population, reaching a record number of 7.4 billion in 2016. According to recent projections issued by the United Nations (UN), the global population will reach 9 billion in 2050, which means there will be 2 billion more people in a time span of only 35 years from now.[1] As a result, the global energy consumption will increase from the current 15 TW to 30 TW by 2050.[2] From these numbers it is clear how global population determines the global energy consumption. On the other hand it is the amount of global energetic availability that influences directly or indirectly the world population growth, shaping governmental policies and corporate investments. In order to meet the ever-increasing demand of energy, the International Energy Agency (IEA) forecasts an increase in the worldwide consumption of petroleum and liquid fuels from 90 million barrels per day (b/d) in 2012 to 121 million b/d in 2040.[3] Such a high demand of oil, mainly from emerging economies in Africa, Asia and the Middle East with strong economic growth and rising populations, is expected to significantly increase the crude oil price up to unsustainable levels over the long term. In contrast, demand for liquid fuels in the United States, Europe and other countries with mature economy is expected to grow slowly or even decrease over the long term. This is partly due to the implementation of government policies with the aim of promoting the use of non-fossil sources, such as renewable and nuclear power. These policies rely on a clear strategic plan, which can be summarised in the following points: 1) boosting the energy security; 2) mitigating the effects of climate change and air/water pollution due to fossil fuel combustion; 3) resilience toward future expected high oil price.

Indeed, renewable energy is now the world's fastest-growing source of energy, at an average of 2.6%/year.[3] In particular, the year 2015 saw a dramatic boost in renewable energy investments, with the largest capacity addition ever recorded, despite low global oil prices and weak economic growth.[4] However several challenges hamper an even more rapid expansion of the renewable energy sector, such as low subsidies compared to those given for fossil fuels, proper integration of variable and intermittent renewable energy in the grid and regulatory barriers and financial constraints.[4] In 2014 renewable energy accounted for 19.2% of the overall energy consumption, as shown in Fig. 1.1. Of this share, traditional biomass used for cooking and heating especially in rural areas of developing countries accounts for 8.9%, with the remaining 10.3% coming from the so-called modern renewables, which comprise hydropower, solar photovoltaics, wind, solar-thermal power, geothermal, biomass, tidal power.

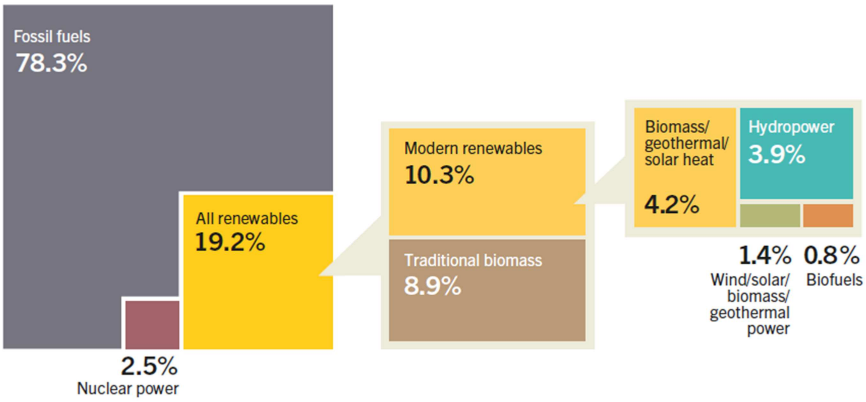

Figure 1.1 *Share in global energy consumption in 2014 (taken from ref. [4])*

The percentage share of renewable energy sources in the global electricity production has seen a sharp increase over the last decade, reaching a value of over 20% as reported in Fig. 1.2.[5] In particular, hydropower source accounts for 70% of the overall generated renewable electricity. Wind power and solar photovoltaics lag significantly behind, despite being the fastest growing sources of renewable electricity production, with over 63 GW and 50 GW of power added in 2014, respectively.[4,6]

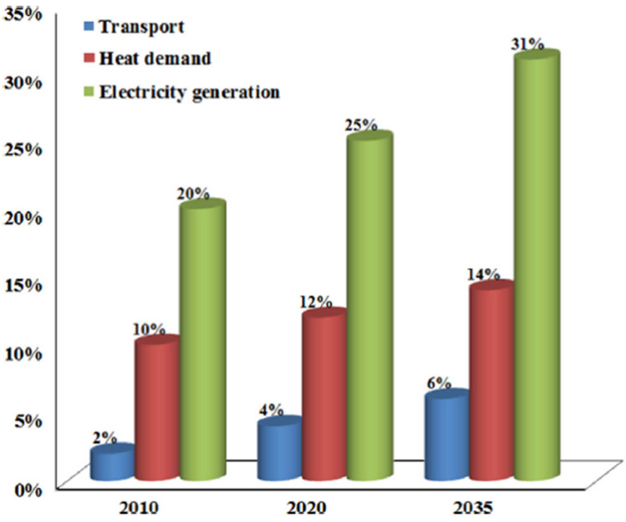

Figure 1.2 *Percentage of renewable energy by sector (taken from ref.[5])*

However, the widespread diffusion of solar and wind power has been limited by the intrinsic intermittency of these sources, which lack of demand flexibility, back-up power and enough electricity storage.[7] In order to tackle this problem, several energy storage systems have been investigated, with considerable investments made in recent years. At present, batteries seem to be the most mature technology, although cost still remains a big hurdle to large-scale deployment. An extensive overview of this topic will be given in Paragraph 1.2.

The percentage share of renewable energy in the heating/cooling sector accounts for 25%, although more than half of this value derives from the traditional biomass such as wood, which is mainly used in developing countries. Currently the most exploited modern renewable sources are biomass, solar thermal power and geothermal power, which account for the remaining 10% of the overall heating/cooling energetic demand. Recent projections have shown that in 2050 the global number of households will grow by 67% and the floor area of service sector buildings by almost 195%.[8] As a result, new government policies have been implemented for increasing the share of renewables, especially in the European Union (EU) where the heating/cooling sector accounts for 50% of the EU's annual energy consumption and 68% of all gas imports.[9]

The transport sector has been growing constantly in recent years, accounting for 30% of the global energy consumption in 2015.[4] Furthermore the transport sector causes severe air pollution in urban areas due to particulate matter, which has been linked to 7 million premature deaths annually.[10]

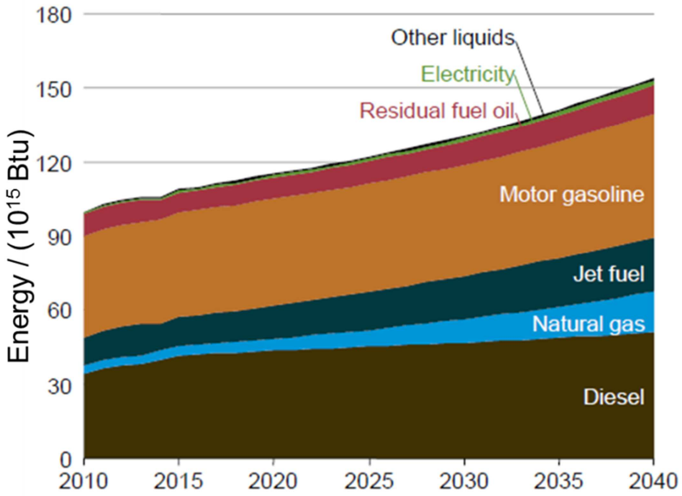

Figure 1.3 *Projection of the world energy consumption in the transport sector based on energy source (adapted from ref.[3])*

As reported in Fig. 1.2, the share of renewable energy in this sector is rather low, accounting for a 4% of the global transport energy demand. Liquid and gaseous biofuels, such as bio-ethanol, bio-diesel and biogas represent the vast majority of renewable energy sources used in the transport sector. However the effective sustainability of biofuels has been recently under intense debate, because of their adverse impacts on natural environment, food security and land use.[11] The latest projections issued by the International Energy Agency suggest that fuels derived from fossil sources will remain the dominant source of transportation energy over the next 25 years, as illustrated in Fig. 1.3. However, there are some regional exceptions to this global forecasted trend. For example, the EU has set the ambitious target of having 10% of the overall European transport fuel from renewable sources by 2020.[12] In the US there are current efforts to promote the diffusion of electric vehicles through significant investments in R&D and infrastructures. REmap 2030, a global roadmap released by the International Renewable Energy Agency (IREA), forecasts a total of 27 million electric vehicles in the US car stock in 2030, reducing the fuel use by a factor of three.[13] Indeed, transport electrification will be sustained by the ever-increasing percentage of electricity derived from renewable sources, thus dramatically lowering the negative urban environmental impact caused by fuel's combustion.

1.2 Renewable energy conversion and storage: current status and research trends

As anticipated in Paragraph 1.1, one of the limiting factors hampering the large scale deployment of wind turbines and solar photovoltaics as renewable electricity sources is represented by the lack of reliable and cost-effective energy storage systems well-integrated with the existing grid. Indeed, energy storage systems are regarded as a key solution to deal with the intermittency of renewable sources, providing a constant power supply.[7] In addition, the energy storage is a strictly required technology for the wide success of the distributed energy generation system, where small scale renewable power sources (small hydro, biomass, biogas, solar power, wind power and geothermal power) are installed close to end-users.[14] This is because the distributed energy network is more susceptible to higher load fluctuations and possibility of line faults than a conventional centralised power generation system. As such, the global energy storage market is set to increase sensibly, from an initial base of 0.34 GW installed in 2013 to 5 GW in 2017 and over 40 GW by 2022.[15]

The principal energy storage technologies are categorized and reported in Tab. 1.1. Currently more than 99% of the global energy storage capacity is made up of large scale pumped hydro storage technology (PHS), with 200,000 MW across 200 sites in the world.[16] As illustrated in Fig. 1.4(b), the PHS is the most mature technology among the various existing energy storage systems. Basically a PHS system is based on pumping water from a lower source into a higher reservoir during excess electric generation. At times of high electricity demand, water is released back into the lower reservoir through a turbine, generating electricity. The remaining 1% of the global energy storage capacity is split according to the pie chart in Fig. 1.4(a).

Mechanical	**Thermal**	**Electrochemical**	**Electric**	**Chemical**
Pumped Hydro Storage (PHS)	Hot Water Systems	Advanced Lead Acid Battery	Supercapacitor	Hydrogen
Compressed Air Energy Storage (CAES)	Pumped Heat Electrical Storage	Lithium-ion Battery	Superconducting Magnetic Energy Storage (SMES)	
Flywheels	Concentrating Solar Power (CSP)	Sodium Sulfur Battery		
Liquid Air Energy Storage		Flow Battery		

Table 1.1 *Classification of the principal energy storage systems*

In particular, battery storage, which accounts for slightly more than 50% at the moment, is becoming increasingly economic due to a constant fall of the manufacturing cost principally driven by the effect of economy of scale. Particularly the cost of lithium-ion battery, which is the technology of choice for the electric vehicle sector, is expected to fall by 50% in the next 5 years as a result of the increasing electric vehicle market expansion.[17] Advanced lead-acid, flow batteries and other types have experienced a less pronounced cost decline, whereas the cost of sodium-sulphur batteries is not expected to decrease. This, in turn, will enable a rapid deployment of battery technologies especially in the renewable solar and wind energy sector, with an expected annual battery storage capacity of 14 GW in 2023, compared to 360 MW in 2014.[18]

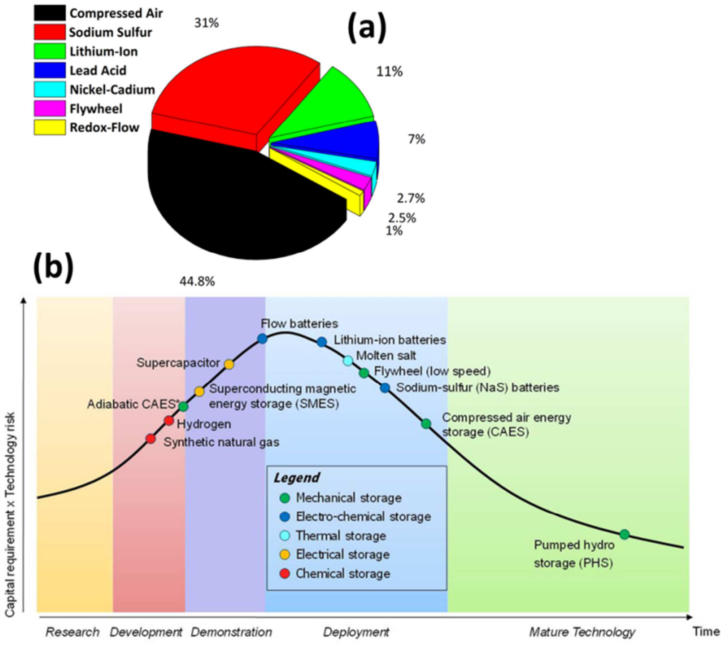

Figure 1.4 *(a) Percentage share of the energy storage systems accounting for 1% of the global storage capacity; (b) Maturity curve for some energy storage technologies (taken from ref.*[19]*)*

Hydrogen energy storage (HES) systems are still at the development stage as highlighted in Fig. 1.4(b), although they have the potential to play an important role in the renewable energy storage sector in the long-term. In fact, HES systems differ sensibly from the more traditional mechanical and electrochemical energy storage technologies in terms of energy storage capacity and versatility of the hydrogen (H_2) as a potential energy carrier and chemical feedstock. The energy which can be stored using these systems is two orders of magnitude higher than batteries, as reported in Fig. 1.5.

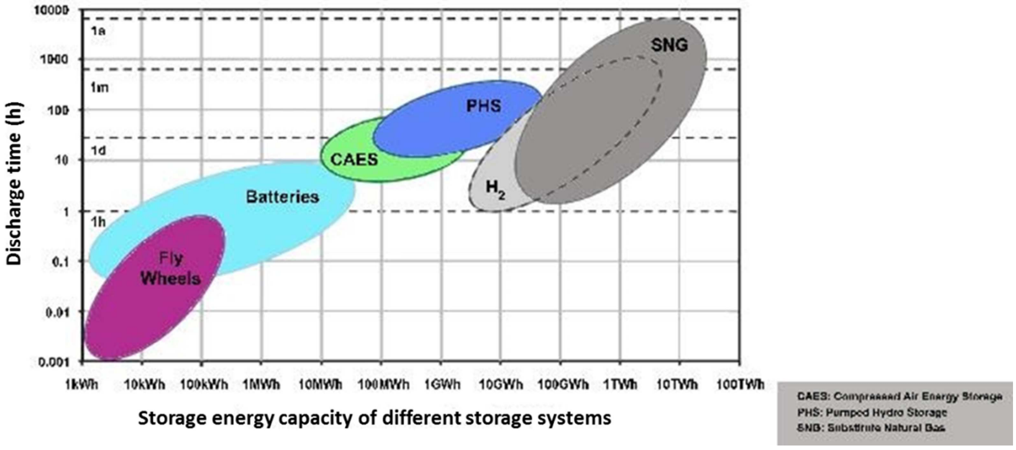

Figure 1.5 *Comparison of different energy storage systems as a function of storage capacity and discharge time (adapted from ref.*[20]*)*

Moreover, the HES systems can involve multiple processes and end-user markets that are not feasible for batteries, pumped hydro or compresses air storage.[21] A schematic diagram of the possible pathways for the HES system is displayed in Fig. 1.6. The hydrogen generated through water electrolysis can be used as fuel, chemical feedstock or blended with natural gas, in response to the prevailing regional market needs. According to a recent analysis, the deployment of the HES technology will be mainly driven by the expansion of the fuel-cell vehicle sector, although at the moment only in limited markets mainly in Japan and California.[22] At present, other entry markets such as the indoor material handling equipment (MHE) and remote backup power systems are stimulating the demand for additional hydrogen production and building of delivery infrastructure.[21]

The blending of hydrogen into natural gas pipeline with low concentrations of less than 5-15% is gaining particular attention as a viable means of increasing the output of large-scale renewable energy facilities, such as wind and solar farms.[23] In particular blending can provide a cost-effective solution for hydrogen storage and delivery to markets across large geographic areas. Blending renewable hydrogen increases the sustainability of the natural gas delivered to consumers, by reducing the greenhouse gas emissions.

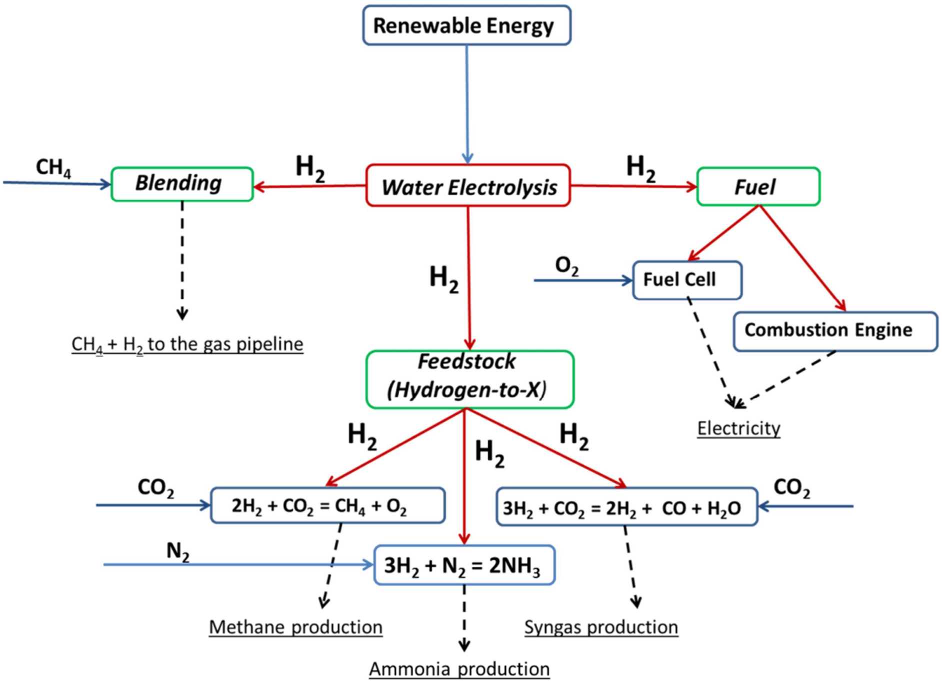

Figure 1.6 *Different pathways and applications for hydrogen as renewable energy storage system*

Also, the blended hydrogen could be extracted and delivered as pure feedstock for electric fuel cell vehicles and stationary fuel cell stations in remote locations, although this is expected to be economically-feasible only in the long-term.[23]

In recent years, particular attention has been paid to developing viable technologies for the conversion of renewable power to methane and syngas using hydrogen and carbon dioxide as reactants, in a general process called “power-to-gas” conversion. This approach represents an alternative to the hydrogen blending, which holds several limitations such as low blending concentration allowed and potentially expensive modifications to the existing natural gas pipelines required. Moreover, the production of syngas is the first step toward making liquid energy carriers and chemicals, thus interconnecting effectively renewable energy with a myriad of other markets. Several demonstration plants are currently under operation in Japan and Germany, where an extensive investigation into the techno-economic feasibility of these systems is currently underway.[24] At present, the power-to-gas technologies have a low efficiency and a high cost, which have been mainly attributed to the water electrolysis step for the hydrogen production. Besides, a high share of renewable energy in the global energy production is indispensable in order to render economically viable these systems, according to previous studies.[25]

1.2.1 Water electrolysis for hydrogen production: fundamental analysis and overview of the different existing technologies

Water electrolysis is a crucial and fundamental component for producing hydrogen from renewable sources, as discussed in Paragraph 1.2. A cheap, efficient, flexible, stable and reliable electrolysis system would dramatically lower the hydrogen production cost, paving the way for a more effective diffusion of the HES technology in the global energy storage sector.

From a fundamental point of view, water is decomposed into hydrogen (H_2) and oxygen (O_2) in an electrochemical cell using electric current and appropriate electrocatalysts at the cathode and anode, respectively. The electrolysis is generally carried out in either acidic or alkaline electrolyte, with the following half redox reactions:

- Cathode (H_2 production) – *Acidic electrolyte*: $2H^+_{(aq)} + 2\ e^- \rightarrow H_{2(g)}$
- Cathode (H_2 production) – *Alkaline electrolyte*: $2H_2O_{(l)} + 2e^- \rightarrow H_{2(g)} + 2OH^-_{(aq)}$
- Anode (O_2 production) – *Acidic electrolyte*: $2H_2O_{(l)} \rightarrow O_{2(g)} + 4H^+_{(aq)} + 4e^-$
- Anode (O_2 production) – *Alkaline electrolyte*: $4OH^-_{(aq)} \rightarrow O_{2(g)} + 2H_2O_{(l)} + 4e^-$
- Overall reaction: $\mathbf{2H_2O_{(l)} \rightarrow 2H_{2(g)} + O_{2(g)}}$

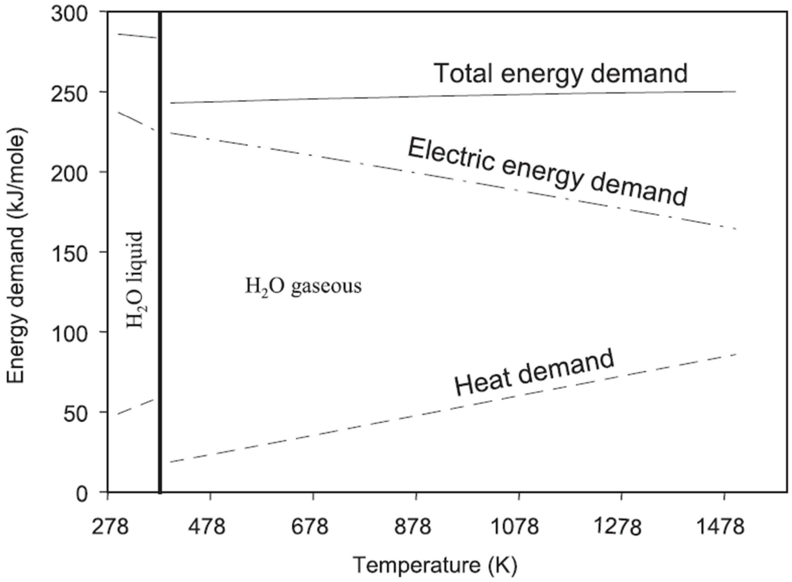

Figure 1.7 *Theoretical cell voltage as function of temperature (taken from ref*[26]*)*

In order to split one mole of liquid water to produce one mole of hydrogen at 25 °C, 285.8 kJ of energy are required, of which 237.2 kJ as electricity and 48.6 kJ as heat according to the Gibbs equation:

$$\Delta H_r^0 = \Delta G^0 + T\Delta S^0 = 285.8\frac{kJ}{mol} = 237.2\frac{kJ}{mol} + 48.6\frac{kJ}{mol} \qquad 1.1$$

The Gibbs free energy ΔG^0 represents the thermodynamic amount of electrical energy required, whereas the last term of the equation ($T\Delta S^0$) corresponds to the thermal energy required to compensate the irreversible entropic losses. Based on these considerations, it is possible to define two important thermodynamic potentials for water electrolysis:

$$E_{rev} = \frac{\Delta G^0}{nF} \tag{1.2}$$

$$E_{th} = \frac{\Delta H_r^0}{nF} \tag{1.3}$$

The reversible potential E_{rev} is the minimum necessary cell voltage to start water electrolysis, and its value is 1.23 V at 25 °C and 1 atm. The thermoneutral potential E_{th} represents the voltage at which hydrogen and oxygen are produced without any excess heat generated or required from the reaction. Therefore at this value, which is 1.48 V at 25 °C and 1 atm, the cell operates adiabatically. The electrolysis efficiency can be defined as the thermoneutral potential over the operating cell potential:

$$\epsilon = \frac{\Delta H_r^0}{\Delta G} = \frac{E_{th}}{E} \tag{1.4}$$

From the above equation, when $E = E_{rev} = 1.23$ V, the electrolysis efficiency reaches its maximum value of 120 %. In this case, external heat is required to supply the remaining energy deriving from the entropic losses ($-T\Delta S$). When $E = E_{th} = 1.48$ V, the efficiency is 100 % and no external heat is required. When $E \geq E_{th}$, the efficiency is lower than 100 % and in this case excess heat is generated from the electrochemical reaction. As shown in Fig. 1.7, at high temperatures a significant part of the total energy demand can be provided by heat. For example, at 80 °C ΔG^0 is 93% of the total energy demand ΔH^0_r, but at 750 °C it is only 77%.[27]

In a working water electrolyser the applied cell voltage is substantially higher than the thermodynamic reversible potential, as a result of several irreversible losses present in the system.

$$E_{wor} = E_{th} + \eta_{an} + |\eta_{cat}| + i \cdot R_A + \eta_{conc} \qquad 1.5$$

The equation 1.5 relates the working cell voltage to the principal sources of irreversibility, which are described below:

- η_{an}, η_{cat}: activation losses attributed to the kinetics of oxygen and hydrogen evolution at the anode and cathode, respectively
- $i \cdot R_A$: ohmic losses induced by the electrical resistance of the cell and ionic resistance of the electrolyte
- η_{conc}: overpotential associated with the mass transport limitations occurring during the reaction

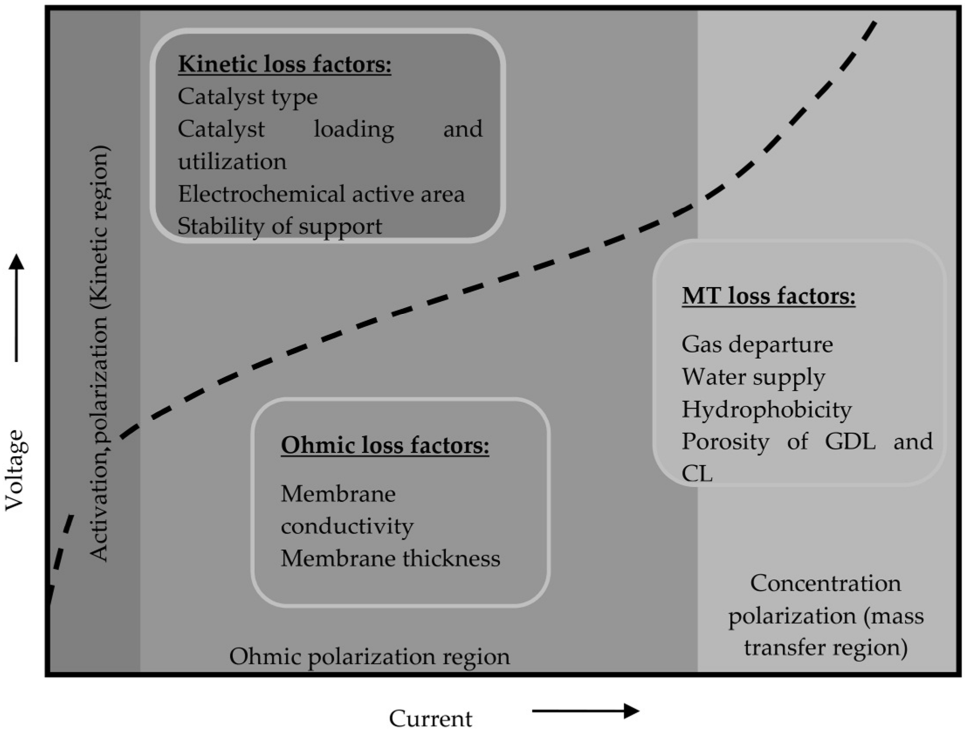

Figure 1.8 *Example of a polarization curve diagram showing the contribution of different losses on the overall cell performance (taken from ref* [28]*)*

A typical polarization curve showing the relationship between cell voltage and current density is reported in Fig. 1.8, which also depicts the contribution of each loss on the overall cell performance. For a well-designed electrolyser, the major source of irreversibility is represented by the activation losses of the oxygen evolution reaction (OER) and hydrogen evolution reaction (HER). The overpotential for the OER is generally dominant, given the more complex nature of this reaction, which is based on a 4-electron transfer process. These overpotentials can be minimized through the design of appropriate electrocatalysts, which will be discussed with more detail in Paragraph 1.3.

From an industrial perspective, there are three main types of water electrolysers, which are summarized in the table below:

Specifications	Alkaline electrolysis	Polymer electrolyte membrane (PEM) electrolysis	Solid oxide electrolysis (SOE)
Electrolyte	Aqueous KOH 30% wt. [29]	Solid polymer electrolyte [28]	ZrO_2-8%Y_2O_3 [27]
Anode catalyst (OER)	Ni/Co/Fe [29]	IrO_2[28]	$La_{1-x}Sr_xMnO_3$ [27]
Cathode catalyst (HER)	Ni/C-Pt [29]	Pt [28]	$La_{1-x}Sr_xMnO_3$ [27]
Operating temperature (°C)	60-80 [30]	50-80 [30]	500-850 [27]
Operating pressure (bar)	< 30 [30]	< 30 [30]	40 [31]
Current density (A/cm^2)	0.2-0.4	0.6-2	1-3 [32]
Cell efficiency (% LHV)	52-69 [30]	57-69 [30]	77 [31]
Cell voltage (V)	1.8-2.4 [30]	1.75-2.20 [30]	1.1-1.4 [32]
Cell area (m^2)	< 4 [30]	< 0.03 [30]	0.05-0.1 [32]
Specific stack energy consumption (kWh/kgH$_2$)	47.0-66.1 [30]	47.0-62.7 [30]	-
Stack H$_2$ production rate (Nm^3/h)	< 760 [30]	< 10 [30]	< 10 [32]
Lifetime stack (h)	< 90,000 [30]	< 20,000 [30]	-
Electrolyser Cost (€/kW)	760-1,100 [33]	1,200-1,940 [33]	-
H$_2$ production cost (€/kg)	3.2[33]	4.1[33]	-
Development stage	Well established technology	Less mature technology than alkaline electrolyser	Laboratory stage

Table 1.2 *Specifications of the three current existing technologies for water electrolysis*

At present the alkaline water electrolysis is the most established technology, largely dominating the market and accounting for nearly all the installed water electrolysis capacity worldwide. Polymer electrolyte membrane (PEM) electrolysis has entered the commercialisation stage over 10 years ago, and its technology is relatively less mature than the alkaline electrolysis, with more room for improvement. In contrast, the so-called solid oxide electrolysis (SOE) process is still at the early development stage, with an expected start of commercialization by 2020. [33] Much attention has been devoted to the development of the SOE, which offers great potential as a new low-cost and high-efficiency process for water electrolysis. Technical advantages of SOE process are a potentially higher electrical system efficiency compared to low-temperature electrolysis and the possibility to use both steam and CO_2 to produce syngas, which is the precursor for the synthesis of liquid fuels.

Currently, several factors limit the widespread diffusion of the water electrolysis process, which are linked principally to high cost and low efficiency. As a result, numerous efforts have been made in order to increase the efficiency and bring down the capital cost of the electrolysers. As for the first point, high electrical efficiencies have already been demonstrated, with little or no further margin of improvement. Therefore, reducing the capital cost of high-efficiency electrolysers is the key for improving their commercial viability.

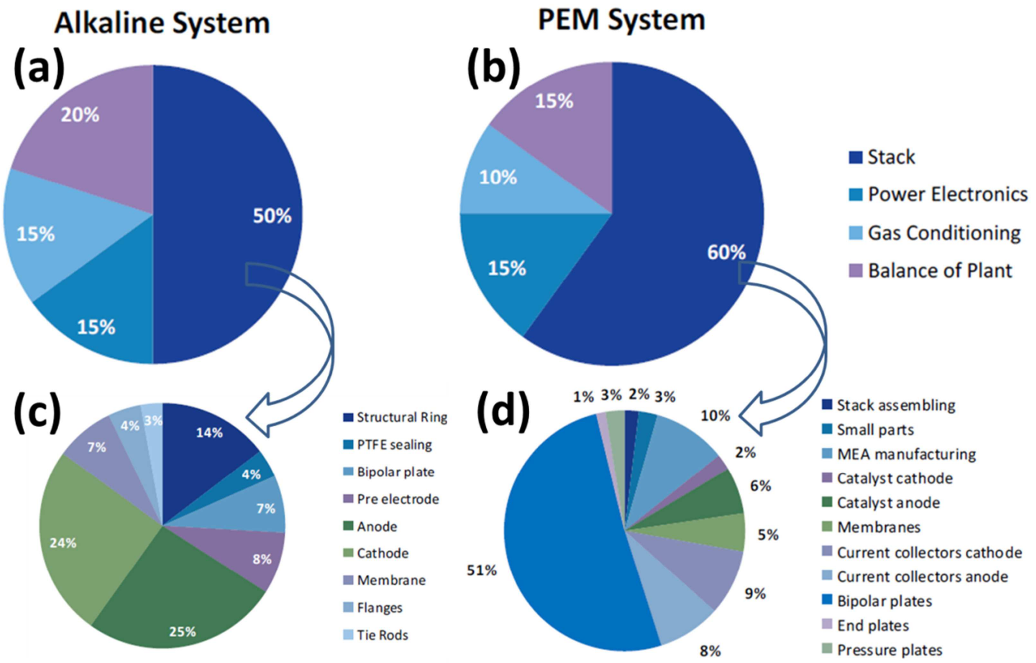

Figure 1.9 *Indicative system cost breakdowns for (a) alkaline and (b) PEM electrolysers; indicative stack cost breakdowns for (c) alkaline and (d) PEM electrolysers (adapted from ref* [33]*)*

As shown in Fig. 1.9(a) and 1.9(b), the incidence of the cost of the cell stack on the overall system cost is significant, for both the alkaline and PEM electrolysers. However, the partition of the cell stack cost is quite different between alkaline and PEM systems (Fig. 1.9(c), 1.9(d)). In the alkaline electrolyser, the cell stack cost is largely driven by the size and weights of the components, because of the large cell geometries necessitated by the intrinsic low current densities available.

In this regard, increasing the current density is one key parameter to lower the system cost. Indeed, much R&D is focused on developing new catalysts with controlled morphologies which are able to increase the current density up to 1 A/cm^2 from the current 0.2-0.4 A/cm^2.[33] In the case of the PEM electrolyser, the cost due to the fabrication of bipolar flow field plates represents the major contribution to the cell stack cost (51%). Catalyst materials, which are made of Pt for the HER and IrO_2 for the OER are non-negligible cost factors, contributing for almost 10% of the overall cell stack cost. Therefore, the design and fabrication of less expensive bipolar plates represents the top-priority for lowering the cost of PEM systems in the near-term. Also, increasing the cell active area is another important factor for minimising the expensive materials required to withstand the acidic environment. Finally, another important area of research is linked to the development of new active electrocatalysts made of earth-abundant elements able to match the current performances of Pt and IrO_2. It is expected that the reduction in catalyst cost will be an important factor in the long-term.

1.2.2 Photoelectrochemical water splitting as a direct way to convert solar energy into chemical energy: a general overview

As part of the continuous effort to find new and reliable technologies able to efficiently convert and store renewable energy, photoelectrochemical (PEC) water splitting can be regarded as a promising method to directly transform solar energy into chemical energy in the form of molecular hydrogen. The main interesting feature of this technology is its ability to combine solar-to-electricity with electricity-to-hydrogen steps in only one device, with potential benefits in terms of capital costs and system complexity compared to the traditional approach based on a photovoltaics/water electrolysis process. This can be better visualized in Fig. 1.10.

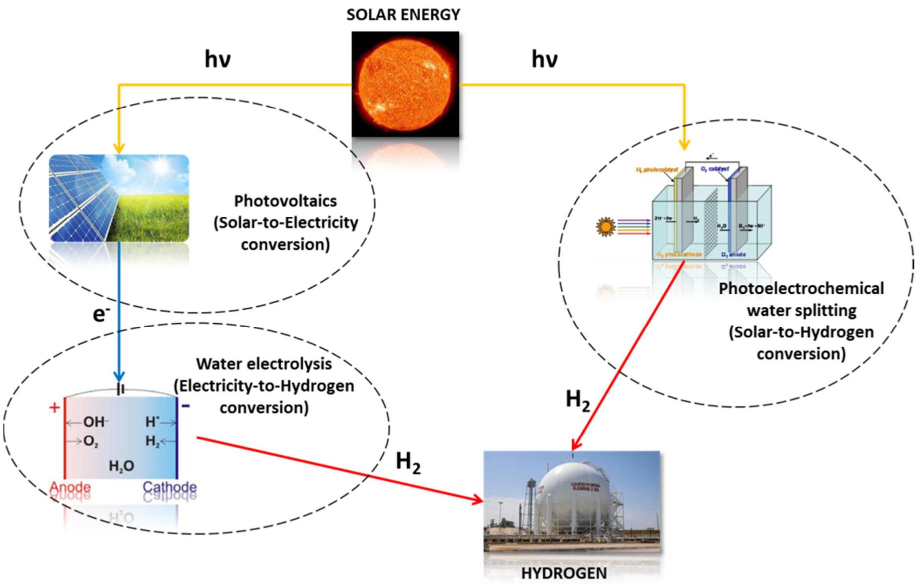

Figure 1.10 *Two different routes for solar energy conversion into hydrogen: PV + water electrolysis versus PEC water splitting*

Although initially demonstrated over 40 years ago,[34] PEC water splitting process is still at the laboratory-stage, mainly because of serious technological barriers which can be summarised in the following points:

- Poor stability
- Low solar-to-hydrogen conversion
- Low technological development of photocells/photoreactors

However, in a hypothetical fossil fuel-free world, the PEC water splitting could play an important role as principal technology for the generation of hydrogen in large-scale solar-to-hydrogen production factories. Hydrogen is currently produced from steam reforming and partial oxidation of natural gas, oil and coal, totally accounting for 96% of the global hydrogen production. The remaining 4% is produced through water electrolysis. Thus, reducing the reliance on fossil fuels could trigger an industrial interest for further development and eventual commercialization of the PEC water splitting technology in the long-term.

Basically, in the PEC water splitting a photoactive semiconductor with the right set of properties is immersed in aqueous electrolyte and irradiated with sunlight. Upon direct contact with the electrolyte, the semiconductor's chemical potential (the Fermi level) is equilibrated with the oxidation/reduction potential of the electrolyte, generating an electric field of width W at the semiconductor-liquid junction (SCLJ). This area is called the space-charge region, and here it is possible to separate the photogenerated electrons in the conduction band from the holes in the valence band upon the absorption of photons with energy greater than the semiconductor's band gap. Then, the photogenerated electrons and holes travel through the semiconductor in opposite directions and reach the solid-liquid interface. Once at the interface, the separated electrons and holes drive the hydrogen evolution and oxygen evolution reaction, respectively. In order to split water through this process, several general conditions must be met, which can be outlined below:

1. The semiconductor band gap must be small enough to absorb a large portion of the solar spectrum, and big enough to generate enough photovoltage to overcome the thermodynamic and kinetic energetic requirements for water splitting
2. The band edge potentials of the semiconductor must straddle the hydrogen and oxygen redox potentials
3. The semiconductor must be stable against corrosion over the long-term
4. The charge transfer from the surface of the semiconductor to the solution must be facile in order to facilitate the kinetics for the hydrogen evolution reaction (HER) and oxygen evolution reaction (OER)

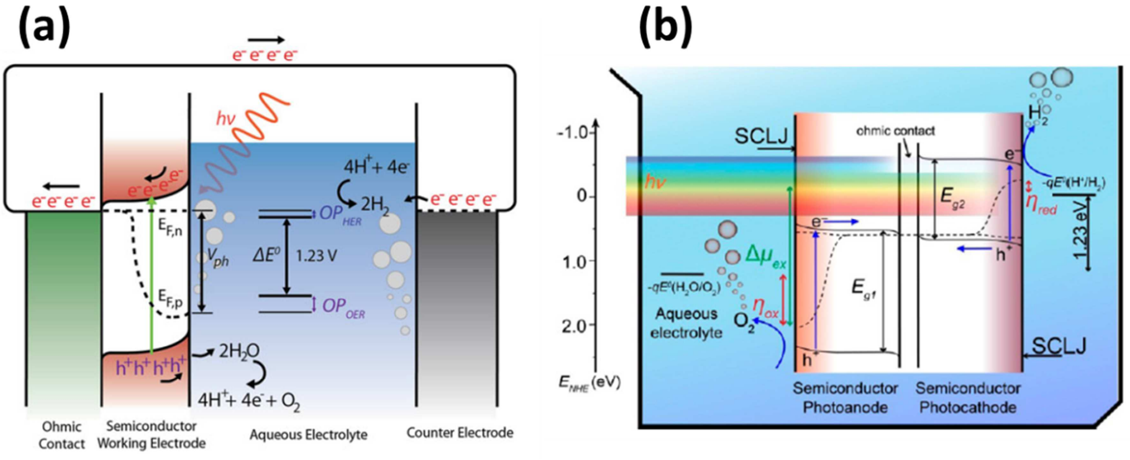

Figure 1.11 *(a) Band energy of a single absorber consisting of n-type photoanode and counter electrode; (b) Band energy of a dual absorber consisting of n-type photoanode and p-type photocathode (adapted from ref*[35,36]*)*

In theory a photoelectrochemical cell could be designed with only one photoabsorber, as depicted in Fig. 1.11(a). In this example the n-type photoanode must generate a photovoltage of at least 1.6-1.7 V, which would be enough to overcome the 1.23 V required to split water and the overpotentials associated with the HER and OER. The generated photovoltage must also enable the quasi-Fermi levels under illumination to straddle the HER and OER redox potentials. To date, only a few single semiconductor materials such as GaN:ZnO solid solution[84], C_3N_4[85] and CoO[86] possessing all these properties have been found, although they all exhibited modest activity. Based on theoretical calculations, a PEC water splitting device consisting of a single absorber can reach a maximum solar-to-hydrogen (STH) efficiency of 16.8%.[37] This can be better understood by looking at the graph reported in Fig. 1.12, where the STH efficiency is plotted against the semiconductor band gap. A STH efficiency of 16.8% requires a material with a band gap of roughly 2 eV, which is the minimum theoretical value required to generate the above-mentioned values of photovoltage. The solar-to-hydrogen (STH) efficiency is defined as:

$$STH = \frac{|J_{sc}(mA/cm^2| \cdot 1.23 \cdot \eta_F}{P_{total}\left(\frac{mW}{cm^2}\right)} \qquad 1.6$$

The numerator is the product between current density, thermodynamic water splitting potential based on ΔG^0 and the faradaic efficiency. The denominator is the incoming solar power density. Thus, this equation simply tells the ratio between energy output – in the form of chemical energy- and energy input – in the form of solar radiation-.

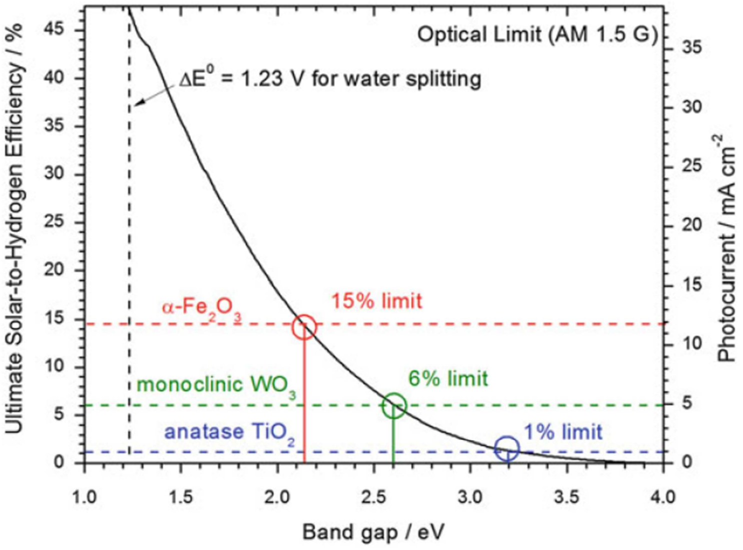

Figure 1.12 *Theoretical STH and photocurrent as a function of the semiconductor band gap (taken from ref* [35]*)*

Another approach schematized in Fig. 1.11 (b) is to couple two photoabsorber semiconductors in the so-called tandem PEC water splitting cell. In particular, the tandem cell is composed of a p-type photocathode and n-type photoanode where the HER and OER occur, in the presence of appropriate electrocatalysts which are placed on top of the semiconductor surfaces. The solar light harvesting property can be optimised by placing the photoelectrodes one on top of the other, and photons not absorbed by the first semiconductor pass through and are eventually absorbed by the second one having a smaller band gap. This configuration offers several advantages compared to the single absorber approach, such as broader selection of suitable photoelectrodes and physical and chemical decoupling of the two redox reactions. Moreover, it has been calculated that the maximum theoretical STH efficiency of a tandem cell is 29.5% by using a photocathode and photoanode with a band gap of 0.95 eV and 1.60 eV, respectively.[36]

In general terms, it is possible to categorize several examples of PEC water splitting devices based on the mechanism by which the photovoltage is generated. In fact, one could also use photovoltaic (PV) materials (silicon) as photoelectrodes, whose photovoltage is generated through a solid-solid junction.[38] In this case it is not required to expose the surface of the semiconductor to the electrolyte because the photovoltage is not dependent on the existence of the solid-liquid junction. Hence, it may be possible to physically separate the semiconductor photoabsorber from the electrocatalysts by wiring the two components and thus avoiding corrosion phenomena on the semiconductors. However this configuration is exactly the same of a typical PV cell + water electrolyser, which cannot be defined as proper PEC water splitting technology. One approach quite investigated in the literature is to integrate the electrocatalysts and the PV photoabsorber in a single compact device, which is immerged in the electrolyte.[39,40] In particular, the PV photoabsorber is first covered by a thin layer of metal/metal oxide in order to prevent the corrosion of the semiconductor; then the electrocatalyst is deposited on top of the protected PV photoabsorber as thin film.

In order to better clarify the differences between the existing configurations found among the PEC water splitting devices, Nielander *et al*. developed a rationale nomenclature based on the type of photoelectrode utilized in the cell.[41] In particular it is possible to distinguish three classes of PEC water splitting cells:

1. ***Photoelectrosynthetic cell (PC):*** a cell whose phovoltage produced by the two photoelectrodes derive from the semiconductor-liquid junction on both sides (SCLJ)-(SCLJ)
2. ***Photovoltaic-biased photoelectrosynthetic cell (PBPC):*** a cell whose photovoltage producing junctions consist of at least one semiconductor-liquid junction and one solid-solid junction (SCLJ)-(SSJ)
3. ***Photovoltaic-biased electrosynthetic cell (PBEC):*** a cell whose photovoltage produced by the two photoelectrodes derive from the solid-solid junction on both

sides (SSJ)-(SSJ). The cell is integrated with electrocatalysts and immersed in the electrolyte

According to the definition given above, the state-of-the-art of the best solar water splitting devices to date is reported in Tab 1.3.

Type of device	Device structure (cathode||anode)	Conditions	STH efficiency (%)	Stability
Photoelectrosynthetic	*(SCLJ)InP(p)||(SCLJ)GaAs(n)* HER catalyst: Pt (integrated), OER catalyst: MnO_x (integrated)	6M KOH	8.2	10 hours (10% drop)
Photovoltaic-biased photoelectrosynthetic	*(SCLJ)$GaInP_2$(p)||(SSJ)GaAs(pn)* HER catalyst: Pt (integrated) OER catalyst: Pt (wired)	3M H_2SO_4, 11 suns	12.4	20 hours (20% drop)
Photovoltaic-biased electrosynthetic	*(SSJ)$Al_{0.15}Ga_{0.85}$As(pn)||(SSJ) Si(pn)* HER catalyst: Pt (integrated) OER catalyst: RuO_2 (integrated)	1M $HClO_4$ P = 135 mW/cm^2	18.3	14 (stable)

Table 1.3 *State-of-the-art of the best solar-driven water splitting devices demonstrated in laboratory scale*

However the reported STH efficiencies lack of a standardized testing protocol, thus making a direct comparison between the values rather difficult. At present the stability remains a crucial issue, which severely limits the potential development advance of these systems.

1.2.3 Methanol as a means of renewable energy storage: insights into its synthetic preparation from renewable hydrogen and its utilisation as fuel in direct methanol fuel cells (DMFCs)

Converting the intermittent electric energy derived from solar and wind into liquid chemical energy is a promising alternative to the various existing energy storage technologies previously discussed. Liquid chemicals are particularly attractive energy carriers, given their ease of storage and transportation, offering important benefits compared to hydrogen which is a lot more expensive to handle and store. Moreover they can be used as precursors for the production of chemicals and products, thus effectively diversifying the types of market to which renewable energy can be indirectly linked. In this regard methanol can be viewed as ideal liquid chemical for renewable energy storage. Indeed, it is a highly versatile compound widely used as fuel and starting precursor for a myriad of organic chemicals and products.

From a synthetic perspective, renewable methanol can be produced by reacting hydrogen generated from electrolysis with carbon dioxide captured in conventional power plants, in the so-called CAMERE (carbon dioxide hydrogenation via reverse-water gas shift) process which is illustrated in Fig. 1.13.

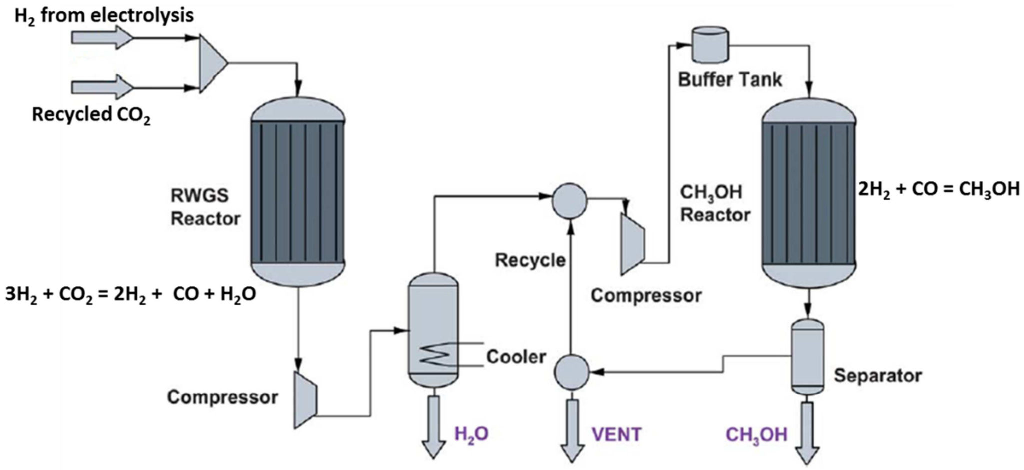

Figure 1.13 *Simplified process flow diagram of the CAMERE (carbon dioxide hydrogenation to form methanol via reverse-water gas shift) process for the renewable methanol production (adapted from ref* [42]*)*

The utilisation of CO_2 as starting material adds further value to the sustainability of the generated methanol, because the carbon cycle can be effectively closed with environmental benefits in terms of global warming. A successful commercial application of this process can be found in Iceland, where a company launched the first plant for renewable methanol production with a capacity of 4,000 t/year.[43] All the energy used in the plant comes from renewable hydro and geothermal sources. The hydrogen is produced by electrolysis and the carbon dioxide is directly captured from flue gas released by a geothermal plant.[44]

Renewable methanol as green fuel has received considerable attention in an attempt to reduce the reliance on fossil fuels, offering two important advantages compared to gaseous hydrogen, namely, i) higher volumetric energy density (see Fig. 1.14) and ii) ease of transport and storage.

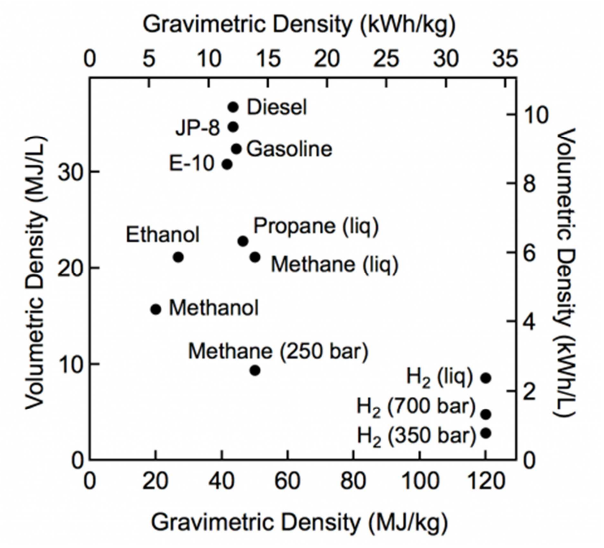

Figure 1.14 *Comparison of gravimetric and volumetric energetic density for some selected fuels based on their lower heating value (taken from ref*[45]*)*

Furthermore methanol has a high octane number and low volatility, making it a suitable gasoline substitute in conventional internal combustion engines. For example in Europe bio-methanol produced from biomass sources can be currently added to gasoline at 3% vol. according to the directive 2009/30/EC in an effort to reduce the net emission of carbon dioxide derived from the combustion of fossil fuels.[46]

Another potential application is to use renewable methanol as fuel in direct methanol fuel cells (DMFCs). According to recent projections, the DMFC market is expected to reach a value of almost 190 million USD by 2020, with a significant expansion in the portable sector.[47] Indeed, the current technological development of DMFCs makes them well-suited as power supply for small vehicles such as forklifts and consumer goods such as laptops, digital cameras and mobile phones.[48] The most interesting feature of the DMFC is represented by its energetic storage density, which is significantly higher than the traditional batteries, as depicted in Fig. 1.15. This means that DMFC can act as power supply for a much longer time, offering also more power available to support the increasing energetic demand of portable electronic devices. Besides, while DMFCs can be refuelled within minutes, batteries take hours to recharge.

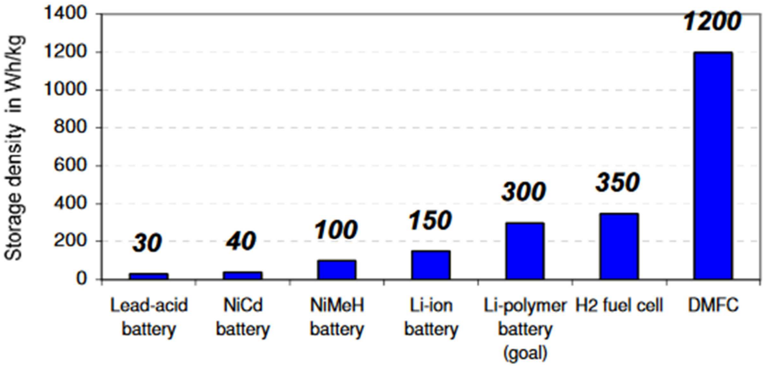

Figure 1.15 *Comparison of energy storage density between batteries and fuel cells (assuming H_2 fuel cell efficiency 40% and DMFC efficiency 25%); (taken from ref* [49]*)*

Basically the DMFC is an electrochemical device that converts chemical energy from methanol to electrical energy. The cell consists of a polymer electrolyte exchange membrane which separates the anode and the cathode where the methanol and oxygen and electrochemically oxidised and reduced, respectively. The stoichiometric reactions are outlined below, depending on the nature of the electrolyte:

- Anode (CH_3OH oxidation) – *Acidic electrolyte*: $CH_3OH + H_2O \rightarrow CO_{2(g)} + 6H^+ + 6e^-$
- Anode (CH_3OH oxidation) – *Alkaline electrolyte*: $CH_3OH + 6OH^- \rightarrow CO_{2(g)} + 5H_2O + 6e^-$
- Cathode (O_2 reduction) – *Acidic electrolyte*: $3/2O_{2(g)} + 6H^+ + 6e^- \rightarrow 3H_2O$
- Cathode (O_2 reduction) – *Alkaline electrolyte*: $3/2O_{2(g)} + 3H_2O + 6e^- \rightarrow 6OH^-$
- Overall reaction: $\mathbf{CH_3OH + 3/2O_2 \rightarrow CO_2 + 2H_2O}$

The reversible thermodynamic efficiency of the DMFC is given by the ratio between the maximum value of electrical work that can be obtained (ΔG^0 = -702.5 kJ/mol) and the total available energy for the process (ΔH^0_r = -726.6 kJ/mol), as shown in equation 1.7.

$$\epsilon_{rev}^{cell} = \frac{\Delta G^0}{\Delta H_r^0} = \frac{n_t F E_{rev}^0}{\Delta H_r^0} = 0.97 \qquad 1.7$$

E^0_{rev} is the equilibrium cell voltage, which is related to the Gibbs free energy through the relationship $\Delta G^0 = -nFE^0_{rev}$, where F is the Faraday constant and n_t the theoretical number of electrons exchanged in the reaction. For the methanol electrooxidation at 25 °C and 1 atm, the value of the equilibrium cell voltage is 1.18 V, with n_t being equal to 6. As previously discussed in the case of water electrolysis, the actual cell potential needs to take into account the various overpotentials and losses occurring during operation, leading to a smaller value than the theoretical voltage.

$$E_{wor} = E_{rev}^{0} - (\eta_{an} + |\eta_{cat}| + i \cdot R_A + \eta_{conc}) \qquad 1.8$$

Based on these considerations it is possible to define the cell voltage efficiency as follows:

$$\epsilon_{vol}^{cell} = \frac{E_{wor}}{E_{rev}^{0}} \qquad 1.9$$

Thus, the real energetic cell efficiency of the DMFC can be written as:

$$\epsilon_{cell} = \frac{n_{exp} F E_{wor}}{\Delta H_r^0} = \frac{n_t F E_{rev}^0 n_{exp} \epsilon_{vol}^{cell}}{\Delta H_r^0 n_t} = \epsilon_{rev}^{cell} \cdot \epsilon_{far}^{cell} \cdot \epsilon_{vol}^{cell} \qquad 1.10$$

ε_{far}^{cell} is the ratio between the number of electrons effectively exchanged in the overall reaction and the theoretical number of electrons required for the complete oxidation of methanol. From a practical perspective, the energetic cell efficiency is significantly lower than the thermodynamic efficiency, with current values between 20 and 30%.[50] These significant losses can be mainly attributed to methanol crossover and sluggish kinetics for the methanol oxidation reaction (MOR) and oxygen reduction reaction (ORR), as shown in the polarization curve reported in Fig. 1.16. Methanol at the anode diffuses through the polymeric membrane to the cathode, reducing the efficiency of the ORR by a competing electrochemical process, known as the mixed potential effect. Besides, the presence of methanol at the cathode induces mass transport limitations of the gaseous O_2, by flooding and plugging the electrocatalyst. As a result, methanol crossover leads to a reduction of the open circuit voltage by 0.2-0.3 V.[50,51]

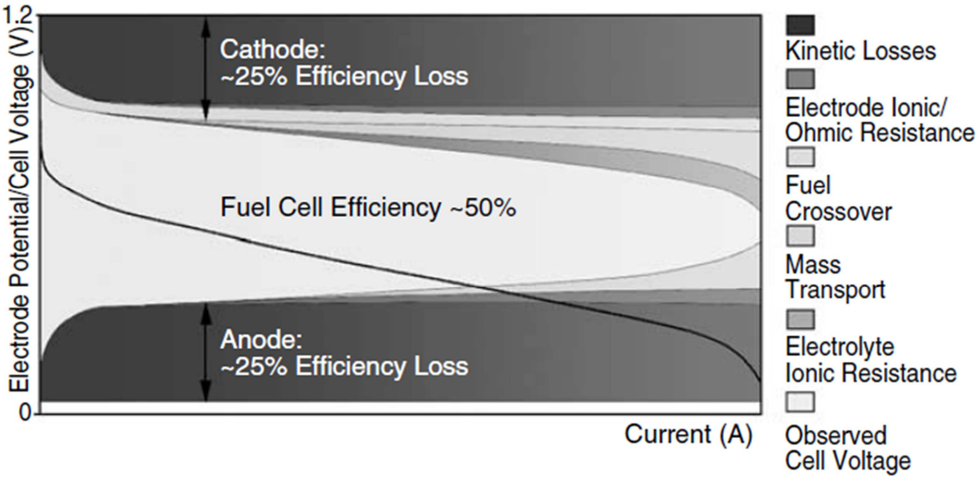

Figure 1.16 *Polarization curve for a generic DMFC, highlighting the principal sources of potential loss(taken from ref* [52]*)*

In order to minimise this problem methanol must be fed to the anode as diluted solution in water, generally with a molar concentration of 0.5-1 M. The design of novel electrocatalysts for the ORR which are inactive toward the methanol oxidation and the development of different membrane materials with low methanol permeation are two other popular strategies to mitigate this voltage loss.

The overpotentials associated with the electrocatalytic activity for the MOR and ORR are strongly dependent on the type of electrolyte used. As reported in Tab. 1.4, the current commercial type of DMFC relies on the utilization of an acidic solid-state polymeric membrane as electrolyte, which is based on a sulfonated polymer.

Specifications	**Proton-exchange DMFC**	**Alkaline DMFC**	**Alkaline anion exchange membrane DMFC**
Electrolyte	Solid state proton conductor membrane (Nafion)	1-5 M $KOH_{(aq)}$	Solid state anion conductor membrane
Methanol concentration	0.5-2 M	0.5-2 M	0.5-2 M
Air feed	Dry air	No particular requirement	Humidified Air
Temperature	25-70 °C	25-70 °C	25-70 °C
Anode catalyst	PtRu alloy (2-10 mg/cm^2)	PtRu, Pt/C, Pt/Ti, Ni	PtRu, Pt/C, Pt/Ti, Ni
Cathode catalyst	Pt (2-10 mg/cm^2)	Pt, Ag, MnO_2	Pt, Ag, MnO_2
Technological development	Early stage commercialisation	Laboratory	Laboratory

***Table 1.4** Specifications of the three types of DMFC (the data were taken from ref [51])*

In this cell the protons H^+, which are responsible for ionic conduction, are formed at the anode by the methanol electrooxidation. Then, the H^+ ions are transported assisted by water through the membrane to the cathode where they react with O_2 to form water, as schematized in Fig. 1.17(a). Here the kinetics of MOR and ORR are particularly slow, requiring a high Pt loading in order to attain reasonable values of current density. Such a high loading of precious metal has a considerable impact on the cost of these devices. Moreover the anode catalyst suffers from low durability due to the poisoning effect induced by the strong binding between CO and the Pt active site. Significant improvements have been made in order to increase the activity and stability and minimise the metal loading, through a better understanding of the reaction mechanisms and nanostructuring of the catalytic active sites.

The liquid alkaline electrolyte DMFC was the first type of methanol fuel cell to be investigated in the 1950s, mainly because of the favourable kinetics of MOR and ORR compared to acidic electrolytes.[51]

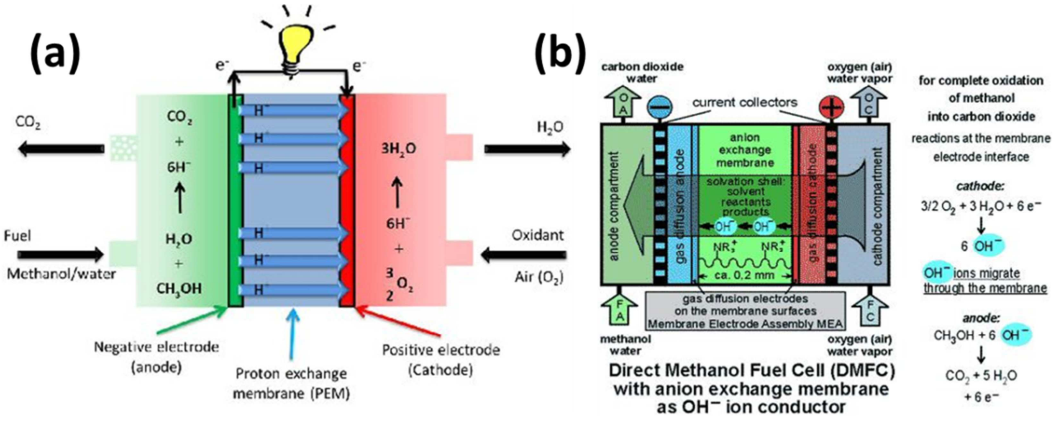

Figure 1.17 *Schematic diagram of (a) proton exchange DMFC and (b) alkaline anion exchange DMFC (taken from ref*[53,54]*)*

Moreover, the less corrosive alkaline environment made possible the selection and utilisation of a broader class of non-noble metal catalysts such as Ni at the anode and Ag at the cathode, with potential benefits in terms of the associated cost. Despite these advantages, the commercial development of liquid alkaline DMFCs was abandoned because of the inevitable acid-base reaction of the generated CO_2 at the anode and the alkaline KOH solution, with precipitation of carbonates in the catalyst pores. The continuous regeneration of the electrolyte was considered unfeasible in terms of practical applications.

Recently there has been growing interest in the development of alkaline anion exchange DMFCs (Fig. 1.17(b)). This is driven by the availability of new solid-state anionic polymeric membranes with satisfactory ionic conductivity values, which are currently half of the typical conductivity of Nafion.[55] These new membranes have the potential to drastically reduce the issue of carbonation associated with the conventional liquid KOH electrolytes. In this case OH^- ions are formed at the cathode through the reduction of O_2 with water added to humidify the air. The OH^- ions are transported through the membrane to the anode, where they react with methanol to form CO_2 and water. As a consequence of the OH^- migration from the cathode to the anode, the methanol crossover is significantly reduced by the effect of electro-osmotic drag. At present all the DMFCs based on this technology have shown higher power density when OH^- ions are added to the methanol feed, because they can flush the carbonate/bicarbonate species formed at the surface of the anode-side membrane.[56] Although promising, alkaline anion exchange DMFC still requires further improvements such as lower carbonation at the anode, higher membrane conductivity, more active electrocatalysts and better engineering design in order to be commercially-viable.

1.3 Electrocatalysis: the fundamental key toward making ever more efficient energy storage and conversion processes

The previous paragraphs provided a general introductory overview on the thematic of renewable energy storage and conversion, elucidating the current state-of-the-art and giving insights into the most promising technologies that are expected to grow and become widespread in the next future. Then, a more detailed description of three selected energy storage and conversion processes was made, explaining their fundamental properties and highlighting drawbacks and strengths of the current technologies. Water electrolysis, photoelectrochemical water splitting and methanol fuel cells, all have in common the presence of electrocatalysts, which play a fundamental role in facilitating the electrochemical reactions taking place at the electrodes. Efficient reactions mean less energetic losses, thus it can be easily understood how important is to constantly research and develop new electrocatalysts in order to further increase the overall efficiency. Ideally, the electrocatalyst should be active, stable, easily scalable, and made of low cost elements.

As it will be better explained in the next section, the objective of this thesis is to report and discuss the experimental work of electrocatalysts for the alkaline hydrogen evolution reaction, the photoelectrochemical oxygen evolution reaction and the alkaline methanol oxidation reaction. Thus, it seems essential to illustrate the principal characteristics of the three above-mentioned processes, elucidating the most common criteria for the evaluation of the electrocatalytic activity of potential new electrocatalysts, and giving insights into the mechanisms of reaction along with some general rules of thumb for the design of novel active materials.

1.3.1 Electrocatalysis for the hydrogen evolution reaction: a fundamental analysis

The hydrogen evolution reaction (HER) is one of the most investigated electrochemical reactions, with numerous studies concerning the understanding of the type of reaction kinetics involved and the development of appropriate electrocatalysts able to minimise the overpotential. Generally, the experimental evaluation of the HER activity and reaction mechanism is based on measuring the generated electric current by applying a specific potential to the electrode. Since the electric current is a direct measure of the electrocatalytic reaction rate, its analysis can give a quantitative description of the activity and reaction mechanisms of the electrocatalysts. The analysis is based on the fitting of the experimental data with the so-called Tafel equation, which is reported below:

$$\eta = a + b\log(j) \qquad 1.11$$

η is the reaction overpotential defined as the difference between the electrode potential and the standard thermodynamic potential for the hydrogen evolution ($E\text{-}E^0_{H+/H2}$), j is the experimental current density at the potential E, b represents the Tafel slope, and a is related to the exchange current density j_0. The Tafel slope gives important insights into the reaction mechanism involved, whereas the exchange current density is a common descriptor for the intrinsic catalytic activity of a selected electrocatalyst.[57] In particular, the Tafel slope indicates how much additional voltage is required to increase the current density by one order of magnitude, and its value can be subjected to variations due to mass transport limitations and changes in catalyst surface structure, which can induce to errors when determining the appropriate reaction mechanism.[58] The exchange current density represents the current at zero overpotential, and its calculation is done through an extrapolation of the Tafel equation for $\eta \rightarrow 0$. Thus, this parameter does not have any practical utility, and as pointed out by Benck *et al.*, its knowledge in absence of other information is not an ideal metric for comparing the catalyst activity, because it depends critically on the structure and morphology of the electrode, such as roughness and chemical doping.[58]

At present, the most accepted overall reaction mechanism of the HER is based on three steps, namely, 1) Volmer step, 2) Heyrovsky step and 3) Tafel step, which are described in Table 1.5 under acidic and alkaline electrolyte.

Step	**Acidic electrolyte (pH ~ 0)**	**Alkaline electrolyte (pH ~ 14)**
Volmer	$H_3O^+ + e^- + M \rightleftharpoons M\text{-}H_{ads} + H_2O$	$H_2O + e^- + M \rightleftharpoons M\text{-}H_{ads} + OH^-$
Heyrovsky	$H_3O^+ + e^- + M\text{-}H_{ads} \rightleftharpoons M + H_2 + H_2O$	$H_2O + e^- + M\text{-}H_{ads} \rightleftharpoons M + H_2 + OH^-$
Tafel	$M\text{-}H_{ads} + M\text{-}H_{ads} \rightleftharpoons H_2$	$M\text{-}H_{ads} + M\text{-}H_{ads} \rightleftharpoons H_2$

***Table 1.5** Summary of the reaction steps involved during the HER in acidic and alkaline electrolyte*

The HER can proceed via the Volmer-Heyrovsky or the Volmer-Tafel mechanism, and the rate-determining step (RDS) is normally identified through the analysis of the Tafel slope. In both cases, the first step is based on the adsorption of hydronium/water molecules onto the active site M, and the resulting bonding strength is another adopted descriptor to evaluate the catalytic activity of chemical elements. According to the Sabatier's principal, which is a fundamental concept of catalysis, the M-H bond should be neither too strong nor too weak in order to have an optimal HER activity. If the adsorption is too strong (exothermic), the desorption step (Heyrovsky or Tafel) will be the RDS, because of the great thermodynamic stability of the M-H bond. If the adsorption is too weak (endothermic), the Volmer step will limit the overall kinetics because the hydrogen adsorption is not thermodynamically favoured. This can be experimentally visualised by calculating the values of Tafel slope. In particular, small values of Tafel slopes (40 - 80 mV/dec) are generally measured when the Volmer step is not the limiting factor, whereas big values (120 mV/dec) are encountered when the Volmer step represents the limiting factor.

As theoretically demonstrated by Parsons and experimentally reported by Trasatti, the exchange current density of chemical elements can be correlated with the free energy of hydrogen adsorption ΔG_H or the metal-hydride bond energy, giving rise to a well-defined volcano plot.[59,60]

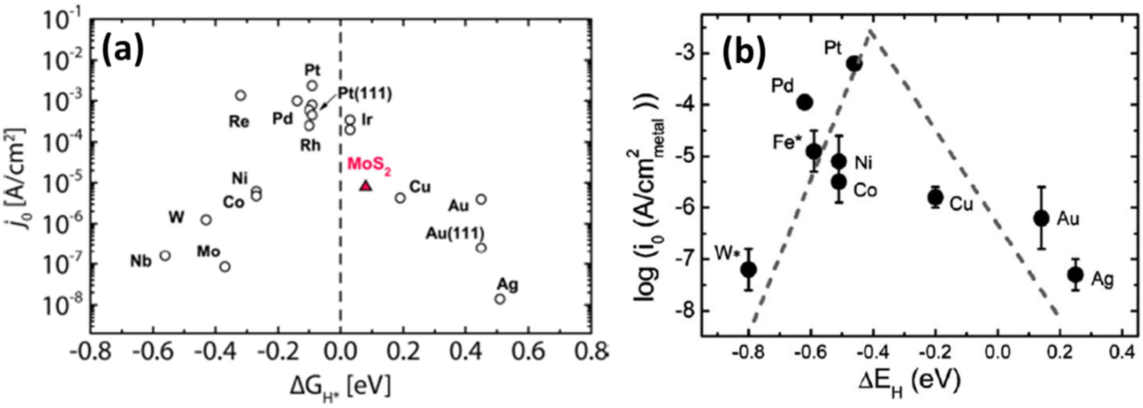

Figure 1.18 *Exchange current density as a function of the free energy of hydrogen adsorption in (a) acid and (b) alkaline media. (Fig. (a) and (b) are taken from [58] and [61])*

From Fig. 1.18 it can be noticed that Pt represents the most active catalyst for the HER in both acidic and alkaline media, since it shows the highest current exchange density and most suitable M-H bond strength. So far, no other material with better catalytic performance toward the HER has been found. By keeping in mind this correlation, numerous *ab-initio* studies based on density functional theory (DFT) calculations have been carried out, with the aim of finding potential new highly active HER electrocatalysts able to match or overcome the state-of-the-art Pt electrode. In 2005, Hinneman *et al*. demonstrated through DFT calculations that the edge of MoS_2 could act as potential highly active site for the HER under acidic environment, since the theoretical value ΔG_H was quite similar with that of Pt. Interestingly, this result was confirmed experimentally 2 years later through the appropriate synthesis of MoS_2 nanoparticles with exposed edge sites, whose number was correlated linearly with the HER activity measurement in acidic electrolyte.[62]

Another common parameter frequently used for the comparison of HER activity between selected electrocatalysts is the overpotential required to reach a specific current density η_j (V vs RHE). As reported in Fig. 1.19(a) and (b), there might be the case where two electrocatalysts show the same overpotential η_j and a different Tafel slope. Clearly, these two catalysts have different HER mechanisms, and both of them could be better or worse depending on the η_j required for a specific application. If the application requires a process operating at current density smaller than 10 mA/cm^2, the catalyst represented in blue would be the best choice, whereas the catalyst in red would be more suitable for current densities bigger than 10 mA/cm^2.

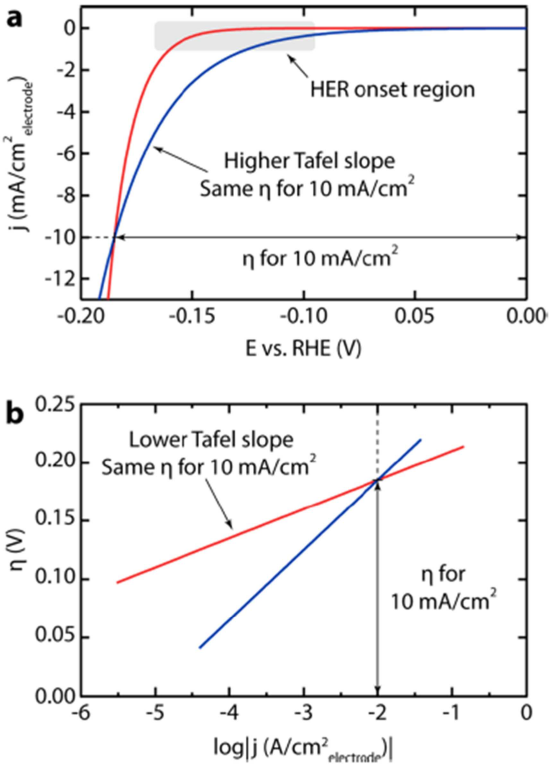

Figure 1.19 *(a) Linear sweep voltammetry of two theoretical catalysts possessing different Tafel slopes and same overpotentials required to reach a defined current density; (b) correspondent Tafel plot (taken from ref* [58]*)*

This suggests that no definite answer is possible when it comes to comparing different electrocatalytic materials for their suitability toward real HER applications.

It is worth noting that the set current defined for the determination of η_j is normalized to the geometric surface area, which is very useful for the comparison of real devices. However with this methodology it is not possible to give a measure of the intrinsic activity of the active sites, because their superficial concentration is normally unknown. Obviously this is not ideal for studies concerning the fundamental understanding of the catalytic properties of a novel material, with the impossibility to establish structure-property relations at atomic level. Therefore, for more fundamental studies the current is generally normalized to the number of active sites, which are measured through the determination of the electrochemically active surface area and quantification of the metal loading.[63] This represents another useful parameter normally reported in the literature.

Finally, the stability and selectivity of the electrocatalysts must be evaluated in order to fully assess their potential viability for commercial applications. Whilst the selectivity is not of particular concern for the HER, the long-term stability required for real devices can be generally an issue, because of possible chemical/electrochemical corrosion phenomena occurring at the electrode. The stability can be tested through several methods, such as chronoamperometry, chronopotentiometry and cyclic voltammetry, with each of them giving important insights into the prolonged electrochemical behaviour of the tested electrocatalysts.[64,65]

From a practical perspective, it is useful to report some guidelines for the appropriate design of new potential active HER electrocatalysts as follows:

- The synthetic methodology must be cheap and feasible to scale-up
- The material must be made of abundant elements
- The catalyst must have a high geometric surface area in order to maximise the exposure of active surface with the electrolyte
- It is highly desirable to have a porous electrode, which can minimise mass transfer limitations due to the formation of hydrogen bubbles
- For materials composed of noble elements (Pt), nanostructuring can be beneficial for maximising the surface-to-volume ratio which leads to a higher catalyst utilisation and therefore to a lower metal loading
- The electrode must minimise the overpotential required to reach a specific geometric current density
- The material must be chemically and electrochemically stable under the selected pH

In Chapter 3 it will be reported and discussed the design of a novel composite HER electrocatalyst based on cobalt and nickel sulfides supported onto Ni foam, paying particular attention to its morphological and structural characteristics and evaluating the HER activity under alkaline electrolyte.

1.3.2 Role of electrocatalysts in the photoelectrochemical water splitting

As briefly illustrated in Section 1.2.2, the commercial viability of photoelectrochemical water splitting devices is severely hampered by several technological factors, such as low solar-to-hydrogen (STH) efficiency, poor chemical stability of the majority of the known photoabsorber materials under the harsh conditions normally encountered during the process and lack of an appropriate engineering design of reactors. At present, researchers are mostly focused on improving the material properties in order to increase the STH and long-term stability. In this regard the most common research strategies currently found in the literature include:

1. Improving the photocurrent through the design of optimal morphological architectures in the absorber layer of the semiconductor for a better light absorption[66]
2. Improving the charge-carrier transfer through nanostructuring the semiconductor[67]
3. Lowering the overpotential for HER and OER at the surface by using active electrocatalysts directly attached at the photoanode (for O_2 evolution) and photocathode (for H_2 evolution)[68]
4. Designing buried p-n junctions in order to improve the charge separation efficiency[69]
5. Coating the absorber semiconductor with surface passivation layers in order to improve the physical and chemical stability of the underlying material[38]
6. Reducing the electron-hole recombination by passivation of surface states through thin materials with non-catalytic or catalytic properties[70]

In particular, given the specific work reported in this thesis, it is useful to elucidate in more detail the fundamental mechanisms summarised in points 3 and 6, which are related to the role of electrocatalysts on the photoelectrochemical activity and stability of absorber semiconductors.

In the case of a n-type semiconductor photoanode, the shift of the onset potential with respect to the thermodynamic redox potential for water oxidation is dependent on the generated photovoltage and kinetic overpotential, as represented in equation 1.12:[71]

$$\Delta V_{shift} = E_{H_2O/O_2} - V_{onset} = V_{ph} - \eta \qquad 1.12$$

where $E_{H2O/O2}$ is the redox potential for water oxidation (1.23 V vs RHE), V_{onset} is the onset potential, V_{ph} is the photovoltage and η is the overpotential. Please note that if ($V_{ph} > \eta$), then ($V_{onset} < E_{H2O/O2}$) and $\Delta V_{shift} > 0$. Clearly, it is highly desirable to shift the onset potential V_{onset} as far as possible from $E_{H2O/O2}$ in order to increase the efficiency, and this can be done by either increasing the photovoltage V_{ph} or decreasing the kinetic overpotential η. As demonstrated in several works reported in the literature, the introduction of thin layers of co-catalysts on the surface of the n-type semiconductor photoanodes prevent the formation of surface defect states and promote a faster charge transfer from the semiconductor to the redox species at the interface.[70,72] This is further schematised in Fig. 1.20, where the presence of a co-catalyst on top of the n-type semiconductor prevents the recombination of the photogenerated electron-hole pairs and increases the rate of holes transfer from the space-charge region to the surface.

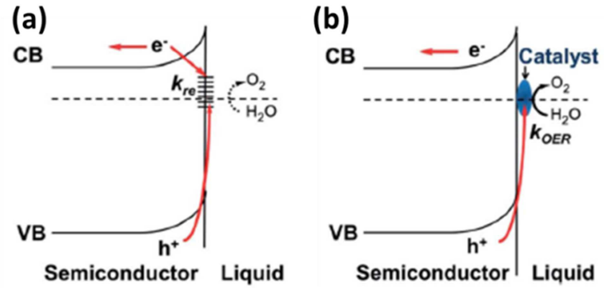

***Figure 1.20** Comparison of a n-type semiconductor photoanode in (a) absence of OER catalyst and (b) presence of OER catalyst (adapted from ref [71])*

It is worth noting that the same concepts are also applied to p-type semiconductor photocathodes for the HER.

Co-catalysts can also prevent photocorrosion reaction of the underlying semiconductors, which is a serious problem for some known photoelectrodes such as n-Ta_3N_5 and p-Cu_2O.[73,74] However, continuous thick catalytic passivation layers typically required for an optimal suppression of the photocorrosion result in unwanted parasitic light absorption which in turn reduce the amount of photogenerated electron-hole pairs. Therefore, in most cases an optimal thickness of the electrocatalytic film must be found in order to have an overall improvement of the activity and stability. In some cases it has been reported that discontinuous catalytic layers which have smaller parasitic light absorption than thick conformal layers can still minimise photocorrosion phenomena by acting as rapid hole scavengers and improving the OER/HER reactions.[75] Fig. 1.21 shows the band structure of photoanode and photocathode semiconductors in the presence of passivation layers, illustrating the suppression of charge recombination and electrode corrosion, concomitantly with an increase in the interfacial charge-transfer for the OER and HER.

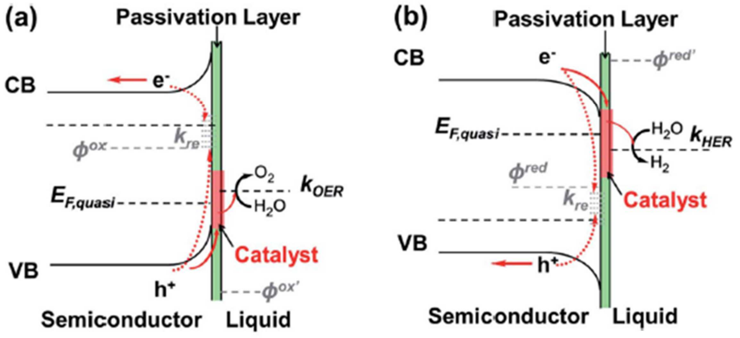

Figure 1.21 *Detailed schematic diagram of (a) n-type semiconductor photoanode and (b) p-type semiconductor photocathode fully covered by catalytic passivation layers (adapted from ref* [71]*)*

In the case of n-type semiconductor photoanode, the choice of a suitable OER catalyst is driven by several considerations, such as catalyst stability, ease of synthesis, knowledge of the intrinsic electrocatalytic activity of the catalyst, type of photoanode, good mechanical adhesion at the interface with the photoanode, good heterojunction formation if the catalyst is a semiconductor. Particularly, one important parameter commonly considered when selecting OER cocatalysts directly comes from studies on electrocatalysts for the “dark” water electrolysis. Similarly to what discussed in the previous Paragraph, the trend in OER activity can be evaluated through some defined descriptors and plotted giving rise to a volcano curve, as reported in Fig. 1.22.

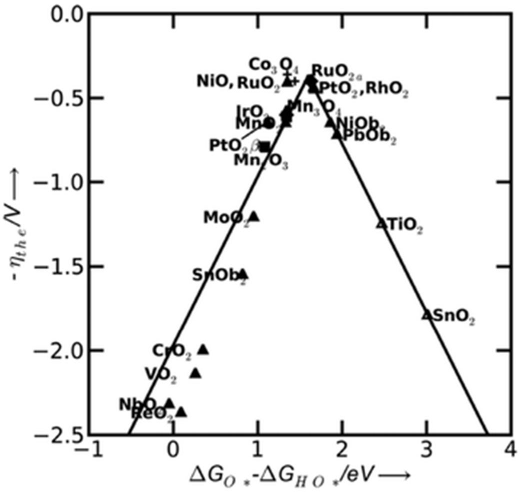

Figure 1.22 *Trend in OER activity for some selected electrocatalysts (taken from ref* [76]*)*

The graph displays the theoretical overpotential as a function of the difference of free energy adsorption between two intermediate species occurring during the OER. Clearly, metal oxides such as Co_3O_4, RuO_2, IrO_2, NiO and Mn_3O_4 present the highest activity. By taking into account this trend, several works were reported concerning the utilisation of these materials as co-catalysts for the photoelectrochemical oxygen evolution. Notable examples include the design and development of n-Fe_2O_3/Co_3O_4,[77] n-Fe_2O_3/IrO_2,[78] n-Si/NiO_x[79] and n-WO_3/IrO_2[80] heterostructures. In Chapter 4 it will be reported and discussed the experimental work concerning the fabrication of a n-WO_3/Co_3O_4 thin film photoanode for the oxygen evolution, elucidating the structural and morphological features of the Co_3O_4 electrocatalyst and its influence on the photoelectrochemical properties of the composite system.

1.3.3 Electrocatalysis for the methanol oxidation reaction: a fundamental analysis

At present Pt represents the most active electrocatalyst for the methanol oxidation reaction (MOR) both in acidic and alkaline media. Several studies have been focused on understanding the mechanism of reaction of MOR, because it can serve as important tool to design new catalysts with a potential superior activity and stability compared to the metallic Pt. A schematic reaction mechanism under alkaline electrolyte is represented as follows:[81]

1. $Pt + OH^- \rightarrow Pt\text{-}(OH)_{ad} + e^-$
2. $Pt + CH_3OH_{sol} \rightarrow Pt\text{-}(CH_3OH)_{ad}$
3. $Pt\text{-}(CH_3OH)_{ad} + OH^- \rightarrow Pt\text{-}(CH_3O)_{ad} + H_2O + e^-$
4. $Pt\text{-}(CH_3O)_{ad} + OH^- \rightarrow Pt\text{-}(CH_2O)_{ad} + H_2O + e^-$
5. $Pt\text{-}(CH_2O)_{ad} + OH^- \rightarrow Pt\text{-}(CHO)_{ad} + H_2O + e^-$
6. $Pt\text{-}(CHO)_{ad} + OH^- \rightarrow Pt\text{-}(CO)_{ad} + H_2O + e^-$
7. $Pt\text{-}(CHO)_{ad} + Pt\text{-}(OH)_{ad} + 2OH^- \rightarrow 2Pt + CO_2 + 2H_2O + 2e^-$
8. $Pt\text{-}(CHO)_{ad} + Pt\text{-}(OH)_{ad} + OH^- \rightarrow Pt + Pt\text{-}(COOH)_{ad} + H_2O + e^-$
9. $Pt\text{-}(CO)_{ad} + Pt\text{-}(OH)_{ad} + OH^- \rightarrow 2Pt + CO_2 + H_2O + e^-$
10. $Pt\text{-}(CHO)_{ad} + Pt\text{-}(OH)_{ad} \leftrightarrow Pt + Pt\text{-}(COOH)_{ad}$
11. $Pt\text{-}(COOH)_{ad} + OH^- \rightarrow Pt\text{-}(OH)_{ad} + HCOO^-$
12. $Pt\text{-}(COOH)_{ad} + Pt\text{-}(OH)_{ad} \rightarrow 2Pt + CO_2 + H_2O$

The methanol is first adsorbed onto the free Pt active site (step 2) and then it undergoes a series of dehydrogenation reactions (steps 3 to 6) with the release of H_2O and electrons. The rate-determining step is the oxidation of the adsorbed CHO and CO species (steps 7 to 12), because they bind strongly to the Pt active sites. This results in a poisoning effect of the active sites which are not able to adsorb methanol, with a decrease in the reaction kinetics. As shown in the volcano plot calculated from DFT calculations and reported in Fig. 1.23, the free energy of CO adsorption on Pt has a negative value, which translates into a good thermodynamic stability of the Pt-CO bond, in agreement with the experimental evidence.

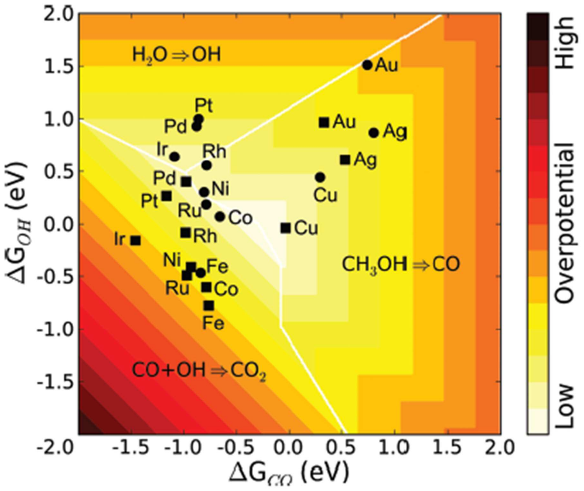

__Figure 1.23__ Volcano plot representing the MOR overpotential as a function of the free energy of OH adsorption ΔG_{OH} and CO adsorption ΔG_{CO} (taken from ref [82])

Thus, it is of extreme importance to increase the rate of CO oxidative removal from the surface of Pt, and in this regard several approaches have been reported in the literature, such as doping and alloying.[83] The mechanistic implications of such improvement of the electrocatalytic activity and stability toward the MOR will be treated carefully in Chapter 5, where the experimental work concerning the development of a highly active catalyst based on Pt, CeO_2, NiO and Ni foam for the alkaline MOR will be presented.

From an experimental point of view, the catalytic MOR activity is evaluated through cyclic voltammetry, and its analysis gives important figures of merit such as onset potential and peak current density normalized to the geometric area (J_g, in mA/cm^2) and to the Pt mass loading (J_{pt}, in mA/mgPt). These figures of merit are commonly employed for the direct comparison of the catalytic activity between different materials. The stability is normally recorded through chronoamperometry or repeated cyclic voltammetry tests, similarly to what previously described in Section 1.3.1.

The common guidelines for the design of active MOR electrocatalysts are similar to those reported for the HER electrocatalysts, therefore they will not be reported in this section.

1.4 References

1. Esa.un.org. (2016). *World Population Prospects - Population Division - United Nations*. (online) Available at: https://esa.un.org/unpd/wpp/Graphs/Probabilistic/POP/TOT/
2. M. I. Hoffert et al., Energy implications of future stabilization of atmospheric CO_2 content. *Nature* **391,** 806–811 (1998).
3. U.S. EIA. *The International Energy Outlook 2016*. **0484,** (2016).
4. *REN 21. 2016. Renewable 2016 Global Status Report*. (2016).
5. Ellabban, O., Abu-Rub, H. and Blaabjerg, F., *Renew. Sustain. Energy Rev.,* (2014), **39,** 748–764
6. *GWEC-Global Wind 2015 Report*. (2015).
7. Chen, H. *et al*., *Prog. Nat. Sci.* **19,** 291–312 (2009).
8. International Energy Agency. *Energy-efficient Buildings: Heating and Cooling Equipment*. (2011).
9. Europa.eu. (2016). *European Commission - PRESS RELEASES - Press release - Towards a smart, efficient and sustainable heating and cooling sector*. (online) Available at: http://europa.eu/rapid/press-release_MEMO-16-311_it.htm.
10. Who.int. (2016). *WHO | 7 million premature deaths annually linked to air pollution.* (online) Available at: http://www.who.int/mediacentre/news/releases/2014/air-pollution/en/.
11. Sheehan, J. J. Biofuels and the conundrum of sustainability. *Curr. Opin. Biotechnol.* **20,** 318–324 (2009).
12. Energy. (2016). *Renewable energy - Energy - European Commission*. (online) Available at: https://ec.europa.eu/energy/en/topics/renewable-energy.
13. International Renewable Energy Agency. *REmap 2030 A renewable energy roadmap*. (2015).
14. Alanne, K. and Saari, A., *Renew. Sustain. Energy Rev.* **10,** 539–558 (2006).
15. Energystorage.org. (2016). *Facts & Figures | Energy Storage Association.* (online) Available at: http://energystorage.org/energy-storage/facts-figures.
16. *Global Energy Storage Market Overview & Regional Summary Report*. (2015).
17. GmbH, S. (2016*). Li-ion battery costs to fall 50% in next 5 years, driven by renewables.* (online) pv magazine. Available at: http://www.pv-magazine.com/news/details/beitrag/li-ion-battery-costs-to-fall-50-in-next-5-years--driven-by renewables_100022051/#axzz4EG4KwxCr.
18. International Renewable Energy Agency. *Battery Storage for Renewables : Market Status and Technology Outlook*. (2015).

19. Sbcenergyinstitute.com. (2016*). Electricity Storage*. (online) Available at: http://www.sbcenergyinstitute.com/Publications/ElectricityStorage.html.
20. Renewableenergyworld.com. (2016). *Hydrogen Energy Storage: A New Solution To the Renewable Energy Intermittency Problem.* (online) Available at: http://www.renewableenergyworld.com/articles/2014/07/hydrogen-energy-storage-a-new-solution-to-the-renewable-energy-intermittency-problem.html.
21. NREL. *Hydrogen Energy Storage: Grid and Transportation Services*. *Electrochemical Energy Storage for Renewable Sources and Grid Balancing* (2015). doi:10.1016/B978-0-444-62616-5.00009-7
22. Umair Irfan, C. (2016). *Japan Bets on a Hydrogen-Fueled Future.* (online) Scientific American. Available at: http://www.scientificamerican.com/article/japan-bets-on-a-hydrogen-fueled-future/.
23. Melaina, M. W., Antonia, O. and Penev, M. *Blending Hydrogen into Natural Gas Pipeline Networks : A Review of Key Issues Blending Hydrogen into Natural Gas Pipeline Networks : A Review of Key Issues*. *Nrel* (2013). doi:10.2172/1068610
24. Götz, M. *et al.* Renewable Power-to-Gas: A technological and economic review. *Renew. Energy* **85,** 1371–1390 (2016).
25. De Boer, H. S., Grond, L., Moll, H. and Benders, R., *Energy* **72,** 360–370 (2014).
26. Jensen, S. H., Larsen, P. H. and Mogensen, *Int. J. Hydrogen Energy* **32,** 3253–3257 (2007).
27. Hansen, J. B., *Faraday Discuss.* **182,** 9–48 (2015).
28. Bladergroen, B. *Overview of Membrane Electrode Assembly Preparation Methods for Solid Polymer Electrolyte Electrolyzer*, Electrolysis, DOI: 10.5772/52947.
29. Schalenbach, M. *J. Electrochem. Soc*., **163**, F3197, (2016).
30. Carmo, M., Fritz, D. L., Mergel, J. and Stolten, *Int. J. Hydrogen Energy* **38,** 4901–4934 (2013).
31. Mathiesen, B. V. *et al. Technology data for high temperature solid oxide electrolyser cells, alkali and PEM electrolysers*. (2013).
32. Minh, N. Q. and Mogensen, M. B., *Interface* **22,** 55–62 (2013).
33. Bertuccioli, L. *et al. Development of Water Electrolysis in the European Union - Fuel Cells and Hydrogen Joint Undertaking*. (2014).
34. Fujishima, A. and Honda, K., *Nature* **238,** 37–38 (1972).
35. Chen, Z., Dinh, H. N. and Miller, E. *Photoelectrochemical Water Splitting*. *CHIMIA International Journal for Chemistry* (2013). doi:10.1007/978-1-4614-8298-7
36. Prevot, M. and Sivula, *J. Phys. Chem. C* **117,** 17879–17893 (2013).
37. Li, Z., Luo, W., Zhang, M., Feng, J. and Zou, Z., *Energy Environ. Sci.* **6,** 347–370 (2013).
38. Hu, S. *et al. Science* **344,** 1005–9 (2014).

39. Verlage, E. *et al.*, *Energy Environ. Sci.* **8,** - (2015).
40. Ager, J. W., Shaner, M. R., Walczak, K. A., Sharp, I. D. and Ardo, S., *Energy Environ. Sci.* **8,** 2811–2824 (2015).
41. Nielander, A. C., Shaner, M. R., Papadantonakis, K. M., Francis, S. A. and Lewis, N. S., *Energy Environ. Sci.* **8,** 16–25 (2015).
42. Centi, G., Quadrelli, E. A. and Perathoner, S., *Energy Environ. Sci.* **6,** 1711–1731 (2013).
43. Stefansson, B. *Power and CO_2 emissions to methanol*. (2015).
44. hardar, s. and hardar, s. (2016). *Projects.* (online) *CRI - Carbon Recycling International.* Available at: http://carbonrecycling.is/projects-1/.
45. Energy.gov. (2016). *Hydrogen Storage | Department of Energy*. (online) Available at: http://energy.gov/eere/fuelcells/hydrogen-storage.
46. Faberi, S. and Paolucci, L. *Methanol : a future transport fuel based on hydrogen and carbon dioxide? Economic viability and policy options*. (2014). doi:10.2861/57305
47. Markets, R. (2016). *The Direct Methanol Fuel Cells (DMFC) Market is Expected to Reach USD 188.82 Million by 2020, at a CAGR of 15.3% from 2015 to 2020*. (online) Prnewswire.com. Available at: http://www.prnewswire.com/news-releases/the-direct-methanol-fuel-cells-dmfc-market-is-expected-to-reach-usd-18882-million-by-2020-at-a-cagr-of-153-from-2015-to-2020-300219632.html .
48. Kamarudin, S.K. *Int. J. Hydrogen Energy* **34,** 6902–6916 (2009).
49. Muller, J. *The ideal fuel for portable fuel cells - hydrogen or methanol?*
50. Ralph, T. R. and Hogarth, M. P., *Platin. Met. Rev.* **46,** 146–164 (2002).
51. Aricò, A., Baglio, V. and Antonucci, V. Direct Methanol Fuel Cells: History, Status and Perspectives. *Electrocatal. Direct Methanol Fuel Cells From Fundam. to Appl.* 1–78 (2009). doi:10.1002/9783527627707.ch1
52. Hogarth, M. *Prospects of the Direct Methanol Fuel Cell (Chapter 7)*. (CRC, 2003).
53. Dti.dk. (2016). *MicroPower.* (online) Available at: http://www.dti.dk/services/micropower/31150.
54. Jörissen, J. *Anion exchange membranes as electrolytes for direct methanol fuel cells,* Available at: http://www.tc.bci.tu-dortmund.de/cms/de/lehrstuhl/mitarbeiter/Professoren/Joerissen_Jakob.html
55. Yu, E. H. and Scott, K., *Electrochem. commun.* **6,** 361–365 (2004).
56. Janarthanan, R. *et al.*, *Electrochim. Acta* **175,** 202–208 (2015).
57. Shinagawa, T., Garcia-Esparza, A. T. and Takanabe, K., *Sci. Rep.* **5,** 13801 (2015).
58. Benck, J. D., Hellstern, T. R., Kibsgaard, J., Chakthranont, P. and Jaramillo, T. F., *ACS Catal.* **4,** 3957–3971 (2014).
59. Parsons, R., *Trans. Faraday Soc.* **54,** 1053–1063 (1958).

60. Trasatti, S., *J. Electroanal. Chem. Interfacial Electrochem.* **39,** 163–184 (1972).
61. Sheng, W., Myint, M., Chen, J. G. and Yan, Y., *Energy Environ. Sci.* **6,** 1509–1512 (2013).
62. Jaramillo, T. F. *et al.*, *Science* **317,** 100–102 (2007).
63. Durst, J. *et al.*, *Energy Environ. Sci.* **7,** 2255–2260 (2014).
64. Velazquez, J. M. *et al., J. Electroanal. Chem.* **716,** 45–48 (2014).
65. Feng, L. L. *et al.*, *J. Am. Chem. Soc.* **137,** 14023–14026 (2015).
66. Boettcher, S. W. *et al.*, *J. Am. Chem. Soc.* **133,** 1216–1219 (2011).
67. Lin, Y., Zhou, S., Sheehan, W. & Wang, D., *J. Am. Chem. Soc.* **133,** 2398–2401 (2011).
68. Tamirat, A. G., Su, W.-N., Dubale, A. A., Chen, H.-M. and Hwang, B.-J., *J. Mater. Chem. A* **3,** 5949–5961 (2015).
69. Li, C. *et al.*, *Energy Environ. Sci.* **8,** 1493–1500 (2015).
70. Barroso, M. *et al.*, *J. Am. Chem. Soc.* **133,** 14868–71 (2011).
71. Liu, R., Zheng, Z., Spurgeon, J. and Yang, X., *Energy Environ. Sci.* **7,** 2504–2517 (2014).
72. Abdi, F. F., Firet, N. and VandeKrol, R., *ChemCatChem* **5,** 490–496 (2013).
73. Li, M. *et al.*, *Angew. Chemie - Int. Ed.* **52,** 11016–11020 (2013).
74. Paracchino, A., Laporte, V., Sivula, K., Grätzel, M. & Thimsen, E., *Nat. Mater.* **10,** 456–461 (2011).
75. Hou, J. *et al.*, *Energy Environ. Sci.* **6,** 3322–3330 (2013).
76. Man, I. C. *et al.*, *ChemCatChem* **3,** 1159–1165 (2011).
77. Riha, S. C. *et al.*, *ACS Nano* **7,** 2396–2405 (2013).
78. Tilley, S. D., Cornuz, M., Sivula, K. & Graetzel, M., *Angew. Chemie - Int. Ed.* **49,** 6405–6408 (2010).
79. Sun, K. *et al.*, *Energy Environ. Sci.* **5,** 7872 (2012).
80. Spurgeon, J. M., Velazquez, J. M. and McDowell, M. T., *Phys. Chem. Chem. Phys.* **16,** 3623–31 (2014).
81. Yu, E. H., Krewer, U. and Scott, K., *Energies* **3,** 1499–1528 (2010).
82. Tritsaris, G. A. and Rossmeisl, J., *J. Phys. Chem. C* **116,** 11980–11986 (2012).
83. Zhao, X. *et al*., *Energy Environ. Sci.* **4,** 2736 (2011).
84. Maeda, K. *et al*., J. Am. Chem. Soc. **127**, 8286 (2005).
85. Zhang, G. *et al*., Chem. Sci. **7**, 3062 (2016).
86. Liao, L. *et al*., Nature Nanotechnology **9**, 69 (2014).

Chapter 2: Experimental

In this chapter a theoretical background of the techniques used for the characterisation of the materials reported in this thesis is given. The detailed experimental methodology of the different techniques will be then discussed with more detailed in each chapter.

2.1 Characterisation techniques

2.1.1 X-ray Powder Diffraction (XRD)

XRD is an analytic technique widely used for the phase identification and unit cell dimension of a crystalline material. From a fundamental point of view, XRD relies on the constructive interference occurring between a monochromatic X-ray and the crystalline planes present in the material. In general X-rays normally used during the measurements have small wavelengths in the range 0.5-2.5 Å, which are of the same order of magnitude as the interatomic distance in solids. The conditions for constructive interference can be easily visualised in the schematic representation in Fig. 2.1.

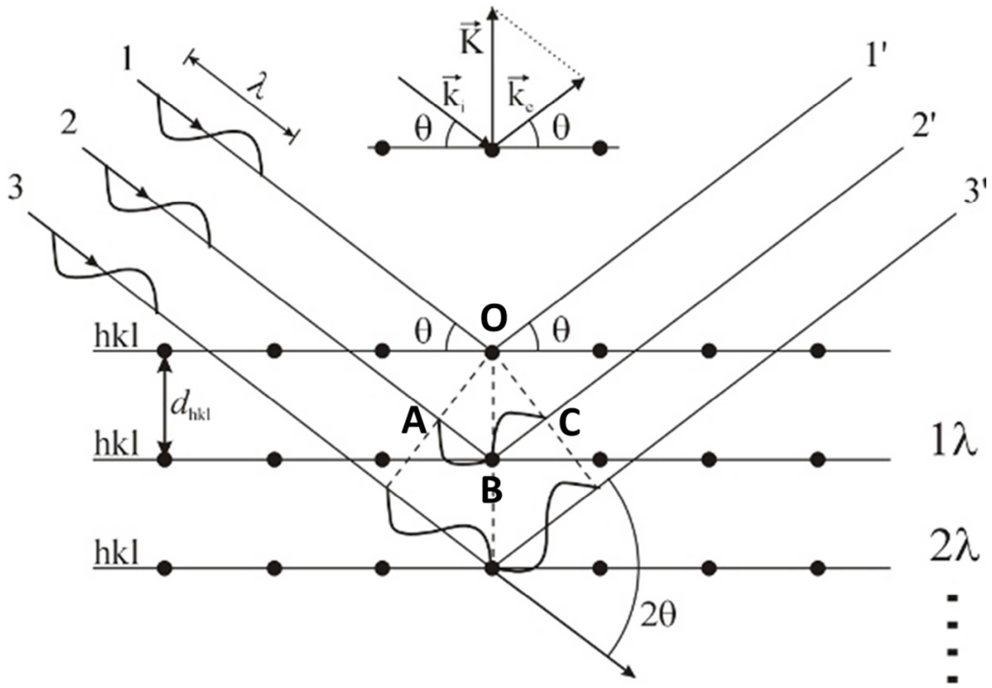

Figure 2.1 *Schematic representation of X-ray diffraction*

In this case a X-ray with wavelength λ is incident on a crystal plane *hkl* at an angle θ. Other X-rays of the same wavelength will be incident on other equidistant planes, with interplanar distance

d_{hkl}. Constructive interference occurs when the X-rays are reflected from the lattice planes at the specular angle θ if the path length difference between X-rays scattered from different hkl-planes is an integer times the wavelength. This can be represented in mathematical forms as follows:

$$n\lambda = AB + BC \qquad 2.1$$

From the crystallographic symmetry of the plane, AB = BC:

$$n\lambda = 2AB \qquad 2.2$$

The interplanar distance d_{hkl} is linked to the distance AB and the X-ray angle of incidence θ through the following trigonometric relation:

$$AB = d_{hkl} \sin\theta \qquad 2.3$$

Then:

$$n\lambda = 2d_{hkl} \sin\theta \qquad 2.4$$

The equation 2.4 is regarded as the Bragg's law of diffraction. Constructive interference occurs whenever this equation is satisfied.

In practical terms, XRD measurement can be performed in a diffractometer with two different geometries, as illustrated in Fig. 2.2

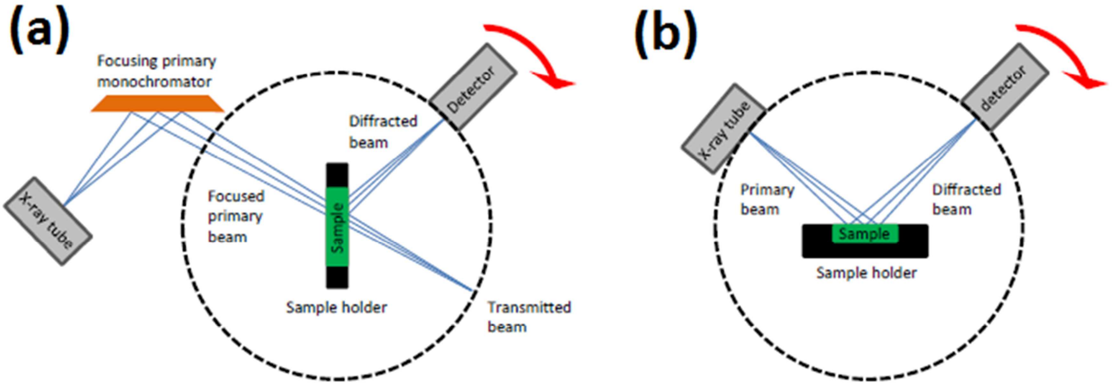

Figure 2.2 *Schematic representation of (a) transmission Debye-Scherrer geometry and (b) reflection Bragg-Brentano geometry*

In both cases, the diffractometer consists of three parts: 1) source of radiation equipped with monochromator, 2) sample holder and 3) detector. The Bragg-Brentano geometry is widely used for samples with strong X-ray absorption, whereas the Debye-Scherrer geometry is normally used for materials with low absorption. The detector scans a broad range of incident angles by rotating about the sample holder, and whenever there is a constructive interference a change in the X-ray intensity is recorded. The resulting measured intensity of the diffraction signal is plotted against the diffraction angle 2θ. The experimental data are then compared with existing literature XRD pattern of the compounds of interest. Each diffraction peak corresponds to a crystallographic plane, and its intensity can give a good indication of the preferential crystallographic orientation of the material. As previously shown, the crystallographic planes can be described as a function of three numbers h,k,l, which represent the Miller indices. These numbers are used to describe the orientation of a lattice plane with respect to the unit cell. The unit cell is the smallest 3D unit that can be continuously repeated to give an extended representation of the crystal structure. There are a total of fourteen different types of unit cells formally known as Bravais unit cells, which can be further classified in seven fundamental categories summarised in Tab. 2.1.

Category	**Cell lengths**	**Cell angles**
Cubic	a=b=c	α=β=γ=90°
Tetragonal	a=b≠c	α=β=γ=90°
Orthorhombic	a≠b≠c	α=β=γ=90°
Hexagonal	a=b≠c	α=β=90° γ=120°
Rhombohoedral	a=b=c	α=β=γ
Monoclinic	a≠b≠c	α≠β=γ=90°
Triclinic	a≠b≠c	α≠β≠γ

Table 2.1 *The seven categories of Bravais unit cells*

A schematic representation of the fourteen different types of Bravais unit cells is displayed in Fig. 2.3. The cubic unit cell has the highest symmetry, whereas the triclinic unit cell shows the lowest symmetry, according to their edge lengths (a,b,c) and internal angles (α, β, γ). For compounds with high degree of crystallographic symmetry, their XRD pattern would appear relatively simple, with only a few peaks as a result of the high multiplicity of the corresponding lattice planes. In contrast, for compounds with low level of symmetry, the XRD would appear complex, with numerous peaks as a result of the low multiplicity of the planes.

In this work, XRD analysis was revealed to be extremely useful for the identification of the different crystalline phases present in the synthesised materials. The diffractometers for the measurements had a typical Bragg-Brentano geometry. All the experimental XRD patterns were compared with published data of the corresponding pure compounds stored in the International Centre for Diffraction Data (ICDD) database.

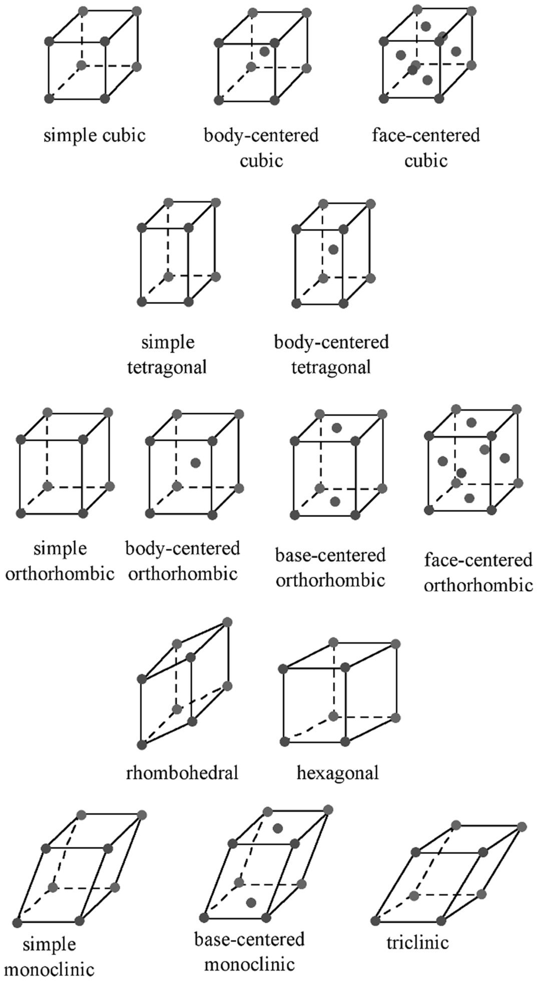

Figure 2.3 *Schematic representation of the fourteen different types of Bravais unit cells*

2.1.2 Scanning Electron Microscopy (SEM)

Scanning electron microscopy is a widely used technique in materials science for the examination and analysis of the morphological features and chemical composition characterisation. Image formation in SEM depends on the type of acquisition signals generated from the electron beam/sample interactions. In general these interactions can be divided into two categories: elastic interactions and inelastic interactions. Elastic scattering is due to the deflection of electrons by the sample atomic nuclei or outer shell electrons of similar energy. This type of interaction leads to negligible energy loss and wide-angle directional change of the scattered electrons. These elastically-scattered electrons are called primary backscattered electrons, and give a useful signal for imaging the sample (Fig. 2.4). Backscattered electrons can be emitted from a sample-depth of approximately 1 µm, and they constitute around 10-50% of the total primary beam electrons. The fraction of backscattered electrons increases as the sample contains heavy atoms as a result of their more positive charges on the nucleus.

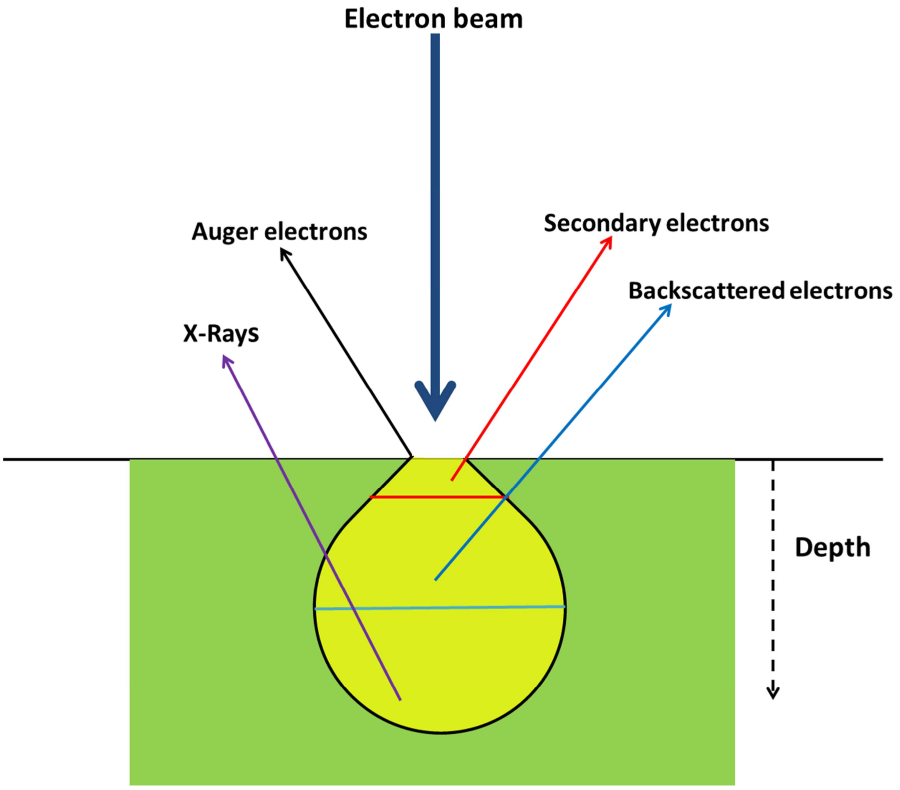

Figure 2.4 *Illustration of the different signals generated by the electron beam-sample interaction during SEM as a function of the bulk penetration depth*

In contrast, inelastic scattering occurs when the incident electrons transfer a significant amount of energy to the atoms/electrons of the sample upon collision. As a result, secondary electrons are emitted due to the displacement of inner-shell electrons by the high-energy incident primary electrons. This has the additional effect of producing characteristics X-rays as the outer-shell electron fall into the inner-shell following an ionisation event. Thus, by the emission of X-ray photon the atom returns to its ground state. The generated characteristics X-rays are used for the elemental analysis in a technique called energy-dispersive X-ray spectroscopy. Secondary electrons are conventionally defined as possessing energies less than 50 eV and can be used to image the sample. They are typically emitted from a thin layer of the surface approximately 5-50 nm thick. As shown in Fig. 2.4, Auger electrons are another type of electronic emission normally observed during the analysis. The Auger effect can occur during inelastic scattering, where the energy from the incident electron knocks out an electron from the inner K-atomic shell. Higher energy electron from the outer shell then drops down in energy, moving to the inner shell. In this case Auger electrons from the outer shells rather than X-ray photons are emitted in order to expel the excess energy. A schematic representation of the two different mechanisms is displayed in Fig. 2.5.

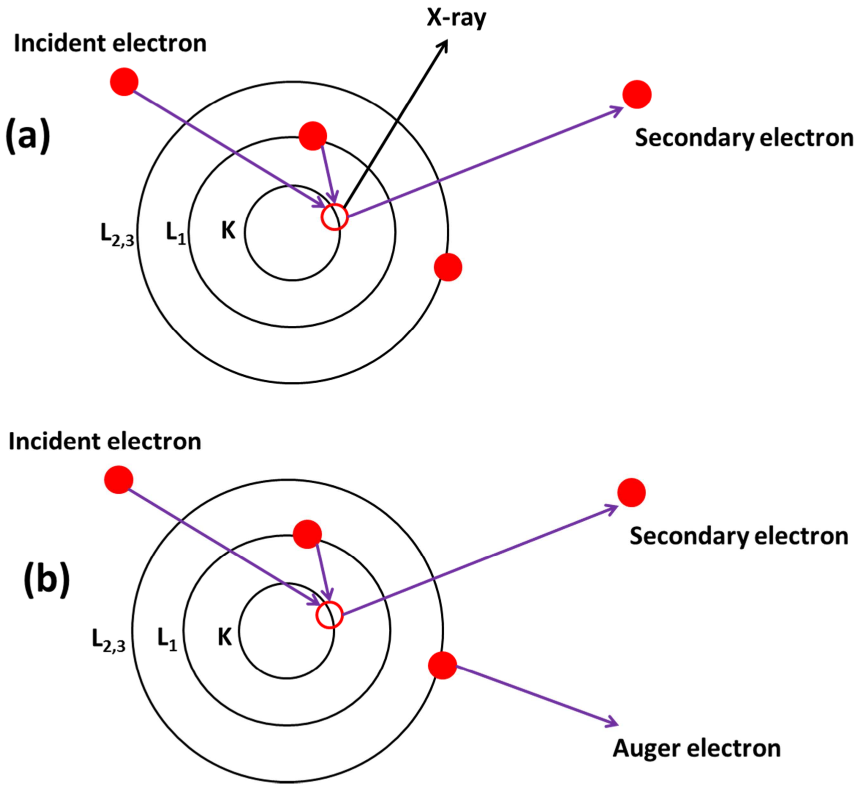

Figure 2.5 *Types of emission resulting from inelastic scattering of incident electrons; a) X-ray emission, b) Auger electron emission*

Auger electrons are only emitted from the first nanometers of the sample, as such they are primarily used in surface analysis.

The generation of a topographical image during SEM is based on the detection of the quantity of secondary electrons emitted from the sample. By changing the orientation of the surface with respect to the electron beam, it is possible to change the shape of the electron penetration volume (Fig. 2.4) which ultimately leads to a shift in the number of detected secondary electrons. This change in number of secondary electrons can be mapped as contrast in a black and white baseline image to produce the typical SEM image. For high-quality images, it is important to have electrically-conductive samples which allow for effective interaction of the incident beam and reduce the build-up of charges. The spatial resolution of SEM mainly depends on the size of the incident electron spot and the corresponding interaction volume of the material. Depending on the instrument, the maximum attainable resolution can be in the range 1-20 nm.

In this work SEM was used to reveal the morphological nature of the synthesised materials. In particular, high-resolution (< 100 nm) images were reported for the cobalt-nickel sulphide (Chapter 3) and Pt-cerium oxide-nickel oxide (Chapter 5) nanostructures. Cross-Section SEM analysis was used for the determination of the thickness of WO_3 thin film (Chapter 4).

2.1.3 Transmission Electron Microscopy (TEM)

Transmission electron microscopy provides useful information in terms of nanoscale morphology, elemental composition and crystallographic nature of a material. Similarly to SEM technique, transmission electron microscopy relies on the interaction between a highly energetic electron beam and the atoms constituting the sample to analyse. However in this case transmitted electrons are detected rather than reflected electrons, therefore the sample specimen must be thin enough to allow the electronic transmission. Typical TEM specimens have a thickness around 100 nm. A schematic representation of the different electronic emissions resulting from the beam-sample interactions is reported in Fig. 2.6.

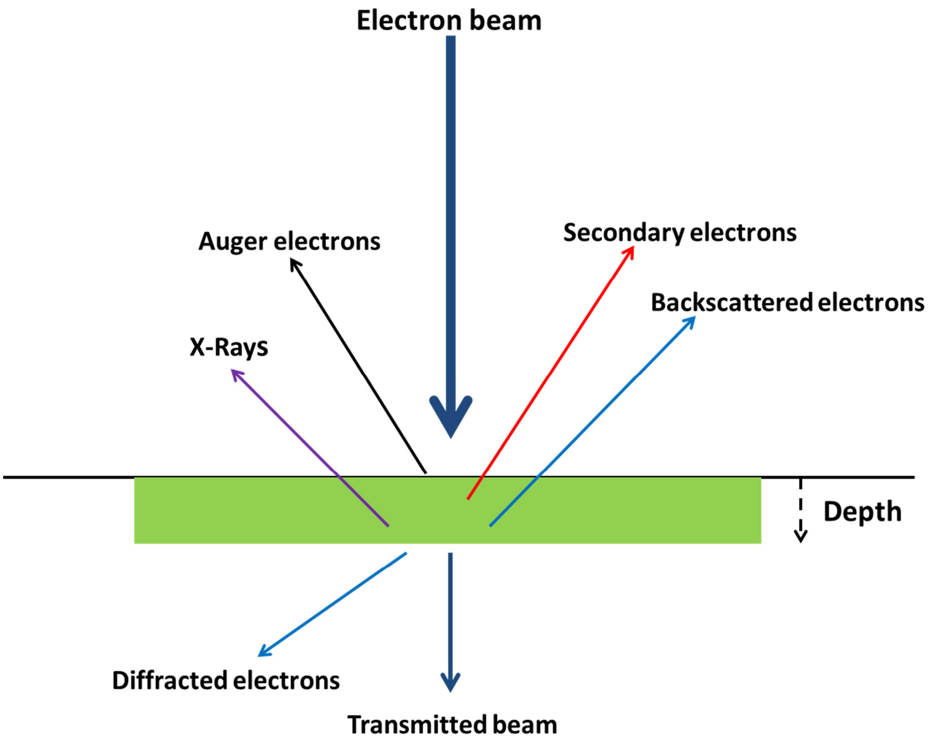

Figure 2.6 *Illustration of the different signals generated by the electron beam-sample interaction during TEM*

Bright field contrast is the most common mode of operation for imaging generation. In this mode, transmitted scattered electrons (both elastically and inelastically) are collected, passing through the objective lens and objective aperture in order to filter out highly scattering electrons. The imaging contrast is based on the different degree of scattering of the transmitted electrons. For instance, thicker regions of the sample will appear as dark, because the number of high-angle scattered electrons is low. In contrast, thinner regions will appear as bright as a result of the high number of collected low-angle scattered electrons.

Another type of contrast mode which is opposite to the bright field is the high annular dark field (HAADF). In this case the electron detector is positioned at a high angle with respect to the transmitted electron beam, resulting in the preferential detection of high-angle scattered electrons. As such, thicker regions will appear as bright whereas thinner regions will appear as dark. TEM images are generally produced in 2D with a resolution power of around 0.2 nm.

A widely used imaging mode especially in the case of nanoparticle characterisation is the high-resolution transmission electron microscopy (HRTEM). This powerful technique allows for the direct imaging of the atomic structure of the sample. The image is formed by the interference of electrons diffracted by lattice planes with the direct beam, resulting in a phase contrast. In some cases it can show directly a 2-D projection of the crystal containing defects.

In this work, TEM technique was used for the morphological and crystallographic determination of cobalt-nickel sulphide nanoparticles, described in Chapter 3. Being an electron diffraction technique, TEM can be used for the determination of the crystallographic structure of nanoparticles through the selected area electron diffraction (SAED) method, which is routinely performed with a TEM microscope. A general description of SAED is reported in Section 2.1.5. TEM and HRTEM were also used in the characterisation of Pt nanoparticles supported on CeO_2/NiO/Ni foam, giving important insights into their mean size and geometry (Chapter 5).

2.1.4 Energy Dispersive X-ray Spectroscopy (EDX)

Energy dispersive X-ray spectroscopy is an analytic technique used for the quantitative elemental analysis of a sample. It is relies on the emission of X-rays resulting from the interaction of incident electron beam with atoms constituting the sample, as previously illustrated in the section about SEM (Section 2.1.2). Thus, this technique is generally associated with SEM analysis. As represented in Fig. 2.5(a), the characteristic X-ray is emitted when an electron from the outer shell drops in the hole at the inner shell. The X-ray wavelength λ can be related to its energy as follows:

$$\lambda = \frac{hc}{\Delta E} \tag{2.1}$$

ΔE represents the energy of the emitted X-rays, which is the difference between the electron energy in the outer shell minus the electron energy in the inner shell. The energetic values of the electron shells are well defined for each chemical element, therefore the experimental energy can be compared with respect to the known reference values to identify the elemental chemical composition of the sample.

In this work EDX analysis was particularly useful for the quantitative elemental composition of cobalt-nickel sulphide materials (Chapter 3).

2.1.5 Selected Area Electron Diffraction (SAED)

As anticipated in Section 2.1.3, selected area electron diffraction is a crystallographic analytic method that can be performed inside a TEM microscope. Similarly to TEM imaging, electrons with high energy of 100-400 kV pass through the sample having small thickness preferably less than 100 nm. According to de Broglie equation, these highly energetic electrons have really small wavelengths on the order of a few thousandths of a nanometer. This length is a hundred times smaller than the spacing between atoms in a crystalline solid, thus allowing electrons to be elastically diffracted under different angles depending on the crystal structure. For single crystals, the resulting diffraction pattern will appear as a series of spots, with each spot corresponding to a satisfied diffraction condition of the sample's crystal structure. For polycrystalline materials SAED pattern will appear as a series of concentring disks, each one representing a particular lattice plane of the crystal.

This technique was used for the crystallographic determination of the multiphasic cobalt-nickel sulphide material in Chapter 3.

2.1.6 Raman Spectroscopy

Raman spectroscopy is a spectroscopy technique used for the detection of vibrational, rotational and other low-frequency modes in a compound. It has widely application in chemistry for the identification of molecules by observing its characteristic fingerprint. The analysis relies on inelastic scattering of incident monochromatic photons, usually from a laser working in the visible, infrared or ultraviolet range. The photons interact with phonons, molecular vibrations or other forms of excitation, resulting in a shift in their energy. This shift in energy can be linked to the particular vibrational modes in the system. In general, the sample is irradiated with a monochromatic laser with defined wavelength, and the elastic scattered photons (Rayleigh scattering) having same energy of the incident laser beam must be filtered out and separated from the inelastic photons (Raman scattering). The inelastic photons result from the interaction between the laser beam and the molecule, which can be in either the ground rovibronic state or an excited rovibronic state. Upon interaction, the molecule is a so-called virtual energy state for a short period of time, before an inelastically scattered photon results. The resulting energy of the emitted photon can be either lower (Stokes) or higher (Stokes) than the incident photon. The corresponding energy diagram of the various states involved in the Raman analysis is displayed in Fig. 2.7.

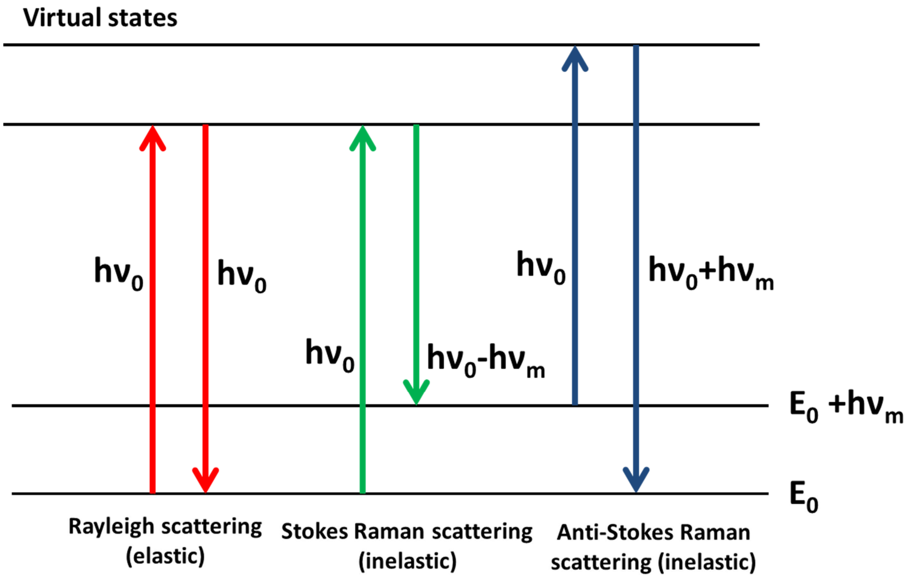

Figure 2.7 *Energy diagram of the three different states occurring during Raman analysis*

Clearly, if the final vibrational state of the molecule has higher energy with respect to its ground state, the corresponding emitted photon will be shifted to lower frequency (lower energy) in order to balance the total energy in the system. This shift in energy is reported in the x-axis of a Raman spectrum, and it is defined as:

$$\Delta\omega = \left(\frac{1}{\lambda_0} - \frac{1}{\lambda_1}\right) \qquad 2.2$$

$\Delta\omega$ is the Raman shift expressed in wavenumber (cm^{-1}), λ_0 is the excitation wavelength and λ_1 is the measured Raman wavelength.

It is worth noting that the Raman-effect is exhibited only by those molecules that are able to change the polarizability of the electric dipole-dipole with respect to the rovibronic state.

In this work Raman spectroscopy was used to probe the presence of Co_9S_8 phase in the multiphasic cobalt-nickel sulphide reported in Chapter 3.

2.1.7 UV-Visible spectroscopy

UV-Visible spectroscopy is a powerful technique for the determination of the optoelectronic characteristics of a material. It relies on the principle of electronic transition in atoms or molecules upon absorbing suitable energy from an incident light source. These electrons are excited from a lower energy state to a higher energy state. This technique was used for the determination of the optical band gap of WO_3 thin film and as such a brief description of UV-Vis analysis on semiconductors is presented. Semiconductors have a well-defined band gap which separates filled states (valence band) from unfilled states (conduction band). In order to determine this band gap, photons with different wavelengths ranging from UV region to near-IR region are directed to the material, and only those photons with energy equal or higher than the band gap will be absorbed. A simplified scheme illustrating the process is displayed in Fig. 2.8.

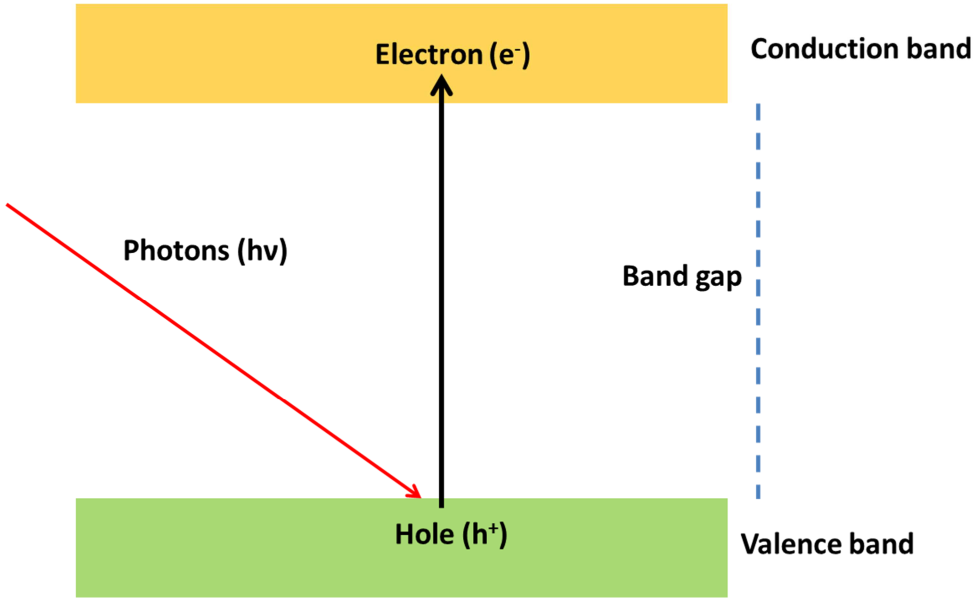

Figure 2.8 *Generation of electron-hole pair upon absorption of photons with energy equal to the band gap of the semiconductor*

Typically a spectrum reporting the absorption of the material as a function the photon wavelength is reported, and the band gap can be roughly determined by looking at the wavelength corresponding to the absorption edge. The spectrum is referenced to a baseline, which is normally generated prior to the analysis. For a more accurate calculation of the band gap, a Tauc analysis is generally used, and its formulation will be presented in Chapter 4.

As reported in Fig. 2.9, UV-Vis spectrophotometers can operate in three different modes, namely 1) reflection, 2) transmission and 3) absorption.

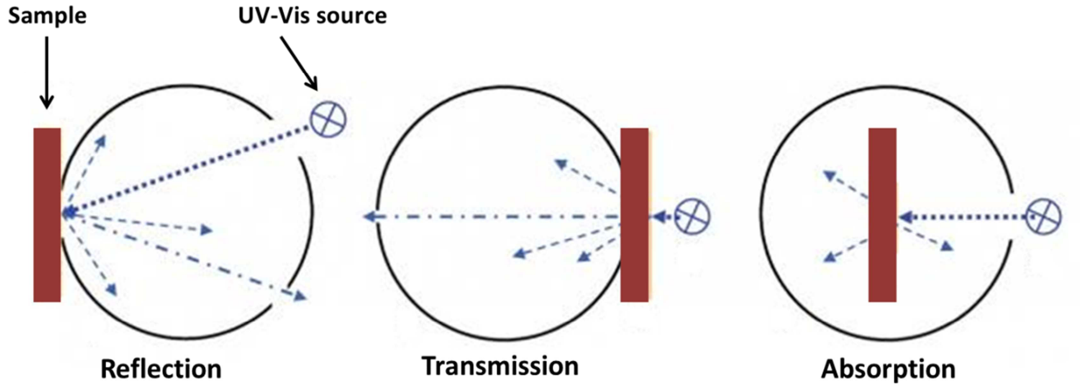

Figure 2.9 *Scheme of the three different configurations normally found in UV-Vis spectrophotometers*

Transmission and absorption modes are highly interrelated, and both can be used for solid, liquid or gas samples. The reflection mode can be extremely useful for the determination of the band gap of powder solids. In this work, UV-Vis absorption spectroscopy was used for the determination of the band gap of WO_3 thin film.

2.1.8 X-ray Photoelectron Spectroscopy (XPS)

X-ray photoelectron spectroscopy is a surface-analysis technique for the identification of the chemical nature of the elemental components of a material, including oxidation states. Indeed, all the elements except from H and He can be detected using this technique. XPS can probe with good accuracy the very top layer of a surface to a depth of about 10 nm. This technique relies on the interaction of incident X-ray photons with the core electrons of an atom. As displayed in Fig. 2.10, photoejection of an electron occur interaction with the incident X-ray photon. The resulting kinetic energy (KE) of the photoejection electron can be written as:

$$KE = h\nu - BE + \varphi \qquad 2.3$$

Where $h\nu$ is the energy of the incoming X-ray photons, *BE* is the binding energy of the photoejected electrons and φ is the spectrometer work function. The binding energies can be easily calculated from equation 2.3, given important information about the chemical nature on the surface of a sample. Each chemical element has a unique value of binding energy, therefore XPS can detect the presence of different elements by comparing the experimental pattern with some reported patterns of the correspondent pure counterparts.

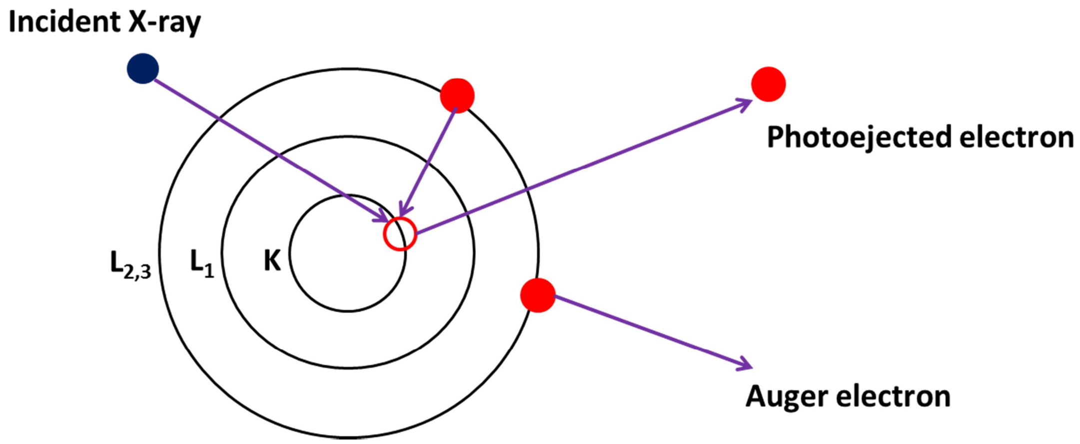

Figure 2.10 *Schematic representation of the atomic ionisation by interaction of a X-ray photon occurring during XPS*

It is worth noting that Auger electrons are generally detected during the process, as shown in Fig. 2.10. Typically, XPS data are plotted as intensity of the detected photoejected electrons versus binding energy, which is related to their kinetic energy. The spectroscopic notation of the peaks is denoted in the form nl_j located at specific binding energies are labelled according to the quantum numbers expressed below:

n: principal quantum number (1, 2, 3, 4 etc.)

l: momentum quantum number (l = 0 = s, l = 1 = p, l = 3 = d, l = 4 = f)

s = spin angular momentum 1/2, -1/2

j: spin-orbit coupling j = l + s

All orbital levels except the s levels give rise to a doublet with two possible states of slightly different binding energy. This process is known as spin-orbit splitting. These peaks will also have specific area ratios according to their degeneracy of each spin state. For instance, the 3d spectra will have peaks attributed to $3d_{5/2}$ and $3d_{3/2}$. The corresponding area ratio of the two spin orbit peaks will be 3:2.

The oxidation state of the chemical elements can be analysed by measuring the shift in binding energy of that element with respect to its metallic counterpart. When an atom is ionised, the relative ionisation energy increases due to the size constriction of the orbitals which induce an increase in attractive forces. As a result, the photoejected electrons of ionised atoms will have higher binding energies, and this can be easily detected by XPS. XPS can also give a quantitative analysis of the different chemical elements on the surface.

In this work XPS was intensively used for the surface characterisation of all three materials under study, helping to elucidate the presence of different oxidation states and chemical concentration on the surface.

2.1.9 Electrochemical Impedance Spectroscopy (EIS)

Electrochemical impedance spectroscopy is a powerful tool widely used for the investigation of the mechanism of electrochemical reactions. It measures the dielectric properties of a medium as a function of the frequency. In general, a small AC signal is applied to the cell, leading to a condition of pseudo-linearity of the system. As displayed in Fig. 2.11, the current (I) response to a sinusoidal potential will be a sinusoid at the same frequency but shifted in phase.

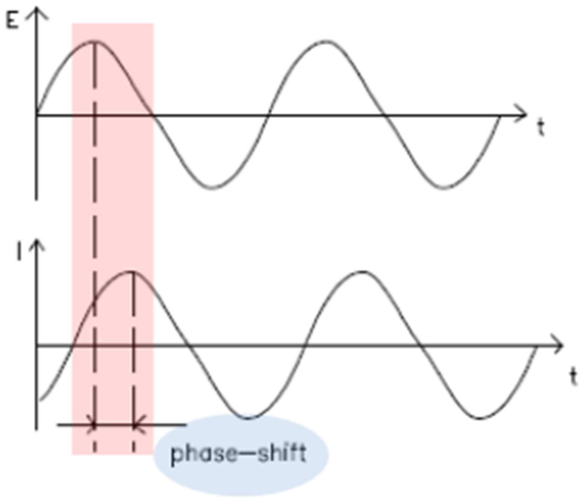

Figure 2.11 *Effect of small excitation signal of potential E on the recorded current I*

In mathematical terms:

$$E = E_0 \sin \omega t \qquad 2.4$$

$$\omega = 2\pi f \qquad 2.5$$

Where E is the potential measured at time t, E_0 is the amplitude of the signal, ω is the radial frequency and f is the absolute frequency. The measured current in a pseudo-linear system can be expressed as:

$$I = I_0 \sin(\omega t + \phi) \quad 2.6$$

Where ϕ is the phase-shift and I_0 is the current amplitude. By using the two expressions for the potential and the current it is possible to define the impedance of the system Z as:

$$Z = \frac{E}{I} = Z_0 \frac{\sin \omega t}{\sin \omega t + \phi} \quad 2.7$$

This equation can be reported in terms of complex numbers according to Euler's theorem:

$$Z(\omega) = Z_0(\cos \phi + \mathrm{j} \cdot \sin \phi) \quad 2.8$$

The impedance can be defined as a complex resistance arising from the flowing current through a circuit composed of different elements, like resistors, capacitors and inductors. This parameter is a function of the frequency, which is normally scanned during the measurement producing a set of impedance data plotted as Nyquist or Bode plots. In a typical Nyquist plot, the imaginary part of the impedance is plotted against its real counterpart. Each data on the generated curve represents the impedance at one frequency.

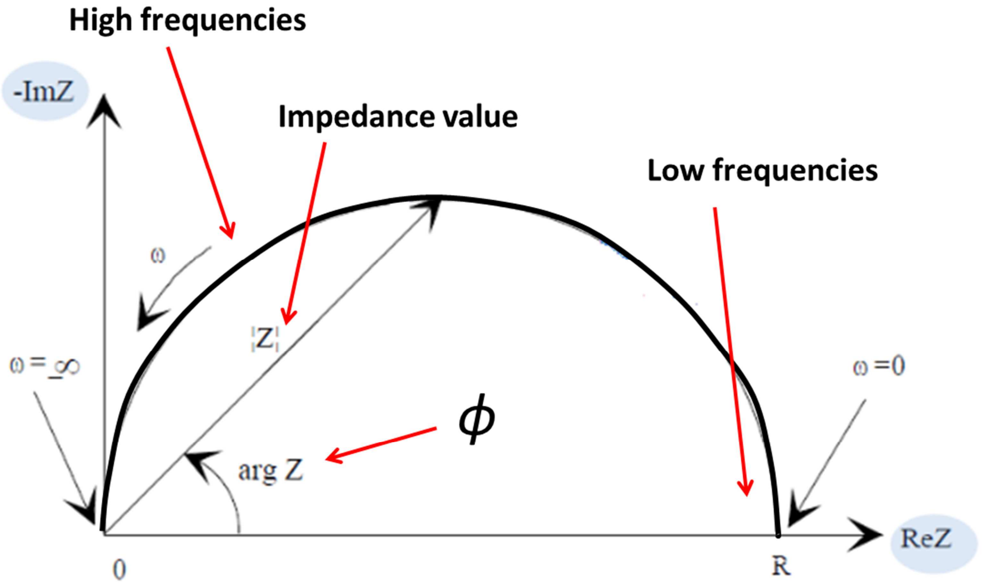

Figure 2.12 *Example of a Nyquist plot*

From a practical point of view, EIS experiments are carried out in a 3-electrode electrochemical cell using a potentiostat. The sample to analyse is electrically-connected to the circuit, minimising unwanted resistance due to hardware and wiring connection. The measurement is generally performed at a fixed AC potential of small amplitude. A range of frequencies is then scanned and the corresponding current is recorded. At the end of the experiment the resulting impedance data at each value of frequency is calculated through equation 2.8 and plotted. The data are then fitted using equivalent electric circuits. The elements composing the equivalent circuits can then model some physical properties of the electrode material under study, such as electron transfer at the interface, bulk resistance, bulk capacitance, electrochemically active surface area etc.

In this work EIS analysis was performed in order to elucidate the reaction mechanisms involved during electrocatalytic reactions. A detailed illustration of the specific equivalent circuits used for the fitting will be given in each experimental chapter.

Chapter 3: Design of active electrocatalyst based on cobalt-nickel sulphide composite electrode for the alkaline hydrogen evolution reaction

Acknowledgments

The following acknowledgements recognise the contributed work of colleagues and collaborators to the presented content of this chapter.

Coryl Jing Jun Lee: For collection of SEM data (Institute of Materials Research and Engineering, Singapore)

Lay Ting Ong: For collection of XPS data (Institute of Materials Research and Engineering, Singapore)

Hui Ru Tan: For collection of TEM data (Institute of Materials Research and Engineering, Singapore)

Dr Hong Liu: For collection of Raman data (Institute of Materials Research and Engineering, Singapore)

William Webb: For collection of XRD data (University of Southampton, UK)

This Chapter has been published: D. Ansovini, C. J. J. Lee, C. S. Chua, L. T. Ong, H. R. Tan, W. R. Webb, R. Raja and Y.-F. Lim, *J. Mater. Chem. A*, 2016, **4**, 9744.

3.1 Introduction

3.1.1 Transition metal sulphides: a promising class of active electrocatalysts for the hydrogen evolution reaction

Recent projections have shown that the world population will increase from 7.2 billion in 2015 to between 9.6 billion and 12.3 billion in 2100.[1] Reconciling the energy needs of a large population while mitigating global warming appears to be strictly dependent on renewable energy sources and their capacity to be cost-effective and easily scalable for a global and diffuse deployment. As discussed in the Introduction, one of the principal drawbacks of relying abundantly on renewable energy is represented by its intermittent nature, which does not guarantee a constant electric supply to the grid. Hence, it is extremely important to develop diversified and reliable technologies of energy storage, and in this regard a comprehensive list of existing energy storage systems was presented in Paragraph 1.2. In general, it was shown that the intermittent renewable energy like solar and wind power could be stored as long-lasting thermal,[2] electrochemical,[3] and chemical[4] energy. Among the various existing technologies hydrogen (H_2) production through solar-driven water electrolysis has received considerable attention, given the potential key role of hydrogen as a clean fuel and energy carrier.[5,6] The fundamental properties of water electrolysis were described in Section 1.2.1, and a detailed analysis of the fundamental characteristics of electrocatalysts for the hydrogen evolution reaction was given in Section 1.3.1.

In order to be commercially viable, water electrolysis requires active, durable and low-cost electrocatalysts for the hydrogen evolution reaction (HER) and the oxygen evolution reaction (OER). At present, platinum (Pt) and its alloys represent the most efficient catalysts for the HER in both acidic and basic environments, although its high cost and scarcity severely preclude a large-scale use for H_2 production.[7,8]

Consequently, numerous efforts have been devoted to the identification of active, stable and low-cost HER electrocatalysts. Relevant examples include first-row (Co, Ni, Fe)[8–13] and group VI (Mo, W)[14–18] transition metal sulphides, nitrides,[19] phosphides,[20–23] group VI transition metal carbides,[24,25] borides[26] and transition metal alloys.[7,27] Particularly in the last 10 years, transition metal sulphides (TMSs) have received considerable attention for their potential application as efficient HER electrocatalysts under wide operating conditions This is because TMSs offer several peculiar characteristics such as low cost, chemical stability and high electronic conductivity.[10] As mentioned in Section 1.3.1, the potential high activity of TMSs was also demonstrated through DFT calculations, where the hydrogen adsorption on the edges of MoS_2 was found to have an optimal value, close to that of Pt, which is reportedly known to be the most active HER catalyst in both acidic and basic environments. Since then, numerous works regarding the electrocatalytic performance of MoS_2 toward the HER have been published, with promising results. For example, Li *et al.* reported the design of MoS_2 nanoparticles grown directly on graphene through a simple solvothermal route.[18] The material showed good activity for the HER in acidic electrolyte, proceeding via a Tafel-Heyrovsky reaction mechanism. In this work the authors wanted to highlight the importance of nanostructuring as an effective way to maximise the direct exposure of active sites with the electrolyte, resulting in higher activity. The role of graphene was found to be essential, acting as nucleation site for the growth of MoS_2 nanoparticles and enhancing the overall electronic conductivity of the material. Another good example of the importance of nanostructuring in the case of MoS_2 was reported by Xie *et al.*, which successfully synthesised ultrathin MoS_2 nanosheets with additional active edge sites through hydrothermal method.[34] By carefully optimising the synthetic methodology, the authors were able to design a defect-rich MoS_2 structure with more exposed edge sites, which are notoriously considered to be the real active sites for the HER. Very recently, new designs based on MoS_2 nanostructures supported onto self-standing electrodes were developed, with enormous benefits in terms of electronic conductivity, low mass transfer resistance due to the large porous structure, easy implementation of the electrode into real devices, control of the metal loading and high exposure of the active sites.[15,35]

After the discovery of the good HER activity of MoS_2, a significant effort was made in order to fully elucidate the electrocatalytic properties of other TMS compounds, mainly based on first-row transition metals such as Co, Ni and Fe. This was also inspired by the fact that transition metals are found in metalloenzymes such as hydrogenase and nitrogenase, which are responsible for efficiently catalysing the hydrogen evolution in biological systems.[9] Based on these considerations, in 2013 Kong *et al.* reported for the first time the HER activity of Co, Ni and Fe sulphide materials with pyritic structure (MS_2), establishing a defined trend in activity depending of the type of metal used and morphological properties.[9] The authors were particularly interested in the pyritic structure because they noticed a similarity with the hydrogenase metalloenzyme in the ligand number and symmetry of some under-coordinated surface cations. Interestingly, the results confirmed the initial hypothesis, showing a good HER activity under acidic electrolyte for all the synthesised materials. In particular CoS_2, NiS_2 and $Fe_{0.47}Co_{0.53}S_2$ emerged as highly active HER electrocatalysts, possessing the lowest Tafel slope among several other compounds. These findings sparked significant interest among the researchers involved in the design of HER electrocatalysts. Indeed, studies regarding the development of compounds such as CoS_2,[8–11,28] Co_9S_8,[29,30] NiS_2,[28,31] Ni_3S_2,[32] Co-S,[33] Ni-S[12] were reported by several authors soon after this work. Faber *et al.* reported an extensive study on the electrocatalytic properties of CoS_2.[10] They developed a synthetic methodology for the creation of CoS_2 micro/nanostructures, which were found to be sensibly more active toward the HER under acidic environment. The best obtained catalyst showed a low overpotential of 145 mV vs RHE to reach a current density of 10 mA/cm^2, comparing well with the best reported TMS HER catalysts at that time. This material also showed excellent chemical and mechanical stability over prolonged chronoamperometric test. The authors wanted to stress the importance of nanostructuring as key factor for the dramatic improvement of the catalytic activity of CoS_2, which can be finely tuned by carefully controlling the synthetic parameters. Another significant work on CoS_2 was recently reported by Zhang *et al.*, where they successfully synthesised CoS_2 nanopyramids on 3D carbon fiber paper using a simple solvothermal reaction.[8] In this case, the composite electrode attained a low overpotential of 140 mV vs RHE to reach 10 mA/cm^2 under acidic environment, possessing also good chemical stability under a wide range of operating pH. The reasons of such high activity were attributed to several factors, such as optimal electronic conduction derived from the tight binding between CoS_2 and carbon fiber, high surface area, 3D porous structure and high crystallinity of the cubic CoS_2 having an intrinsic metallic character with negligible electronic resistance. Apart from CoS_2, other cobalt sulphide species with different structures started to be investigated as potential HER electrocatalysts. In 2013, Sun *et al.* reported a facile methodology for the electrodeposition of amorphous Co-S thin film.[33] The material showed good activity and stability toward the HER under neutral pH, having a low onset of 93 mV and maintaining a stable current for 40 hours. XPS and ICP analyses suggested that the dominant superficial composition was attributed to CoS, with some minor presence of $CoO/Co(OH)_2$. The catalyst was demonstrated to be stable also in basic electrolyte, although its activity was substantially poor. Very recently Feng *et al.* explored the properties of the cubic Co_9S_8 phase for the HER under a wide range of pH (0-14).[29] Specifically, the authors fabricated Co_9S_8 nanosheets grown on carbon cloth using a facile one-pot solvothermal reaction. Again, nanostructuring is the key for the enhancement of the catalytic activity, in a similar manner to what has been demonstrated with other materials. The excellent HER activity under neutral conditions (175 mV vs RHE to reach 10 mA/cm^2 at pH 7) was attributed to the intrinsic great catalytic activity of Co_9S_8 in neutral electrolyte, excellent electronic transport due to the metallic nature of Co_9S_8, presence of the conductive carbon cloth in tight contact with the active sites, and the large surface area as a result of the morphological features of the electrode.

Without any doubt the design of an optimal synthetic methodology represents the key factor behind the dramatic improvement in the catalytic properties of cobalt sulphide materials for the HER. In general the *in situ* growth of electrocatalytic materials onto binder-free and three-dimensional (3D) substrates can play a crucial role in obtaining composite electrodes with high mechanical stability and strong interface adhesion.[8,11,15] This is also true for nickel sulphide compounds, which have been extensively investigated as another class of HER catalysts. Wu *et al.* reported the synthesis of pyritic NiS_2 nanosheets supported on graphite substrate using a surfactant-templated reaction followed by sulfidation.[31] The material showed high activity and stability toward the HER in acid and basic electrolytes. The authors demonstrated through detailed electrochemical impedance spectroscopy that the reason of such high activity was attributed to the high electrochemically active surface area of the electrode. Other nickel sulphide structures were reported as efficient HER catalysts. For example, in 2015 Tang *et al.* demonstrated the high catalytic activity in neutral and alkaline media of Ni_3S_2 nanosheets array supported on Ni foam.[32] The self-standing 3D electrode was synthesised through a simple hydrothermal method, using nickel nitrate and thiourea as starting materials. The high HER activity (123 and 220 mV overpotentials at 10 mA/cm^2 in basic and neutral electrolytes, respectively) was attributed to the high loading of Ni_3S_2 nanosheets on the 3D Ni foam macrostructure and the easy release of H_2 bubbles from the active sites. Another relevant work about the HER catalytic activity of Ni_3S_2 was reported by Feng *et al.*[52] By controlling the synthetic parameters, the authors were able to make Ni_3S_2 nanosheets on Ni foam with the predominant presence of thermodynamically unstable high-index facets. According to DFT calculations, the hydrogen adsorption energy on these high-index facets was found to have a more suitable value compared to the low-index facets of the Ni_3S_2. This explained why this material showed impressive high HER activity in acidic electrolyte. Moreover, the morphological arrangement of Ni_3S_2 nanosheets on 3D Ni foam macroporous structure contributed significantly to the high exposure of active sites, which led to high electrochemical active surface area. An interesting work concerning the direct comparison between the intrinsic HER electrocatalytic properties of NiS, NiS_2 and Ni_3S_2 phases was recently carried out by Jiang *et al.*[36] The different compounds were carefully synthesised through a microwave-assisted solvothermal method, in order to make small nanoparticles with comparable crystallinity and surface area. The experimental activity trend for the HER in alkaline medium revealed that the rhombohedral Ni_3S_2 phase was the most active, followed by NiS_2 and NiS. This result corroborated nicely with theoretical calculations. The reason of the higher intrinsic electrocatalytic activity of Ni_3S_2 was attributed to its large electrochemically active surface area and high electronic conductivity. In contrast, NiS_2 and NiS phases were found to be semiconductors with band gaps of 1.1 and 0.4 eV, respectively, leading to higher resistance and hence lower electronic conductivity.

Other research trends are based on combining different elements in order to probe the existence of possible synergistic effects. However this route is at an early stage of development, with substantial room of improvement. For example, Liu *et al.* investigated the HER catalytic activity of $NiCo_2S_4$ nanowires array on carbon cloth.[56] The material was fabricated through sulphidization of the $NiCo_2O_4$ precursor, which was previously prepared by hydrothermal method. Interestingly the material showed good catalytic activity toward HER and OER in basic electrolyte, demonstrating its potential bifunctionality which is a relevant property not easily found in the majority of the existing compounds. Indeed, the authors were able to build an alkaline water electrolyser using the same electrocatalyst as anode and cathode, requiring a voltage of 1.68 V in order to attain a current density of 10 mA/cm^2. The high activity was due to the high electronic conductivity provided by the tight contact between the carbon cloth and active sites and the high electrochemical active surface area derived from the nanowire morphology. Han *et al.* investigated the electrocatalytic properties of amorphous Ni-S-Co thin film for the HER in alkaline environment. The film was fabricated through a simple electrodeposition process using thiourea as sulfur source.[59] It was found that the activity of Ni-S-Co was higher than the amorphous Ni-S, and the authors attributed such good performance to the large amount of adsorbed H atoms as a result of the fast Volmer step occurring at the electrode.

3.1.2 Objectives

The objectives of this chapter are schematically summarised in the following points:

1. To synthesise a catalyst based on transition metal sulphides (Co_9S_8, Ni_xS_y) supported onto a 3D self-standing Ni foam electrode using a straightforward thermal decomposition method
2. To investigate the structural and morphological properties of the synthesised material
3. To test the catalytic activity and stability of the material toward the alkaline hydrogen evolution reaction
4. To investigate the main mechanism of reaction and elucidate the nature of active sites
5. To establish structure-property relations of the synthesised materials through a combined characterisation and testing analysis

3.2 Results and Discussion

3.2.1 Description of the synthetic methodology based on thermal decomposition of cobalt-thiourea molecular complex

The synthetic strategy followed in this work was inspired by previous works reporting the formation of pure cobalt sulphide nanoparticles through the thermal annealing under inert atmosphere of a preformed Co-thiourea molecular complex.[37,38] Kumar *et al.* evaluated the formation of cobalt sulphide species from the thermal decomposition of cobalt-thiourea molecular complex under selected annealing temperatures for 2 hours.[38] Their experiments were performed in N_2 in order to prevent oxidation of the sulphide materials. According to their findings, pure pyritic CoS_2 was formed at low temperature of 400 °C, whereas a mixture of CoS and Co_9S_8 was obtained at temperatures ranging from 400 °C to 1000 °C. Only pure Co_9S_8 was found for annealing temperatures higher than 1000 °C. The structural nature of the different phases was analysed through XRD technique. Ganesan *et al.*, taking inspiration from the above-mentioned fundamental study, prepared cobalt sulphide nanoparticles dispersed on graphene oxide hybrids using a thermal decomposition of cobalt-thiourea complex. Also in this case different cobalt sulphide phases were obtained as a function of the annealing temperature. In particular, pure nanosized CoS_2 was formed at 400 and 500 °C, whereas only cubic Co_9S_8 was observed at 600 °C. It is worth noting that no CoS phase was detected, in contrast to the results reported by Kumar *et al.* The obtained composite compounds possessed small particle size, which was calculated through SEM and ranging from 42 nm in the case of CoS_2/graphene oxide annealed at 400 °C to 81 nm in the case of Co_9S_8/graphene oxide annealed at 600 °C. Interestingly, the particle size of the control sample made of CoS_2 without the presence of graphene oxide was found to be equal to 200 nm, with significant agglomeration. Thus, graphene oxide played a crucial role for the synthesis of well-dispersed cobalt sulphide species with small particle size.

In general, this synthetic methodology for the generation of cobalt sulphide compounds offers several advantages compared to the more traditional routes based on solvothermal, hydrothermal and thermal sulphidization using H_2S or sulphur. First of all, the cobalt-thiourea molecular complex is simple to make, and it can be easily mixed with other compounds in order to create novel composite materials, as in the case of the work previously described. Second, the thermal decomposition does not require the addition of sulfurizing agents such as H_2S and sulphur, which are notoriously hazardous. In this case sulphur is directly provided by thiourea. Third, the whole fabrication process is relatively faster compared to the time-consuming solvothermal and hydrothermal reactions.

Aim of this work was to explore the applicability of this synthetic methodology to the generation of cobalt sulphide species supported on 3D metallic Ni foam for the first time. Ni foam is a substrate of particular interest considering its unique 3D macroporous structure, high electronic conductivity and low cost, making it suitable as good support for the fabrication of electrodes. In general terms, three main synthetic steps are involved in the whole fabrication process: 1) preparation of a methanolic solution containing cobalt precursor and thiourea with thiourea/Co molar ratio of 4; 2) immersion of cleaned Ni foam into the Co-thiourea solution; 3) thermal annealing under inert atmosphere. The metal loading in the sample can be controlled simply by repeating the two steps of immersion-thermal annealing. Particularly, annealing temperature and time were systematically varied, in order to better understand the principal morphological and structural transformations involved during the thermal treatment. The annealing temperature was fixed at 400 and 500 °C, and the annealing time was maintained at 10 and 90 min. Surprisingly, XRD revealed the formation of pure cubic Co_9S_8 along with a multitude of nickel sulphide phases, regardless of the annealing temperature or annealing time used. Contrary to what was observed in the above-described referencing works, CoS_2 was not detected. The formation of different nickel sulphide phases suggested that thiourea can react with metallic Ni during the thermal decomposition, providing gaseous reactive sulfurized compounds able to activate the superficial Ni atoms under a gas-solid reaction. This phenomenon was confirmed from the analysis of the control sample experiment, which was synthesised without the presence of cobalt ions in the methanolic solution. In this case only thiourea was dissolved in methanol, and the XRD results gave evidence of the formation of pure rhombohedral Ni_3S_2, without presence of other nickel sulphide phases. Also in this case the formation of Ni_3S_2 was independent on the annealing temperature and time. The detailed structural and morphological characterisation of the various samples is reported in Section 4.2.2. Samples obtained by the thermal decomposition of thiourea at a specific temperature (T) and time (t) will be referred as Ni_3S_2/Nif(T,t), whereas those obtained by the thermal decomposition of Co-thiourea complex will be referred as Co_9S_8-Ni_xS_y/Nif(T,t). Unless otherwise stated, all the characterized samples showed below were synthesised by performing 5 cycles of dip coating-annealing.

3.2.2 Structural and morphological characterisation

X-ray diffraction (XRD) patterns for the Co_9S_8-Ni_xS_y/Nif and the Ni_3S_2/Nif electrodes are reported in Fig. 3.1 and Fig. 3.2, respectively. In the case of the monometallic system, the XRD patterns show the formation of a pure rhombohedral Ni_3S_2 (JCPDS no. 30-0863) for all the different annealing conditions. The strongest peak was located at 31.1° and it was indexed to the (110) plane. No secondary phases were detected, apart from the presence of two strong peaks at 44.5° and 51.8°

which were assigned to the (111) and (200) planes of the face-centered cubic metallic Ni foam. These three peaks were consistently found in the bimetallic system. This is the first time that pure Ni_3S_2 supported on Ni foam was successfully synthesised using a simple thermal decomposition of thiourea under inert atmosphere. Previous works related to the synthesis of Ni_3S_2/Nif were mainly based on hydrothermal or solvothermal reactions, where Nif was positioned inside a Teflon liner containing nickel salt and thiourea/thioacetamide and let to react under high temperatures for several hours.[32,52] A contrasting behaviour can be observed for the Co_9S_8-Ni_xS_y/Nif electrode, with the formation of a variety of nickel sulphide phases and the cubic Co_9S_8. The diffraction peaks were carefully indexed by comparing the experimental pattern with reported data, and compounds such as NiS_2 (JCPDS no. 03-0734), $Ni_{17}S_{18}$ (JCPDS no. 76-2306), NiS (JCPDS no. 12-0041), Ni_7S_6 (JCPDS no. 24-1021) and Ni_3S_2 (JCPDS no. 30-0863) were identified. Only one phase of cobalt sulphide was detected, with the main diffraction peak at 30.0° indexed to the (220) plane of the cubic Co_9S_8 (JCPDS no. 86-2273) for all the synthetic conditions used. However in the XRD spectrum of the sample annealed at 400 °C for 10 min displayed in Fig. 3.1(a), the peak related to Co_9S_8 was not discernible from the strong peak at 30.0° and corresponding to the (300) plane of the hexagonal $Ni_{17}S_{18}$. As briefly discussed in Section 4.2.1, the absence of the pyritic CoS_2 is in contrast to the previous findings of Kumar *et al.* and Ganesan *et al.*, where they both reported the formation of CoS_2 at 400 °C. In the work reported by Kumar et al., Co_9S_8 started to appear at 500 °C, whereas Ganesan *et al.* were able to synthesise Co_9S_8 only at 600 °C. The cubic Co_9S_8 phase is sulphur-deficient (Co/S = 1.125), and it is thermodynamically favoured in sulphur-poor environments. When the annealing temperature goes up, sulphur tends to evaporate, leading to the formation of sulphur-deficient species. Indeed, Kumar *et al.* were able to synthesise pure Co_9S_8 only at extremely high temperature of 1000 °C. In this case, given the concomitant presence of metallic Ni which reacted with sulfurized compounds coming from the thermal decomposition of thiourea, the local environment at atomic level did not have enough sulphur to guarantee the formation of sulphur-rich CoS_2 (Co/S = 0.5). For the same reason, nickel sulphide species with sulphur-deficient phases (Ni/S > 1) were favoured at high temperatures and long annealing times. For instance, the Co_9S_8-Ni_xS_y/Nif(500,90) showed only the presence of Ni_3S_2 (Ni/S = 1.5) along with Co_9S_8, in stark contrast with the multitude of phases observed for the other investigated conditions. It is important to outline that the formation of several phases of nickel sulphide was only observed in the sample containing cobalt. From a thermodynamic point of view, nickel sulphide presents a very complex phase diagram, containing binary phases like $Ni_{3+x}S_2$, Ni_3S_2, Ni_4S_{3+x}, Ni_6S_5, Ni_7S_6, Ni_9S_8, NiS, Ni_3S_4 and NiS_2 in a wide range of temperatures between 200 and 1000 °C.[60] Hence, it is surprising that the thermal decomposition of thiourea in absence of cobalt ions may lead to the formation of pure Ni_3S_2 without evidence of secondary phases, even at low temperature of 400 °C and for short annealing time. It is worth noting that the quantitative understanding of the principal mechanisms occurring during the synthesis of these materials was beyond the scope of this work, and the interpretation of the structural results were only driven by qualitative considerations based on previous published works.

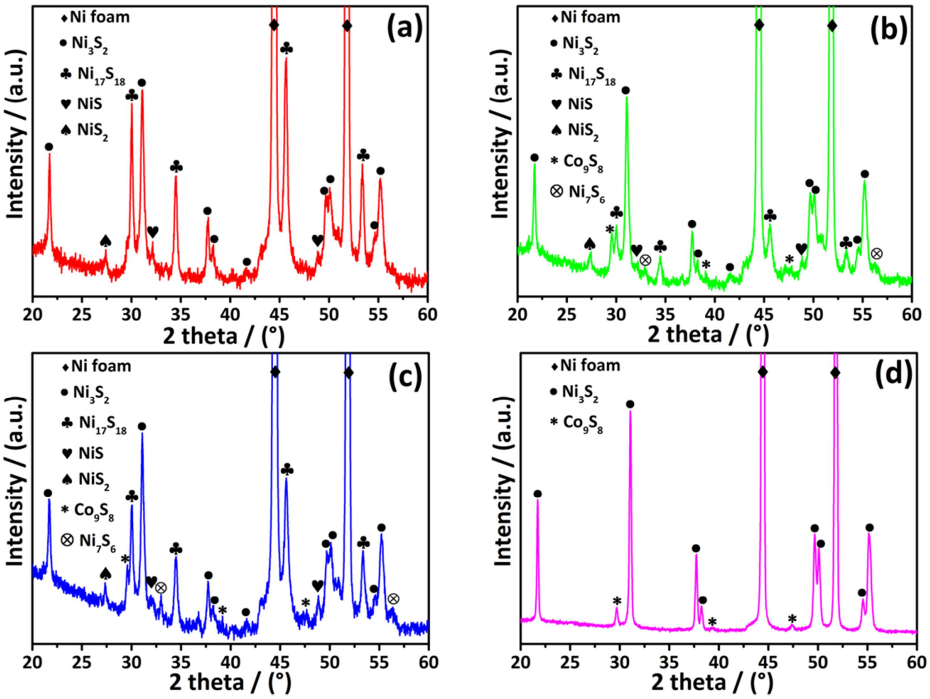

Figure 3.1 *XRD patterns for Co_9S_8-Ni_xS_y/Nif different annealing temperatures and times (a) 400 °C 10 min, (b) 400°C 90 min; (c) 500°C 10 min, (d) 500°C 90 min*

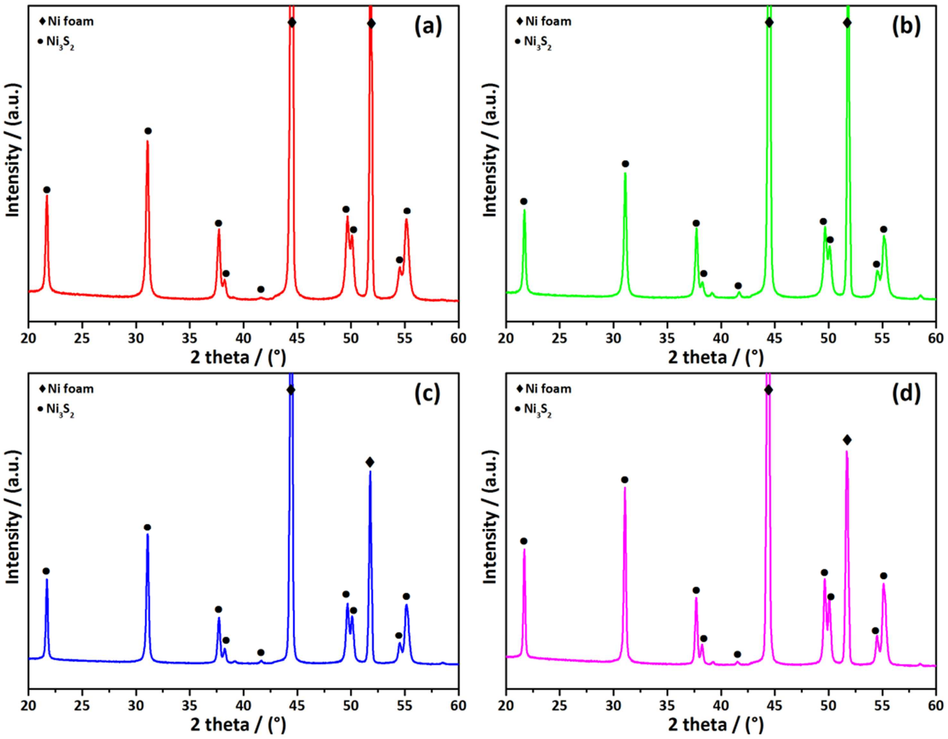

Figure 3.2 *XRD patterns for the Ni_3S_2/Nif at different annealing temperatures and times (a) 400 °C 10 min, (b) 400°C 90 min, (c) 500°C 10 min, (d) 500°C 90 min*

The presence of Co_9S_8 was further confirmed by Raman spectroscopy as highlighted in Fig. 3.3, where two peaks located at 510 cm^{-1} and 1040 cm^{-1} match well with those reported for the pure Co_9S_8.[39] These peaks were consistently individuated for all the investigated annealing temperatures and times. In particular, the peak located at 510 cm^{-1} for the Co_9S_8-Ni_xS_y/Nif(500,90) sample in Fig. 3.3(d) was sensibly sharper compared to the other samples, possibly as a result of higher crystallinity of Co_9S_8 under the annealing temperature of 500 °C for 90 min. A broad peak at around 300-350 cm^{-1} was found in the characteristic range of Ni_3S_2,[40] although its poor resolution hindered a defined deconvolution of the peaks documented in the literature. Typical peaks found in the literature and related to pure Ni_3S_2 are located at 188, 202, 224, 304, 325 and 350 cm^{-1}. This could be also due to an overlapping with the other nickel sulphide phases which may have a similar Raman pattern. Kong *et al.* reported the Raman spectrum of the pyritic NiS_2, composed of three peaks at 272, 283 and 477 cm^{-1}.[9] The assignment of Raman bands for the millerite NiS was carried out by Guillaume *et al.*, which detected eight peaks located at 149, 208, 230, 247, 250, 300, 352 and 373 cm^{-1}.[61] As for the hexagonal $Ni_{17}S_{18}$ phase, no Raman spectra can be found in the literature.

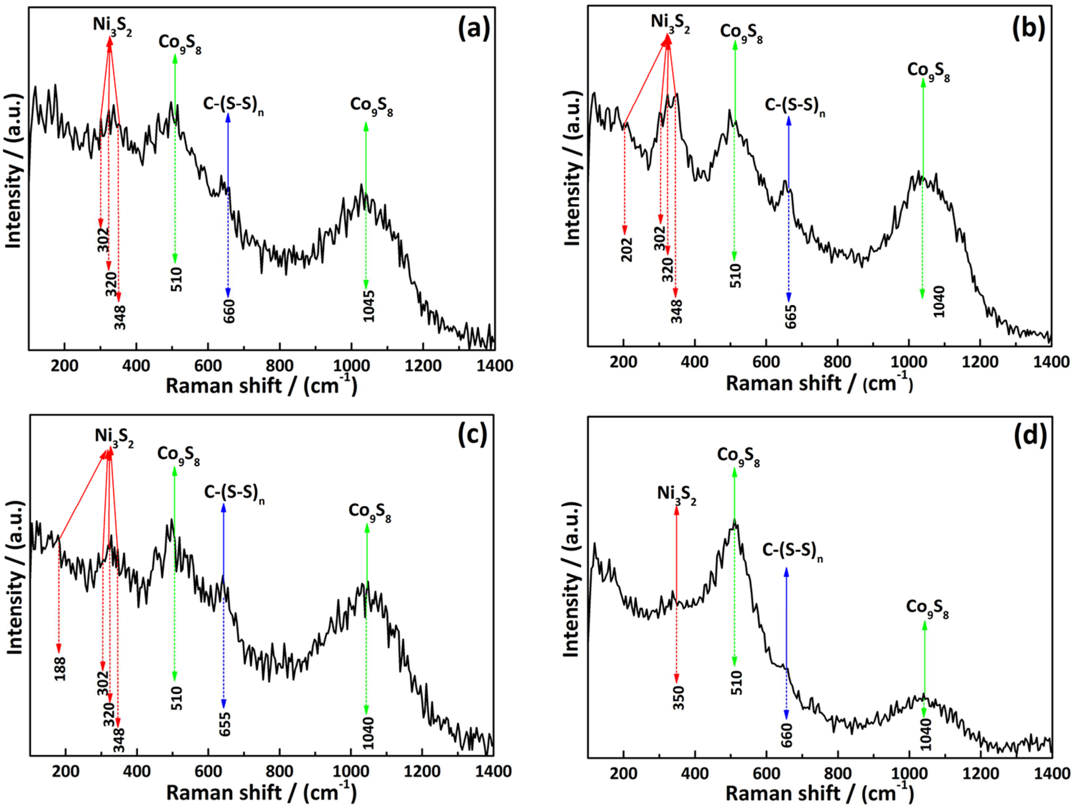

Figure 3.3 *Raman spectra for Co_9S_8-Ni_xS_y/Nif at different annealing temperatures and times (a) 400 °C 10 min, (b) 400°C 90 min, (c) 500°C 10 min, (d) 500°C 90 min*

The SEM images for the Co_9S_8-Ni_xS_y/Nif (Fig. 3.4) and Ni_3S_2/Nif (Fig. 3.5) reveal the formation of nanoparticulate morphology of similar nature for both electrodes. In the high-magnification SEM images of the Co_9S_8-Ni_xS_y/Nif samples it was possible to observe the morphological evolution of the material as a function of the annealing temperature and time. For the sample annealed at 400 °C for 10 min (inset of Fig. 3.4(a)), a clear presence of small nanoparticles with size of less than 100 nm agglomerated into large chunks was observed. By increasing the annealing temperature and time, these nanoparticles are prone to coalescence, resulting in large chunks without that defined nanometric morphology previously noticed. This same trend was also observed for the Ni_3S_2/Nif, with the high-magnification SEM images reported in the insets of Fig 3.5(a), (b), (c) and (d). TEM analysis was performed on the Co_9S_8-Ni_xS_y/Nif samples in order to elucidate the nanoparticulate morphology with more accuracy. For all the annealing conditions under study, nanoparticles having a mean diameter of less than 20 nm were individuated. The resulting images are reported in Fig. 3.6. Given the extremely complex multiphasic nature of the materials, selected area electron diffraction (SAED) patterns for the Co_9S_8-Ni_xS_y/Nif(500,10) and Co_9S_8-Ni_xS_y/Nif(500,90) samples were measured. SAED is a diffraction technique which is able to identify the crystallographic nature of nanoparticles. In particular with SAED it is possible to reveal if the nanoparticle is amorphous, monocrystalline or polycrystalline. The main advantage of SAED compared to the classic XRD is that SAED can examine small geometric areas as small as several hundred of nanometers in size, whereas XRD samples much bigger areas in the scale of centimeters. Hence, SAED is able to resolve crystallography structures at nanometric level, which is useful when the sample to analyse is a composite material with several compounds of different size. According to the crystallographic nature of the nanoparticles, the SAED pattern can contain diffuse rings if the material is amorphous, small spots making up rings of different sizes if the material is polycrystalline or composed of different crystallographic phases and bright spots if the material is monocrystalline with no other crystallographic phases. In the SAED patterns recorded for the Co_9S_8-Ni_xS_y/Nif(500,10) and Co_9S_8-Ni_xS_y/Nif(500,90) samples and reported in Fig. 3.6 (e) and (f), respectively, the presence of small spots making up different rings of different sizes suggested the existence of polycrystalline and multiphasic nature of the nanoparticles. This result is in agreement with the XRD patterns previously illustrated. Each ring represents a crystallographic plane, and their determination can be done by comparing the calculated d-spacing with the d-spacing derived from XRD. The d-spacing of each ring can be calculated using the following formula:

$$d = \frac{\lambda l}{R} \qquad 3.1$$

Where λ is electron wavelength, *l* is camera focal length and *R* is the distance between the central spot and the diffracted ring. The d-spacing of crystallographic planes detected through XRD can be calculated using Bragg's law, as follows:

$$d = \frac{2\lambda_{CuK\alpha}}{\sin\vartheta} \qquad 3.2$$

Where $\lambda_{CuK\alpha}$ is the X-ray wavelength and θ is the diffraction angle where the peak occurs. In the Co_9S_8-Ni_xS_y/Nif(500,10) sample (Fig. 3.6(e)), rings attributed to the (400) and (511) planes of Co_9S_8 were detected, corresponding to XRD peaks located at 36.3° and 47.6°, respectively. Rings attributed to the (110) plane of the rhombohedral Ni_3S_2 phase and (303) plane of the hexagonal $Ni_{17}S_{18}$ phase were found, thus reflecting the multiphasic nature of the material. In the Co_9S_8-Ni_xS_y/Nif(500,90) sample (Fig. 3.6(f)), no rings attributed to $Ni_{17}S_{18}$ phase could be detected, in perfect agreement with the experimental XRD reported in Fig. 3.1(d) which showed the absence of any hexagonal $Ni_{17}S_{18}$. However, different rings assigned to the (110), (003), (211) and (122) planes of Ni_3S_2 were found, along with the presence of rings attributed to the (311), (400) and (511) planes of the cubic Co_9S_8. The (110), (003), (211) and (122) planes of Ni_3S_2 correspond to XRD peaks located at 31.1°, 37.8°, 50.1° and 55.1°, respectively. The (311) plane of the cubic Co_9S_8 corresponds to the XRD peak located at 30.0°. It is worth noting that all these peaks detected through SAED analysis were consistently found in the experimental XRD patterns in Fig. 3.1(d). However not all the phases identified through XRD can be traced in the SAED patterns, given the small proximity of the diffracted peaks and the intrinsic low angular resolution of the electron diffraction technique.

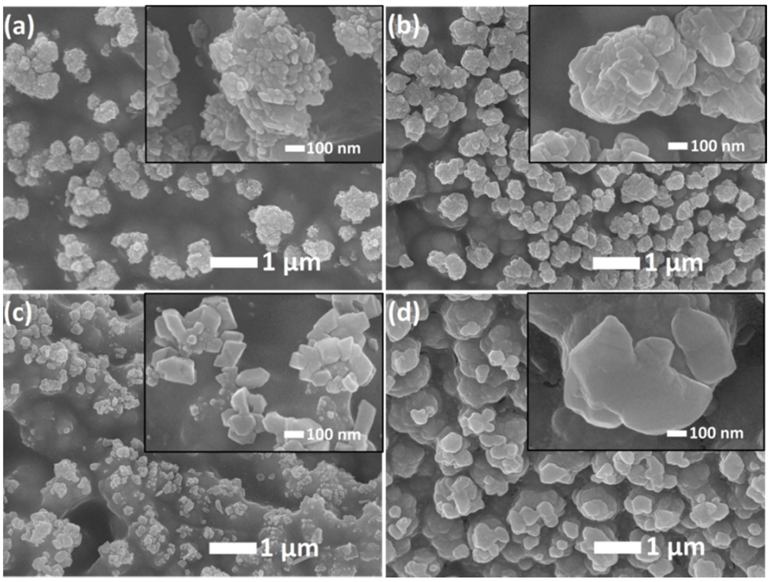

Figure 3.4 *Low- and high-magnification SEM images for Co_9S_8-Ni_xS_y/Nif at different annealing temperatures and times (a) 400 °C 10 min, (b) 400°C 90 min; (c) 500°C 10 min, (d) 500°C 90 min*

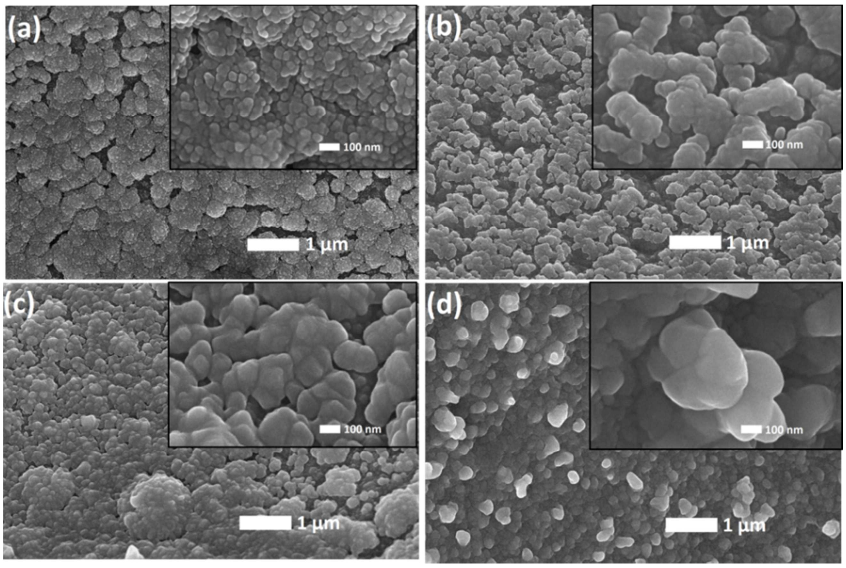

Figure 3.5 *Low- and high-magnification SEM images for Ni_3S_2/Nif at different annealing temperatures and times (a) 400 °C 10 min, (b) 400°C 90 min, (c) 500°C 10 min, (d) 500°C 90 min*

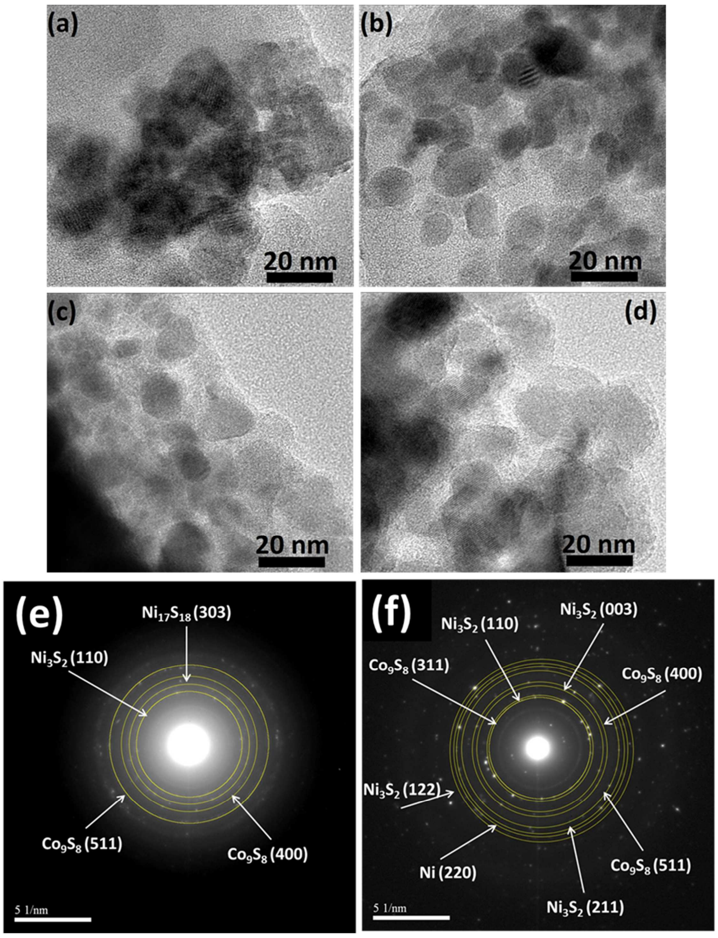

Figure 3.6 *TEM images for Co_9S_8-Ni_xS_y/Nif at different annealing temperatures and times (a) 400 °C 10 min, (b) 400°C 90 min; (c) 500°C 10 min, (d) 500°C 90 min. Selected area electron diffraction patterns for Co_9S_8-Ni_xS_y/Nif at (e) 500°C 10 min and (f) 500°C 90 min*

The quantitative determination of the atomic percentage of the different chemical elements composing the samples was performed using energy-dispersive X-ray spectroscopy (EDX) technique. The results obtained from the Co_9S_8-Ni_xS_y/Nif material under different annealing temperatures and times are summarised and reported in Fig. 3.7. The atomic percentage of Co is around 4%, regardless of the annealing conditions used. This is not surprising because the amount of Co in the sample exclusively depends on the number of cycles used during the synthesis. Significant amount of elemental carbon (C) and nitrogen (N) was detected as a result of the formation of side products originating from the pyrolitic decomposition of thiourea.[41] However for the sample annealed at 500 °C for 90 min, the atomic concentrations of elemental C and N were sensibly smaller in comparison with the other samples, attaining values of 28% and 1.1 %, respectively. As reported by the work of Breml *et al.*, the thermal decomposition of thiourea in a closed system under inert atmosphere can lead to the production of melamine and its polymeric associated adducts.[41] Melamine is an organic base having chemical formula $C_3H_6N_6$, which is relatively prone to sublimation at temperature higher than 300 °C. Thus, the long annealing time (90 min) at high temperature of 500 °C of the Co_9S_8-Ni_xS_y/Nif sample could have led to the loss of melamine and its polymeric adducts through sublimation/evaporation. This phenomenon could not be observed for low annealing temperature (400 °C) and short annealing time (10 min). The thermal decomposition of thiourea could have also led to the formation of carbon nitride, although further analysis is required to fully elucidate its possible presence. It is known that graphitic carbon nitride can be readily formed by thermal decomposition of thiourea in air at 550 °C, as reported by Dong *et al.*[64]

By recording the net gaining in weight of the sample after the synthesis it was possible to calculate a semi-quantitative estimate of the mass loading of Co_9S_8 for the Co_9S_8-Ni_xS_y/Nif, using the following formula.

$$M_{Co9S8}\left({}^{mg}/_{cm^2}\right) = \left[\frac{\left(M_{Nif(a.s.)} - M_{Nif(b.s.)}\right)}{Area}\%wt_{Co}\right]\frac{RMM_{Co9S8}}{9RMM_{Co}} \qquad 3.3$$

Where $M_{Nif(a.s.)}$ (in g) is the weight of the sample after synthesis, $M_{Nif(b.s.)}$ (in g) is the weight of the sample before synthesis, *Area* is the geometric area (in cm^2), $\%wt_{Co}$ is the Co weight percentage calculated on Ni free basis, RMM_{Co9S8} is the molecular mass of Co_9S_8 (786.85 g/mol) and RMM_{Co} is the atomic mass of Co (58.93 g/mol). The resulting Co_9S_8 mass loading calculated with this method gave a value of almost 2 mg/cm^2. This formula could also be applied for the calculation of the mass loading of Ni_xS_y, with some modifications as follows:

$$M_{Ni3S2}\left({}^{mg}/_{cm^2}\right) = \left[\frac{\left(M_{Nif(a.s.)} - M_{Nif(b.s.)}\right)}{Area}\left(\%wt_{St} - \%wt_{S(Co9S8)}\right)\right]\frac{RMM_{Ni3S2}}{2RMM_S} \qquad 3.4$$

In this case, the difference between the total weight percentage of elemental sulphur (obtained from EDX) and the weight percentage of elemental sulphur included in the Co_9S_8 (derived from previous calculation) is assumed to be equal to the percentage of sulphur belonging to nickel sulphide species. Given the impossibility to perform the analysis for the quantitative determination of the different nickel sulphide phases, the calculation was made by assuming that the overall Ni/S molar ratio was equal to Ni_3S_2. Based on these hypotheses, Ni_xS_y (modelled as Ni_3S_2) was estimated to be equal to 7 mg/cm^2 for Co_9S_8-Ni_xS_y/Nif samples. The same calculation could be performed for Ni_3S_2/Nif sample, using the EDX data displayed in Fig. 3.8, giving a value of 7 mg/cm^2 for Ni_3S_2.

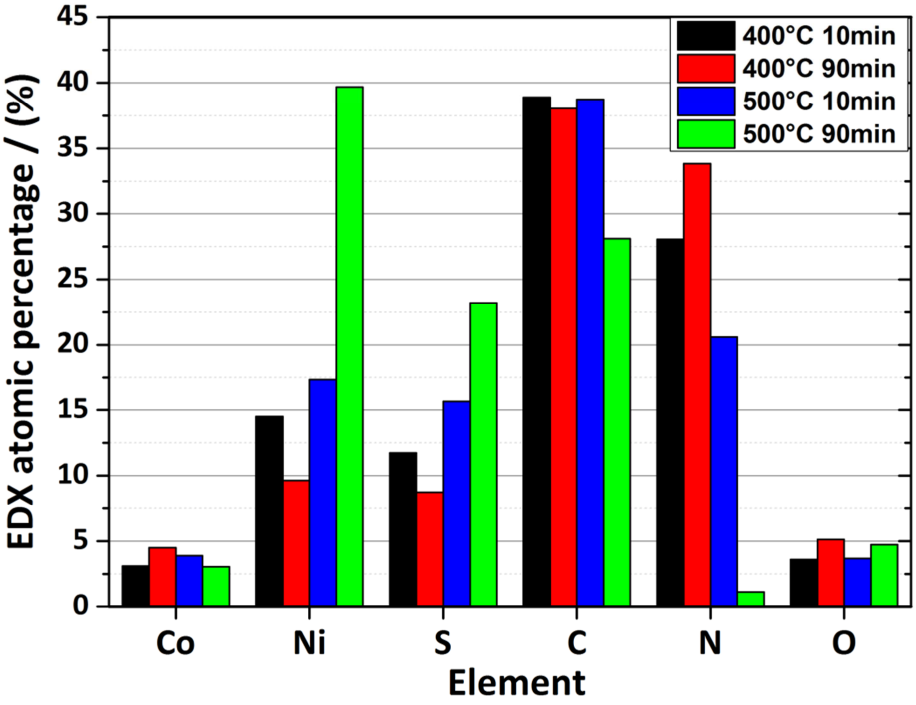

Figure 3.7 *EDX analysis for Co_9S_8-Ni_xS_y/Nif at different annealing temperatures and times*

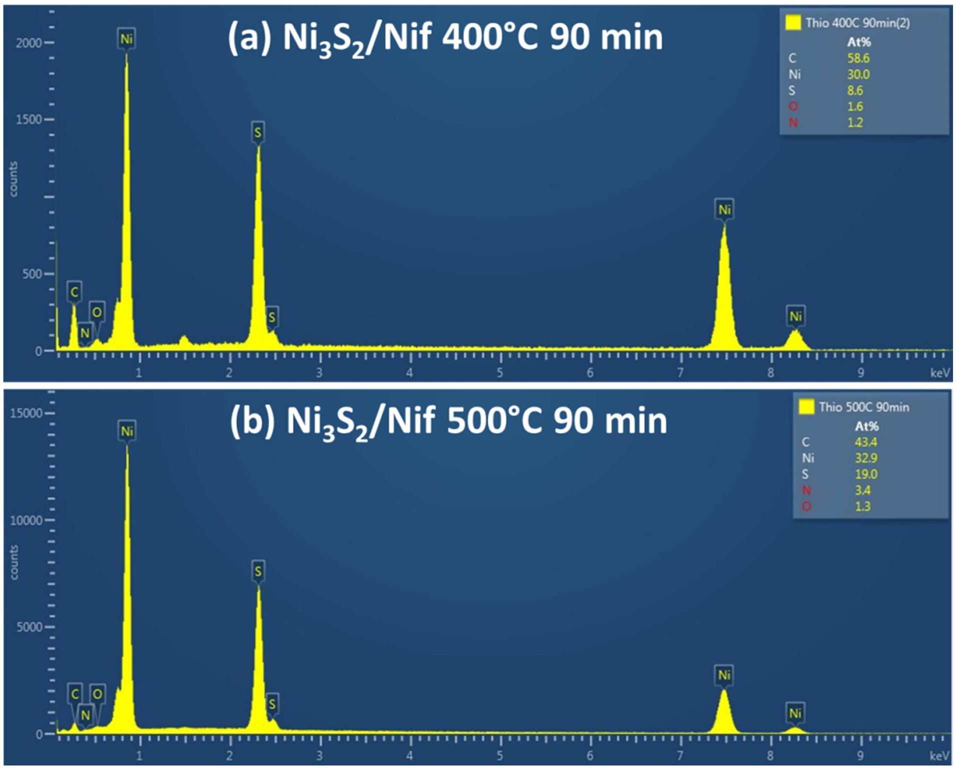

Figure 3.8 *EDX analysis for Ni_3S_2/Nif at (a) 400 °C 90 min, (b) 500 °C 90 min*

X-ray electron photoelectron spectroscopy (XPS) was performed in order to analyse the chemical composition of the samples and the oxidation state of the elements. The Ni2p, Co2p and S2p XPS spectra of the Co_9S_8-Ni_xS_y/Nif materials are reported in Fig. 3.9, 3.10, and 3.11, respectively. The Ni2p patterns showed the presence of a mixed Ni^0/Ni^{2+} oxidation states for the Co_9S_8-Ni_xS_y/Nif(400,10) and Co_9S_8-Ni_xS_y/Nif(500,90), with the typical binding energy of 853.0 eV for Ni^0 and 856.0 eV for Ni^{2+}. Marcus *et al*. reported similar values attributable to pure Ni_3S_2.[62] In particular the authors noticed that the peak located at 852.8 eV had the same binding energy as Ni in its metallic state. Thus, in this case the presence of this peak could be also related to metallic Ni foam, whose surface was not completely covered by metal sulphide species. The same peak was consistently observed by Zhou *et al.* in their work concerning Ni_3S_2 nanorods supported on Ni foam.[42] Interestingly, the Ni^0 peak at 853.0 eV of the Co_9S_8-Ni_xS_y/Nif(500,90) was sensibly bigger than that of Co_9S_8-Ni_xS_y/Nif(400,10). This can be principally explained by two factors:

1) higher crystallinity of Ni_3S_2 phase
2) sublimation/evaporation of products derived from the pyrolysis of thiourea, resulting in a more exposed area of metallic Ni

In the same previously mentioned work, Marcus *et al.*, suggested that the Ni2$p_{3/2}$ peak at 856.0 eV could be attributed to the presence of $Ni(OH)_2$ formed on the surface of the Ni_3S_2 upon exposure to atmospheric air. This result was later confirmed by Buckley *et al.*, where they demonstrated that Ni_3S_2 readily oxidises under ambient atmosphere[43]. This peak related to the nickel sulphide oxidation at the surface was consistently present for all the samples, regardless of the adopted annealing condition. From the XPS data it was not possible to draw any distinction between the different nickel sulphide phases, given the close proximity of the different binding energies, leading to a strong overlapping. In contrast, the Ni2p spectra of Co_9S_8-Ni_xS_y/Nif(400,90) and Co_9S_8-Ni_xS_y/Nif(500,10) materials showed a slightly different chemistry, with the presence of peaks at 853.7 eV and 856.0 eV. The Ni2p value at 853.7 eV was reported to be attributed to various nickel sulphide phases, like NiS and Ni_3S_2.[44] However the absence of the peak at binding energy close to 853.0 eV can exclude the presence of metallic Ni^0 at the surface of these samples. This discrepancy with the previous two samples could be related to the relative existing inhomogeneity of the materials during the measurement.

The Co2p XPS spectra reveal the presence of Co^{2+} species for all the samples, with a binding energy of 781.0-782.0 eV (Co2$p_{3/2}$), characteristic of Co_9S_8.[29] Co^{3+} species was detected only for the Co_9S_8-Ni_xS_y/Nif(500,90), with the Co2$p_{3/2}$ peak located at 778.4 eV. The presence of Co^{3+} in Co_9S_8 was also observed by Feng *et al.* in their work concerning the synthesis of Co_9S_8 nanosheets on carbon cloth.[29] In particular they noticed that the amount of Co^{3+} with respect to Co^{2+} was higher with increasing crystallinity of Co_9S_8. Thus, the presence of the peak attributed to Co^{3+} at 778.4 eV in the Co_9S_8-Ni_xS_y/Nif(500,90) sample reflected the higher crystallinity of the cubic Co_9S_8 under high annealing temperature (500 °C) and long annealing time (90 min). This result is in perfect agreement with the XRD and SAED data presented above, which showed an increase in crystallinity of Co_9S_8 at synthetic conditions of 500 °C and 90 min. The S2p XPS spectra are in agreement with the typical binding energies for nickel and cobalt sulphides, with the S2$p_{3/2}$ peak located at 161.4-162.4 eV attributed to a S^{-2} oxidation state bonded to the metal cation.[29,42] It was possible to identify another S2$p_{3/2}$ peak located at binding energy of 168.0-169.0 eV, which could be attributed to the presence of SO_3^{-2}/SO_4^{-2} species as a result of the oxidation of the metal sulphide surface upon exposure to air.[43] However, as displayed in Fig 3.11, this peak related to sulphite/sulphate species was more prominent for the samples annealed at 400 °C than those annealed at 500 °C. It is likely that Co_9S_8 and other nickel sulphide phases with lower crystallinity, as in the case of Co_9S_8-Ni_xS_y/Nif(400,10) and Co_9S_8-Ni_xS_y/Nif(400,90) samples, are more prone to oxidation upon exposure to atmospheric oxygen than compounds with higher crystallinity. By analysing the S2p XPS patterns of the monometallic Ni_3S_2/Nif sample reported in Fig. 3.12, no peaks related to the presence of SO_3^{-2}/SO_4^{-2} species were detected for all the synthetic conditions used, in contrast with the results derived from the bimetallic samples. Given the very different structural nature of the monometallic and bimetallic samples, it was not possible to directly compare and justify this contrasting behaviour. The Ni2p XPS patterns of the monometallic Ni_3S_2/Nif sample are reported in Fig. 3.12. The pattern was found to match well with that of Ni_3S_2 nanorods supported on Ni foam, as reported by Zhou et al.[42] Similarly to the previous case for the bimetallic system, the peak located at 852.7 eV could be attributed to Ni_3S_2 and the exposed surface of the metallic Ni foam, with the impossibility to discern the contribution derived from each compound. The peak located at 856.0 eV which was consistently detected regardless of the annealing temperature and time, was attributed to the presence of hydrated nickel oxide, as previously discussed.

A detailed quantitative analysis of the XPS derived from the fitting of the experimental spectra for the Co_9S_8-Ni_xS_y/Nif can be found in Tab. 3.1. The results showed that the Co/Ni atomic ratio was 1.2, 1.0, 0.5 and 3.3 for the Co_9S_8-Ni_xS_y/Nif(400,10), Co_9S_8-Ni_xS_y/Nif(400,90), Co_9S_8-Ni_xS_y/Nif(500,10) and Co_9S_8-Ni_xS_y/Nif(500,90), respectively. Furthermore, the S/(Co+Ni) ratio was lower for the electrodes treated at 500°C, which was in line with the structural modifications observed by XRD and SAED, with sulphur-poor nickel sulphide phases favoured at high temperature. As already discussed, the amount of S^{2-} ions with respect to sulphite/sulphate ions was substantially higher for the samples annealed at 500 °C. The highest calculated S^{2-}/SO_4^{2-} atomic ratio was attributed to Co_9S_8-Ni_xS_y/Nif(500,90) sample, as reported in Tab. 3.1.

Annealing condition	Co/Ni atomic ratio	S/(Co+Ni) atomic ratio	Co^{3+}/Co^{2+} atomic ratio	$S^{-2}/(SO_4^{-2})$ atomic ratio
400°C 10 min	1.22	1.02	0	1.95
400°C 90 min	1.04	0.99	0	2.0
500°C 10 min	0.53	0.74	0	6.37
500°C 90 min	3.28	0.68	0.04	29.85

Table 3.1 *XPS quantitative analysis of the elemental composition on the surface of* Co_9S_8-Ni_xS_y*/Nif electrode for different synthetic conditions*

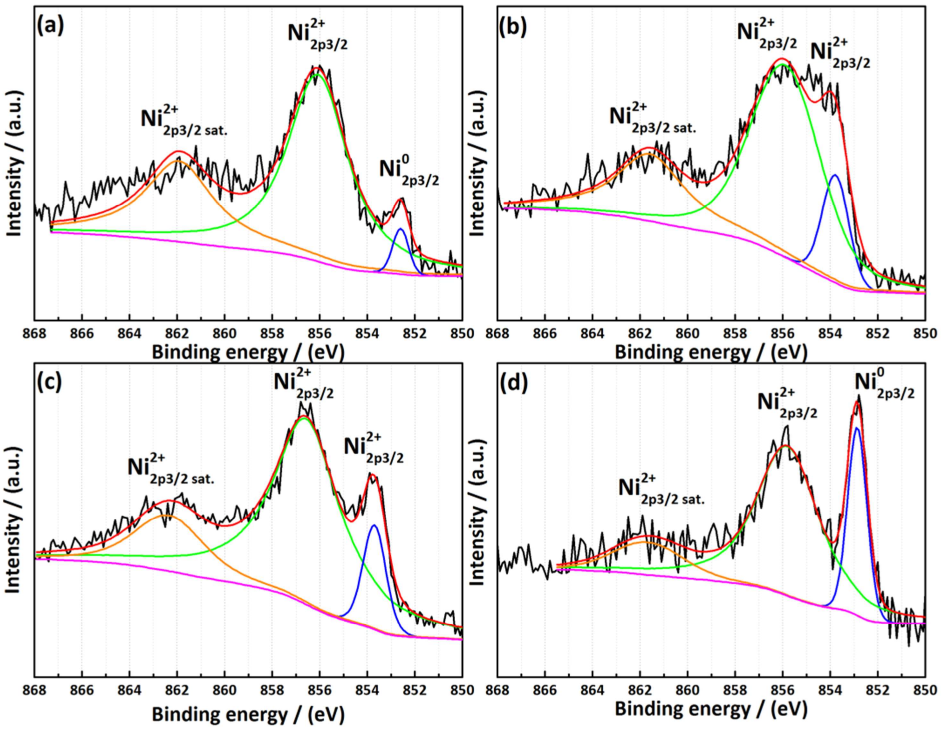

Figure 3.9 *Ni2p XPS patterns for Co_9S_8-Ni_xS_y/Nif at different annealing temperatures and times (a) 400 °C 10 min, (b) 400°C 90 min, (c) 500°C 10 min, (d) 500°C 90 min*

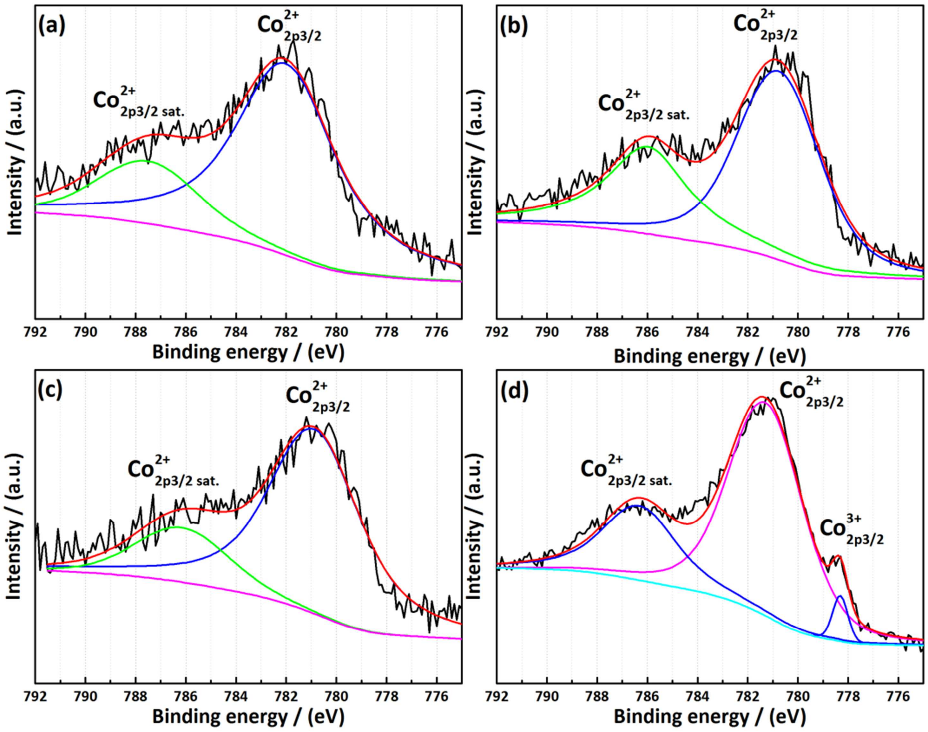

Figure 3.10 *Co2p XPS patterns for Co_9S_8-Ni_xS_y/Nif at different annealing temperatures and times (a) 400 °C 10 min, (b) 400°C 90 min, (c) 500°C 10 min, (d) 500°C 90 min*

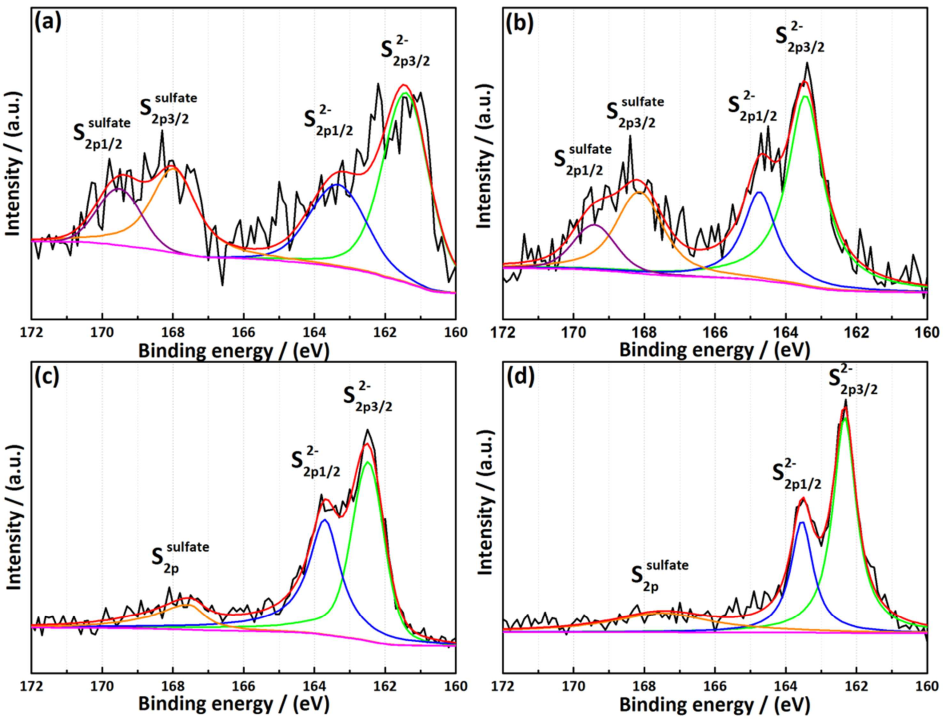

Figure 3.11 *S2p XPS patterns for Co_9S_8-Ni_xS_y/Nif at different annealing temperatures and times (a) 400 °C 10 min, (b) 400°C 90 min, (c) 500°C 10 min, (d) 500°C 90 min*

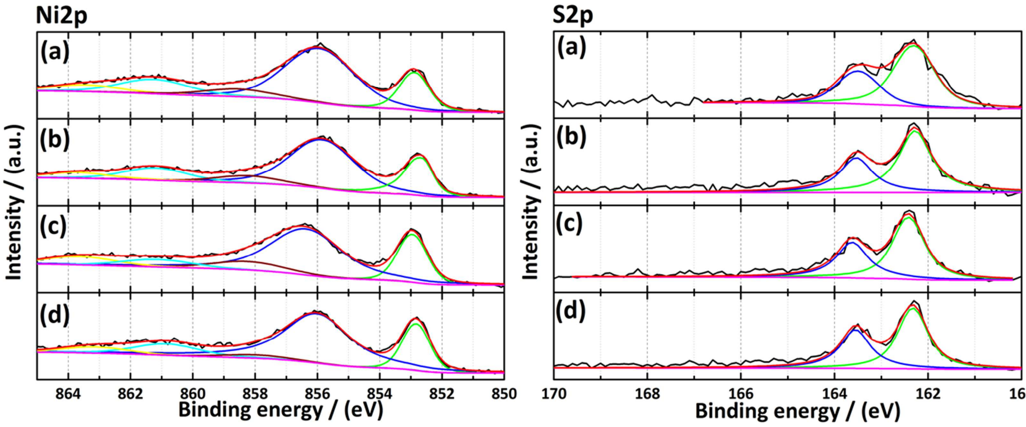

Figure 3.12 *Ni2p (left) and S2p (right) XPS patterns for Ni_3S_2/Nif at different annealing temperatures and times (a) 400 °C 10 min, (b) 400°C 90 min, (c) 500°C 10 min, (d) 500°C 90 min*

3.2.3 Analysis of the hydrogen evolution reaction: understanding the links between structural and catalytic properties of the synthesised electrocatalysts

The HER activity of the Co_9S_8-Ni_xS_y/Nif and Ni_3S_2/Nif electrodes was evaluated through linear sweep voltammetry (LSV) in 1.0 M KOH aqueous electrolyte (pH ~ 13.8) at slow scan rate of 1 mV/s. As reported in detail in Section 3.4.6, the electrochemical tests were performed in a 3-electrode cell, with Pt foil as counter electrode and silver/silver chloride as reference electrode. The geometric area of the working electrode was the same for all the tested samples and equal to 0.5 cm^2. Each fresh sample was subject to 20 LSV scans, and the last one was used for the electrocatalytic analysis. As suggested by Faber *et al.* in their work on the HER activity of nanostructured CoS_2, it is important to perform preliminary LSV scans on fresh electrodes in order to stabilise the current and therefore have more reliable values.[10] After each LSV test, the cell resistance R_s was calculated using electrochemical impedance spectroscopy (EIS) in order to quantify all the sources of resistance derived from wiring, electrolyte, and electrical connections. During the measurement a voltage drop is normally observed as a result of this resistance, and its severity depends linearly on the amount of current passing between the electrodes. Thus, in order to directly compare the electrocatalytic performances of different materials described in the literature, it is important to eliminate the effect of voltage drop, which is simply the product between current and cell resistance R_s:

$$V_{iR} = |V_{exp}| - I(V_{exp}) \cdot R_s \tag{3.5}$$

Where V_{iR} is the calculated potential after IR correction, V_{exp} is the experimental potential, $I(V_{exp})$ is the measured current related to a specific value of V_{exp} and Rs is the cell resistance. The experimental determination of the value of R_s will be discussed below.

The polarization curves after IR correction of Co_9S_8-Ni_xS_y/Nif and Ni_3S_2/Nif electrodes are displayed in Fig. 3.13(a) and (b), respectively. The principal figures of merit like overpotential required to reach 1 mA/cm^2 ($\eta_{1mA/cm2}$), overpotential required to reach 10 mA/cm^2 ($\eta_{10mA/cm2}$) and Tafel slope for all the tested samples are summarised and reported in Tab. 3.2. A very common figure of merit widely used in the literature for the comparison of the electrocatalytic activity of materials toward the HER is $\eta_{10mA/cm2}$. As explained by Benck *et al.*, an hypothetical water splitting electrolytic device driven by PV cells with an overall 12.3 % solar-to-hydrogen efficiency would operate at a current density of 10 mA/cm^2.[45] This explains why this overpotential is the most commonly highlighted figure of merit in this field. According to the values reported in Tab. 3.2, the Co_9S_8-Ni_xS_y/Nif(400,10), Co_9S_8-Ni_xS_y/Nif(400,90) and Co_9S_8-Ni_xS_y/Nif(500,10) sample require smaller overpotentials to reach a current density of 10 mA/cm^2 compared to the monometallic

Ni_3S_2/Nif electrode. However this is not true for the Co_9S_8-Ni_xS_y/Nif sample annealed at 500 °C for 90 min, which was found to have the largest value of $\eta_{10mA/cm2}$. Surprisingly, the electrocatalytic performance of this sample was even worse than the Ni foam, which was used as reference and control experiment. The Co_9S_8-Ni_xS_y/Ni sample annealed at 500 °C for 10 min showed the best performance with a required small overpotential of 163 mV to reach a current density of 10 mA/cm^2.

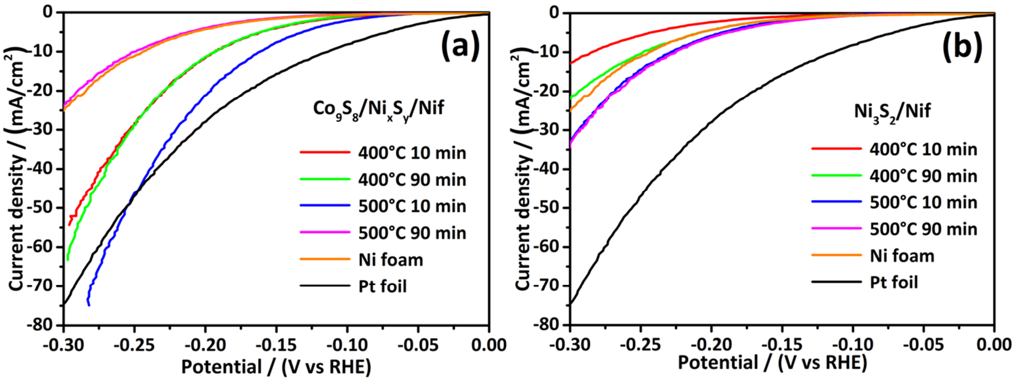

Figure 3.13 *IR-corrected polarization curves for (a) Co_9S_8-Ni_xS_y/Nif and (b) Ni_3S_2/Nif at different annealing temperatures and times in 1M KOH electrolyte*

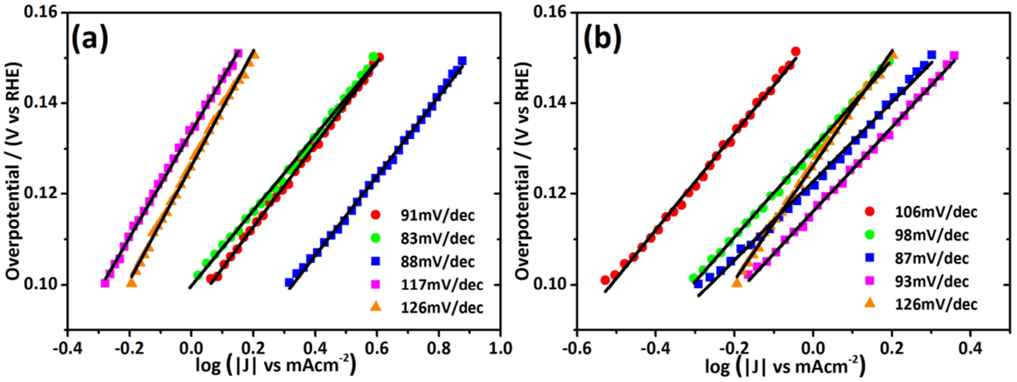

Figure 3.14 *IR-corrected Tafel plots for (a) Co_9S_8-Ni_xS_y/Nif and (b) Ni_3S_2/Nif at different annealing temperatures and times in 1M KOH electrolyte*

This value is only 47 mV higher than that of a commercial Pt foil under identical conditions, as indicated in Tab. 3.2. The reported activity of Co_9S_8-Ni_xS_y/Nif(500,10) sample compares well with the best reported earth-abundant metal HER electrocatalysts under alkaline media, and a quantitative comparison in terms of $\eta_{10mA/cm2}$ can be found in Tab. 3.3. The $\eta_{10mA/cm2}$ value of Co_9S_8-Ni_xS_y/Nif(500,10) was found to be only 11 mV higher than that of Co_9S_8 nanosheets supported on carbon cloth recently reported by Feng *et al.*[29] As for the monometallic samples, the Ni_3S_2/Nif electrode annealed at 500 °C for 90 min showed the highest activity, with a $\eta_{10mA/cm2}$ value of 225 mV. This obtained value is in line with the typical measured HER activity of Ni_3S_2

materials in alkaline media. The $\eta_{10mA/cm2}$ values for Ni_3S_2 nanorods and Ni_3S_2 nanosheets tabulated in Tab. 3.3 are only 25 mV and 2 mV lower compared to the $\eta_{10mA/cm2}$ of Ni_3S_2/Nif(500,90) sample. As already discussed in Section 1.3.1, Tafel slope analysis is normally carried out in order to determine the mechanism of reaction occurring during the HER for a specific material. The corresponding Tafel plots of the tested samples are displayed in Fig. 3.14. The overpotential (on the y-axis) is plotted against the logarithm of the current density (on the x-axis), resulting in a linear data trend. By fitting the data using a linear regression analysis it is possible to calculate the slope of each set of data, thus determining the value of Tafel slope. The calculated values for each sample are reported in Tab. 3.3. In alkaline electrolyte, the overall reaction mechanism of the HER is composed of three steps, which are recalled below:

1. Volmer (Electrochemical adsorption): $H_2O + e^- + M \rightleftharpoons M\text{-}H_{ads} + OH^-$
2. Heyrovsky (Electrochemical desorption): $H_2O + e^- + M\text{-}H_{ads} \rightleftharpoons M + H_2 + OH^-$
3. Tafel (Chemical desorption): $M\text{-}H_{ads} + M\text{-}H_{ads} \rightleftharpoons H_2$

In particular, the reaction mechanism can proceed following either a Volmer-Heyrovsky or a Volmer-Tafel pathway. The knowledge of the Tafel slope tells the type of pathway and its rate-determining step (RDS).

- Tafel slope ~ 30 mV/dec → Volmer-Tafel pathway, Tafel step is the RDS
- Tafel slope ~ 40-80 mV/dec → Volmer-Heyrovsky pathway, Heyrovsky step is the RDS
- Tafel slope ~ 120 mV/dec → Volmer-Tafel/Heyrovsky pathway, Volmer step is the RDS

In general, a good HER electrocatalyst should exhibit a small value of Tafel slope. In other words, the HER electrocatalyst should be able to greatly favour the adsorption of water molecules on their active sites (Volmer step), because it represents the first crucial step of the overall mechanism. Thus, according to these considerations, the reaction mechanism of Co_9S_8-Ni_xS_y/Nif(400,10), Co_9S_8-Ni_xS_y/Nif(400,90) and Co_9S_8-Ni_xS_y/Nif(500,10) electrodes proceeds via a Volmer-Heyrovsky pathway, with the RDS due to the Heyrovsky step. These materials present values of Tafel slope ranging from 83 to 91 mV/dec. For the Co_9S_8-Ni_xS_y/Nif sample annealed at 500 °C for 90 min, the large value of Tafel slope (117 mV/dec) suggests the existence of Volmer-Tafel/Heyrovsky pathway, with the RDS due to the Volmer step. The values of Tafel slopes for the monometallic Ni_3S_2/Nif electrodes are typical of a Heyrovsky RDS, in line with the described reaction mechanism of Co_9S_8-Ni_xS_y/Nif(400,10), Co_9S_8-Ni_xS_y/Nif(400,90) and Co_9S_8-Ni_xS_y/Nif(500,10) samples. Ni foam presents a large value of Tafel slope (126 mV/dec), typical of a Volmer RDS as in the case of Co_9S_8-Ni_xS_y/Nif(500,90).

Sample	**Annealing conditions**	**η (1mA/cm^2) (mV)**	**η (10 mA/cm^2) (mV)**	**Tafel slope (mV/dec)**	**C_{dl} (mF/cm^2)**	**R_{ct} (Ω)**
Co_9S_8-Ni_xS_y/Nif	400°C 10 min	95	193	91	58.9	3.5
Co_9S_8-Ni_xS_y/Nif	400°C 90 min	100	193	83	43.7	3.6
Co_9S_8-Ni_xS_y/Nif	500°C 10 min	79	163	88	63.8	2.9
Co_9S_8-Ni_xS_y/Nif	500°C 90 min	135	252	117	17.4	4.2
Ni_3S_2/Nif	400°C 10 min	157	284	106	10.3	23.0
Ni_3S_2/Nif	400°C 90 min	130	248	98	8.1	7.8
Ni_3S_2/Nif	500°C 10 min	122	230	87	12.9	4.8
N_3S_2/Nif	500°C 90 min	116	225	93	15.6	4.8
Bare Nif	-	128	245	126	$3.8 \cdot 10^{-4}$	9.3
Pt foil	-	22	116	-	-	-

Table 3.2 *Summary of the electrochemical properties of the Co_9S_8-Ni_xS_y/Nif and Ni_3S_2/Nif electrodes for the HER in 1M KOH*

The much lower activity of the Co_9S_8-Ni_xS_y/Nif(500,90) sample can be ascribed to the different structural, compositional and morphological properties. In particular, three factors appear to be significantly different from the more active bimetallic electrodes: i) higher Co/Ni superficial atomic ratio, as detected by XPS ii) absence of other nickel sulphides phases apart from Ni_3S_2, as measured through XRD and SAED iii) morphological agglomeration, as showed by SEM, iv) higher crystallinity as evidenced by XRD and SAED. In the Co_9S_8-Ni_xS_y/Nif(500,90) sample, the amount of cubic Co_9S_8 particles is predominant at the surface compared to the amount of Ni_3S_2 particles, with a Co_9S_8/Ni_3S_2 molar ratio of 3.28, as reported in Tab. 3.1. In the other bimetallic samples, the Co_9S_8/Ni_xS_y molar ratio is lower than this value. For instance, the Co_9S_8/Ni_xS_y molar ratio of the highly active Co_9S_8-Ni_xS_y/Nif(500,10) results to be the lowest, with a small value of 0.53. From the Tafel slope analysis of the pure monometallic Ni_3S_2/Nif samples it was shown that these materials present a relatively fast Volmer step, which was not detected as RDS regardless of the specific annealing temperature and time. This means that the rhombohedral Ni_3S_2 has a thermodynamically favoured adsorption capacity of water molecules in alkaline environment. The good adsorption property of Ni_3S_2 was also recently documented in the work by Jiang *et al.*[36] Recently, the HER mechanism of Co_9S_8 nanotubes in alkaline media was evaluated by Jin *et al*.[63] The authors measured large Tafel slope value of 135 mV/dec, thus suggesting a Volmer RDS for this compound. According to these findings the adsorption property of Co_9S_8 can be considered inferior with respect to that of pure Ni_3S_2. Thus, the reason of the poor HER activity of the Co_9S_8-Ni_xS_y/Nif sample annealed at 500 °C for 90 min is due to the high fraction of Co_9S_8 particles at the surface in comparison with Ni_3S_2, which leads to a rather poor adsorption capacity of water molecules at the surface. Recently, Feng *et al*. showed a rather poor HER activity of Co_9S_8 in alkaline media, with a required overpotential of 250 mV to reach a current density of 10 mA/cm^2.[30] This value is in agreement with the performance of the Co_9S_8-Ni_xS_y/Nif(500,90), leading to the conclusion that pure Co_9S_8 is not a particularly active catalyst for the HER.

However it is worth noting that even the pure Ni_3S_2/Nif has a much lower activity compared to the active bimetallic electrodes. In this regard, the concomitant presence of Co_9S_8 and Ni_3S_2 phases under an optimal atomic ratio may lead to the creation of synergistic effects, such as increase in the total surface area, more thermodynamically favourable adsorption of water molecules on the active sites and better superficial electronic properties. Such synergistic effects had also been previously observed in Ni-Co alloys for hydrogen evolution, which were found to be superior to pure Ni or pure Co catalysts.[46]

Material	Electrolyte	$\eta_{(10mAcm-2)}$	Tafel slope (mV/dec)	Reference
CoS_2 nanopyramids/3D CFP	1M KOH	250	-	[8]
CoS_2	1M KOH	244	133	[48]
Co_9S_8 nanosheets	1M KOH	152	-	[29]
Co_9S_8/C	1M KOH	250	-	[30]
$Zn_{0.76}Co_{0.24}S/CoS_2$	1M KOH	238 (20 mA/cm^2)	164	[49]
Amorphous CoSe	1M KOH	121	84	[50]
NiS_2 nanosheets/CC	1M KOH	149	104	[51]
NiS_2 nanosheets	1M NaOH	190	80	[31]
Ni_3S_2 nanosheets	1M KOH	223	-	[52]
Ni_3S_2 nanorods	1M KOH	200	107	[53]
NiS	1M KOH	380	-	[54]
NiS/Ni foam	1M KOH	158 (20 mA/cm^2)	83	[55]
$NiCo_2S_4$ nanowires	1M KOH	228 (20 mA/cm^2)	141	[56]
Ni_3Se_2 film	1M KOH	100	98	[57]
Pt/C	1M KOH	70	55	[58]
Co_9S_8-Ni_xS_y/Nif (500C 10m)	**1M KOH**	**163**	**88**	**This work**

Table 3.3 *Comparison of the HER performance between selected electrocatalysts based on earth-abundant elements in alkaline media*

Electrochemical impedance spectroscopy (EIS) was performed in order to characterise the electrochemical properties of the samples during the HER. Generally during the EIS measurement a small sinusoidal potential of selected amplitude is applied at a fixed frequency *f* and the corresponding current is recorded. The value of the amplitude has to be small enough to guarantee a pseudo-linear response of the electrochemical system. In in this way it is possible to calculate the value of impedance *Z* at that specified frequency, which is the ratio between applied potential and recorded current. This measurement must be repeated for a wide range of frequencies, obtaining a series of impedance values which can be plotted. Nyquist plots are typically used, and in this graphs the imaginary part of the impedance *Z(im)* is plotted against the real part of the impedance *Z(Re)*. These data can be modelled using equivalent electric circuit with different elements such as resistor, capacitor and inductor. These elements are able to model the electrochemical behaviour of the electrode under the specific potential, providing information on the dynamics of electron transfer at the electrode/electrolyte interface and the capacitive behaviour of the system. The Nyquist plots for the Co_9S_8-Ni_xS_y/Nif and Ni_3S_2/Nif are reported in Fig. 3.15. The measurement was carried out a potential of -0.230 V vs RHE for all the samples. The experimental data of Ni foam were also calculated and consistently plotted in each graph for a direct comparison with the synthesised samples. The impedance data were fitted using a simplified Randles circuit, consisting of two resistors R_s and R_{ct}, and a constant phase element (CPE).

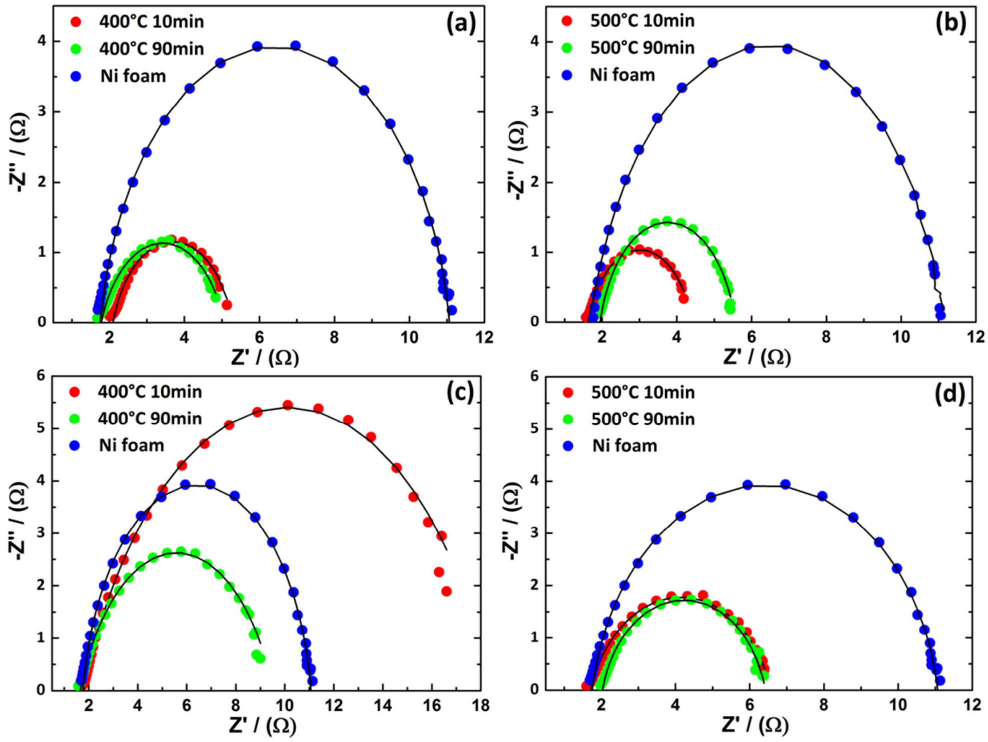

Figure 3.15 *Nyquist plots of (a)-(b) Co_9S_8-Ni_xS_y/Nif, (c)-(d) Ni_3S_2/Nif recorded under potentiostatic mode at -0.230 V vs RHE in 1.0 M KOH. The fitting was performed using the simplified Randles circuit*

The simplified Randles electric circuit is reported in Fig. 3.16. This type of electric circuit is normally used for modelling the electrochemical properties of HER electrocatalysts.[31] The resistor element R_s is related to the cell resistance, which is a measure of the ohmic resistance of the system due to wiring, electrolyte and electrical connections. The value of R_s can also be obtained graphically, by taking the value of the real impedance when the imaginary part is set equal to 0. From the Nyquist plots, R_s results to be similar for all the samples, with a value of 2 Ω. This value was used in the calculation of the potential drop due to ohmic losses, which is then subtracted to the experimental potential for the correction of the LSV data, as previously described. The resistor element R_{ct} gives a measure of the ease of electron transfer at the electrode/electrolyte interface[11]. The values of R_{ct} for all the samples are reported in Tab. 3.2. The most active Co_9S_8-Ni_xS_y/Nif sample annealed at 500 °C for 10 min showed the lowest value of charge transfer resistance R_{ct} (2.9 Ω), in agreement with its superior HER performance compared to the other samples. The highest value of R_{ct} (23.0 Ω) among all the tested samples was measured for the monometallic Ni_3S_2/Nif(400,10), which is also the worst performing material toward the HER, with an overpotential required to reach 10 mA/cm^2 of 284 mV.

Another relevant parameter is the double-layer capacitance (C_{dl}), which is derived from the constant phase element (CPE) data. The CPE is normally used to take into account the effect of porosity, roughness and non-uniform current distribution of the electrode. The calculation of the C_{dl} can be derived from the knowledge of the CPE parameters found through data fitting. At the electrode/electrolyte interface, two layers of ions with opposing polarity form under the application of voltage. In other words, the surface of the electrode can be negatively or positively charged under the application of voltage, and upon immersion in electrolyte the ions of opposing charge are attracted to the surface, forming a so-called double layer separated by a monolayer of water molecules, acting as dielectric in a capacitor. Clearly, this capacitive effect which can be measured by EIS as already mentioned depends on the exposed surface area in contact with the electrolyte. Thus the calculation of C_{dl} can give a qualitative estimate of the electrochemically active surface area (ECSA) of the electrode.[47]

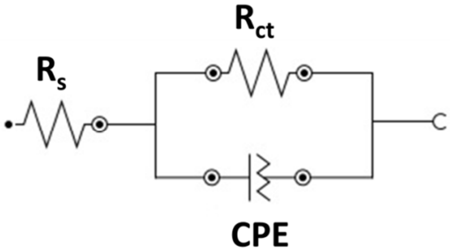

Figure 3.16 *Simplified Randles circuit used for the fitting of the EIS data;* R_s*, series resistance;* R_{ct}*, charge-transfer resistance; CPE, constant phase element*

The values of C_{dl} for all the samples are reported in Tab. 3.2. As expected, the most active Co_9S_8-Ni_xS_y/Nif sample annealed at 500 °C for 10 min showed the highest value of double layer capacitance C_{dl} (63.8 mF/cm^2). The Co_9S_8-Ni_xS_y/Nif(400,10) and Co_9S_8-Ni_xS_y/Nif(400,90) samples also showed high values of C_{dl} (58.9 and 43.7 mF/cm^2), in line with their good HER activity. The lower value of C_{dl} calculated for Co_9S_8-Ni_xS_y/Nif(500,90) reflects the rather low superficial active area of this sample compared to the other bimetallic systems. The low superficial active area of Co_9S_8-Ni_xS_y/Nif(500,90) sample results from the long annealing time which induces dramatic structural and morphological modifications. In particular, a long annealing time under high temperature can lead to the following phenomena:

- Suppression of sulphur-rich nickel sulphide phases, with the generation of single phase sulphur-poor Ni_3S_2, resulting in less structural defects and more ordered morphology
- Increase in crystallinity of Co_9S_8 and Ni_3S_2, resulting in agglomeration

These two aspects are directly responsible for the decrease in active surface area of Co_9S_8-Ni_xS_y/Nif(500,90) sample. The C_{dl} values of the monometallic Ni_3S_2/Nif electrodes were found to be comparable with the Co_9S_8-Ni_xS_y/Nif(500,90). Thus, the concomitant presence of Co_9S_8 and multiphasic nickel sulphide plays a determinant role in the higher superficial active area of the the bimetallic system compared to the pure Ni_3S_2 supported on Ni foam.

In the main discussion Ni_3S_2 was considered as the only active nickel sulphide phase in the system providing active sites for the HER without taking into account the possible effect of other phases. However EIS analysis suggested that the presence of other nickel sulphide phases could actively contributed to the structural disorder observed for the most active Co_9S_8-Ni_xS_y/Nif(500,90), Co_9S_8-Ni_xS_y/Nif(500,90) and Co_9S_8-Ni_xS_y/Nif(500,90), leading to high active surface areas. In this regard it must be noted that given the extremely complex nature of the system it is challenging to perfectly determine the single effect of each compound to the overall HER activity. Nonetheless, an appropriate combination of characterisation and testing techniques can significantly help to understand the general structure-property relations of the materials under investigation. In this particular case, the reason why the other nickel sulphide phases were not considered as active sites can be justified by three main observations:

1) XRD and SAED gave evidence of a predominant presence of the Ni_3S_2 and $Ni_{17}S_{18}$ phases (only small diffraction peaks attributed to NiS, Ni_7S_6 and NiS_2 phases)
2) XRD analysis after the stability test evidenced the disappearance of the $Ni_{17}S_{18}$ phase (Fig. 3.17(b)), despite the fact that no current decay was observed after 72 hours for the most active sample (Co_9S_8-Ni_xS_y/Nif(500,10)), as shown in Fig. 3.17(a)
3) XRD analysis after the stability test confirmed the presence of Co_9S_8 and Ni_3S_2

The chronoamperometric test was performed on the Co_9S_8-Ni_xS_y/Nif(500,10) sample, under a constant potential of -0.161 V vs RHE (after IR-correction) in 1.0 M KOH solution for 72 hours with gentle stirring. These two observations derived from the long-stability chronoamperometric test lead to the conclusion that Co_9S_8 and Ni_3S_2 are the active sites for the HER. By tuning the relative atomic composition of the two phases at the surface it was possible to maximise the HER activity, as demonstrated with the Co_9S_8-Ni_xS_y/Nif(500,10) sample. Moreover, the concomitant presence of other nickel sulphide phases was found to increase the active surface area through the existence of structural disorder.

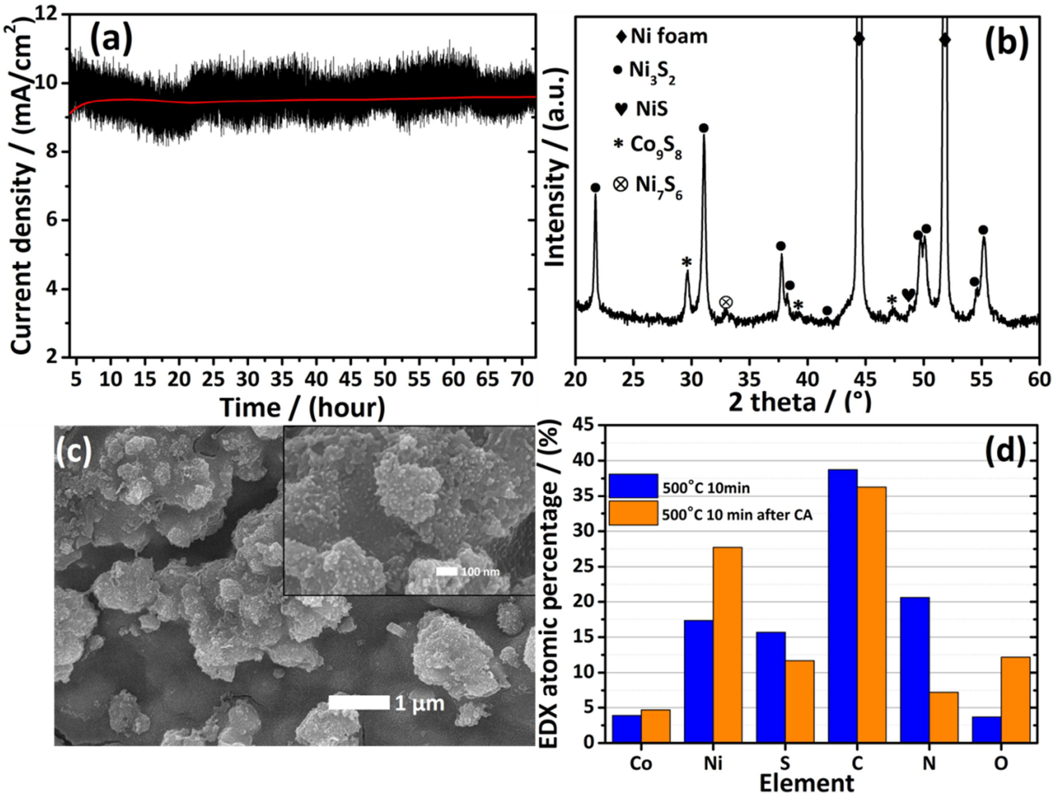

Figure 3.17 *(a) Chronoamperometry test for Co_9S_8-Ni_xS_y/Nif annealed at 500°C 10 min at -0.161 V vs RHE in 1M KOH. (b) XRD spectrum, (c) Low- and high magnification SEM, (d) EDX chart of Co_9S_8-Ni_xS_y/Nif after 72 hours of stability test*

The Ni2p, Co2p and S2p XPS patterns of the Co_9S_8-Ni_xS_y/Nif(500,10) after chronoamperometry are reported in Fig. 3.18. In this case the Ni^0 peak located at 853.0 eV disappeared. The same observation was reported by Zhou *et al.* in the case of Ni_3S_2 nanorods after prolonged chronoamperometry for the oxygen evolution reaction.[42] The only detection of the $Ni2p_{3/2}$ peak at 856.0 eV suggested the formation of a thin layer of $Ni(OH)_2$ covering the exposed metallic Ni foam and the nickel sulphide. It is worth noting that $Ni(OH)_2$ was not detected with XRD, and this could be due to its amorphous nature/small presence. The Co2p pattern matches well with the Co2p spectrum of the as-synthesised sample reported in Fig. 3.10(c). The S2p pattern showed the presence of prominent amount of SO_4^{2-} species. It is likely that these species mainly arise from the surface of Co_9S_8, since Ni_3S_2 was found to be covered by a thin layer of hydroxide species. The quantitative analysis of the XPS derived from the fitting of the experimental spectra is summarised in Tab. 3.4. The calculated Co/Ni atomic ratio at the surface of the Co_9S_8-Ni_xS_y/Nif(500,10) after chronoamperometry was found to be slightly higher than the as-synthesised sample. This could be due to a partial morphological rearrangement occurring during the long-term stability test, mainly as a result of the dissolution of $Ni_{17}S_{18}$ phase. A direct comparison between the SEM image (Fig. 3.17(c)) of the Co_9S_8-Ni_xS_y/Nif(500,10) after long-term stability and the SEM of the as-synthesised sample (Fig. 3.4(c)) further highlights the existence of a small morphological difference. No cobalt leaching was observed as probed by EDX technique and summarized in the chart reported in Fig. 3.17(d), with a value consistent with the as-synthesised sample. The atomic percentage of elemental oxygen of the Co_9S_8-Ni_xS_y/Nif(500,10) after long-term stability was found to be sensibly higher, with a value of around 12%. This is in agreement with the Ni2p and Co2p XPS spectra which evidenced the presence of oxygenated species like $Ni(OH)_2$ and Co-S-O at the surface of the electrode.

Annealing condition	Co/Ni atomic ratio	S/(Co+Ni) atomic ratio	Co^{3+}/Co^{2+} atomic ratio	$S^{-2}/(SO_4^{-2})$ atomic ratio
500°C 10 min before chronoamperometry	0.53	0.74	0	1.32
500°C 10 min after chronoamperometry	1.15	0.81	0	0.31

Table 3.4 *XPS quantitative analysis of the elemental composition on the surface of Co_9S_8-Ni_xS_y/Nif electrode before and after the stability test*

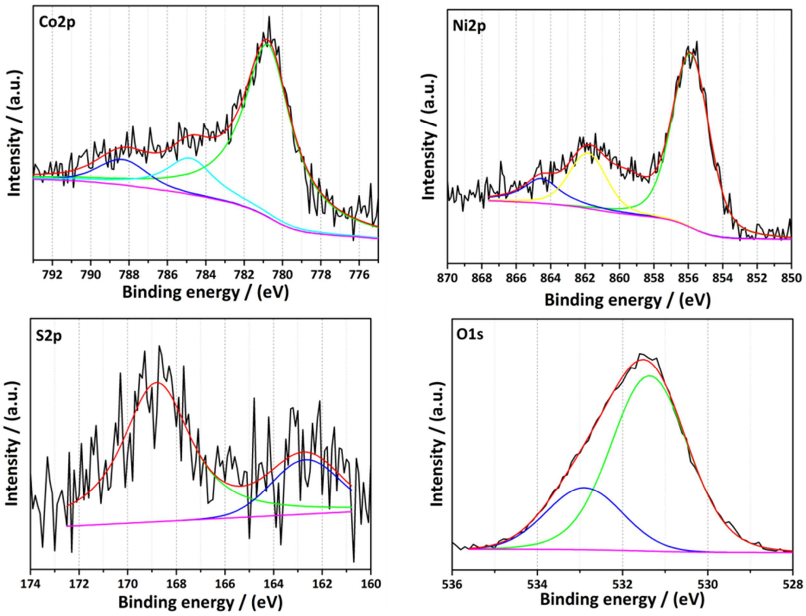

Figure 3.18 *XPS patterns for Co_9S_8-Ni_xS_y/Nif annealed at 500°C 10 min after chronoamperometry test for 72 hours*

3.3 Conclusions

In this work a novel and facile synthetic method for the fabrication of bimetallic Co_9S_8-Ni_xS_y and monometallic Ni_3S_2 nanoparticles supported onto a 3-dimensional Ni foam was reported and carefully discussed. The method is based on the thermal decomposition of pre-adsorbed Co-thiourea complex in the case of Co_9S_8-Ni_xS_y and pure thiourea in the case of Ni_3S_2 onto the metallic Ni foam, generating *in situ* the nanoparticulate metal sulphides. The Co_9S_8-Ni_xS_y samples were found to contain nanocrystalline Co_9S_8 and different nickel sulphide phases (Ni_3S_2, $Ni_{17}S_{18}$, NiS, NiS_2, Ni_7S_6). The annealing temperature and time played a crucial role in controlling the relative amount of nickel sulphide phases present in the composite material. In particular, it was found that the formation of sulphur-poor nickel sulphide phases was favoured under high temperature and long annealing time. At temperature of 500 °C and annealing time of 90 min, a pure biphasic mixture of crystalline Co_9S_8 and Ni_3S_2 was obtained, with no detection of other phases. In contrast, the monometallic Ni_3S_2/Nif was found to contain only a pure crystalline Ni_3S_2 phase, for all the synthetic conditions used. The nanoparticulate nature of the bimetallic Co_9S_8-Ni_xS_y/Nif samples was probed using TEM, with the detection of small nanoparticles of 20 nm. A slight morphological agglomeration was observed through SEM with increasing annealing temperature and time for all the samples. The results of the compositional analysis at the surface performed by XPS revealed the existence of well-defined Co/Ni atomic ratios, which were found to be dependent on the annealing temperature and time. The materials were tested for the HER in alkaline media, and a clear trend in activity was observed as a function of their structural and morphological properties. The bimetallic Co_9S_8-Ni_xS_y/Nif annealed at 500 °C for 10 min showed the highest HER activity, requiring a small overpotential of 163 mV at a current density of 10 mA cm^{-2} in 1.0 M KOH electrolyte. This result was compared and found to be in line with the best reported electrocatalysts made of earth-abundant elements in alkaline media. The HER performance of the best monometallic Ni_3S_2/Nif was similar to other Ni_3S_2 electrocatalysts reported in the literature. The results from Tafel analysis revealed a Heyrovsky rate-determining step for the Co_9S_8-Ni_xS_y/Nif(400,10), Co_9S_8-Ni_xS_y/Nif(400,90) and Co_9S_8-Ni_xS_y/Nif(500,10) materials. The same Heyrovsky rate-determining step was found to occur for all the monometallic Ni_3S_2/Nif samples, regardless of the annealing parameters. However, for the Co_9S_8-Ni_xS_y/Nif(500,10) sample a Volmer rate-determining step was reported, which was the same as that of pure Ni foam. The different mechanism occurring on this electrode was attributed to its significant structural difference compared to the other bimetallic samples. In particular, the predominant presence of Co_9S_8 with respect to Ni_3S_2 at the surface was ascribed as possible reason of this different mechanistic behaviour. This hypothesis was supported by previous evidence in the literature for which pure Co_9S_8 is not a particular active HER catalysts, showing large Tafel slope values. Thus, the reason of the high HER activity of the Co_9S_8-Ni_xS_y/Nif material synthesised under well-defined conditions was mainly linked to the existence of an optimum superficial Co/Ni ratio and a high active surface area due to the disordered structure induced by the presence of different nickel sulphide phases. The HER trend was further correlated to the electrochemical properties of the electrodes such as double layer capacitance and charge transfer resistance. Consistent results were found, with the most active bimetallic Co_9S_8-Ni_xS_y/Nif sample annealed at 500 °C and 10 min having the largest value of double-layer capacitance and smallest value of charge-transfer resistance R_{ct}. The most active Co_9S_8-Ni_xS_y/Nif(500,10) electrode was subject to chronoamperometry test, and great long-term stability was observed, with a constant current density maintained over 72 hours of reaction. The sample was characterised after the stability test through XRD, SEM, EDX and XPS techniques. From XRD it was found that the peaks belonging to $Ni_{17}S_{18}$ phase disappeared, suggesting a possible dissolution or electrochemical transformation. The other crystallographic phases such as Co_9S_8 and Ni_3S_2 were perfectly retained. Their presence was confirmed also confirmed by XPS, which evidenced the presence of a thin layer of $Ni(OH)_2$ covering the surface of the exposed metallic Ni foam and nickel sulphide particles. This observation led to the conclusion that Co_9S_8 and Ni_3S_2 were the real active sites of the HER. This is due to their predominance compared to other secondary phases such as NiS and Ni_7S_6 and the fact that even after the disappearance of $Ni_{17}S_{18}$ no current decay was observed during the chronoamperometric test. Small morphological modifications were observed by SEM possibly as a result of the dissolution of the unstable $Ni_{17}S_{18}$ phase. This synthetic approach can be easily generalized and extended to the design of others 3D composite materials holding novel properties in a broad variety of applications such as HER/OER catalysts, supercapacitors and batteries.

3.4 References

1. P. Gerland, A. E. Raftery, H. Ševčíková, N. Li, D. Gu, T. Spoorenberg, L. Alkema, B. K. Fosdick, J. Chunn, N. Lalic, G. Bay, T. Buettner, G. K. Heilig and J. Wilmot, *Science*, 2014, **346**, 234–237.
2. Y. Tian and C. Y. Zhao, *Appl. Energy*, 2013, **104**, 538–553.
3. T. L. Gibson and N. A. Kelly, *J. Power Sources*, 2010, **195**, 3928–3932.
4. J. Luo, I. Jeong-Hyeok, M. T. Mayer, M. Schreier, M. K. Nazeeruddfn, P. Nam-Gyu, D. S. Tilley, F. Hong Jin and M. Grätzel, *Science*, 2014, **345**, 1593–1596.
5. S. A. Bonke, M. Wiechen, D. R. MacFarlane and L. Spiccia, *Energy Environ. Sci.*, 2015, **8**, 2791–2796.
6. J. a Turner, *Science*, 2004, **305**, 972–974.
7. Q. Lu, G. S. Hutchings, W. Yu, Y. Zhou, R. V Forest, R. Tao, J. Rosen, B. T. Yonemoto, Z. Cao, H. Zheng, J. Q. Xiao, F. Jiao and J. G. Chen, *Nat. Commun.*, 2015, **6**, 6567.
8. H. Zhang, Y. Li, G. Zhang, T. Xu, P. Wan and X. Sun, *J. Mater. Chem. A*, 2015, **3**, 6306–6310.
9. D. Kong, J. J. Cha, H. Wang, H. R. Lee and Y. Cui, *Energy Environ. Sci.*, 2013, **6**, 3553–3558.
10. M. S. Faber, R. Dziedzic, M. A. Lukowski, N. S. Kaiser, Q. Ding and S. Jin, *J. Am. Chem. Soc.*, 2014, **136**, 10053–10061.
11. S. Peng, N. Li, X. Han, W. Sun, M. Srinivasan, S. G. Mhaisalkar, F. Cheng, Q. Yan, J. Chen and S. Ramakrishna, *Angew. Chemie - Int. Ed.*, 2014, **53**, 12594–12599.
12. N. Jiang, L. Bogoev, M. Popova, S. Gul, J. Yano and Y. Sun, *J. Mater. Chem. A*, 2014, **2**, 19407–19414.
13. A. I. Carim, F. H. Saadi, M. P. Soriaga and N. S. Lewis, *J. Mater. Chem. A*, 2014, **2**, 13835.
14. T. F. Jaramillo, K. P. Jørgensen, J. Bonde, J. H. Nielsen, S. Horch and I. Chorkendorff, *Science*, 2007, **317**, 100–102.
15. Y. H. Chang, C. Te Lin, T. Y. Chen, C. L. Hsu, Y. H. Lee, W. Zhang, K. H. Wei and L. J. Li, *Adv. Mater.*, 2013, **25**, 756–760.
16. L. Cheng, W. Huang, Q. Gong, C. Liu, Z. Liu, Y. Li and H. Dai, *Angew. Chemie - Int. Ed.*, 2014, **53**, 7860–7863.
17. M. a Lukowski, A. S. Daniel, C. R. English, F. Meng, A. Forticaux, R. J. Hamers and S. Jin, *Energy Environ. Sci.*, 2014, **7**, 2608–2613.
18. Y. Li, H. Wang, L. Xie, Y. Liang, G. Hong and H. Dai, *J. Am. Chem. Soc.*, 2011, **133**, 7296–7299.
19. W. F. Chen, K. Sasaki, C. Ma, A. I. Frenkel, N. Marinkovic, J. T. Muckerman, Y. Zhu and R. R. Adzic, *Angew. Chemie - Int. Ed.*, 2012, **51**, 6131–6135.
20. N. Jiang, B. You, M. Sheng and Y. Sun, *Angew. Chemie - Int. Ed.*, 2015, **54**, 6251–6254.

21. J. Tian, Q. Liu, A. M. Asiri and X. Sun, *J. Am. Chem. Soc.*, 2014, **136**, 7587−7590.
22. X. Wang, Y. V. Kolen'Ko, X. Q. Bao, K. Kovnir and L. Liu, *Angew. Chemie - Int. Ed.*, 2015, **54**, 8188–8192.
23. P. Xiao, M. Alam Sk, L. Thia, X. Ge, R. J. Lim, J.-Y. Wang, K. H. Lim and X. Wang, *Energy Environ. Sci.*, 2014, **7**, 2624–2629.
24. W.-F. Chen, C.-H. Wang, K. Sasaki, N. Marinkovic, W. Xu, J. T. Muckerman, Y. Zhu and R. R. Adzic, *Energy Environ. Sci.*, 2013, **6**, 943–951.
25. F. Harnisch, G. Sievers and U. Schröder, *Appl. Catal. B Environ.*, 2009, **89**, 455–458.
26. H. Vrubel and X. Hu, *Angew. Chemie - Int. Ed.*, 2012, **51**, 12703–12706.
27. Y. Wang, G. Zhang, W. Xu, P. Wan, Z. Lu, Y. Li and X. Sun, *ChemElectroChem*, 2014, **1**, 1138–1144.
28. M. S. Faber, M. a Lukowski, Q. Ding, N. S. Kaiser and S. Jin, *J. Phys. Chem. C*, 2014, **118**, 21347–21356.
29. L.-L. Feng, M. Fan, Y. Wu, Y. Liu, G.-D. Li, H. Chen, W. Chen, D. Wang and X. Zou, *J. Mater. Chem. A*, 2016, -.
30. L. L. Feng, G. D. Li, Y. Liu, Y. Wu, H. Chen, Y. Wang, Y. C. Zou, D. Wang and X. Zou, *ACS Appl. Mater. Interfaces*, 2015, **7**, 980–988.
31. X. Wu, B. Yang, Z. Li, L. Lei and X. Zhang, *RSC Adv.*, 2015, **5**, 32976–32982.
32. C. Tang, Z. Pu, Q. Liu, A. M. Asiri, Y. Luo and X. Sun, *Int. J. Hydrogen Energy*, 2015, **40**, 4727–4732.
33. Y. Sun, C. Liu, D. C. Grauer, J. Yano, J. R. Long, P. Yang and C. J. Chang, *J. Am. Chem. Soc.*, 2013, **135**, 17699–17702.
34. J. Xie, H. Zhang, S. Li, R. Wang, X. Sun, M. Zhou, J. Zhou, X. W. Lou and Y. Xie, *Adv. Mater.*, 2013, **25**, 5807–5813.
35. X. Li, G. Zhu, Q. Kang, Z.-D. Huang, X. Feng, Y. Li, R. Liu and Y. Ma, *RSC Adv.*, 2015, **5**, 55396–55400.
36. N. Jiang, Q. Tang, M. Sheng, B. You, D. Jiang and Y. Sun, *Catal. Sci. Technol.*, 2015,.
37. P. Ganesan, M. Prabu, J. Sanetuntikul and S. Shanmugam, *ACS Catal.*, 2015, **5**, 3625–3637.
38. N. Kumar, N. Raman and A. Sundaresan, *Zeitschrift fur Anorg. und Allg. Chemie*, 2014, **640**, 1069–1074.
39. P. Yin, L. Sun, Y. Gao and S. Wang, *Bull. Mater. Sci.*, 2008, **31**, 593–596.
40. Z. Cheng, H. Abernathy and M. Liu, *J. Phys. Chem. C Lett.*, 2007, **111**, 17997–18000.
41. N. E. Braml, A. Sattler and W. Schnick, *Chem. - A Eur. J.*, 2012, **18**, 1811–1819.
42. W. Zhou, X.-J. Wu, X. Cao, X. Huang, C. Tan, J. Tian, H. Liu, J. Wang and H. Zhang, *Energy Environ. Sci.*, 2013, **6**, 2921.
43. A. N. Buckley and R. Woods, *J. Appl. Electrochem.*, 1991, **21**, 575–582.

44. D. L. Legrand, H. W. Nesbitt and G. M. Bancroft, *Am. Mineral.*, 1998, **83**, 1256–1265.
45. J. D. Benck, T. R. Hellstern, J. Kibsgaard, P. Chakthranont and T. F. Jaramillo, *ACS Catal.*, 2014, **4**, 3957–3971.
46. C. Lupi, A. Dell'Era and M. Pasquali, *Int. J. Hydrogen Energy*, 2009, **34**, 2101–2106.
47. C. C. L. McCrory, S. Jung, J. C. Peters and T. F. Jaramillo, *J. Am. Chem. Soc.*, 2013, **135**, 16977–16987.
48. H. Zhang, Y. Li, G. Zhang, P. Wan, T. Xu, X. Wu and X. Sun, *Electrochim. Acta*, 2014, **148**, 170–174.
49. Y. Liang, Q. Liu, Y. Luo, X. Sun, Y. He and A. M. Asiri, *Electrochim. Acta*, 2016, **190**, 360–364.
50. T. Liu, Q. Liu, A. M. Asiri, Y. Luo and X. Sun, *Chem. Commun.*, 2015, **51**, 16683–6.
51. C. Tang, Z. Pu, Q. Liu, A. M. Asiri and X. Sun, *Electrochim. Acta*, 2015, **153**, 508–514.
52. L. L. Feng, G. Yu, Y. Wu, G. D. Li, H. Li, Y. Sun, T. Asefa, W. Chen and X. Zou, *J. Am. Chem. Soc.*, 2015, **137**, 14023–14026.
53. C. Ouyang, X. Wang, C. Wang, X. Zhang, J. Wu, Z. Ma, S. Dou and S. Wang, *Electrochim. Acta*, 2015, **174**, 297–301.
54. D. Y. Chung, J. W. Han, D.-H. Lim, J.-H. Jo, S. J. Yoo, H. Lee and Y.-E. Sung, *Nanoscale*, 2015, **7**, 5157–5163.
55. W. Zhu, X. Yue, W. Zhang, S. Yu, Y. Zhang, J. Wang and J. Wang, *Chem. Commun.*, 2016, **1**, 3–6.
56. D. Liu, Q. Lu, Y. Luo, X. Sun and A. M. Asiri, *Nanoscale*, 2015, **7**, 15122–15126.
57. J. Shi, J. Hu, Y. Luo, X. Sun and A. M. Asiri, *Catal. Sci. Technol.*, 2015, **5**, 4954–4958.
58. L. Ma, L. R. L. Ting, V. Molinari, C. Giordano and B. S. Yeo, *J. Mater. Chem. A*, 2015, **3**, 8361–8368.
59. Q. Han, K. Liu, J. Chen, X. Li and X. Wei, *Int. J. Hydrogen Energy*, 2004, **29**, 243–248.
60. N. Kumar, N. Raman and A. Sundaresan, *Journal of Solid State Chemistry*, 2013, **208**, 103-108.
61. F. Guillaume, S. Huang, K.D.M. Harris, M. Couzi and D. Talaga, *J. Raman Spectrosc.*, 2008, **39**, 1419-1422.
62. P. Marcus, J. Oudar and I. Olefjord, *Mater. Sci. Eng.*, 1980, **42**, 191-197.
63. L. Jin, C. Lv, J. Wang, H. Xia, Y. Zhao and Z. Huang, *American Journal of Analytical Chemistry*, 2016, **7**, 210-218.
64. F. Dong, Y. Sun, L. Wu, M. Fu and Z. Wu, Catal. Sci. Technol., 2012, 2, 1332-1335.

3.5 Appendix

3.5.1 Experimental methods

3.5.1.1 Chemicals and Materials

Cobalt nitrate hexahydrate ($Co(NO_3)_2 6H_2O$, ACS reagent ≥ 98%), thiourea ($CS(NH_2)_2$, ACS reagent ≥ 99%), methanol (CH_3OH, anhydrous 99.8%), sulphuric acid (H_2SO_4), potassium hydroxide (KOH) were purchased from Sigma Aldrich, Fisher Scientific and used without further purification. Nickel foam (Ni ≥ 99.8%, PPI = 110, thickness = 1 mm, volumetric porosity ≥ 95%, area mass density = 300 g/m^2) was purchased from Latech Scientific Supply.

3.5.1.2 Synthesis of cobalt-thiourea complex

The procedure was taken and adapted from Kumar *et al.*[38] For a typical synthesis, cobalt nitrate hexahydrate (2.3282 g, 0.008 mol) was dissolved in 20 mL of methanol under stirring at room temperature. The concentration of the cobalt ions was fixed at 0.4 M. Upon complete dissolution of the metal salt thiourea (2.4358 g, 0.032 mol) was added into the solution under stirring at room temperature. The molar ratio between thiourea and the cobalt salt was equal to 4. After thiourea was dissolved in the stirring solution the colour changed from dark pink to dark blue. The obtained complex was stirred for further 2 hours before being used for the next synthetic step.

3.5.1.3 Synthesis of Co_9S_8-Ni_xS_y/Ni foam electrode

Ni foam (2 cm x 1.5 cm) was first ultrasonicated at room temperature in 1) 37% HCl_{aq}, 2) ethanol, 3) DI water, 4) acetone, each step for 5 minutes. At the end it was dried using a N_2 gun before further processing. All the synthetic steps were performed inside a N_2-filled glovebox. Etched Ni foam (2cm x 1.5 cm) was dipped into the methanolic solution containing the fresh cobalt-thiourea complex for 1 min. Then the excess trapped solution in the pores was removed with a cotton cloth by capillarity. The foam was dried at 100°C for 2 minutes before being annealed at 300°C for 5 minutes. During this step the colour of the foam changed from pale silvery to black, with formation of visible vapours due to the thermal decomposition of the cobalt-thiourea complex. This cycle can be repeated in order to increase the metal loading. After the last cycle the electrode was annealed at a selected temperature and time (400°C-500°C, 10 min-90 min). The electrode was then soldered to a Ni wire and the upper edge was sealed using silicone, defining a geometric area of 1 cm^2.

3.5.1.4 Synthesis of Ni_3S_2/Ni foam electrode

Thiourea (1.8269 g, 0.024 mol) was first dissolved in 20 mL of 2-methoxyethanol at room temperature. The molar concentration of thiourea was the same as for the Co-thiourea precursor and equal to 1.6 M. The procedure for the fabrication of the electrode is the same as that reported above.

3.5.1.5 Structural characterisation

The electrodes were characterized by X-ray diffraction (XRD), scanning electron microscopy (SEM), transmission electron microscopy (TEM), Raman spectroscopy, energy-dispersive X-ray spectroscopy (EDX) and X-ray photoelectron spectroscopy (XPS). XRD patterns were acquired with a Rigaku SmartLab, using monochromatic Cu Kα radiation (1.540598 Å). The morphology of the samples was characterized using a JEOL-JSM 7200 field-emission scanning electron microscope (FE-SEM) using an acceleration voltage of 15kV. EDX analysis for the determination of the elemental composition was carried out with the same SEM apparatus used for the morphological analysis. TEM and selected area electron diffraction (SAED) pattern imaging were carried out using Philips CM300 FEG TEM operated at an accelerating voltage of 300 kV. Raman measurements were performed using a Witec Alpha 300R confocal Raman microscope equipped with a 532 nm Nd:YAG laser. XPS data were collected with a Thermo Fisher Scientific Theta Probe X-ray photoelectron spectrometer using monochromatic Al Kα radiation (1486.6 eV) as X-ray source. The binding energies were charge corrected using adventitious C 1s peak at 285.0 eV as reference.

3.5.1.6 Electrochemical characterisation

All the electrochemical measurements were performed in a 3-electrode configuration using silver/silver chloride (Ag/AgCl (3 M KCl)) as reference, a Pt foil as counter and the sample as working electrode. The geometric area of the working electrode was set equal to 1 cm^2 for all the experiments. Linear sweep voltammetry (LSV) tests were carried out using a Metrohm Autolab PGSTAT101 potentiostat in 350 mL 1 M KOH (aq). Fresh deionized water (18 MΩ·cm) was used for the preparation of the electrolyte. Before each experiment, the solution was purged for 30 minutes with pure argon in order to strip off any dissolved gas. The pH of the electrolyte was measured using a Fisher Scientific accumet basic AB15 pH meter resulting equal 13.79. All the potentials were reported versus the reversible hydrogen electrode (RHE) using the following relation: $E_{RHE} = E^0_{Ag/AgCl,3MKCl} + E_{Ag/AgCl,3MKCl} + 0.059 \cdot pH$, where $E^0_{Ag/AgCl,3MKCl} = +0.210$ V vs RHE. For the LSV measurements the potential was scanned from 0 to -0.4 V versus RHE at a scan rate of 1 mV s^{-1}. For each sample, at least 20 LSV scans were performed, with the last scan always used for analysis. The polarization curves were IR-corrected for each sample. Electrochemical impedance spectroscopy (EIS) was carried out using a Metrohm Autolab PGSTAT302N potentiostat in potentiostatic mode at -0.230 V vs RHE, with a scanning frequency from 100 kHz to 50 mHz and an amplitude of 10 mV. The stability test was performed under chronoamperometric conditions at -0.161 V vs RHE (after IR correction) for 72 hours. Each data point of the measured current was taken every 5 seconds and the electrolyte was constantly stirred throughout the experiment in order to get rid of the hydrogen bubbles.

Chapter 4: Correlating the structural properties of Co_3O_4 cocatalyst to the photoelectrochemical activity of Co_3O_4/WO_3 photoanode

Acknowledgments

The following acknowledgements recognise the contributed work of colleagues and collaborators to the presented content of this chapter.

Dr Chin Sheng Chua: For useful discussions and for help conducting photoelectrochemical experiments (Institute of Materials Research and Engineering, Singapore)

Lay Ting Ong: For collection of XPS data (Institute of Materials Research and Engineering, Singapore)

This chapter has been published: C. S. Chua, D. Ansovini, C. J. J. Lee, Y. T. Teng, L. T. Ong, D. Chi, T. S. A. Hor, R. Raja and Y.-F. Lim, *Phys.Chem.Chem.Phys.*, **2016**, 18, 5172.

4.1 Introduction

4.1.1 Tungsten oxide as photoanode for the photoelectrochemical water splitting: description of the effect of synthetic methodology and presence of cocatalyst on its photocurrent generation

The general fundamental mechanisms occurring during the photoelectrochemical (PEC) water splitting were presented in Section 1.2.2, along with a brief description of the different existing technological configurations currently under investigation. PEC water splitting is an attractive process as it stores the intermittent renewable solar energy directly in the form of hydrogen gas.[1] In simple terms, three main steps are found to occur in the PEC water splitting process:

1. Absorption of photons and generation of electron-hole pairs by a photoabsorber semiconductor with selected band-gap
2. Separation and migration of electron-hole pair
3. Surface redox reaction via photogenerated electrons and holes occurring at catalytic active sites

In order to split water, two surface redox reactions are required, the hydrogen evolution reaction (HER) occurring at the photocathode and the oxygen evolution reaction (OER) occurring at the photoanode.[2] The efficiency of these reactions strictly depends on the presence and type of co-catalysts normally placed on top of photoabsorber semiconductors. The effect of co-catalysts in the PEC water splitting was discussed in Section 1.3.2, giving insights into their beneficial role for improving the photocurrent and increasing the stability of the photoabsorber semiconductors. In particular OER has revealed to be more kinetically difficult than HER, as it requires multiple interactions and the removal of four protons and electrons for oxygen to evolve.[3] As such, much work had focused on improving the solar-to-oxygen conversion efficiency of photoanodes, through the deposition of appropriate co-catalyst materials which possess an intrinsic high activity toward the OER.

As already discussed in Section 1.2.2, photoanode materials used for OER are n-type semiconductors (larger electron concentration than hole concentration) which are able to absorb photons with energy *hv* equal or higher than their band-gap and generate electron-hole pairs. The photogenerated electrons transfer from the valence band (VB) to the conduction band (CB), leaving a photogenerated hole behind. In this way the electrons and holes are effectively separated, and they start to migrate in opposite directions. The band bending of the semiconductor induced by the contact with the liquid electrolyte drives the holes to its surface. The holes are further transferred to the co-catalyst where the OER occurs.

N-type metal oxide semiconductors have been widely investigated as photoanodes for the OER, given their favourable VB position for the OER, chemical stability, photoelectrochemical stability, low toxicity and ease of synthesis. Typical examples found in the literature include n-TiO_2,[4] n-Fe_2O_3,[5] n-$BiVO_4$,[6] n-WO_3,[7] n-$CuWO_4$.[8] In particular, given the objective of this work, it is useful to report further details about the literature concerning tungsten oxide (WO_3) as photoanode for the OER, paying particular attention to the documented synthetic methodologies for the fabrication of thin films. The significant amount of work related to improving the PEC performance of WO_3 has been mainly driven by the suitable properties of this material, which can be summarised below:

- Good stability in neutral to acidic solution[9]
- Good charge properties[10]
- High oxidation power of valence band holes (+3.1–3.2 V vs normal hydrogen electrode (NHE))[11]
- Band gap ranging from 2.5-3.0 eV, depending on stoichiometry, crystal structure and defects[12]

These favourable properties explain the reason why WO_3 was used as photoanode material in this study. Chakrapani *et al.* reported the fabrication of WO_3 nanowires supported on transparent conductive FTO/glass substrate through a chemical vapour deposition method involving the deposition of metal oxide vapours generated from the oxidation of W metal wire under high temperature.[13] The material had a band gap of 2.9 eV and it showed good PEC activity under AM 1.5 solar light in acid media, with a photogenerated current density of 1.6 mA/cm^2 at 2.0 V vs SCE. In 2010 Meda *et al.* prepared nanostructured WO_3 on FTO/glass by preparing a H_2WO_4 colloidal precursor containing organic dispersing agent and then depositing the precursor on FTO using a blade-spreading technique.[14] The obtained thin film was subsequently annealed at different temperatures (500-600 °C) in air and it was found that the photocurrent generation is greater for smaller particle sizes. The authors attributed this behaviour to the fact that smaller nanocrystals lead to higher surface area, which in turn is responsible for the increase in photocurrent. Furthermore, they found that a thin film thickness of 400-500 nm was a good compromise between light absorption and charge separation efficiency. Another interesting synthetic methodology was reported for the first time by Liu *et al.*, where they used the atomic layer deposition (ALD) technique for the deposition of WO_3 thin films on transparent ITO conductive support with a well-defined thickness of 180 nm.[15] After the deposition the film was annealed at 550 °C under O_2 atmosphere in order to further improve the crystallinity and decrease the amount of oxygen deficiencies in the lattice. As outlined by the authors, the ALD method presents several important properties such as high degree of material purity, high control of the thickness and conformal coating of the substrate. The resulting photoanode showed good PEC activity under simulated sunlight at pH 4, with a measured photocurrent of almost 2 mA/cm^2 at 1.23 V vs RHE. Vidyarthi *et al.* reported the fabrication of polycrystalline WO_3 thin films using reactive magnetron sputtering technique at a substrate temperature of 350 °C.[16] The authors investigated the PEC characteristics of the synthesised WO_3 thin films as a function of the thickness and microstructural variations. Interestingly, the PEC activity under visible light in acidic pH was higher for WO_3 films having porous structure with small crystallites and thickness of 600 nm. In contrast, compact WO_3 films showed much smaller photocurrent, and the activity was found to further decrease for thickness larger than 200 nm. Cristino *et al.* were able to synthesise WO_3 nanostructures through potentiostatic anodization of metallic W foil under appropriate conditions.[17] Morphological analysis of the synthesised material after annealing at 550 °C in air revealed the formation of irregular porous oxide layer of 3-5 µm thick, with an overall wormlike appearance. The best synthesised material showed high photocurrent generation of 3.5 mA/cm^2 at 1.5 vs SCE in 1 M H_2SO_4 under simulated solar light with intensity of 0.15 W/cm^2. Hydrothermal process for the synthesis of WO_3 with plate-like structure was reported by Amano *et al.*, which was based on the hydrothermal reaction of metallic W nanosheets in a dilute nitric acid solution under different temperatures and times.[18] The final calcination step at 450 °C in air was found to be essential in order to convert the formed tungsten oxide hydrate into crystalline monoclinic WO_3. The authors investigated the effect of synthetic conditions on the PEC activity in acidic electrolyte. It was found that low temperature for the hydrothermal reaction leads to smaller thickness, which is beneficial for reducing charge recombination and improving photogenerated current density. The best synthesised material showed a photocurrent of 3.5 mA/cm^2 at 1.2 vs Ag/AgCl in 0.1 M H_2SO_4 under lamp with UV and blue-visible light. Hill *et al.* reported the fabrication of WO_3 thin film on FTO using electrodeposition of peroxo-tungstic acid solution.[19] The formation of the monoclinic crystalline phase of WO_3 was obtained through final annealing at 500 °C in air. In the electrodeposition bath, the presence of stabilising agents was found to be essential in order to prevent uncontrolled precipitation of the precursor. The resulting high porosity of the obtained film was due to the presence of stabilising agents, which were responsible for a diffusion-limited growth. The good PEC activity of this material was attributed to the extremely high porosity obtained by optimal synthetic conditions during the electrodeposition process.

The effect of cocatalysts on the PEC performance of crystalline WO_3 has been documented in the literature using different materials and synthetic techniques. For example, Liu *et al.* explored the influence of a Mn-based cocatalyst on the PEC activity of the WO_3 thin film deposited through ALD, as previously described.[15] The cocatalyst was synthesised directly on top of WO_3 through thermal decomposition at low temperature of a Mn complex. The main function of the cocatalyst was to act as protecting layer for WO_3, without affecting the PEC performance. However, no substantial improvement in the photocurrent generation was observed. The effect of iridium oxide (IrO_2) on the photocurrent generation of WO_3 was reported by Spurgeon *et al.*[20] IrO_2 is regarded as one of the most active OER catalysts in acidic media, as previously illustrated in Section 1.3.2. In particular, the work was based on exploring different synthetic techniques for the deposition of IrO_2 on WO_3 and testing their influence on the overall efficiency. Interestingly, a thin layer of IrO_2 prepared by sputtering was found to optimally cover the surface of WO_3 and improve the O_2 production yield at 1.2 V vs RHE in 1M H_2SO_4. The faradaic efficiency for O_2 production was almost 100 % for thick IrO_2 film, whereas only 60% efficiency was measured for thin films. However the authors pointed out that the thickness of the cocatalyst should not be too large, in order to minimise parasitic light absorption and a decrease in the photocurrent generation. Liu *et al.* reported the design of a nanoporous WO_3 thin film with cobalt-phosphate (Co-Pi) cocatalyst, which was synthesised through photoelectrodeposition directly on the surface of WO_3.[21] The presence of the cocatalyst increased the photocurrent generation the photoanode compared to the bare WO_3, with an overall improvement of 20 % at 0.8 V vs SCE in neutral pH. The beneficial effect of Co-Pi on the overall efficiency was attributed to a more facile charge transfer and reduced recombination of photogenerated electron/hole pairs induced by the adequate junction formed between the catalyst and the porous WO_3. Recently, the PEC performance of an optically-transparent FeOOH cocatalyst deposited on WO_3 was reported by Kwong *et al.*[22] The FeOOH was directly synthesised on the surface of WO_3 as nanoparticles using a simple electrodeposition technique, resulting in even coverage of the WO_3 surface. It was found that the presence of the cocatalyst enhanced the photocurrent density by three times compared to the bare WO_3 photoanode at 1 V vs RHE in 0.5 M K_2SO_4. Furthermore, the O_2 faradaic efficiency increased from 70 % of the bare WO_3 to 100 % of the FeOOH/WO_3 photoanode. The authors linked the beneficial effect of FeOOH to the lower resistance of hole transfer to the electrolyte due to the good water oxidation kinetics of this material and higher charge separation efficiency.

4.1.2 Objectives

The objectives of this chapter are schematically summarised in the following points:

1. To synthesise the composite n-WO_3/Co_3O_4 thin film photoanode using a facile sol-gel spin coating method
2. To investigate the structural and morphological properties of the material
3. To evaluate the photoelectrochemical activity of the composite photoanode as a function of the annealing temperature of the Co_3O_4 electrocatalyst
4. To explain and demonstrate the trend in activity of materials annealed at different temperatures

4.2 Results and Discussion

4.2.1 Deposition of WO_3 and Co_3O_4 thin films using sol-gel method: an overview

In this work WO_3 thin films were deposited on transparent conductive FTO substrate using a simple sol-gel spin coating method. In particular, the initial preparation of the sol precursor was inspired by earlier works reporting the formation of stable tungsten alkoxide sols derived from the reaction of tungsten(VI) chloride and ethanol under anhydrous conditions.[23] In this case the sol-gel synthesis is defined as non-hydrolytic, because the oxygen donor is the alcohol rather than the more commonly used water.[24] As described in the experimental section of this chapter, WCl_6 and methanol (CH_3OH) were mixed in the presence of acetylacetone and polyethylene glycol. In the first step of reaction, CH_3OH reacts with WCl_6 according to the following equation:

$W\text{-}Cl + CH_3OH \rightarrow W\text{-}O\text{-}CH_3 + HCl$ 4.1

The formation of gaseous HCl was experimentally observed during the mixing of the two reactants. In order to avoid possible uncontrolled hydrolysis of WCl_6 upon reaction with atmospheric moisture the entire preparation of the sol-gel precursor was carried out inside a N_2-filled glovebox. Interestingly, the presence of acetylacetone as stabilising agent was found to be essential to prevent the uncontrolled precipitation of the W-alkoxide.

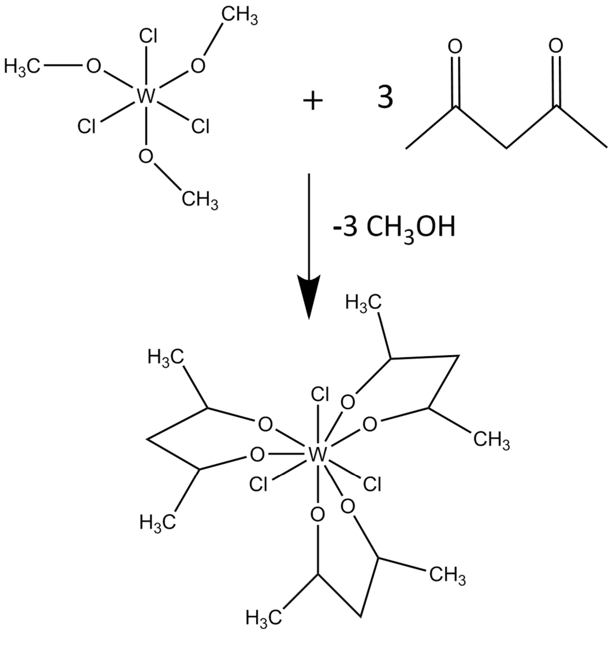

***Figure 4.1** Simplified scheme of the chelating effect of acetylacetone on the W alkoxide by replacement of methanol molecules*

As shown in Fig. 4.1, acetylacetone acts a chelating agent by partially or totally replacing the methoxy groups previously formed during the first step of reaction between WCl_6 and CH_3OH. The same role of acetylacetone as stabilising agent was documented in the work published by Bertus *et al.*[25] The authors reported the synthesis of WO_3 thin films by surfactant-assisted spray pyrolysis of a solution containing WCl_6, ethanol, acetylacetone and polymeric surfactants. Finally, polyethylene glycol 200 (PEG-200) was added to the solution in order to increase the final porosity of the film upon thermal annealing. This is supported by earlier reports related to the effect of PEG on the structural and morphological properties of metal oxide thin films. Fang *et al.* investigated the role of PEG on the properties of WO_3 thin films prepared by sol-gel.[26] It was found that under annealing temperatures higher than 250 °C, PEG was removed from the thin film material, creating a porous structure. It can also play a role as modulator for crystal growth and orientation, influencing the final crystallinity of the thin film. Furthermore, the presence of PEG can improve the wettability of the solution during spin-coating, resulting in the formation of more homogeneous and crack-free thin films, as reported by Oral *et al.* in their work concerning the fabrication of CuO thin films using sol-gel spin coating method.[27] The obtained solution was then aged for 4 days under constant stirring inside the glove-box, in order to obtain a complete network of stabilised W-alkoxides.

As described in Section 4.4.2, FTO/glass slides were used as substrates for the deposition of the W-sol by spin-coating technique under atmospheric air. FTO (fluorine-doped tin oxide) is commonly used as conductive transparent substrate for the fabrication of photoelectrodes, given its high electronic conductivity, high transparency and high thermal resistance. After each spin-coating, the film was annealed at 300 °C in order to create an amorphous structure and eliminate volatile compounds, like methanol, acetylacetone, HCl and PEG-200. Pure crystalline WO_3 was obtained at final annealing temperature of 500 °C. This particular value of temperature was chosen according to previous reports which indicated that WO_3 thin films with high porosity and small crystal size showing good PEC activity were formed at 500 °C.

The deposition of Co_3O_4 cocatalyst on WO_3/FTO thin films was performed by sol-gel spin coating method. The solution was prepared using cobalt(II) acetylacetonate, methanol and ethanolamine. The role of ethanolamine was to increase the solubility of the Co metal-organic precursor and to stabilise the solution. The concentration of the Co salt was low (0.02 M) in order to minimise the thickness of the single layer formed during the spin-coating. The effect of the annealing temperature on the resulting crystallinity of Co_3O_4 was systematically investigated, and the results are discussed below. Some works related to the fabrication of Co_3O_4 thin films by sol-gel spin coating are described in the literature. For instance, Chougule *et al.* prepared Co_3O_4 thin films by spin-coating a non-hydrolytic sol-gel solution made of cobalt(II) acetate and methanol.[28] Crystalline Co_3O_4 thin films were formed at annealing temperature of 400 °C. Jeon *et al.* used cobalt(II) nitrate and ethanol as starting solution for the synthesis of Co_3O_4 thin films by spin coating method.[29] Highly crystalline Co_3O_4 was found to occur at annealing temperature of 500 °C.

However, the fabrication of WO_3/Co_3O_4 thin film heterostructures and their investigation as photoanodes for the PEC water splitting has never been reported in the literature.

4.2.2 Structural and morphological characterisation

The XRD pattern of the deposited WO_3 film on FTO glass annealed at 500 °C for 1 hour is shown in Fig. 4.2(a).

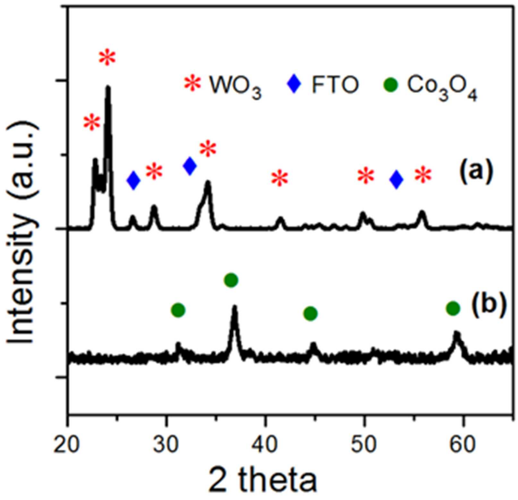

Figure 4.2 *XRD patterns of (a) WO_3 film on FTO glass annealed at 500 °C and (b) Co_3O_4 on silicon annealed at 500 °C*

The WO_3 film shows distinct peaks at 23.1°, 24.8°, 34.6°, and 50.3°, corresponding to the (002), (200), (220) and (140) planes of the monoclinic WO_3 (JCPDS 01-083-0950). The other peaks can be assigned to the tetragonal phase of FTO substrate. (JCPDS 46-1088). From a qualitative analysis of the peak intensity it is possible to observe a preferential growth along the (200) plane of the monoclinic structure. The same preferential growth along this plane was reported by Cheng *et al.* in their work concerning the synthesis of WO_3 thin films by sol-gel dip coating process.[23] It is known that WO_3 can exist under different crystallographic structures such as monoclinic, orthorhombic, triclinic, tetragonal, cubic and hexagonal. The formation of one specific phase depends on the particular synthetic methodology, annealing temperature, annealing time and annealing atmosphere. In this case the formation of pure monoclinic WO_3 is in agreement with other works based on the fabrication of WO_3 thin films by sol-gel spin coating method which are based on a similar thermal treatment at 500 °C under atmospheric air.[23,30] It is worth noting that the monoclinic crystal phase presents the highest photoactivity among the various possible crystallographic arrangements for WO_3.[31]

In order to detect the crystallographic behaviour of Co_3O_4 as function of the annealing temperature, thick Co_3O_4 films were prepared on single crystal silicon substrates. The corresponding XRD pattern of the Co_3O_4/Si material annealed at 500 °C for 1 hour is displayed in Fig. 4.2(b). The peaks highlighted by the green circles and located at 31.2°, 36.8°, 44.7° and 59.2° are attributed to the (220), (311), (400) and (511) crystallographic planes of the pure cubic Co_3O_4 phase (JCPDS 073-1701). This result is in line with the majority of previous works related to Co_3O_4 materials, which indicate the formation of nanocrystalline cubic Co_3O_4 at annealing temperature of 500 °C in air.[28,29]

The structural crystallographic evolution of thick Co_3O_4 supported on single crystal Si was investigated by analysing XRD patterns of samples annealed at different temperatures. As displayed in Fig. 4.3, the XRD spectrum of the sample annealed at 200 °C shows no diffraction peaks, suggesting an amorphous structure under this specific temperature. Peaks belonging to the cubic Co_3O_4 phase start to appear at 300 °C, and their intensities grow as temperature increases. The determination of the crystallite size of Co_3O_4 was performed using the Scherrer's equation. This formula relates the size of nanocrystallites with the experimentally-measured peak width. In particular, Scherrer demonstrated that the peak width is inversely proportional to the crystallite size:

$$d_c = \frac{K\lambda}{\beta \cos\theta} \qquad 4.2$$

Where K is a dimensionless shape factor (0.94 for spherical crystal of cubic symmetry), λ is the X-ray wavelength, β is the full width at half maximum of the analysed peak (FWHM) and θ is the Bragg angle. The calculation was made on the more predominant (311) plane of the cubic Co_3O_4. The corresponding calculated nanocrystallite size was 3.7 nm for sample annealed at 400 °C and 7.8 nm for the sample annealed at 500 °C. This nanocrystallite size is much smaller than the typical values reported for Co_3O_4 synthesised by sol-gel spin coating method. For instance, Chougule *et al.* calculated a crystallite size of 53.4 and 58.2 nm for Co_3O_4 samples annealed at 400 °C and 500 °C, respectively.[28] Crystallite size of 20 nm was reported by Jeon *et al.* for Co_3O_4 synthesised by thermal annealing at 500 °C of a solution containing cobalt nitrate.[29] It is likely that the much smaller crystallite size found for the Co_3O_4 described in this work is linked to the different choice of molecular precursors used during the preparation of the sol.

The XRD spectrum of the FTO/WO_3/Co_3O_4 thin film heterostructure is reported in Fig. 4.4. In this case, only 1 layer of Co_3O_4 sol-gel precursor was spin coated on top of the preformed FTO/WO_3 thin film, and then subject to annealing at 500 °C for 1 hour in air. Clearly, no peaks related to the presence of crystalline Co_3O_4 could be detected. This is due to the extremely low amount of deposited Co_3O_4 on the surface of WO_3, thus preventing its detection by XRD.

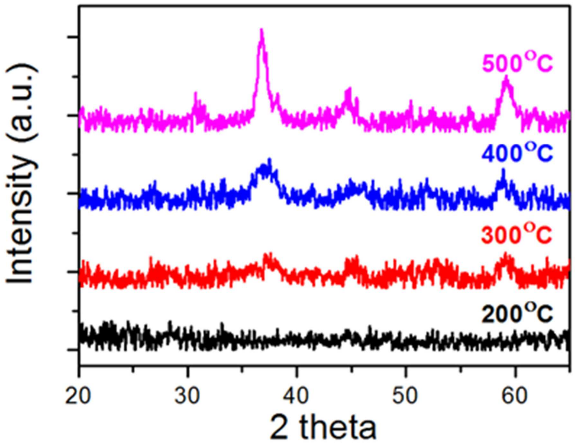

Figure 4.3 *Evolution of XRD pattern of* Co_3O_4 *film on silicon at different annealing temperatures*

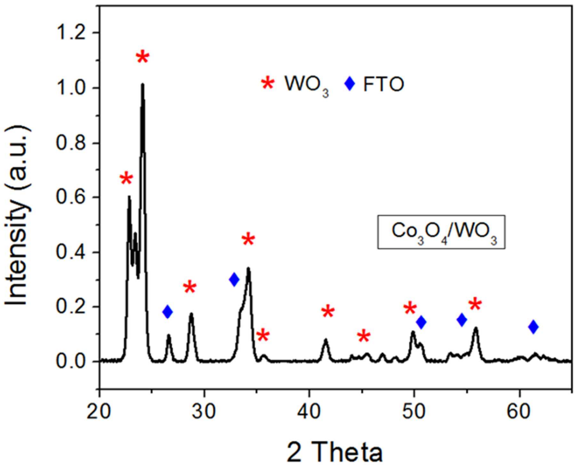

Figure 4.4 *XRD spectra of 1 layer* Co_3O_4 *(annealed at 500 °C) on FTO/*WO_3*. Due to the thin* Co_3O_4 *layer, only* WO_3 *and FTO layer is detected*

The FTO/WO_3 thin film was subject to UV-Vis spectroscopy analysis for the determination of the optical band-gap. Furthermore, the effect of the presence of Co_3O_4 on the light absorption characteristic of the WO_3 photoabsorber was investigated, and the corresponding plots representing the absorbance as function of the wavelength is reported in Fig. 4.5(a). Co_3O_4 is a p-type semiconductor with documented fundamental band gaps ranging from 0.7 eV to 1.5 eV, as a result of the crystal field splitting and cation-anion orbital hybridization.[32,33] In this case, a very slight increase in light absorption can be observed in the presence of an ultra-thin layer of Co_3O_4 (1 layer, annealed at 500 °C) compared to the bare WO_3. The increase is more evident in the portion of the spectrum attributed to the visible light (> 400 nm), as a result of the strong light absorption of the nanocrystalline Co_3O_4. In both cases, a sharp increase in light absorption is measured at 450 nm, corresponding to the yellow portion of the visible spectrum. The calculation of the optical band gap is done using the so-called Tauc analysis method. First of all, the absorption coefficient of the material can be estimated with the following formula:

$$\alpha=2.302\ A/t \qquad 4.3$$

where α is the absorption coefficient (in cm^{-1}), *A* is the absorbance which is experimentally measured as function of the wavelength and t is the thickness of the film. As displayed in the cross-Section SEM image reported in Fig 4.7 the film thickness is around 1.4 µm. This equation is directly derived from the Lambert-Beer's law, which relates the attenuation of light to the properties of a material. From these values it is then possible to proceed with the construction of the Tauc plot, whose equation is reported as follows:

$$(\alpha h v)^{1/n} \propto \mathrm{A}(h v - E_g) \qquad 4.4$$

Where *n* represents the nature of the electronic transition (n = 1/2 for direct allowed transition, n = 3/2 for direct forbidden transition, n = 2 for indirect allowed transition, n = 3 for indirect forbidden transition), *h* is Planck's constant, *v* is the photon's frequency, *A* is a proportionality constant (set equal to 1) and E_g is the optical band gap. In this case *n* is equal to 2, given the typical indirect band gap of WO_3 widely documented in the literature.[34] By plotting $(\alpha h v)^{1/2}$ versus *hv* it is possible to calculate the value of E_g by extrapolating the linear part of the data and setting the y-axis equal to 0, as represented in Fig. 4.5(b). The calculated band gap of the FTO/WO_3/Co_3O_4 is 2.6 eV, in agreement with previous works based on pure crystalline WO_3 thin films.[12]

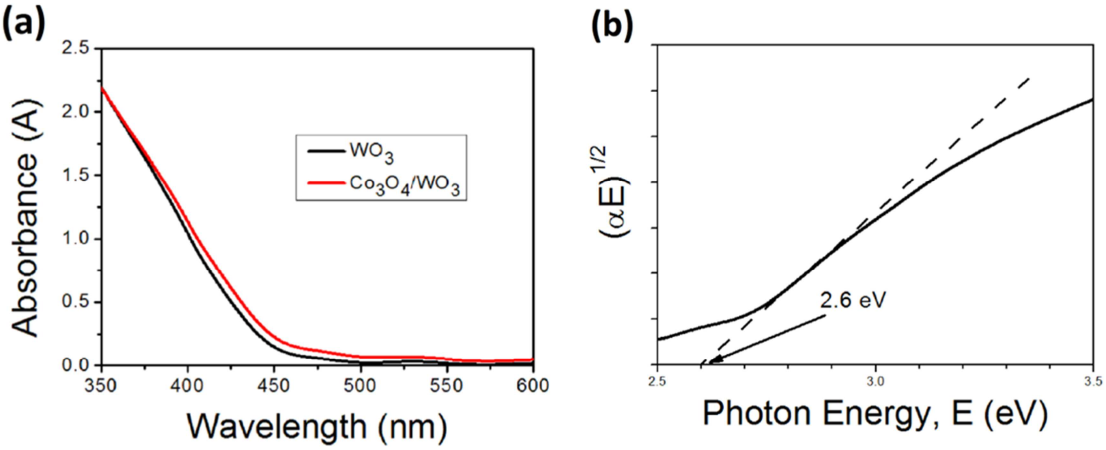

Figure 4.5 *(a) UV-Vis absorption spectra of FTO/WO_3 (black) and FTO/WO_3/Co_3O_4 (red) film, (b) Tauc plot and band gap determination of WO_3 film*

The SEM images of FTO/WO_3 and FTO/WO_3/Co_3O_4 (Co_3O_4, 1 layer, annealed at 500 °C) thin film samples are reported in Fig. 4.6(a) and 4.6(b), respectively. Both films show a porous structure consisting of spherical particles with size of around 200 nm. These particles are interconnected through the existence of short rods on the surface of the films. This porous structure is typical of WO_3 thin films synthesised by sol-gel spin coating method using PEG as organic template.[26] Clearly, the overall morphology is not affected by the presence of the ultra-thin layer of Co_3O_4, as the two SEM images show a strong similarity. As already mentioned in the description for the calculation of the optical band gap, a thickness of 1.4 µm was measured for the WO_3 film by cross-Section SEM, with the corresponding image reported in Fig. 4.7. Energy dispersive X-ray spectroscopy (EDX) analysis was performed in order to quantify the presence of metallic elements in the bulk of FTO/WO_3/Co_3O_4 thin film sample. This technique relies on the interaction of high-energy X-ray photons with the elements present in the material. As a result of the high-energy of the beam, the penetration depth can be on the order of 1-2 µm. As expected, the EDX spectrum displayed in Fig. 4.8 shows the presence of only W (from WO_3) and Sn (from FTO), without any trace of Co. This is due to two main factors:

- Much smaller presence of elemental Co compared to W and Sn
- Elemental Co must be located only at the surface, confined in a ultra-thin layer of a few nanometers

The total absence of Co in the EDX spectrum suggests that Co ions did not diffuse inside WO_3 film upon thermal annealing.

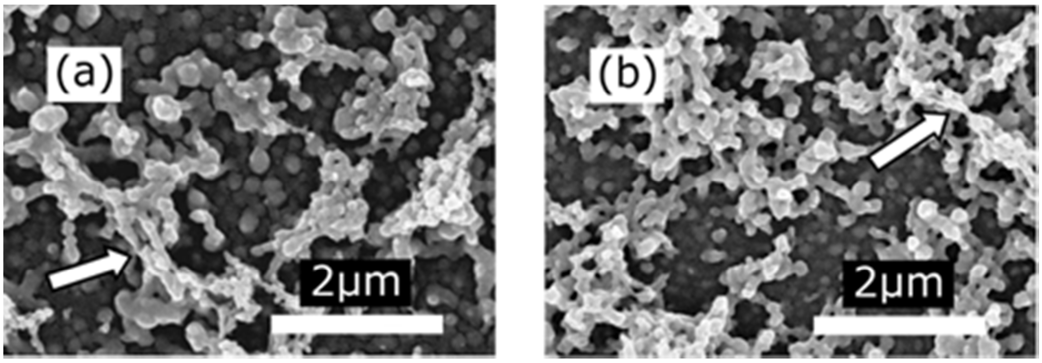

Figure 4.6 *Surface morphology of (a)FTO/WO_3 film, and (b) FTO/WO_3/Co_3O_4 film (Co_3O_4 was annealed at 500 °C). The arrows point to the short interconnecting rods between growth regions*

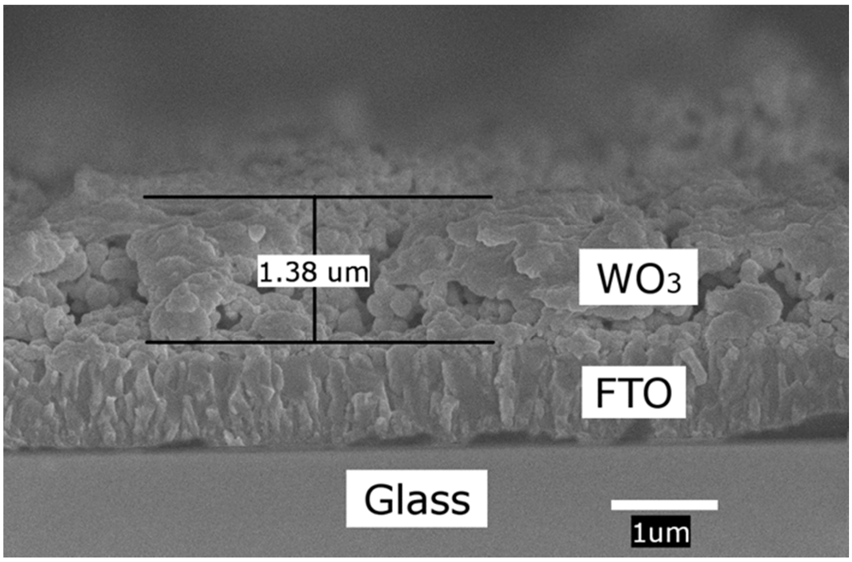

Figure 4.7 *Cross-Sectional view of FTO/WO_3/Co_3O_4 film*

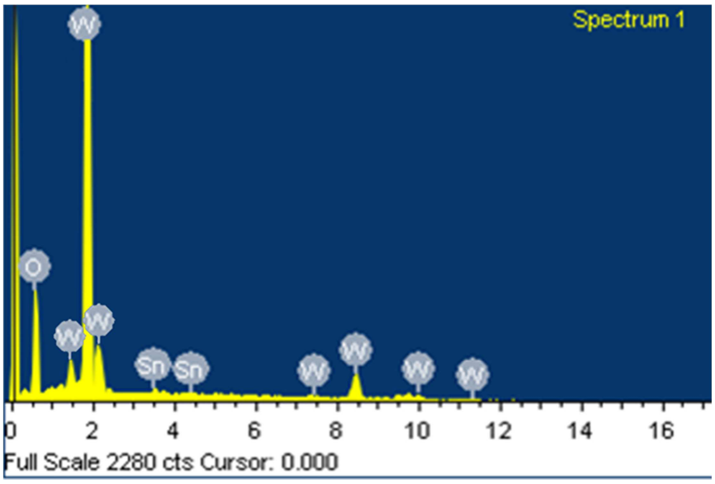

Figure 4.8 *EDX analysis of FTO/WO_3/Co_3O_4 film*

The analysis of the elemental composition on the surface of FTO/WO_3/Co_3O_4 thin film was performed by X-ray photoelectron spectroscopy (XPS) analysis. As opposed to XRD and EDX which are typical bulk spectroscopic techniques, XPS can detect the presence and nature of metallic and non-metallic elements on the material surface, within a range of 10 nm. Thus, XPS technique is suitable to probe the presence of Co ions on the surface of the film. The corresponding Co2p XPS spectrum of the FTO/WO_3/Co_3O_4 (Co_3O_4, 1 layer, annealed at 350 °C) is reported in Fig. 4.9. The detection of the two main peaks at binding energies of 781.2 eV and 797.1 eV ($Co2p_{1/2}$) confirm the presence of Co ions on the surface. The main peak located at 781.2 eV corresponds to $Co2p_{3/2}$, and its value is slightly higher than the typical $Co2p_{3/2}$ binding energy range commonly reported for pure Co_3O_4 (780.0-780.9 eV).[46,47] Given the poor resolution of the spectrum it was not possible to deconvolute the $Co2p_{3/2}$ peak in order to discern the various oxidation states of the Co ions. It is known that Co_3O_4 adopts a typical spinel structure with Co^{2+} ions on tetrahedral coordination sites and Co^{3+} ions on octahedral coordination sites. Typical binding energies of the Co^{3+} and Co^{2+} ions resulting from the deconvolution of the main $Co2p_{3/2}$ peak are normally located at binding energies of 780.0 and 782.0 eV, respectively.[47] Thus, the slight shift of the main $Co2p_{3/2}$ peak toward higher binding energies may be indicative of the presence of more Co^{2+} ions on the surface. As reported by Ding *et al.*, a high annealing temperature favours the formation of more Co^{3+} ions, as a result of the oxidation of Co^{2+} species on the surface of Co_3O_4.[35] As such, the predominant presence of Co^{2+} ions may due to the low annealing temperature (350 °C) used for the synthesis of the Co_3O_4 cocatalyst. The other two peaks at 787.1 eV and 803.1 eV 803.1 can be attributed to the satellite peaks of $Co2p_{3/2}$ and $Co2p_{1/2}$.[48]

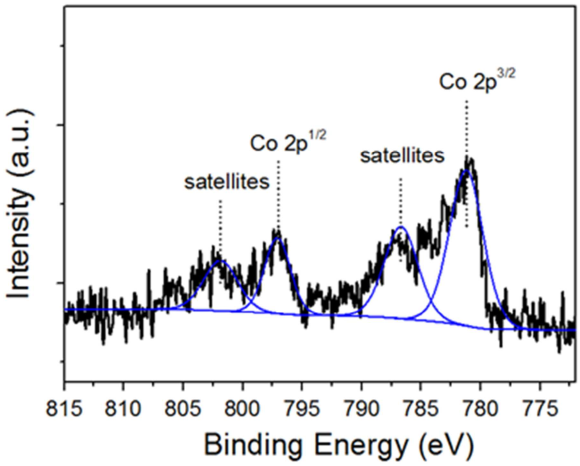

Figure 4.9 *XPS spectra of Co 2p for* Co_3O_4/WO_3 *film with the cocatalyst annealed at 350 °C*

4.2.3 Photoelectrochemical water oxidation analysis of Co_3O_4/WO_3 thin film: effect of the annealing temperature on the photocurrent generation

The PEC properties of the synthesised FTO/WO_3 and FTO/WO_3/Co_3O_4 film photoelectrodes were investigated by performing linear sweep voltammetry (LSV) under light and dark conditions in a 3-electrode cell setup with Pt foil as counter electrode and Ag/AgCl as reference electrode in 0.1 M Na_2SO_4 aqueous solution. During the experiment the photoelectrode was illuminated with a Xe-lamp equipped with AM 1.5 solar simulator filter. The light intensity was measured and set equal to 100 mW/cm^2. The illuminated area of each sample was set equal to 1 cm^2, and the current density was normalised to this value of geometric area. The potential was scanned between 0 V vs Ag/AgCl and 1.6 V vs Ag/AgCl in the anodic direction. The corresponding LSV curves of FTO/WO_3 and FTO/WO_3/Co_3O_4 samples are displayed in Fig. 4.10. It is worth noting that the dark current recorded for all the samples was negligible. For the sake of clarity, only the dark current of the FTO/WO_3 was reported. In this case the effect of Co_3O_4 thickness on the photocurrent generation was investigated. As such, samples with 1 layer and 3 layers of Co_3O_4 deposited on top of WO_3 film were made. The final annealing temperature for the synthesis of Co_3O_4 cocatalyst was 350 °C. Interestingly, FTO/WO_3/Co_3O_4 (1 layer) shows the best performance, attaining a photocurrent density of 0.43 mA/cm^2 at 0.85 V vs Ag/AgCl. This value is 40% higher than that measured for FTO/WO_3, thus suggesting that the presence of the cocatalyst significantly improves the PEC activity of the photoanode. However, the measured photocurrent of the sample containing 3 layers of Co_3O_4 was even lower than the bare FTO/WO_3. A thick layer of Co_3O_4 may lead to parasitic light absorption which lowers the amount of photons absorbed by WO_3, resulting in a low photocurrent generation. The same observation has been reported by Spurgeon *et al.* in their work based on WO_3/IrO_2 photoanode.[20] Thick layers of IrO_2 drastically decreased the amount of photogenerated current. They also demonstrated that with sufficiently thick IrO_2 material no photocurrent could be detected. A quantitative comparison of the measured PEC activities with some published works related to WO_3 thin film photoanodes can be found in Tab. 4.1. A lack of proper optimisation may explain the rather low performance of the materials described in this chapter compared to other WO_3 materials reported in the literature. However, the aim of this work was to investigate the effect of Co_3O_4 cocatalyst on the PEC properties of WO_3 thin film, with major focus on establishing trends in activity rather than looking at the absolute values. Nonetheless it is important to make a sharp comparison in terms of measured photocurrent in order to understand the potential applicability of the photoanode in real devices.

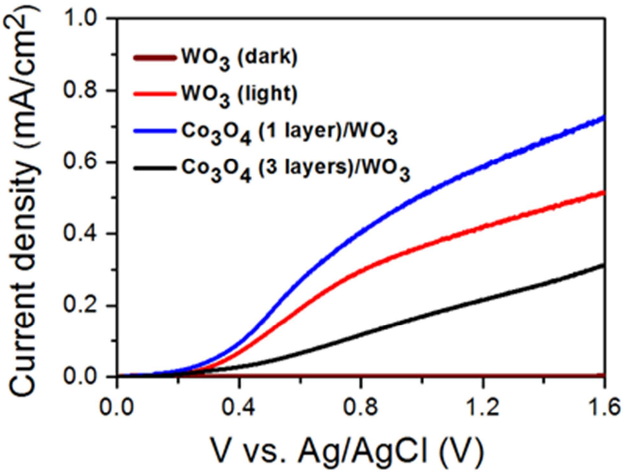

Figure 4.10 *Photocurrent densities of bare FTO/WO_3 and FTO/WO_3/Co_3O_4 in 0.1 M Na_2SO_4 (pH 5.8) under a light intensity of 100 mW/cm^2(Co_3O_4, 1 layer annealed at 350 °C, blue), (Co_3O_4, 3 layers annealed at 350 °C, black)*

Material	Fabrication	Electrolyte	Photocurrent density	Reference
FTO/WO_3	Drop casting	0.1 M Na_2SO_4 (pH 7) UV-Vis (100 mW/cm^2)	0.2 mA/cm^2 (0.8 V vs Ag/AgCl or 1.4 V vs RHE)	36
FTO/WO_3	Spray pyrolysis	0.5 M K_2SO_4 (pH 6.6) AM 1.5G (100 mW/cm^2)	1.2 mA/cm^2 (1.4 V vs RHE)	22
FTO/WO_3	Drop casting	0.1 M K_2SO_4 (pH 3.5) Xe-lamp (50 mW/cm^2)	0.11 mA/cm^2 (1.36 V vs RHE)	37
FTO/WO_3	Sol-gel spin coating	0.5 M Na_2SO_4 Solar simulator (100 mA/cm^2)	1.35 mA/cm^2 (1.4 V vs RHE	38
FTO/WO_3	Sol-gel spin coating	0.5 M NaCl (pH 2) AM 1.5 (100 mW/cm^2)	1.7 mA/cm^2 (1.4 vs RHE)	39
FTO/WO_3	Sol-gel spin coating	0.1 M Na_2SO_4 (pH 5.8) AM 1.5 (100 mW/cm^2)	0.3 mA/cm^2 (0.85 V vs Ag/AgCl or 1.4 V vs RHE)	**This work**
FTO/WO_3/Co_3O_4	Sol-gel spin coating	0.1 M Na_2SO_4 (pH 5.8) AM 1.5 (100 mW/cm^2)	0.43 mA/cm^2 (0.85 V vs Ag/AgCl or 1.4 V vs RHE)	**This work**

Table 4.1 *Comparison of the PEC activity of some WO_3-based thin film photoanodes found in the literature*

The trend in photocurrent generation of the FTO/WO_3/Co_3O_4 photoanode as a function of the Co_3O_4 annealing temperature is reported in Fig. 4.11. The photocurrent of the bare FTO/WO_3 sample recorded at 1.2 V vs Ag/AgCl under AM 1.5 illumination was taken as reference point. The y-axis represents the percentage change in the measured photocurrent of the different FTO/WO_3/Co_3O_4 samples with respect to the FTO/WO_3 reference. In this case, 1 layer of Co_3O_4 cocatalyst was deposited during the synthesis for all the samples under investigation. Interestingly, the photoactivity increases with increasing Co_3O_4 annealing temperature before reaching a maximum corresponding to the sample annealed at 350 °C. At the maximum, the measured photocurrent is 40% higher with respect to the reference. The LSV curve of this sample was explicitly reported and discussed in Fig. 4.10. By further increasing the Co_3O_4 annealing temperature there is a decrease in photoactivity, with the sample annealed at 500 °C showing the worst performance which is even inferior to that of the bare reference FTO/WO_3. The same trend was also observed with NiO cocatalyst, which was prepared as control experiment in order to verify if this behaviour could be present in other materials. In this case, the highest performance was obtained for NiO cocatalyst annealed at 300 °C, whereas the worst performance was obtained for NiO annealed at 500 °C as shown in Fig. 4.13. From the XRD spectra of thick NiO films deposited on monocrystalline silicon by sol-gel spin coating it is possible to notice that at 300 °C the structure is completely amorphous, with the total absence of diffraction peaks (Fig. 4.12). In contrast, sharp peaks located at 37. 2°, 43.2° and 62.9° and attributed to the (111), (200) and (220) planes of the cubic NiO phase were detected for the sample annealed at 500 °C. Surprisingly, even in this case there is a logic relation between photocurrent and structural properties of the cocatalyst. Clearly, a drastic decrease in photocurrent with increasing crystallinity can be observed for both Co_3O_4 and NiO.

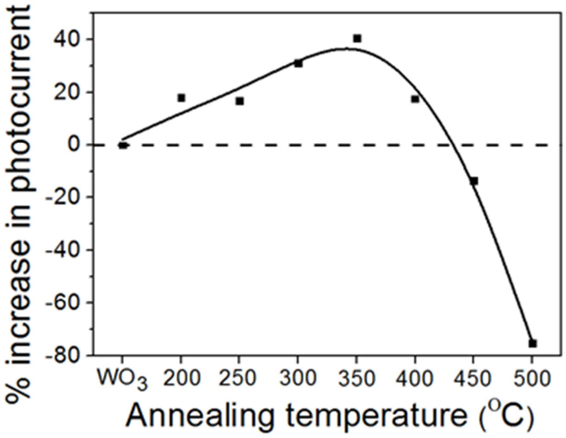

Figure 4.11 *Percentage change in photocurrent (with respect to bare WO_3) with cocatalyst annealing temperature for FTO/WO_3/Co_3O_4 films at 1.2 V vs Ag/AgCl in 0.1 M Na_2SO_4 (pH 5.8) under a light intensity of 100 mW/cm^2*

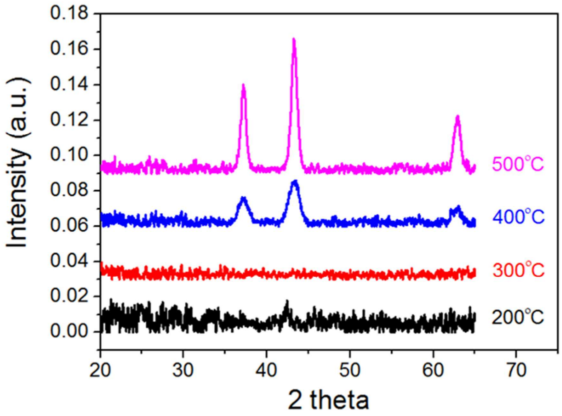

Figure 4.12 *XRD spectra of* NiO_x *film on silicon at different annealing temperatures*

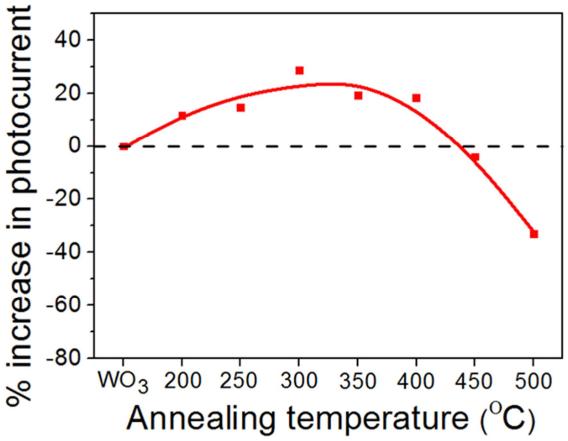

Figure 4.13 *Percentage change in photocurrent (with respect to bare* WO_3*) with cocatalyst annealing temperature for* NiO_x/WO_3 *film at 1.2 V vs Ag/AgCl in 0.1 M* Na_2SO_4 *(pH 5.8) under a light intensity of 100* mW/cm^2

As already shown in Chapter 3, electrochemical impedance spectroscopy (EIS) is a powerful technique which is able to reveal the main mechanisms occurring during electrochemical processes. In this case, EIS analysis was performed on FTO/WO_3/Co_3O_4 samples at fixed potential of 1.2 V vs Ag/AgCl under light illumination. The corresponding Nyquist plots of the bare FTO/WO_3 and the FTO/WO_3/Co_3O_4 film annealed at 350 °C are reported in Fig. 4.14 (a). For the sake of clarity, the impedance data of the other samples are not plotted, given their similarity in the trend. The equivalent circuit used for the fitting of the impedance data is displayed in Fig. 4.14.

This circuit is composed of two simplified Randles circuits in series. A detailed description of the simplified Randles circuit was given in Section 3.2.3. The resistor element R_s is related to the electric resistance due to wiring, electric connections and electrolyte. The first simplified Randles circuit models the impedance data recorded at high frequency which correspond to the small arc highlighted in Fig. 4.14 (a). The impedance data measured at low frequency (big arc) are modelled by the second simplified Randles circuit. The resistor element R_{Bulk} takes into the account the charge transfer resistance series in the bulk WO_3, which is the sum of the resistance at the FTO/WO_3 interface, resistance across the WO_3 film and resistance at the WO_3/Co_3O_4 interface. In the same way, the resulting capacitance modelled by the constant phase element CPE_{Bulk} is the sum of the capacitance at the FTO/WO_3 interface, capacitance across the WO_3 film and capacitance of the space-charge region at the WO_3/Co_3O_4 interface. The values of these two elements explicitly derive from the fitting of the high frequency arc. R_{CT} and CPE_{CT} model the charge transfer resistance and the capacitance at the Co_3O_4/electrolyte interface, respectively, with their values deriving from the fitting of the low-frequency arc. A similar electric circuit for the fitting of impedance data for WO_3 thin films was reported by Zhao *et al.*[31]

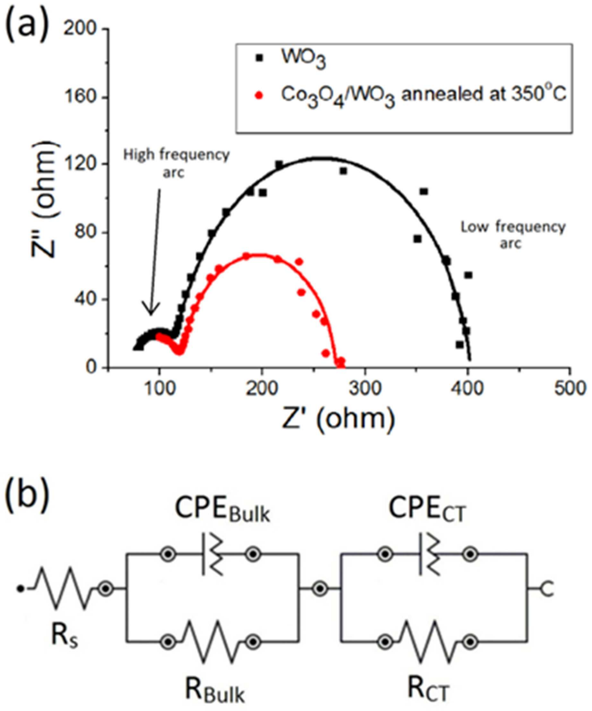

__Figure 4.14__ a) Nyquist plot of electrochemical impedance spectroscopy data for WO_3 and Co_3O_4/WO_3 film annealed at 350 °C at 1.2V vs Ag/AgCl. (b) Equivalent circuit used for modelling the electrochemical cell. All capacitances are modelled using constant phase element (CPE) to achieve a good fitting. R_{Bulk} and CPE_{Bulk} refer to the resistance and capacitance across the bulk semiconductor while R_{CT} and CPE_{CT} correspond to the charge transfer interfacial layer between the electrode and the electrolyte

The obtained values of the circuit elements for all the samples synthesised at different temperatures are reported in Tab. 4.2.

Samples	Cocatalyst annealing temperature (°C)	R_{Bulk} (Ω)	CPE_{Bulk} (μF)	R_{CT} (Ω)	CPE_{CT} (μF)
WO_3	-	49	1.10	284	55.8
Co_3O_4/WO_3	200	73	0.26	148	217
	300	52	0.28	172	138
	350	51	0.42	150	130
	400	43	0.55	139	126
	500	351	19.10	303	5.15

Table 4.2 *R_{Bulk}, CPE_{Bulk}, R_{CT}, CPE_{CT} values as obtained from electrochemical impedance spectroscopy simulation fit*

In the case of the bare FTO/WO_3 sample, R_{CT} and CPE_{CT} represent the charge transfer resistance and the capacitance at the WO_3/electrolyte interface, respectively. As displayed in Fig. 4.15, a clear correlation can be observed between the obtained circuit element values and the measured difference in photocurrent of the samples which is expressed as percentage with respect to the bare FTO/WO_3. When the Co_3O_4 cocatalyst is subject to annealing temperatures up to 400 °C, the charge transfer resistance is significantly smaller than the value obtained without cocatalyst. Smaller values of R_{CT} are associated with more efficient electron transfer at the interface between the electrolyte and the catalytic active species. The CPE_{CT} is related to the capacitance of the material at the interface, and it is a measure of the electrochemically active surface area. These values increase for samples with Co_3O_4 annealed at temperatures up to 400 °C. Overall, high CPE_{CT} and low R_{CT} values lead to an improvement in the photocurrent generation, as clearly represented in Fig. 4.15 (a) and (b). Co_3O_4 is known to possess high electrocatalytic activity for the OER, and some studies regarding the effect of its structural and morphological features on the activity were reported. It was found that crystalline size, surface area and porosity can significantly affect the resulting electrocatalytic properties. In turn, these features strongly depend on the annealing temperature and synthetic methodology. Zhou *et al.* made an investigation into the OER activity of ultrathin porous Co_3O_4 nanoplates as function of the annealing temperature.[40] They found that Co_3O_4 synthesised at low annealing temperature of 250 °C showed the highest OER activity. Interestingly, the OER activity was found to decrease with increasing annealing temperature. The high activity of the sample annealed at 250 °C was attributed to the high surface area and the presence of small crystallites (3 nm) resulting from the low annealing temperature. As suggested by the authors, small crystallites favour the exposure of more active edge and corner cobalt species with low coordination number. A similar trend was reported by Mellsop *et al.* in their work based on correlating the annealing temperature of Co_3O_4 prepared by electrodeposition on nickel substrate with the OER activity.[41] The activity was found to decrease with increasing annealing temperature. The reason of the observed trend was attributed to the decrease in surface area which is inversely proportional to the annealing temperature.

As previously discussed in Section 1.3.2, the presence of cocatalyst on top of photoanodes can shift the onset potential V_{onset} upon illumination. The onset potential is directly related to the generated photovoltage and the overpotential for the OER. From equation 1.12 it is possible to express the mathematical dependence of V_{onset} with respect to the photovoltage V_{ph} and the overpotential η:

$$V_{onset} = E_{H_2O/O_2} + \eta - V_{ph} \tag{4.5}$$

In the ideal case, the presence of the cocatalyst should minimise the overpotential and maximise the photovoltage in order to cathodically shift the onset potential for a n-type semiconductor photoanode. As reported in the LSV graph in Fig. 4.10, the FTO/WO_3/Co_3O_4 annealed at 350 °C shows the same onset potential of the bare FTO/WO_3 photoanode, whose value is located at around 0.2 V vs Ag/AgCl. Thus, it seems that the catalytic improvement of Co_3O_4 is offset by a lower photovoltage, resulting in an unchanged onset potential. The ultra-thin layer of Co_3O_4 introduces surface states at the interface with WO_3, which ultimately are responsible for the occurrence of partial Fermi-level pinning. This phenomenon arises when the presence of surface states pin the Fermi level of the semiconductor, reducing the band bending and consequently the attainable photovoltage.[42] Surface states can derive mainly from impurities, structural defects and under-coordinated elements. A notable example of Fermi-level pinning effect in photoanodes is the Fe_2O_3/MnO_x system, which was reported by Yang *et al.*[43] It was found that MnO_x cocatalyst on top of Fe_2O_3 shifted significantly the onset potential in anodic direction compared to the bare Fe_2O_3, despite the good electrocatalytic properties of MnO_x. This was due to the existence of surface states induced by MnO_x, which decreased the band bending of Fe_2O_3 and consequently the photovoltage. The hypothesis of partial Fermi-level pinning induced by Co_3O_4 is confirmed by analysing the difference between the R_{Bulk} and CPE_{Bulk} values of FTO/WO_3 and FTO/WO_3/Co_3O_4 annealed at 350 °C in Tab. 4.2. The CPE_{CT} value of the sample with the Co_3O_4 cocatalyst is smaller (0.55 µF) than that of FTO/WO_3 (1.10 µF). A smaller value of CPE_{CT} means that the majority carriers in the space-charge region are not efficiently depleted as a result of the smaller band bending induced by the presence of surface states. The values of R_{Bulk} for the two samples are similar, suggesting that the charge transport resistance is not affected by the presence of surface states brought by the presence of Co_3O_4 annealed at 350 °C. Furthermore, the ultra-thin nature of Co_3O_4 helps to minimise the charge transport resistance in the bulk of the cocatalyst, resulting in efficient electron transport across the cocatalyst nanocrystallites.

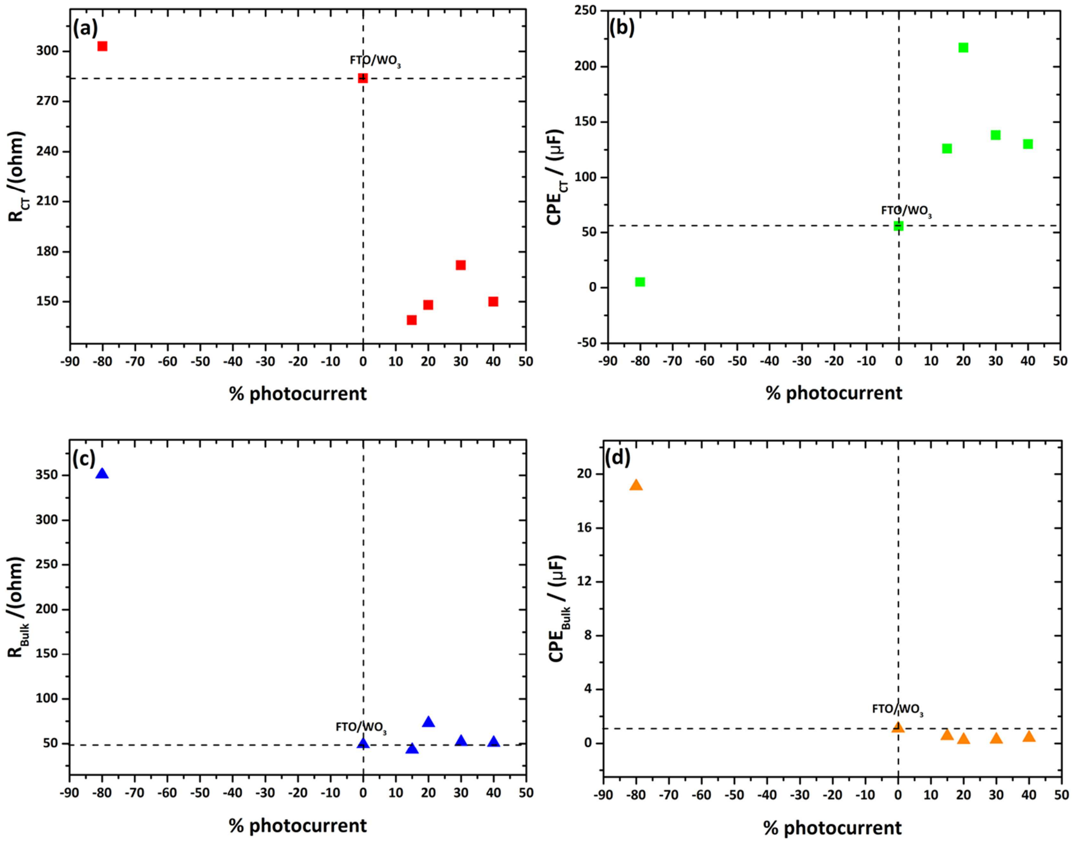

Figure 4.15 *Correlation between the circuit element values and the measured photocurrent percentage with respect to the bare FTO/WO_3 sample taken as reference; a) R_{CT}, b) CPE_{CT}, c) R_{Bulk}, d) CPE_{Bulk}*

As previously mentioned, the FTO/WO_3/Co_3O_4 annealed at 500 °C shows the worst performance in photocurrent, significantly differing from the trend observed for the other samples prepared at lower annealing temperature (≤ 400 °C). EIS data were analysed to reveal the reason of such different behaviour. Clearly, a high annealing temperature in the synthesis of Co_3O_4 favours the formation of larger crystals, which in turn are responsible for a decrease in surface area. Furthermore, the amount of highly active cobalt species located at edge and corner sites with low coordination number is decreased as a result of the more ordered structure resulting from the higher degree of crystallization of Co_3O_4. These aspects were previously described by discussing some examples in the literature related to the detrimental effect of the annealing temperature on the OER activity of Co_3O_4 electrocatalysts. Thus, it is not surprising that the FTO/WO_3/Co_3O_4 sample annealed at 500 °C shows the highest value of R_{CT} and lowest value of CPE_{CT} (Fig. 4.15 (a) and (b)).

The higher value of R_{Bulk} measured for the Co_3O_4 annealed at 500 °C indicates inefficient charge transfer between the cocatalyst and WO_3 film. Indeed, the bulk resistance increases dramatically from 43 Ω to 351 Ω when comparing cocatalysts annealed at 400 °C and 500 °C. This striking difference can be clearly visualised in Fig. 4.15(b). As previously mentioned in Section 4.2.2, crystalline Co_3O_4 is a p-type semiconductor with small documented band-gap of 0.7-1.5 eV. Thus, it is useful to estimate the band edge positions for n-WO_3 and p-Co_3O_4 in order to elucidate the overall band diagram of the formed p-n heterojunction. By following a theoretical approach reported by Butler *et al.*, the electron affinity of the semiconductor can be calculated using the following formula:[44]

$$A = \chi - 0.5E_b \tag{4.6}$$

As shown in Fig. 4.16, the electron affinity *A* represents the energetic gap between the conduction E_{cb} of a semiconductor and the reference vacuum level. Strictly speaking this term is defined as the energy obtained by moving an electron from the vacuum to the bottom of the conduction band.

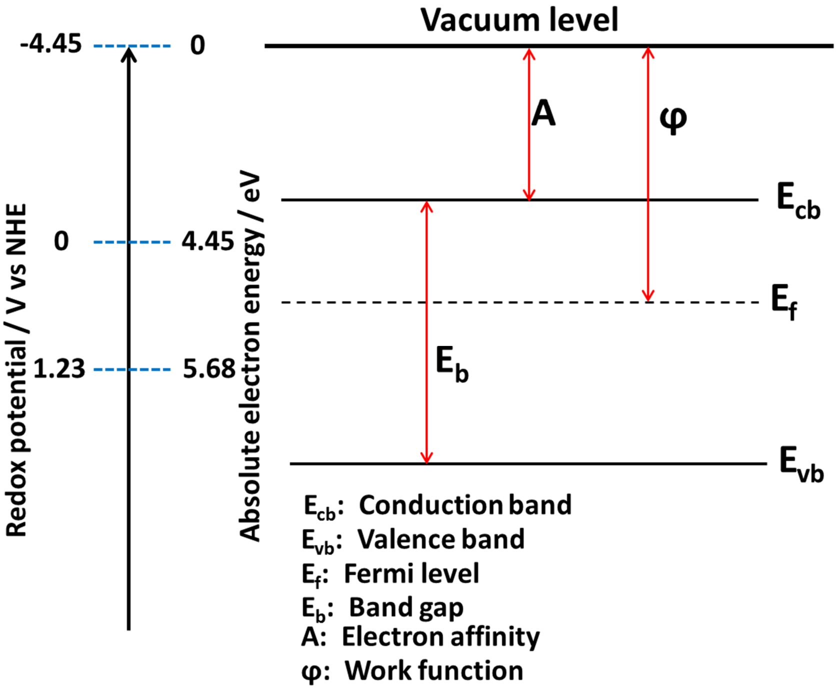

Figure 4.16 *Band diagram of a semiconductor with energy band levels. The vacuum level is taken as the zero energy reference*

χ is the semiconductor electronegativity, which is defined as the geometric mean of the electronegativity of the constituent atoms of the material. In this case, the electronegativity for WO_3 and Co_3O_4 can be expressed as:

$$\chi(WO_3) = \sqrt[1/4]{(\chi(W) \cdot \chi^3(O)} \qquad 4.7$$

$$\chi(Co_3O_4) = \sqrt[1/7]{(\chi^3(Co) \cdot \chi^4(O)} \qquad 4.8$$

The atomic electronegativity is calculated according to following formula developed by Mulliken:

$$\chi(atom) = \frac{(A_{atom}+I_{atom})}{2} \qquad 4.9$$

A_{atom} is the atomic electron affinity and I_{atom} is the atomic first ionization potential. These values are tabulated for a vast series of elements. In the equation 4.6, E_b is the band gap of the semiconductor. The resulting calculated band energy values of WO_3 and Co_3O_4 are summarised in Tab. 4.3.

Material	**E_b (eV)**	**χ (eV)**	**A (eV)**	**E_{cb} (eV)**	**E_{vb} (eV)**
WO_3	2.6	6.59	5.29	5.29	7.89
Co_3O_4	1.0	5.91	5.41	5.41	6.41

***Table 4.3** Band energy values calculated for WO_3 and Co_3O_4 (the values are referred to the absolute electronic energy scale)*

The value of the band gap for Co_3O_4 was taken from the work reported by Deori *et al*, which lies in the common range of band gap values reported in the literature for this material.[45]

The construction of the energy band diagram of the heterojunction between n-WO_3 and p-Co_3O_4 is made by following the Anderson's rule, which states that the conduction band offset between two semiconductors is simply given by the difference of their electron affinities. From the energy band diagram of the n-WO_3/p-Co_3O_4 system displayed in Fig. 4.17 it can be seen that Co_3O_4 forms an unfavourable Type I heterojunction with WO_3. In particular, the lower position of the Co_3O_4 conduction band effectively blocks the transfer of to the WO_3 film, resulting in a dramatic increase in charge recombination at the interface. This phenomenon explains the origin of the high bulk resistance observed in the case of the Co_3O_4 cocatalyst annealed at 500 °C. Furthermore, the high value of bulk capacitance (CPE_{Bulk}) observed for this sample (Tab. 4.2) is the result of the accumulation of negative charges at the interface due to the impossibility for the electrons to cross the junction. This, in turn, further increases the band banding of WO_3 with strong depletion of electrons in the space-charge region, leading to an increase of the capacitance at the interface. It is critically important to note that this type of band transport between two semiconductors can be possible only in the case of materials with high crystallinity which possess well-defined energy bands. For amorphous or poorly-crystallised materials with high number of defects the charge transport is typically described by a variable-range hopping model.[49] The presence of defects in highly disordered structures creates localised stated which are able to pin the Fermi level, as previously observed for the samples containing Co_3O_4 fabricated using low annealing temperatures (≤ 400 °C). As a result, the charge transport in the presence of poorly crystallised Co_3O_4 cocatalysts is significantly less affected by the unfavourable band alignment. In contrast, the charge transport in the case of less defective and highly crystalline Co_3O_4 proceeds through a pure band transport mechanism. Hence, the origin of the extremely poor photocatalytic of the Co_3O_4 cocatalyst annealed at 500 °C can be summarised in the following four points:

1. Low surface area
2. Larger crystal size
3. More ordered structure with low exposure of highly active uncoordinated cobalt species
4. Unfavourable band alignment with the WO_3 photoanode

It should be noted that these four points are strongly interconnected, since the morphological and structural properties directly influence the modality of charge transfer in the cocatalyst.

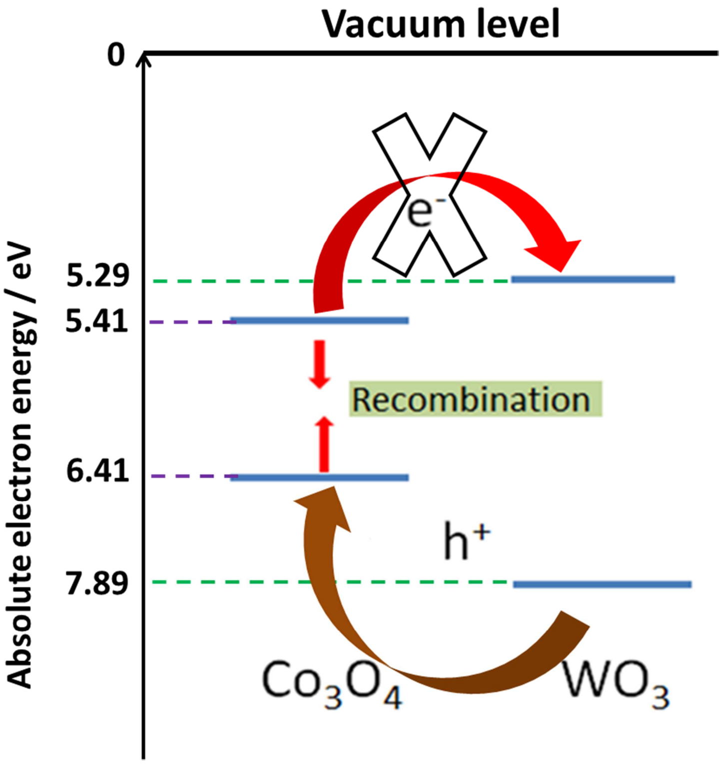

***Figure 4.17** Energy band diagram of the n-WO_3/p-Co_3O_4 heterojunction*

The bare FTO/WO_3 and the most active FTO/WO_3/Co_3O_4 photoelectrodes (Co_3O_4, 1 layer, 350 °C) were subject to gas evolution measurement in a 2-electrode cell using Pt foil as counter electrode under simulated solar illumination. As displayed in Fig. 4.18, a linear gas evolution curve for both H_2 (a,b) and O_2 (c,d) was observed as function of reaction time.

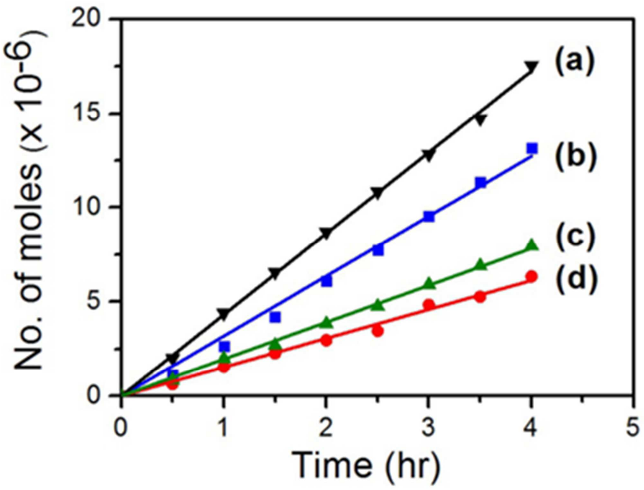

Figure 4.18 *Hydrogen evolution under light illumination of (a) Co_3O_4/WO_3 and (b) WO_3; Oxygen evolution under light illumination of (c) Co_3O_4/WO_3 and (d) WO_3. The gases were measured by in-line GC*

From the gradient of the gas evolution curve, bare FTO/WO_3 film shows a H_2 evolution rate of 3.2 µmol/h and an O_2 evolution rate of 1.5 µmol/h. This corresponds to a H_2:O_2 ratio of 2.13 which is close to the stoichiometry ratio of water splitting (H_2:O_2 = 2). In the case of FTO/WO_3/Co_3O_4, a high H_2 and O_2 evolution rates of 4.3 µmol/h and 1.9 µmol/h are measured, corresponding to a stoichiometric H_2:O_2 ratio of 2.26. This observed discrepancy in both samples with respect to the theoretical stoichiometric ratio could originate from systematic errors occurring during the measurement. In any case, the higher H_2 and O_2 evolution rate measured for the FTO/WO_3/Co_3O_4 sample further confirms its superior photocatalytic activity.

4.3 Conclusions

In this work, the effect of the presence of Co_3O_4 cocatalyst on the PEC performance of WO_3 thin film was investigated. Crystalline WO_3 thin films supported on conductive FTO/glass were first prepared using a sol-gel spin coating process, with a final annealing of 500 °C. Then, ultra-thin layer of Co_3O_4 cocatalyst was deposited by sol-gel spin coating on top of the preformed WO_3. In particular, different FTO/WO_3/Co_3O_4 materials were prepared by varying the final annealing temperature used for the formation of Co_3O_4 in order to investigate the effect of this parameter on the PEC activity. Given the intrinsic difficulty of bulk techniques such as XRD and EDX to detect extremely small amount of compounds, the successful presence of the thin layer of Co_3O_4 on top of WO_3 was confirmed by XPS. By analysis the XRD pattern of thick Co_3O_4 films deposited on silicon it was found that low annealing temperatures favoured the formation of poorly crystalline Co_3O_4 structures with small crystal size. On the other hand, annealing temperature of 500 °C sensibly increased the crystallinity of the material, with the evidence of bigger crystal size as measured by the Scherrer's equation. The PEC activity toward the oxygen evolution reaction of the synthesised samples was probed under simulated solar light in 0.1 M Na_2SO_4 electrolyte. It was found that the presence of Co_3O_4 annealed at temperatures up to 400 °C significantly improved the photocurrent generation compared to the bare WO_3. The most active FTO/WO_3/Co_3O_4 annealed at 350 °C showed an improvement in photocurrent of 40% compared to the bare WO_3. However, the PEC activity of the Co_3O_4 cocatalyst annealed at 500 °C showed a considerable decline in photocurrent generation, with a decrease of 80% with respect to the reference WO_3 film. EIS measurements were performed in order to understand the origin of such different behaviour in the PEC activity as a function of the cocatalyst annealing temperature. It was demonstrated that the poorly crystalline and highly disordered nature of Co_3O_4 annealed at low temperature positively affects the PEC activity, because it favours the formation of large surface area and more exposure of active cobalt sites with low-coordination number. Furthermore, the type of charge transport occurring between WO_3 and the poorly crystalline cocatalyst was attributed to a variable-range hopping mechanism. It was also explained that the presence of localised stated due to the disordered structure of the poorly crystalline Co_3O_4 induced Fermi-level pinning, reducing the photovoltage of the WO_3 photoabsorber. However the decrease in photovoltage was offset by a lower kinetic overpotential required to drive the OER. This in turn explained the absence of any shift of the onset potential.

In contrast, the high crystallinity of the Co_3O_4 cocatalyst synthesised at 500 °C was found to be directly responsible for the dramatic decrease in photocurrent. In particular, the more ordered structure allowed a different typology of charge transport between cocatalyst and WO_3 based on band transport mechanism. Theoretical calculations showed that WO_3 and Co_3O_4 formed an energetically-unfavourable band alignment, resulting in high charge recombination at the interface. This hypothesis was experimentally supported by the large values of bulk resistance and bulk capacitance measured by EIS analysis. Furthermore, as confirmed in previous studies reported in the literature, the intrinsic OER electrocatalytic activity of Co_3O_4 decreases with increasing annealing temperature, as a result of lower surface area and less exposure of highly active cobalt sites due to structural defects. Thus, the combined effect of poor intrinsic catalytic activity and unfavourable electronic transport of the highly crystalline Co_3O_4 in combination with WO_3 were the main causes of the poor PEC performance of this sample. These fundamental results want to help to understand the complex existing relations between photoabsorber and cocatalysts, giving some guidelines for an appropriate fabrication of novel and efficient photoelectrodes for the PEC water splitting.

4.4 References

1. N. S. Lewis and D. G. Nocera, Proc. Natl. Acad. Sci. U. S. A., 2006, 103, 15729-15735.
2. M. G. Walter, E. L. Warren, J. R. McKone, S. W. Boettcher, Q. Mi, E. A. Santori and N. S. Lewis, Chem. Rev., 2010, 110, 6446-6473.
3. H. Dau, C. Limberg, T. Reier, M. Risch, S. Roggan and P. Strasser, ChemCatChem,
4. Z. Hu, J. C. Yu, T. Ming and J. Wang, *Appl. Catal. B Environ.*, 2015, **168**–**169**, 483–489.
5. S. D. Tilley, M. Cornuz, K. Sivula and M. Graetzel, *Angew. Chemie - Int. Ed.*, 2010, **49**, 6405–6408.
6. T. W. Kim and K.-S. K.-S. Choi, *Science (80-.).*, 2014, **343**, 990–994.
7. X. Liu, F. Wang and Q. Wang, *Phys. Chem. Chem. Phys.*, 2012, **14**, 7894–7911.
8. J. E. Yourey and B. M. Bartlett, *J. Mater. Chem.*, 2011, **21**, 7651.
9. R. Abe, M. Higashi and K. Domen, ChemSusChem, 2011, 4, 228-237.
10. S. J. Hong, S. Lee, J. S. Jang and J. S. Lee, Energy Environ. Sci., 2011, 4, 1781-1787.
11. J. Kim, C. W. Lee and W. Choi, Environ. Sci. Technol., 2010, 44, 6849-6854.
12. G. W. Ho, K. J. Chua and D. R. Siow, *Chem. Eng. J.*, 2012, **181**–**182**, 661–666.
13. V. Chakrapani, J. Thangala and M. K. Sunkara, *Int. J. Hydrogen Energy*, 2009, **34**, 9050–9059.
14. L. Meda, G. Tozzola, A. Tacca, G. Marra, S. Caramori, V. Cristino and C. Alberto Bignozzi, *Sol. Energy Mater. Sol. Cells*, 2010, **94**, 788–796.
15. R. Liu, Y. Lin, L. Y. Chou, S. W. Sheehan, W. He, F. Zhang, H. J. M. Hou and D. Wang, *Angew. Chemie - Int. Ed.*, 2011, **50**, 499–502.
16. V. S. Vidyarthi, M. Hofmann, A. Savan, K. Sliozberg, D. K??nig, R. Beranek, W. Schuhmann and A. Ludwig, *Int. J. Hydrogen Energy*, 2011, **36**, 4724–4731.
17. V. Cristino, S. Caramori, R. Argazzi, L. Meda, G. L. Marra and C. A. Bignozzi, *Langmuir*, 2011, **27**, 7276–7284.
18. F. Amano, M. Tian, G. Wu, B. Ohtani and A. Chen, *ACS Appl. Mater. Interfaces*, 2011, **3**, 4047–52.
19. J. Hill and K. Choi, *J. Phys. Chem. C*, 2012, **116**, 7612–7620.
20. J. M. Spurgeon, J. M. Velazquez and M. T. McDowell, *Phys. Chem. Chem. Phys.*, 2014, **16**, 3623–31.
21. Q. Liu, Q. Chen, J. Bai, J. Li, J. Li and B. Zhou, *J. Solid State Electrochem.*, 2014, **18**, 157–161.
22. W. L. Kwong, C. C. Lee and J. Messinger, *J. Phys. Chem. C*, 2016, **3**, acs.jpcc.6b02432.
23. W. Cheng, E. Baudrin, B. Dunn and J. I. Zink, *J. Mater. Chem.*, 2001, **11**, 92-97.
24. D. P. Debecker and P. U. Mutin, *Chem. Soc. Rev.,* 2012, **41**, 3624-3650.

25. L. M. Bertus, C. Faure, A. Danine, C. Labrugere, G. Campet, A. Rougier and A. Duta, *Materials Chemistry and Physics*, 2013, **140**, 49-59.
26. Y. Fang, X. Sun and H. Cao, *J. Sol-Gel Sci Technol*, 2011, **59**, 145-152.
27. A. Y. Oral, E. Mensur, M. H. Aslan and E. Basaran, *Materials Chemistry and Physics*, 2004, **83**, 140-144.
28. M. A. Chougule, S. G. Pawar, P. R. Godse, R. D. Sakhare, S. Sen and V. B. Patil, *J. Mater Sci: Mater Electron*, 2012, **23**, 772-778.
29. H. S. Jeon, M. S. Jee, H. Kim, S. J. Ahn, Y. J. Hwang and B. K. Min, *ACS Appl. Mater. Interfaces*, 2015, **7**, 24550-24555.
30. C. R. Lhermitte, G. J. Verwer and B. M. Bartlett, *J. Mater. Chem. A*, 2016, **4**, 2960-2968
31. S. S. Kalanur, Y. J. Hwang, S. Y. Chae and O. S. Joo, *J. Mater. Chem. A*, 2013, **1**, 3479-3488.
32. A. Gulino, P. Dapporto, P. Rossi and I. Fragala', *Chem. Mater.*, 2003, **15**, 3748-3752.
33. L. Qiao, H. Y. Xiao, H. M. Meyer, J. N. Sun, C. M. Rouleau, A. A. Puretzky, D. B. Geohegan, I. N. Ivanov, M. Yoon, W. J. Weber and M. D. Biegalski, *J. Mater. Chem. C*, 2013, **1**, 4628-4633.
34. M. Farhadian, P. Sangpour and G. Hosseinzadeh, *RSC Adv.*, 2016, **6**, 39063-39073.
35. K. Ding, D. Wang, P. Yang, P. Hou and X. Cheng, *RSC Adv.*, 2016, **6**, 16208-16214.
36. K. M. Nam, E. A. Cheon, W. J. Shin and A. J. Bard, *Langmuir*, 2015, **31**, 10897-10903
37. J. Zhao, E. Olide and F. E. Osterloh, *Journal of the Electrochemical Society*, 2015, **162**, H65-H71.
38. A. Memar, C. M. Phan and M. O. Tade, *Int. J. Hydrogen Energy*, 2015, **40**, 8642–8649.
39. P. J. Barczuk, A. Krolikowska, A. Lewera, K. Miecznikowski, R. Solarska and J. Augustynki, *Electrochimica Acta*, 2013, **104**, 282-288.
40. X. Zhou, Z, Xia, Z. Tian, Y. Ma and Y. Qu, *J. Mater. Chem. A*, 2015, **3**, 8107-8114.
41. S. R. Mellsop, A. Gardiner and A. T. Marshall, *Electrocatalysis*, 2014, **5**, 445-455.
42. A. J. Bard, A. B. Bocarsly, F. Ren, F. Fan, E. G. Walton and M. S. Wrighton, *J. Am. Chem. Soc.*, 1980, **102**, 3671-3677.
43. X. Yang, C. Du, R. Liu, J. Xie and D. Wang, *Journal of Catalysis*, 2013, **304**, 86-91.
44. M. A. Butler and D. S. Ginley, *J. Electrochem. Soc.*, 1978, **25**, 228-231.
45. K. Deori and S. Deka, *CrystEngComm*, 2013, **15**, 8465-8474.
46. Q. Hao, D. Zhao, H. Duan and C. Xu, *ChemSusChem*, 2015, **8**, 1435-1441.
47. L. Lv, Y. Su, X. Liu, H. Zheng and X. Wang, J ALLOY COMPD, 2013, **553**, 163-166.
48. Y. Feng, L. Li, S. Niu, Y. Qu, Q. Zhang, Y. Li, W. Zhao, H. Li and J. Shi, *Appl. Catal. B*, 2012, **111**, 461-466.
49. M. Grünewald and P. Thomas, *Phys. Status Solidi B*, 1979, **94**, 125-133.

4.5 Appendix

4.5.1 Experimental methods

4.5.1.1 Synthesis of WO_3 sol-gel precursor solution

The deposition of WO_3 thin film was carried out by spin-coating WO_3 sol-gel precursor solution onto fluorine-doped tin oxide (FTO) coated glass. The WO_3 precursor solution was prepared by first adding 0.4 ml of acetylacetone into 5 ml of methanol, after which the solution mixture was slowly added into 0.5 g of WCl_6 (Sigma Aldrich) before undergoing further dilution with 5 ml of methanol (0.13 M). 0.25 g of poly(ethylene glycol) (Sigma Aldrich, average molecular weight of 200) was then added to the solution to improve the film quality during spin-coating. The solution was allowed to age under constant stirring for 4 days before use. All of the above steps were carried out inside a nitrogen-filled glovebox.

4.5.1.2 Thin film deposition

Prior to the spin-coating process, the substrates were cleaned by sonication in ethanol for 5 minutes followed by oxygen plasma treatment with Trion Sirus reactive ion etcher at 100 W for 2 minutes. The sol-gel solution was pre-filtered with a 0.45 µm PVDF Whatman syringe filter, and then spin-coated onto the substrate at 2000 rpm for 30 seconds. After each spin-coating cycle, the substrates were annealed at 300 °C for 2 minutes to convert the organic layer into oxide. The process was repeated for 20 cycles to obtain a WO_3 film with a final thickness of about 1.4 µm. To obtain crystalline WO_3 film, the substrates were subjected to a final annealing step at 500 °C for 1 hour. Co_3O_4 was deposited on WO_3 through sol-gel spin-coating. Its precursor solution is prepared by mixing 0.05 g of cobalt(II) acetylacetonate (0.02 M) into 10 ml of methanol with 0.1 ml of ethanolamine as a stabilizer. The precursor solution is stirred overnight before spin-coating onto the WO_3 film using the same spin parameters as that for WO_3. The cocatalyst solution was spin-coated for 1 cycle followed by annealing on a hotplate for 15 minutes. For comparison purposes, WO_3 samples loaded with NiO_x cocatalysts were also prepared; the NiO_x was deposited from a nickel acetate precursor solution of similar concentration (0.02 M).

4.5.1.3 Structural characterisation

X-ray diffraction (XRD) spectra of the deposited films were analysed using Bruker D8 general area detector diffraction system (GADDS). Film morphology was characterized using ESM-9000 field-emission scanning electron microscope (FE-SEM). X-ray photoelectron spectroscopy (XPS) was carried out with VG Thermo ESCALab 220i-XL X-ray photoelectron spectrometer using monochromatic Al Kα (1486.6 eV) as the X-ray source. The binding energies were charge corrected using adventitious C 1s peak at 285.0 eV as a reference. UV-Vis absorbance studies were carried out using Shimadzu 3101 UV-VIS-NIR spectrophotometer.

4.5.1.4 PEC measurement

Photoelectrochemical (PEC) measurements were carried out in a 3-electrode configuration using Ag/AgCl reference electrode, Pt counter electrode and the cocatalyst/WO_3 film coated on FTO glass as the working electrode. A black tape was used to define the active area of 1 cm2 on the coated sample. The electrodes were immersed inside a 0.1 M Na_2SO_4 aqueous electrolyte solution, with a pH of 5.84 as measured by a Hanna Instruments pH meter. The PEC measurement was carried out using Metrohm Autolab PGSTAT101 potentiostat. The light source used was an Oriel solar simulator using a 150 W Xenon arc lamp fitted with an AM 1.5 filter, with light intensity maintained at 100 $mWcm^{-2}$. Using Metrohm Autolab PGSTAT302N potentiostat, electrochemical impedance spectroscopy (EIS) data was collected with an amplitude setting of 10 mV and frequency varying from 0.1 to 100,000 Hz. The electrolyte used is 0.1 M Na_2SO_4 solution and at a potential of 1.2 V vs Ag/AgCl.

Chapter 5: Design of active and durable self-standing Pt-CeO_2-NiO-Ni foam electrocatalyst for the alkaline methanol oxidation

Acknowledgments

The following acknowledgements recognise the contributed work of colleagues and collaborators to the presented content of this Chapter.

Coryl Jing Jun Lee: For collection of SEM data (Institute of Materials Research and Engineering, Singapore)

Lay Ting Ong: For collection of XPS data (Institute of Materials Research and Engineering, Singapore)

Dr Gillian Collins: For helpful discussions and collection of TEM data (University College Cork, Ireland)

5.1 Role of metal oxide support in the catalytic activity of Pt-based electrocatalysts for the methanol oxidation reaction

Direct methanol fuel cells (DMFCs) hold great promise as a valid alternative to batteries and accumulators for portable energy supply, because of their high energy density and long operating times before refuelling.[1] A chomprensive overview of the current technolgical state-of-the art of DMFCs was given is Section 1.2.3. Despite the significant technological progress achieved in the development of efficient DMFCs, different factors still severely limit their widespread commercialization, which can be substantially identified in the high cost of electrocatalysts based mainly on platinum (Pt), poor activity and durability of the anode catalyst where the methanol oxidation occurs, and the lack of stable and cheap ion exchange membranes.[2–4] Direct methanol alkaline fuel cells (DMAFCs) could potentially overcome the first two limitations, considering that the anodic methanol oxidation reaction (MOR) and the cathodic oxygen reduction reaction (ORR) are intrinsically more facile in alkaline environment compared to the acidic counterpart.[5] This can lead to a lower Pt loading which can be further minimized by nanostructuring, with a dramatic reduction of the associated cost.[6]

As reported in Section 1.3.3, Pt is regarded as the most active catalyst for the MOR in both acidic and alkaline media. However the stability of the Pt remains an unsolved issue, although to a lesser extent than the conventional acid DMFCs. During the MOR, the Pt active sites are poisoned by surface-adsorbed carbonaceous species such as CO, leading to quick loss of activity. One common adopted strategy to ameliorate the problem is the fine tuning of the electronic state of the metal surface through the alloying of Pt with a series of oxophilic metals such as Ru,[7] Si,[8] Sn,[9] which promote the selective adsorption of OH_{ads} adspecies in close proximity to the atomic Pt active sites. These OH_{ads} adspecies then react with the poisoning CO bonded onto Pt through a Langmuir-Hinshelwood mechanism, with a complete regeneration of the site. Another common way is to directly weaken the Pt-CO bond through the alloying with Au, where Au atoms act as surface electronic modifiers.[10]

Notwithstanding the evident improvements of these systems, especially in terms of activity, only marginal gains in durability have been achieved. Apart from the aforesaid CO poisoning issue, this is also due to the dramatic agglomeration of the NPs occurring during the reaction, which can be linked to a lack of strong interaction to the support, with carbon black being the most widely used.[11] In this regard metal oxides represent a promising alternative as supports for Pt NPs, offering two main advantages: 1) strong interaction with NPs, preventing their agglomeration;[12] 2) they can promote the adsorption of OH_{ads}, facilitating the CO removal from the Pt active sites.[2,5,11] Indeed, several metal oxides such as TiO_2, SnO_2, CeO_2, NiO and $Ni(OH)_2$ have received considerable attention as supports for Pt NPs in DMFCs, showing impressive results in terms of activity and long-term durability. For instance, Li *et al.* tested the MOR activity in acidic medium of Pt NPs supported on Sn-doped TiO_2 modified carbon.[13] Characterisation analysis gave evidence of the formation of well-dispersed small Pt NPs with size of 3 nm mainly deposited on the boundaries of the support. The high MOR activity of this material was attributed to the high electrochemically active surface area derived from the good utilisation of the Pt active sites. The authors also suggested that the oxophilic nature of the Sn-doped TiO_2 support provided OH species which were found to promote the CO removal and improve the stability. Another interesting work regarding the understanding of the effect of metal oxide support on the MOR activity of Pt NPs active sites was reported by Lin *et al.*[47] In this case SnO_2 combined with carbon nanotubes (CNTs) was used as metal oxide support for the preparation of Pt NPs with size of 5-6 nm. The superior MOR activity in acidic electrolyte showed by Pt/SnO_2/CNT compared to the Pt/CNT control experiment was due to the presence of SnO_2 which provided larger amount of OH species needed for the CO removal. Also, SnO_2 was found to promote uniform dispersion of the deposited Pt NPs. Amin *et al.* investigated the effect of NiO/C as support for the deposition of Pt NPs on the catalytic performance for the MOR in acidic electrolyte.[15] TEM analysis showed the formation of Pt NPs with size of 4-5 nm bonded on NiO. The MOR activity of this electrocatalyts was found to be higher compared to the control experiment Pt/C. This was due to the smaller Pt NPs induced by the presence of NiO, which resulted to a higher dispersion of the active sites with better mass utilisation. Furthermore, NiO played an active role in the CO oxidative removal step, by providing OH species to the adjacent Pt site through a Langmuir-Hinshelwood mechanism as previously described. Recently, Huang *et al.* designed a novel Pt-$Ni(OH)_2$-graphene composite material with extremely high activity toward the MOR in alkaline media.[2] TEM analysis revealed the formation of ultra-small Pt NPs of 2 nm strongly anchored to the highly defective and poorly-crystalline $Ni(OH)_2$ support. The disordered and defective nature of $Ni(OH)_2$ was found to play a key role in the MOR for two main reasons: first, a disordered structure provides a larger surface area which is a key requirement to obtain a good dispersion of Pt NPs, preventing agglomeration; second, crystallographic defects greatly expedite water dissociation, resulting in the formation of more OH species which actively participate in the CO oxidative removal on the Pt active sites. The role of graphene was to increase the electronic conductivity of the material and to suppress the aggregation of supported Pt and $Ni(OH)_2$. The design and catalytic investigation toward the MOR in alkaline medium of Pt NPs supported on CeO_2 was reported by Xu *et al.*[14] In particular, a direct comparison in terms of catalytic activity was made between Pt/CeO_2/C and Pt/C materials, in order to understand the potential beneficial role of CeO_2 on the overall performance. It was found that the presence of an optimum amount of CeO_2 significantly improved the catalytic activity. The authors suggested that CeO_2 could provide oxygenated species which increased the rate of CO removal, although they did not provide enough experimental evidence to confirm this hypothesis.

In this regard, an extensive study focused on elucidating the beneficial effect of CeO_2 was reported by Ou *et al.*[17] A detailed characterisation analysis based on high-resolution electron microscopy was performed in order to observe the microstructural interaction occurring at atomic level between Pt and CeO_2. The results gave evidence of an existing strong interaction, which could be responsible for the improved electrocatalytic performance of the Pt/CeO_2 composite material. It was suggested that OH groups generated by CeO_2 at the interface could react with CO adsorbed on Pt NPs. Recently Katayama *et al.* investigated the role of CeO_2 during the alkaline methanol oxidation, concluding that its high oxophilic nature promotes the adsorption of OH species and accelerates the removal of carbonaceous species bonded onto the Pt active sites.[5]

In general the principal drawback of metal oxides and particularly of CeO_2 is represented by their poor electronic conductivity, which can be partially overcome by metal doping or physical mixing with the more conductive carbon, as previously. Metal doping has been especially investigated for TiO_2 supports in order to increase its conductivity. Sim *et al.* reported the design of Pt supported on Nb-doped TiO_2 electrocatalyst for the methanol oxidation reaction in acidic media.[18] It is known that Nb doping can significantly improve the electronic conductivity of TiO_2 under specific synthetic conditions. The material showed good activity mainly as a result of the better electron transfer between Pt and metal oxide support. In contrast, CeO_2 doping as method to improve the electronic conduction has not been reported in the fabrication of MOR electrocatalysts.

Another important strategy is nanostructuring, where the morphology can be finely tuned in order to increase the surface area and the electron transfer between the liquid/solid interface and the current collector. For example, Saha *et al.* showed that SnO_2 nanowires directly grown on carbon paper offered a much larger surface area for the deposition of Pt-Ru NPs, resulting in higher mass loading and catalytic activity toward the MOR.[19] Menendez *et al.* investigated the MOR activity in alkaline media of Pt NPs supported on CeO_2 nanorods.[25] The high surface area offered by the nanostructured metal oxide support significantly increased the supply of OH groups for the CO oxidative removal from the Pt active sites, positively affecting the overall catalytic performance. A direct comparison between the catalytic properties of Pt/TiO_2 and Pt/TiO_2 nanotubes was investigated by Abida *et al.*, leading to interesting results.[48] It was found that Pt/TiO_2 nanotube catalyst could oxidise more efficiently the poisononing CO adsorbed on Pt compared to the non-structured TiO_2 support. Similarly to the case of CeO_2 nanorods, the nanostructured TiO_2 provided a larger number of OH groups which ultimately led to improved CO removal. Also, as pointed out by Wu *et al.*, a large surface area is a key requirement for attaining a uniform dispersion of Pt NPs, preventing possible agglomeration during the reaction.[6]

Ni foam can be regarded as potential ideal support, considering its high surface area and electronic conductivity. Despite these favourable characteristics, only a handful of works related to its utilisation as support have been published in the literature. Skowronski *et al.* deposited Pt NPs on Ni foam and investigated its catalytic activity toward MOR in alkaline electrolyte.[49] They found that the bare Ni foam showed a decent degree of activity which was mainly due to its ability to form the active NiOOH species on the surface upon anodic scan. However, its performance was still much lower when compared to the sample containing Pt NPs. It was suggested that Pt-Ni and Pt-NiOOH interactions could play an important role in increasing the activity and stability of the catalyst. Even in this case, Ni species acted as OH donors to the adjacent Pt sites.

5.1.1 Objectives

The objectives of this chapter are schematically summarised in the following points:

1. To synthesise a self-standing 3D electrode based on Pt nanoparticles supported onto nanocrystalline CeO_2 and NiO using a facile hydrothermal method
2. To investigate the structural and morphological properties of the material
3. To test the catalytic activity and stability of the material toward the alkaline methanol oxidation reaction
4. To investigate the main mechanism of reaction and elucidate the nature of active sites
5. To establish structure-property relation

5.2 Results and Discussion

5.2.1 Analysis of the synthetic steps for the fabrication of Pt-CeO_2-NiO-Ni foam electrocatalyst

The first two steps for the fabrication of the ternary Pt-CeO_2-Ni foam were the hydrothermal synthesis of the CeO_2 precursor directly onto the Ni foam, and the subsequent calcination for the generation of nanocrystalline CeO_2 particles. Hydrothermal process for the synthesis of metal oxide nanostructures has received considerable attention over the last 15 years, with an annual number of publications containing the keywords “hydrothermal” and “nano” of more than 5000 in 2011.[50] This method is based on the crystal growth through chemical reactions which are conducted in aqueous solution under high temperature and pressure. Normally, these reactions are carried out at temperatures which are above the normal boiling point of water (100 °C), therefore special steel-autoclaves fitted with highly resistant Teflon liners are used to stand the generated high vapour pressure. The hydrothermal growth of CeO_2 on Ni foam was performed with $Ce(NO)_3$ and urea as metal precursor and precipitating agent, respectively, in water at 120 °C. This synthetic methodology was inspired by previous works reporting the hydrothermal synthesis of CeO_2 nanostructures. As reported by Hirano *et al.* the main reaction mechanism occurring the formation of CeO_2 under these conditions can be summarised below:[51]

$$CO(NH_2)_2 + 2H_2O \rightarrow CO_3^{2-} + 2NH_4^+ \qquad 5.1$$

$$2[Ce(H_2O)_n]^{2+} + 3CO_3^{2-} \rightarrow Ce_2O(CO_3)_2 \cdot H_2O + CO_2 + (n-1)H_2O \qquad 5.2$$

Urea starts to decompose in water at 80 °C, releasing carbonate (CO_3^{2-}) and ammonium (NH_4^+) ions in solution (equation 5.1).[52] At the operating reaction temperature (120 °C), the hydrated Ce^{3+} ions can react with CO_3^{2-}, forming the orthorhombic cerium carbonate $Ce_2O(CO_3)_2 \cdot H_2O$, as shown in equation 5.2. Ni foam was placed inside the reaction mixture, with the aim to directly grow the cerium carbonate particles on top of its surface area. This approach has been used for the fabrication of different composite materials, such as Co_3O_4/Ni foam,[53] $NiCo_2O_4$/Ni foam[54] and NiO/Ni foam.[55] After the hydrothermal synthesis, the material was thoroughly washed in order to remove unreacted chemical precursors and particles loosely bonded on the surface of Ni foam. Then a calcination step in static air was performed at 350 °C and 500 °C to convert the cerium carbonate into cerium oxide CeO_2. According to the same above-mentioned work reported by Hirano *et al.*, cerium carbonate is converted into nanocrystalline CeO_2 with high surface area at 300 °C. As normally expected, a linear decrease in surface area was observed with increasing annealing temperature.

After the calcination step, ultra-small Pt NPs were formed directly on the surface of the composite support by hydrothermal method. In this case H_2PtCl_6 and poly(vinyl pyrrolidone) (PVP) were dissolved in water and the reaction was performed in autoclave at 160 °C. This synthetic methodology was inspired by a recent work reporting the generation of ultra-small Pt NPs by a simple hydrothermal process.[20] During the reaction, the OH-terminated PVP polymer can have a dual function of reducing and stabilising agent, first transforming Pt^{4+} ions into metallic Pt^0 and then stabilising the obtained cluster in order to prevent further growth of the NP.

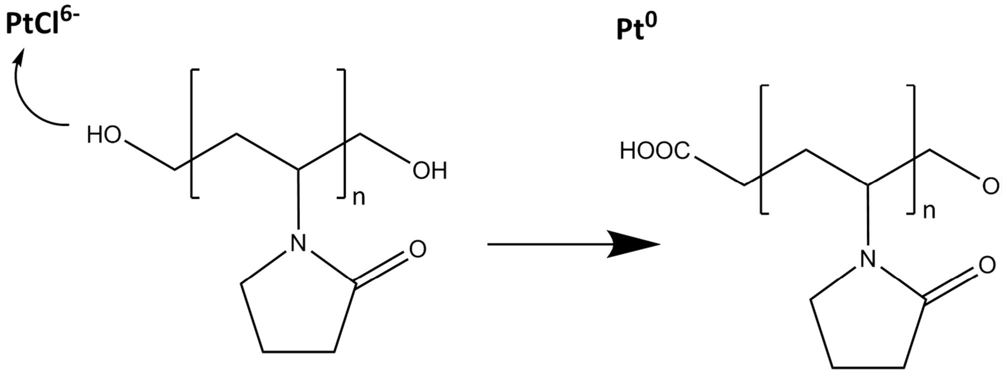

Figure 5.1 *Scheme of the reaction mechanism occurring during the reduction of Pt^{4+} due to the OH-terminated group of PVP*

As shown in Fig. 5.1, the terminal OH group is oxidised to carboxylic COOH group. It is known that alcohols can reduce noble metal ions with the formation of nanoparticles.[57] It is also known that the reducing power of an alcohol decrease with increasing alkyl chain length. In order to synthesise ultra-small NPs with narrow size range it is desirable to use mild reactants which favour a slow nucleation. As such, long chain alcohols like ethylene glycol are normally employed as mild reductants. The reducing properties of PVP were only realised in 2006, when Xiong *et al.* reported the synthesis of noble metal nanoplates in aqueous solution using this method.[56] Till then, PVP was only used as steric stabiliser or capping agent. The main advantage of PVP is represented by its dual functional role as mild reductant and stabiliser, which are two fundamental requirements for the generation of ultra-small NPs with well-defined morphology and narrow size range.

Pt-Ni foam binary electrode was synthesised as control sample in order to investigate the effect of CeO_2 on the structural and electrocatalytic properties of the electrocatalysts. Unless otherwise stated, the samples will be referred to as Pt-CeO_2(350)/NiF, Pt-CeO_2(500)/NiF and Pt-NiF.

5.2.2 Structural and morphological characterisation

As seen in Fig. 5.2, the XRD patterns of Pt-CeO_2(350)/NiF and Pt-CeO_2(500)/NiF show the presence of distinctive peaks indexed to the (111), (200), (220) and (311) planes of the cubic fluorite CeO_2 (JCPDS no. 34-0394). Interestingly, prominent diffraction peaks attributed to the cubic NiO (JCPDS no. 71-1179) can be found in the Pt-CeO_2(500)/NiF. Peaks belonging to NiO are also detected in the Pt-CeO_2(350)/NiF, although with a significant lower magnitude. In contrast, no NiO peaks can be found in the control sample Pt/NiF. According to the work of Ni *et al.*, Ni foam is prone to electrochemical corrosion in water under hydrothermal conditions, with the formation of $Ni(OH)_2$ nanostructures directly onto the foam itself.[21]

$$Ni + nH_2O \rightarrow [Ni(H_2O)_n]^{2+} + 2e^- \tag*{5.3}$$

$$O_2 + 2H_2O + 4e^- \rightarrow 4OH^- \tag*{5.4}$$

$$[Ni(H_2O)_n]^{2+}\ 2OH^- \rightarrow Ni(OH)_2 + nH_2O \tag*{5.5}$$

Thus, it is highly likely that the same phenomenon occurred in this case, leading to the formation of a superficial biphasic NiO-CeO_2 nanostructure, with a specific degree of crystallinity depending on the calcination temperature. The successful formation of the cubic Pt NPs (JCPDS no. 01-1194) is confirmed through the identification of its main diffraction peak indexed to the (111) plane located at 40.2°, which is present for all the synthesized samples.

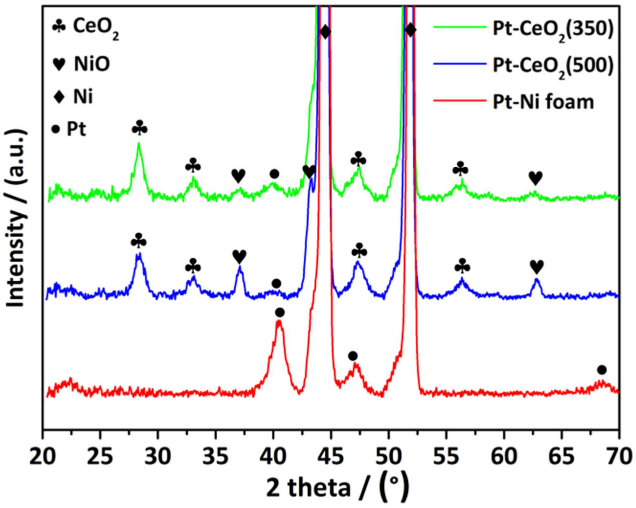

Figure 5.2 *XRD patterns of the as-synthesized Pt-CeO_2(350)/NiF (green), Pt-CeO_2(500)/NiF (blue) and Pt/NiF (red)*

The SEM images of the Pt-CeO_2(350)/NiF reveal the formation of a porous network having a nanoflake morphology composed of small nanoparticles with diameter less than 100 nm, as clearly evidenced in the high-magnification image reported in Fig. 5.3(b). In the case of Pt-CeO_2(500)/NiF, the morphology appears to be slightly different, with the presence of a disordered porous structure made of coalesced nanoparticles (Fig. 5.3(c)-(d)). In contrast, the SEM images of the Pt/NiF show only the presence of spherical agglomerates of nanoparticles without the existence of a defined porous network, as reported in Fig. 5.4.

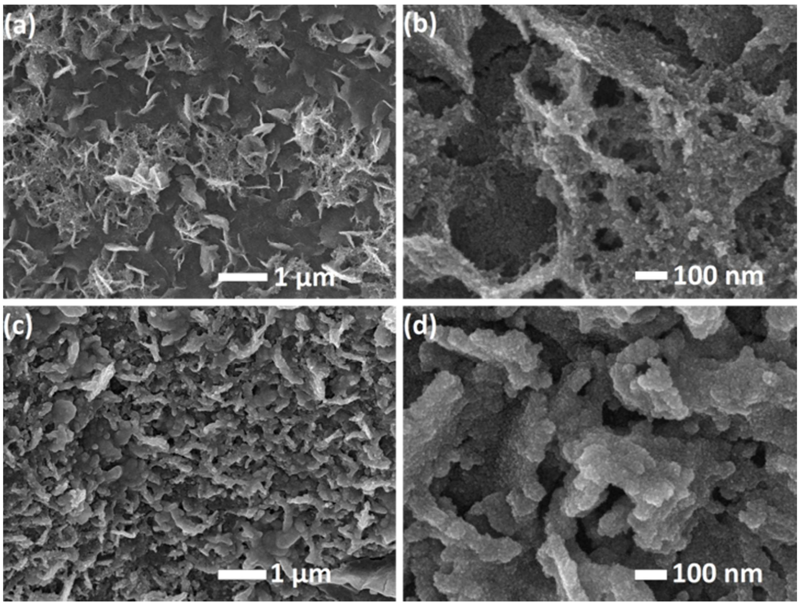

Figure 5.3 *Low- and high-magnification SEM images of (a)-(b) Pt-*CeO_2*(350)/NiF and (c)-(d) Pt-*CeO_2*(500)/NiF*

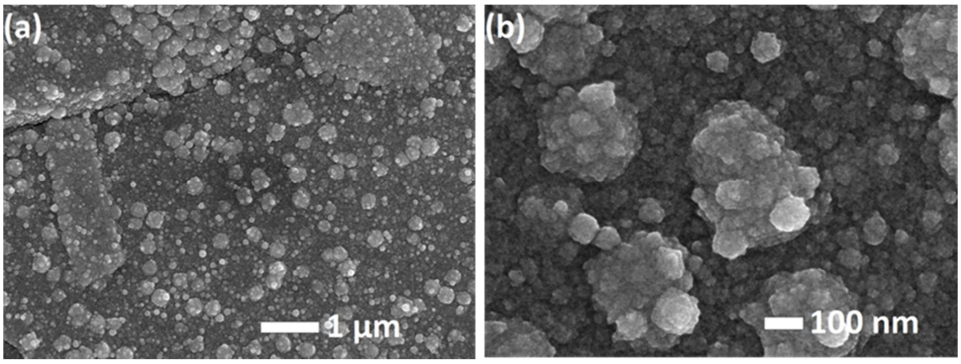

Figure 5.4 *Low- and high-magnification SEM images of Pt/NiF*

In order to understand whether this nanoflake-type porous network was formed before or after the hydrothermal synthesis of Pt NPs, SEM images of CeO_2(350)/NiF and CeO_2(500)/NiF were taken and displayed in Fig. 5.5. It can be observed that these samples possess well-defined porous nanoflake morphology, which is in line with what has been encountered in the case of the samples after the hydrothermal synthesis of Pt NPs.

Clearly, a porous interconnected morphology results in high available surface area which is highly beneficial for the synthesis of Pt NPs, favouring their dispersion and increasing their loading onto the support. Indeed, according to the ICP analysis reported in Tab. 5.1, the Pt mass loading of the Pt-CeO_2(350)/NiF and Pt-CeO_2(500)/NiF is 0.17-0.18 mg/cm^2, one order of magnitude higher than that of Pt/NiF. Given the complexity of these hybrid materials, a detailed TEM analysis was performed in order to unravel and quantify their nanoparticulate morphology.

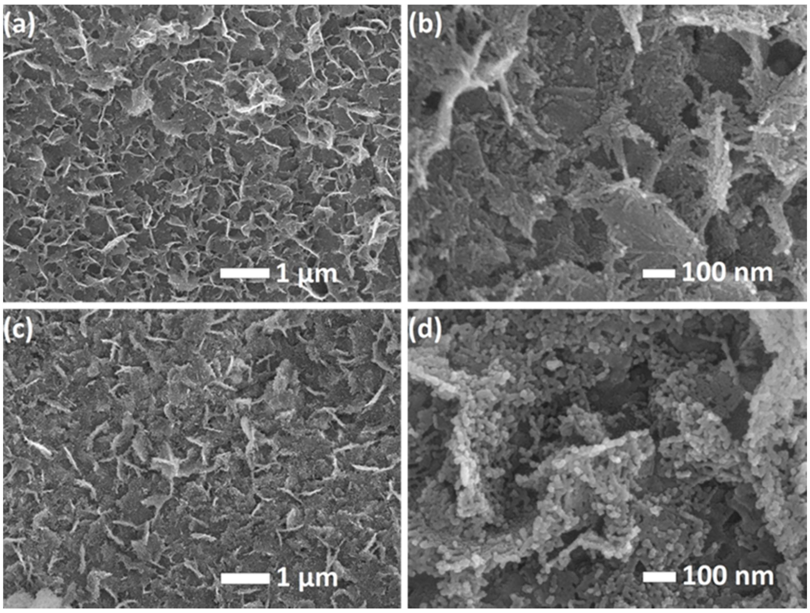

Figure 5.5 *Low- and high-magnification SEM images of (a)-(b) CeO_2(350)/NiF and (c)-(d) CeO_2(500)/NiF*

Sample	**Pt (mg/cm^2)**	**CeO_2 (mg/cm^2)**
Pt-CeO_2(350)/NiF	0.17	1.26
Pt-CeO_2(500)/NiF	0.18	1.14
Pt/NiF	0.07	-

Table 5.1 *Mass loading of Pt and CeO_2 calculated through ICP*

Fig. 5.6(a) shows a typical low resolution TEM image of the Pt-CeO_2(350)/NiF electrocatalyst. The sample consists of well dispersed Pt NPs having ultra-small diameter of 1.7 nm with a narrow size distribution, as displayed in Fig. 5.6(c). The image showing the single crystalline Pt NP is reported in in the inset of Fig. 5.6(c). The CeO_2 is dispersed throughout the Ni foam predominately as NPs ranging from 5-20 nm, as illustrated in Fig. 5.6(b). HRTEM images of the Ni foam support and CeO_2 are reported in the insets of Fig. 5.6(a) and Fig. 5.6(b), respectively. In contrast, the overall structure and morphology of the Pt-CeO_2(500)/NiF sample is non-uniform, as shown in Fig. 5.6(d).

Although discreet and well-dispersed Pt NPs are observed in the low resolution TEM (Fig. 5.6(e)), the HRTEM image reported in the inset of Fig. 5.6(e) shows considerable aggregation of the Pt NPs with the formation of elongated nanostructures. In addition to the Pt aggregation, larger crystalline domains of CeO_2 are observed compared to the sample annealed at 350 °C, as demonstrated in Fig. 5.6(f). Interestingly, nanocrystallites of NiO are observed in the Pt-CeO_2(500)/NiF sample, further confirming the results obtained from XRD analysis. The inset of Fig. 5.6(d) shows the interplanar distance of 0.24 nm, which is consistent with the (111) plane of NiO. For comparison, the TEM image of the Pt/NiF control sample is displayed in Fig. 5.7. It is worth noting that in this case the Pt is poorly deposited on the Ni foam in the absence of CeO_2, in perfect agreement with the low Pt metal loading measured through ICP, forming aggregated and irregular shaped nanostructures. Thus, it is clear how the presence of CeO_2 dramatically affects the size, morphology, dispersion and loading of the Pt NPs.

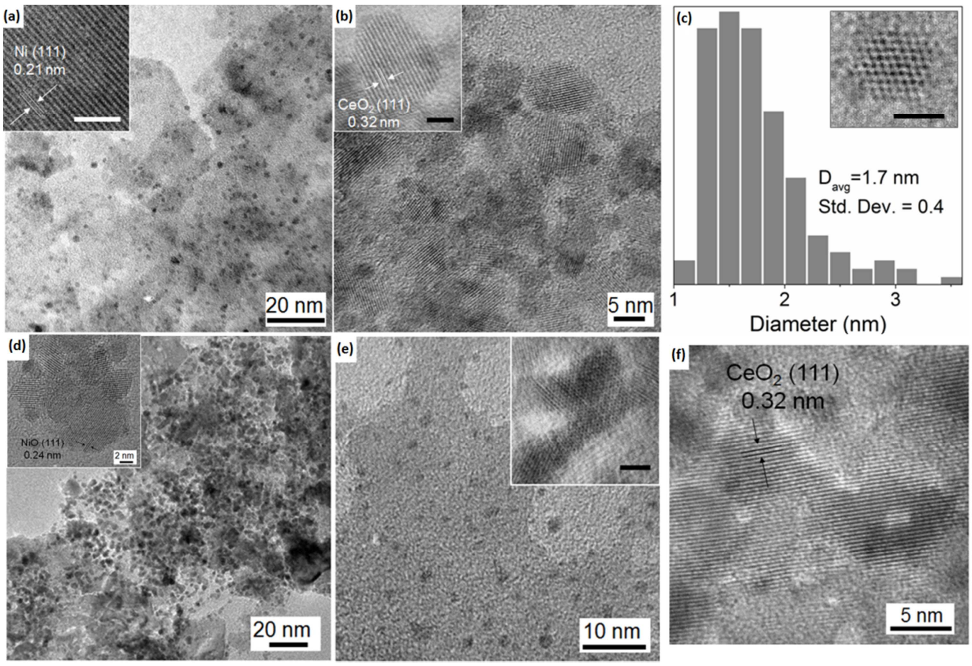

Figure 5.6 *(a)-(b) TEM and HRTEM (insets) images of the Pt-CeO_2(350)/NiF sample. (c) Pt NPs size distribution of Pt-CeO_2(350)/NiF sample. (d)-(e)-(f) TEM and HRTEM (insets) images of the Pt-CeO_2(500)/NiF sample*

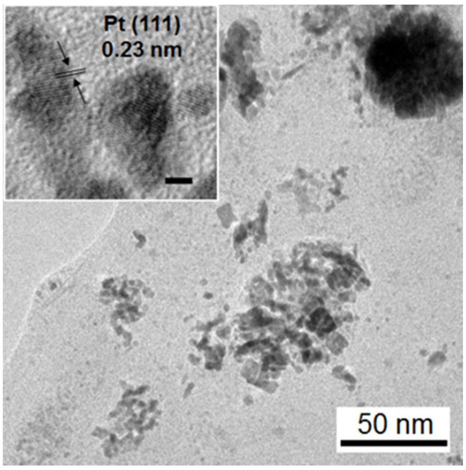

Figure 5.7 *TEM and HRTEM (inset) images of the Pt/NiF sample*

X-ray photoelectron spectroscopy (XPS) was performed in order to elucidate the chemical composition and oxidation state of the various elements at the surface of the electrocatalysts. The XPS patterns of the Pt-CeO_2(350)/NiF, Pt-CeO_2(500)/NiF and the control sample Pt/NiF are reported in Fig. 5.8, 5.9 and 5.10, respectively.

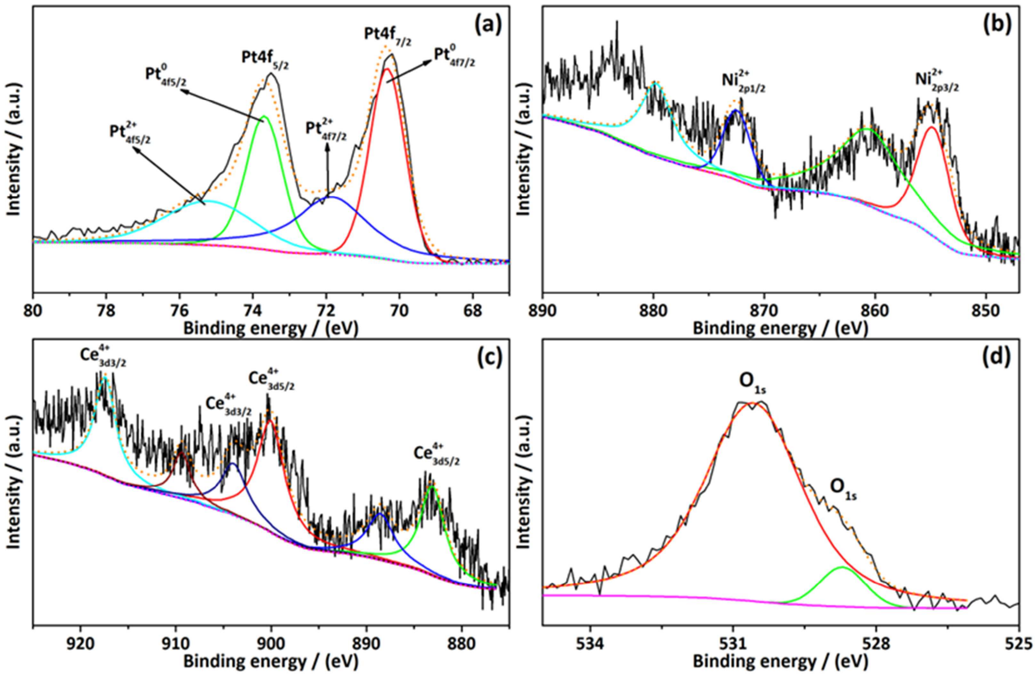

Figure 5.8 *XPS patterns of the as-synthesised Pt-CeO_2(350)/NiF*

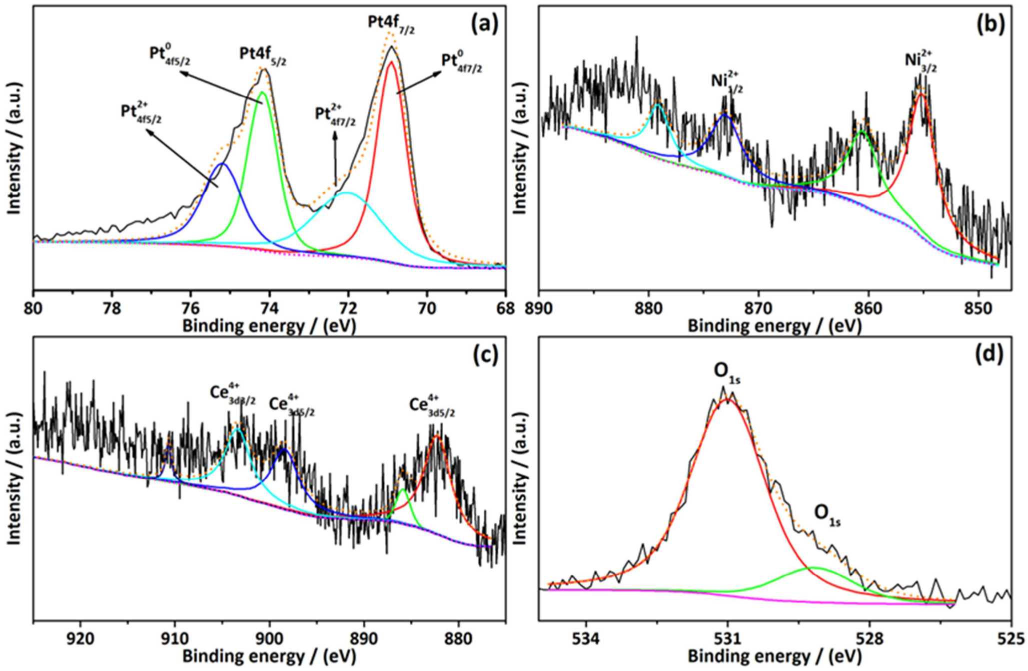

Figure 5.9 *XPS patterns of the as-synthesised Pt-CeO_2(500)/NiF*

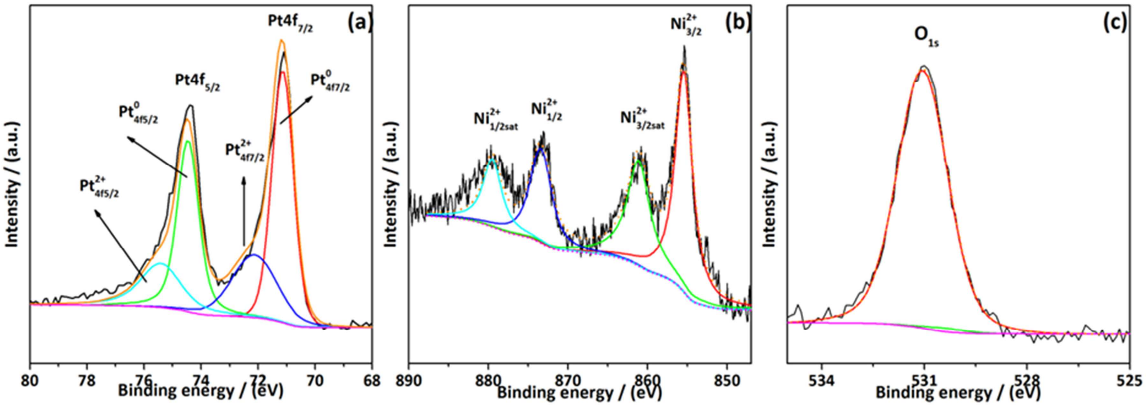

Figure 5.10 *XPS patterns of the as-synthesised Pt/NiF*

For all the three investigated samples, the Pt 4f spectra show the presence of mixed Pt^0/Pt^{2+} oxidation states upon deconvolution of the $Pt_{4f7/2}$ peak. In the case of the electrocatalysts containing CeO_2, a lower atomic percentage of metallic Pt is detected compared to the Pt/NiF sample, with values of 55-58 % calculated from the fitting of the experimental spectra and reported in Tab. 5.2.

Sample	Pt 4f7/2 binding energy (eV)	Pt^0 atomic percentage (%)	Pt^{2+} atomic percentage (%)
Pt-CeO_2(350)/NiF	70.3	55	45
Pt-CeO_2(500)/NiF	70.9	58	42
Pt/NiF	71.1	65	35

Table 5.2 *XPS quantitative analysis of the Pt^0 and Pt^{2+} oxidation states of the as-synthesised samples*

This can be explained by the fact that the more agglomerated nature of the Pt NPs in the Pt/NiF sample results in bigger nanostructures, which are in general less prone to oxidation upon ambient air exposure.[22,23] It is interesting to note that the $Pt^0_{4f7/2}$ peak of the Pt-CeO_2(350)/NiF and Pt-CeO_2(500)/NiF samples is located at binding energy of 70.3 eV and 70.9 eV, respectively. These values are negatively shifted compared to the $Pt^0_{4f7/2}$ peak of the Pt/NiF sample located at 71.1 eV, which is also the binding energy value normally recorded for bulk Pt.[24] This negative shift is in line with a recent work concerning the synthesis of Pt/CeO_2 nanorods, with reported $Pt^0_{4f7/2}$ binding energy of 70.5 eV.[25] The reason of such shift has been attributed to the existence of strong Pt-CeO_2 interactions, resulting in a charge transfer from the support to the Pt with subsequent alteration of the electronic properties of the particles.[25–27] Indeed, it is known that metal NPs have the ability to bind strongly to CeO_2 NPs, particularly around defects (steps, kinks or vacancies).[12] Therefore, the larger negative shift of $Pt^0_{4f7/2}$ binding energy observed for Pt-CeO_2(350)/NiF is likely due to the lower annealing temperature for the synthesis of CeO_2 NPs, which results in smaller crystallites and higher fraction of defects. This in turn leads to stronger interaction with the Pt NPs compared to the sample annealed at 500 °C. The detection of Ni 2p and Ce 3d XPS patterns in the case of Pt-CeO_2(350)/NiF and Pt-CeO_2(500)/NiF suggest the existence of a biphasic superficial nature of the two samples. In particular, the Ni 2p XPS patterns reported in Fig. 5.8(b) and 5.9(b) reveal the presence of Ni^{2+} species, with a binding energy of 855.0-855.2 eV ($Ni_{2p3/2}$), characteristic of $Ni(OH)_2$.[28] Thus, the NiO phase detected through XRD and TEM is covered by a layer of $Ni(OH)_2$, which could have been formed during the hydrothermal synthesis of Pt NPs. This is suggested by the fact that the Ni 2p spectrum of the control sample Pt/NiF (Fig. 5.10(b)) also matches that of $Ni(OH)_2$, with no peaks related to metallic Ni. The Ce 3d XPS spectra reported in Fig. 5.8(c) and 5.9(d) match with that of CeO_2, with no peaks attributed to Ce^{3+} species for both Pt-CeO_2(350)/NiF and Pt-CeO_2(500)/NiF samples.[29] The results derived from the fitting of the experimental spectra show that the $Ni(OH)_2/CeO_2$ atomic ratios are 1 and 3.2 for the Pt-CeO_2(350)/NiF and Pt-CeO_2(500)/NiF, respectively. From what has been discussed above, it can be concluded that Pt NPs formed during hydrothermal reaction are more prone to binding with CeO_2 NPs rather than with $Ni(OH)_2$, resulting in well-dispersed metallic NPs with strong adhesion.

5.2.3 Methanol oxidation activity and stability: evaluation of the catalytic performance of the synthesised materials and investigation into the principal mechanisms of reaction involved

Before assessing the electrochemical activity toward the AMOR, the three electrodes were first activated by performing several cyclic voltammetry (CV) scans in N_2-saturated 1 M NaOH solution, and the resulting curves are displayed in Fig. 5.11(a). All the three electrodes show a similar curve shape, with the anodic peak located at -0.75/-0.65 V vs Ag/AgCl corresponding to the hydrogen desorption step from the Pt NPs. Given the intrinsic difficulty in measuring reliable baselines for the integration of the hydrogen desorption charge, the values of the electrochemical active surface area (ECSA) of the Pt NPs were not calculated. This behaviour is reportedly characteristic of Pt/metal oxide systems, which failed to give meaningful results for the ECSA.[30] The anodic and cathodic peaks observed for all the three electrodes in the potential range between -0.25 and -0.45 V vs Ag/AgCl are attributed to the $Ni(OH)_2$/NiO(OH) redox couple.[31]

The AMOR activity of the three electrodes was evaluated through CV scans in 0.5 M methanol/1 M NaOH aqueous solution and the corresponding curves reporting the geometric current density vs potential after iR correction are displayed in Fig. 5.11(b). The prominent peak located at -0.27 V vs Ag/AgCl and recorded during the anodic scan is attributed to the electrocatalytic MOR. Clearly, the Pt-CeO_2(350)/NiF electrocatalyst shows the best performance, with a high peak geometric current density of 202 mA/cm^2 at -0.27 V vs Ag/AgCl. Interestingly, this value is one order of magnitude higher than that of the Pt/NiF, which attains a moderate peak geometric current density of 57 mA/cm^2.

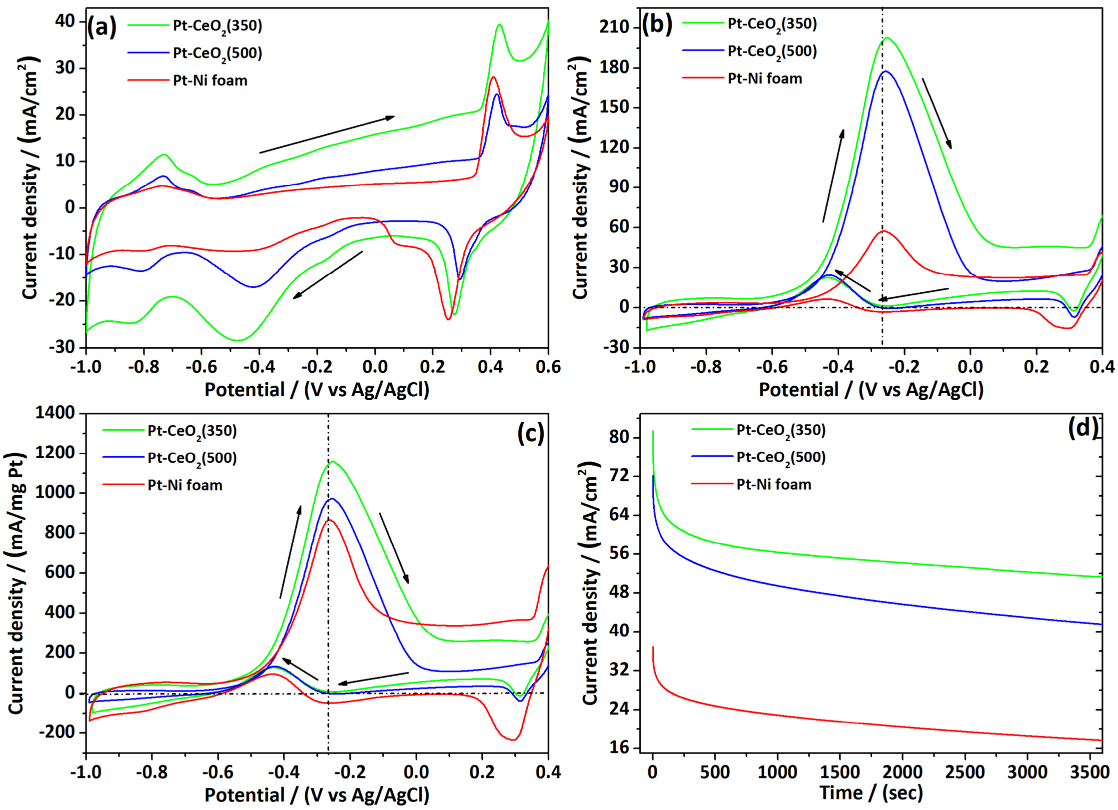

Figure 5.11 *(a) Cyclic voltammetry (CV) curves of Pt-CeO$_2$(350)/NiF (green), Pt-CeO$_2$(500)/NiF (blue) and Pt/NiF (red) electrodes in N$_2$-saturated 1 M NaOH at a scan rate of 50 mV/s; (b)-(c) iR-corrected CV curves of the three electrodes in 0.5 M methanol/1 M NaOH at a scan rate of 50 mV/s; (d) short-term chronoamperometry test of the three electrodes at -0.3 V vs Ag/AgCl in 0.5 M methanol/1 M NaOH. In (b) and (c), the recorded electric currents are divided by the geometric area of the electrodes and the mass loading of Pt, respectively*

Another figure of merit widely used for the determination of the MOR activity is the current density normalized to the actual Pt mass loading, because it gives a direct measure of the intrinsic performance of the Pt active sites. As reported in Fig. 5.11(c), the same activity trend can be observed, with the Pt-CeO$_2$(350)/NiF electrocatalyst having the highest activity. The impressive recorded peak mass current density of 1160 mA/mgPt at -0.27 vs Ag/AgCl compares well with the best reported MOR electrocatalysts in alkaline electrolyte, and a quantitative comparison in terms of MOR activity can be found in Tab. 5.3. According to a recent work by Zhao *et al.*, the small oxidation peaks detected during the cathodic scan at -0.43 V vs Ag/AgCl and reported for both the CV curves in Fig. 5.11(b) and 5.11(c) originate from the oxidation of methanol, which is triggered by the reduction of PtO$_x$ species formed in the preceding anodic scan.[32]

The short-term stability of the electrodes was assessed through chronoamperometry at a fixed potential of -0.3 V vs Ag/AgCl, and the results are reported in Fig. 5.11(d). After 3600 seconds, the Pt-CeO$_2$(350)/NiF electrode showed the highest stability, retaining 63% of the initial geometric current density, followed by Pt-CeO_2(500)/NiF and Pt/NiF with 57% and 48%, respectively. As reported in Tab. 5.3, these values are in line with the best MOR electrocatalysts in alkaline media.

Electrocatalyst	**Electrolyte**	**Anodic peak current**	**Short-term durability after 3600 seconds**	**Reference**
Pt/$Ni(OH)_2$/rGO	1M KOH + 1M methanol	1070 $mAmg^{-1}$ 150$mAcm^{-2}$	90% activity retention	2
Pt/CeO_2/C	1 M KOH + 1 M methanol	120 $mAmg^{-1}$ 36$mAcm^{-2}$	-	14
Pt/CeO_{2-x} nanorods	0.1 M KOH + 1 M methanol	- 18 $mAcm^{-2}$	-	25
Pt/rGO	0.5 M KOH + 0.5 M methanol	552 $mAmg^{-1}$ -	88.6% activity retention	6
Pd-MoS_2	0.5 M KOH + 1 M methanol	440 $mAmg^{-1}$ -	-	41
Pt on graphene and vanadium carbonitride	1 M KOH + 0.5 M methanol	- 45 $mAcm^{-2}$	60% activity retention after 5000 s	42
PtNi/C	1 M NaOH + 1 M methanol	1200 $mAmg^{-1}$ 120 $mAcm^{-2}$	-	43
Pt/karst- Ni thin film	1 M KOH + 1 M methanol	- 14 $mAcm^{-2}$	30% activity retention	44
Pt-rich shell coated Ni nanoparticles	1 M KOH + 1 M methanol	300 $mAmg^{-1}{}_{Pt}$ -	-	45
PdAu/C	0.5 M KOH + 1 M methanol	900 $mAmg^{-1}$ -	45% activity retention after 1000 s	46
Pt-CeO_2(350)/NiF	1 M NaOH + 0.5 M methanol	**1160 $mAmg^{-1}$** **202 $mAcm^{-2}$**	**63% activity retention**	**This work**

***Table 5.3** Comparison of the alkaline MOR performance between selected electrocatalysts in the literature*

The superior activity and short-term stability of the Pt-CeO_2(350)/NiF electrocatalyst toward the AMOR is essentially due to its unique morphological and structural properties. These properties mainly arise from the ultra-small size and well-dispersed arrangement of Pt NPs in a highly porous triphasic structure consisting of defective CeO_2 NPs, poorly-crystalline $Ni(OH)_2$/NiO species and metallic Ni foam framework. The fraction of metallic Pt NPs which are in intimate contact with CeO_2 NPs constitute the active sites for the methanol oxidation. The oxidation process can be divided into four main steps, namely, 1) OH^- adsorption, 2) methanol adsorption, 3) methanol dehydrogenation and 4) regeneration of Pt active sites. The methanol dehydrogenation step is mediated by the presence of free OH^- anions present in the electrolyte, leading to the formation of $(CHO)_{ads}$ and $(CO)_{ads}$, which are strongly bonded onto the Pt. These species block the Pt surface from further methanol adsorption, therefore they need to be oxidised in order to regenerate the active sites, according to the following reactions:[1]

$Pt\text{-}(CHO)_{ads} + Pt\text{-}(OH)_{ads} + 2OH^- \rightarrow 2Pt + CO_2 + 2H_2O + 2e^-$ 5.6

$Pt\text{-}(CO)_{ads} + Pt\text{-}(OH)_{ads} + OH^- \rightarrow 2Pt + CO_2 + H_2O + 2e^-$ 5.7

In particular, CO has been confirmed as the main poisoning species, since its total oxidation reported in equation 5.6 is widely regarded as the limiting factor for an optimal regeneration of the active sites.[33] From a mechanistic point of view, the presence of CeO_2 NPs in direct contact with Pt NPs dramatically accelerates the oxidation of the poisonous CO, because of two main effects:

- CeO_2 provides numerous adsorbed OH species to the nearby Pt NPs which participate directly in the CO oxidation through a Langmuir-Hinshelwood mechanism.[2,25,34]
- The strong bond between CeO_2 and Pt induces an electron transfer from Ce atoms to 3d-orbitals of Pt, weakening the Pt-CO bond.[35]

Moreover, the concomitant presence of $Ni(OH)_2$ on the surface further contributes to OH^- adsorption and supply to neighbouring Pt NPs for the oxidative removal of CO, given its suitable bonding strength with OH.[2,36] Indeed, the role of $Ni(OH)_2$ also explains why even the Pt/NiF electrode shows a good activity and short-term stability, even though its overall performance is still well below that of the samples containing CeO_2.

Electrochemical impedance spectroscopy (EIS) measurements were extremely useful for quantifying the different mechanistic steps of the three investigated electrodes. The Nyquist plots recorded at -0.6 and -0.3 V vs Ag/AgCl in 0.5 M methanol/1 M NaOH are displayed in Fig. 5.12(a) and (c), respectively. At potential of -0.6 V vs Ag/AgCl, the data were fitted using a simplified Randles circuit, as represented in Fig. 5.12(b). Here R_s is the solution resistance, R_∞ is the resistance for the methanol dehydrogenation (step 3) and CPE represents the constant-phase element, which models the double-layer capacitance C_{dl} at the rough and porous catalyst interface.[37,38] The C_{dl} is a measure of the adsorption of OH^- and methanol on the electrochemically active surface area (steps 1 and 2).[39] The impedance data recorded at -0.3 V vs Ag/AgCl were fitted using the equivalent circuit displayed in Fig. 5.12(d). In this case the circuit contains two additional elements compared to the simplified Randles circuit, which are related to the modelling of the oxidative removal of CO, namely, R_0 and L. R_0 represents the reaction resistance of the CO oxidation, and L is the inductance of CO oxidation, which is a measure of the slowness of $(CO)_{ads}$ coverage relaxation upon potential perturbation.[37,40] In other words this inductive effect is due to the fact that the $(CO)_{ads}$ coverage decreases with increasing potential, but the new steady-state coverage is time-delayed with respect to the potential perturbation.

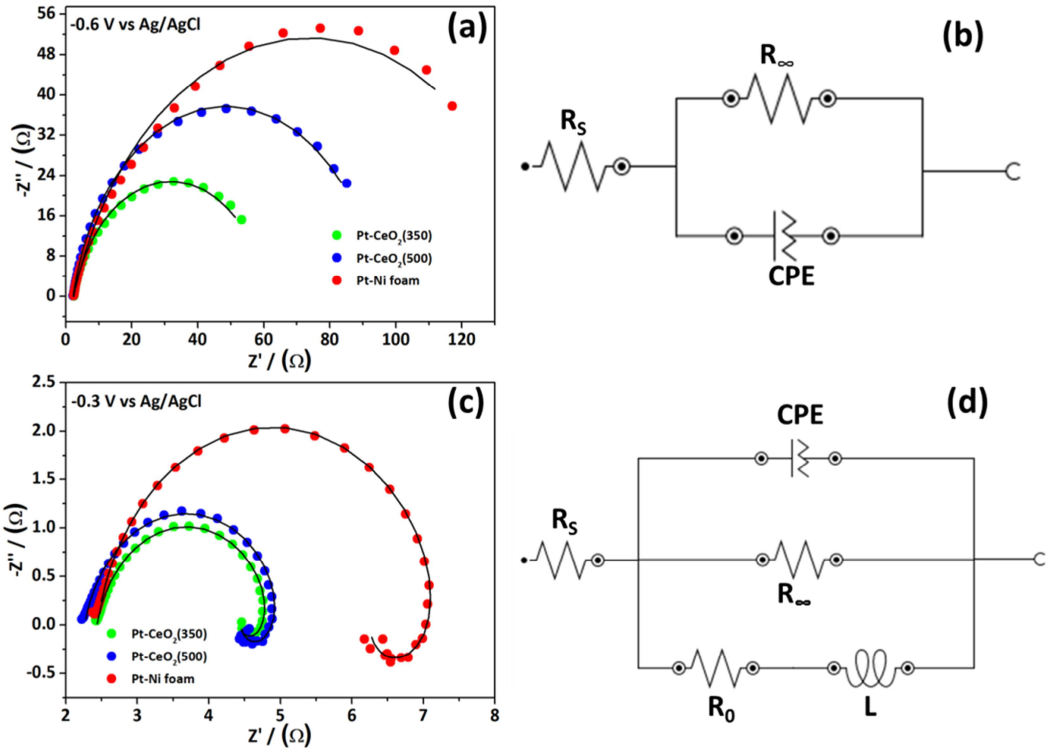

Figure 5.12 *(a) Nyquist plot for Pt-CeO$_2$(350)/NiF (green), Pt-CeO$_2$(500)/NiF (blue) and Pt/NiF (red) electrodes under potentiostatic mode at -0.6 V vs Ag/AgCl in 0.5 M methanol/1 M NaOH and (b) correspondent fitting equivalent circuit. (c) Nyquist plot for the same electrodes at -0.3 V vs Ag/AgCl in 0.5 M methanol/1 M NaOH and (d) correspondent fitting equivalent circuit*

The fitting parameters of Pt-CeO$_2$(350)/NiF, Pt-CeO$_2$(500)/NiF and Pt/NiF electrocatalysts are reported in Tab. 5.4. It is interesting to note that the samples containing CeO$_2$ present the lowest values of R_∞ ,R_0, L and the highest values of C_{dl}, thus in perfect agreement with their superior activity and short-term stability as previously discussed.

Potential	-0.6 V vs Ag/AgCl		-0.3 V vs Ag/AgCl			
Sample	**C_{dl} (mF/cm^2)**	**R_∞ (Ω·cm^2)**	**C_{dl} (mF/cm^2)**	**R_∞ (Ω·cm^2)**	**R_0 (Ω·cm^2)**	**L (H/cm^2)**
Pt-CeO$_2$(350)/NiF	16.1	29.4	12.6	1.3	4.9	5.8
Pt-CeO$_2$(500)/NiF	8.6	46.4	7.6	1.4	4.7	4.0
Pt/NiF	8.2	71.5	4.7	2.5	8.4	10.4

Table 5.4 *Fitting parameters resulting from the modelling of EIS measurements at -0.6 and -0.3 V vs Ag/AgCl for Pt-CeO$_2$(350)/NiF, Pt-CeO$_2$(500)/NiF and Pt/NiF electrocatalysts*

Even more interesting is the direct comparison between the fitting parameters of Pt/CeO$_2$(350)/NiF and Pt-CeO$_2$(500)/NiF electrocatalysts in order to understand the mechanistic reason of the superior activity of the sample calcined at 300 °C. Thus, the origin of the superior performance of the Pt-CeO$_2$(350)/NiF toward the AMOR compared to the sample annealed at 500 °C is principally due to the higher value of C_{dl}, which means a higher value of electrochemically active surface area. In fact, all the other values reported at -0.3 V vs Ag/AgCl and concerning the kinetics of methanol dehydrogenation and CO oxidation are quite similar. This property corroborates the morphological features revealed through SEM and TEM, which gave evidence of a more porous structure, better dispersion of Pt NPs and smaller size of CeO$_2$ NPs in the case of Pt-CeO$_2$(350)/NiF sample.

The potential long-term durability and reactivation capacity of the highly active Pt-CeO$_2$(350)/NiF electrocatalyst was evaluated through a series of chronoamperometry tests at -0.3 V vs Ag/AgCl. The catalyst shows an overall good long-term durability, retaining 40 % of the initial geometric current density after 6 hours (Fig. 5.13(a)). Surprisingly, by following the methodology reported by Huang *et al.*,[2] our catalyst can be fully reactivated by performing a few CV scans in 1 M NaOH after each stability test with negligible activity loss, as evidenced in the cumulative chronoamperometric curve reported in Fig. 5.13(a). In the experiment three cycles were carried out, with a total cumulative time of 18 hours. This property of complete catalytic reactivation offers tremendous benefits in terms of minimising energetic losses and prolonging the overall lifetime of real alkaline DMFC devices.

After 18 hours of cumulative long-term stability test, the Pt 4f XPS pattern of the Pt-CeO$_2$(350)/NiF electrocatalyst (Fig. 5.12(b)) shows the appearance of Pt^{4+} species, probably due to the oxidation of PtO/Pt(OH)$_2$ during the AMOR. The Pt^0, Pt^{2+} and Pt^{4+} atomic percentages resulting from the fitting of the XPS spectrum are 60.6 %, 18.6 % and 20.8 %, respectively. Also, the catalyst maintains a porous morphology after the cumulative long-stability test, with slightly different features due to a modest particle agglomeration, as observed in the SEM images of Fig. 5.14. TEM analysis further confirms the morphological similarity between the used and as-synthesised Pt-CeO$_2$(350)/NiF sample, with Pt and CeO$_2$ NPs dispersed across the Ni foam support (Fig. 5.13(c)). However from the histogram shown in Fig. 5.13(d), an increase in the mean diameter of the Pt NPs from 1.7 nm to 3.2 nm is observed.

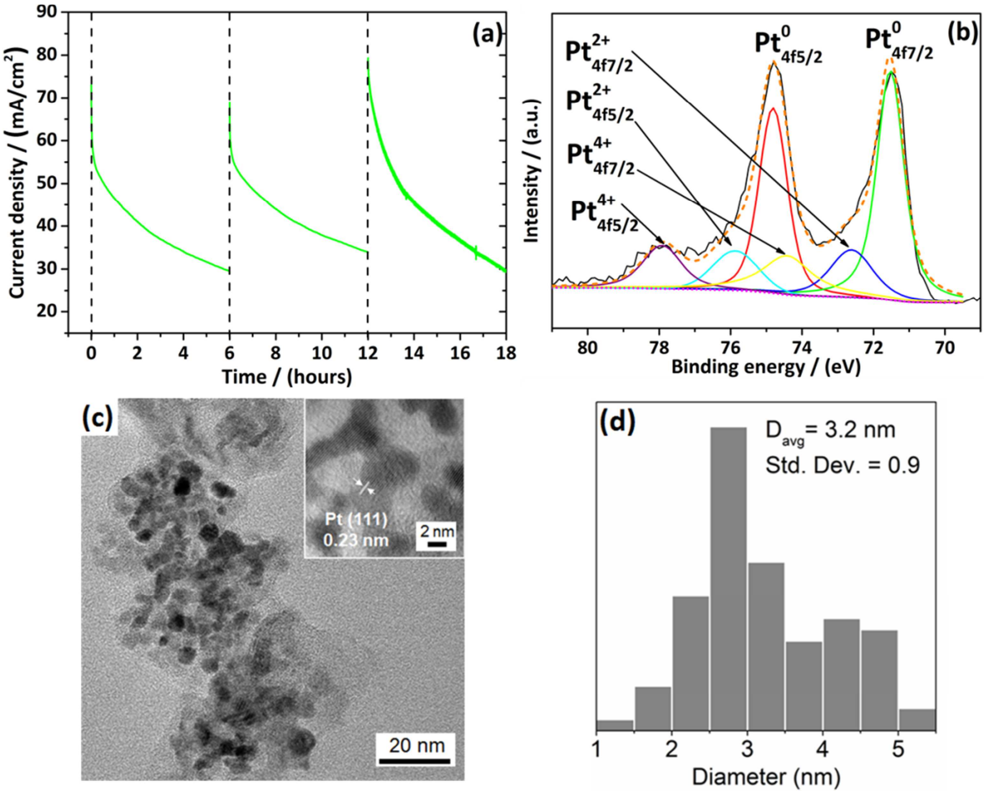

Figure 5.13 *(a) Cumulative long-term chronoamperometry test of Pt-CeO$_2$(350)/NiF electrocatalyst at -0.3 V vs Ag/AgCl in 0.5 M methanol/ 1 M NaOH; (b) Pt4f XPS pattern, (c) TEM and (d) Pt NPs size distribution of the catalyst after 18 hours of chronoamperometry*

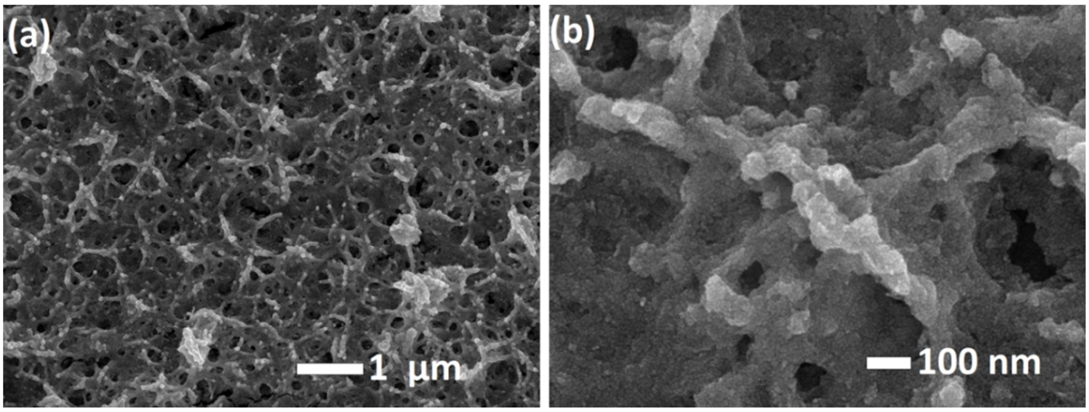

Figure 5.14 *Low- and high-magnification SEM images of the Pt-CeO$_2$(350)/NiF after long-term chronoamperometry test*

5.3 Conclusions

In this work, a highly active and durable electrocatalyst for the alkaline methanol oxidation reaction was presented, consisting of ultra-small Pt nanoparticles strongly embedded in a porous CeO_2/NiO/Ni foam ternary support. The novel synthetic approach is based on three defined steps: a first hydrothermal process for the synthesis of CeO_2 nanoparticles directly on the 3D Ni foam, a second calcination step and a final hydrothermal reaction for the generation of ultra-small Pt nanoparticles strongly bonded onto the porous triphasic support. The generated catalyst showed extremely high activity for the alkaline methanol oxidation, with peak mass and geometric current density values of 1160 mA/mgPt and 202 mA/cm^2. Detailed mechanistic studies were carried out in order to unveil the reasons of such impressive performance, through an appropriate combination of structural/morphological characterisation and EIS techniques. According to the findings, defective and poorly crystalline CeO_2 nanoparticles evenly dispersed throughout the Ni foam are in close contact with ultra-small Pt nanoparticles of 1.7 nm, acting as OH donors to the adjacent metallic active sites, with dramatic acceleration of the oxidative removal of CO. Moreover, the strong existing bond between CeO_2 and Pt can alter the electronic properties of the metallic nanoparticles, weakening the Pt-CO bond. Also, the concomitant presence of the superficial $Ni(OH)_2$ is thought to contribute to the supply of OH species to the Pt, given its suitable bond strength with OH. Finally, the highly porous morphology is responsible for the good dispersion of Pt nanoparticles, significantly affecting the available electrochemically active surface area. Without doubt the most interesting properties of this catalyst are represented by its long-term durability and the possibility to be fully reactivated. Long-stability tests demonstrated that the most active catalyst retained 40 % of the initial geometric current density after 6 hours, and the activity could be totally restored through straightforward CV scans in 1 M NaOH. This study paves the way for a further technological improvement of these novel composite materials, which can be regarded as promising anode electrocatalysts in real alkaline DMFC devices.

5.4 References

1. E. H. Yu, U. Krewer and K. Scott, *Energies*, 2010, **3**, 1499–1528.
2. W. Huang, H. Wang, J. Zhou, J. Wang, P. N. Duchesne, D. Muir, P. Zhang, N. Han, F. Zhao, M. Zeng, J. Zhong, C. Jin, Y. Li, S.-T. Lee and H. Dai, *Nat. Commun.*, 2015, **6**, 10035.
3. X. M. Qu, L. X. You, X. C. Tian, B. W. Zhang, G. D. Mahadevan, Y. X. Jiang and S. G. Sun, *Electrochim. Acta*, 2015, **182**, 1078–1084.
4. M. Ahmed and I. Dincer, *Int. J. energy Res.*, 2011, **35**, 1213–1228.
5. Y. Katayama, T. Okanishi, H. Muroyama, T. Matsui and K. Eguchi, *ACS Catal.*, 2016, 2026–2034.
6. S. Wu, J. Liu, Z. Tian, Y. Cai, Y. Ye, Q. Yuan and C. Liang, *ACS Appl. Mater. Interfaces*, 2015, **7**, 22935–22940.
7. X. Zhao, M. Yin, L. Ma, L. Liang, C. Liu, J. Liao, T. Lu and W. Xing, *Energy Environ. Sci.*, 2011, **4**, 2736.
8. A. A. Permyakova, B. Han, J. O. Jensen, N. J. Bjerrum and Y. Shao-Horn, *J. Phys. Chem. C*, 2015, **119**, 8023–8031.
9. F. Colmati, E. Antolini and E. R. Gonzalez, *Electrochim. Acta*, 2005, **50**, 5496–5503.
10. J. Suntivich, Z. Xu, C. E. Carlton, J. Kim, B. Han, S. W. Lee, N. Marzari, L. F. Allard, H. A. Gasteiger, K. Hamad-Schifferli and Y. Shao-Horn, *J. Am. Chem. Soc.*, 2013, **135**, 7985–7991.
11. Z. Zhang, J. Liu, J. Gu, L. Su and L. Cheng, *Energy Environ. Sci.*, 2014, **7**, 2535.
12. J. a Farmer and C. T. Campbell, *Science (80-.).*, 2010, **329**, 933–936.
13. Y. Li, C. Liu, Y. Liu, B. Feng, L. Li, H. Pan, W. Kellogg, D. Higgins and G. Wu, *J. Power Sources*, 2015, **286**, 354–361.
14. C. Xu and P. K. Shen, *Chem. Commun.*, 2004, 2238–2239.
15. R. S. Amin, R. M. A. Hameed, K. M. El-Khatib, M. E. Youssef and A. A. Elzatahry, *Electrochim. Acta*, 2012, **59**, 499–508.
16. M. A. Scibioh, S.-K. Kim, E. A. Cho, T.-H. Lim, S.-A. Hong and H. Y. Ha, *Appl. Catal. B Environ.*, 2008, **84**, 773–782.
17. D. R. Ou, T. Mori, H. Togasaki, M. Takahashi, F. Ye and J. Drennan, *Langmuir*, 2011, **27**, 3859–3866.
18. K. S. Sim, S. M. Lim, H. D. Kwen and S. H. Choi, *J. Nanomater.*, 2011, **2011**.
19. M. S. Saha, R. Li and X. Sun, *Electrochem. commun.*, 2007, **9**, 2229–2234.
20. W. Ji, W. Qi, S. Tang, H. Peng and S. Li, *Nanomaterials*, 2015, **5**, 2203–2211.
21. S. Ni, X. Lv, T. Li, X. Yang and L. Zhang, *J. Mater. Chem. A*, 2013, **1**, 1544–1547.
22. J. Prabhuram, T. S. Zhao, C. W. Wong and J. W. Guo, *J. Power Sources*, 2004, **134**, 1–6.

23. A. Eguizabal, L. Uson, V. Sebastian, J. L. Hueso and M. P. Pina, *RSC Adv.*, 2015, **5**, 90691–90697.
24. F. Şen and G. Gökağaç, *J. Phys. Chem. C*, 2007, **111**, 5715–5720.
25. C. L. Menendez, Y. Zhou, C. M. Marin, N. J. Lawrence, E. B. Coughlin, C. L. Cheung and C. R. Cabrera, *RSC Adv.*, 2014, **4**, 33489–33496.
26. J. R. Croy, S. Mostafa, J. Liu, Y. H. Sohn and B. Roldan Cuenya, *Catal. Letters*, 2007, **118**, 1–7.
27. S. Laursen and S. Linic, *Phys. Rev. Lett.*, 2006, **97**, 1–4.
28. M. Qin, W. A. Maza, B. M. Stratakes, S. R. Ahrenholtz, A. J. Morris and Z. He, *J. Electrochem. Soc.*, 2016, **163**, F437–F442.
29. S. Kato, M. Ammann, T. Huthwelker, C. Paun, M. Lampimäki, M.-T. Lee, M. Rothensteiner and J. A. van Bokhoven, *Phys. Chem. Chem. Phys.*, 2015, **17**, 5078–83.
30. T. Binninger, E. Fabbri, R. Kotz and T. J. Schmidt, *J. Electrochem. Soc.*, 2013, **161**, H121–H128.
31. X. Niu, H. Zhao and M. Lan, *J. Power Sources*, 2016, **306**, 361–368.
32. Y. Zhao, X. Li, J. M. Schechter and Y. Yang, *RSC Adv.*, 2016, **6**, 5384–5390.
33. J. S. Spendelow, J. D. Goodpaster, P. J. A. Kenis and A. Wieckowski, *Langmuir*, 2006, **22**, 10457–10464.
34. C. Xu, R. Zeng, P. K. Shen and Z. Wei, *Electrochim. Acta*, 2005, **51**, 1031–1035.
35. M. A. Scibioh, S.-K. Kim, T.-H. Lim, S.-A. Hong and H. Y. Ha, *ECS Trans.*, 2007, **6**, 93–110.
36. R. Subbaraman, D. Tripkovic, K.-C. Chang, D. Strmcnik, A. P. Paulikas, P. Hirunsit, M. Chan, J. Greeley, V. Stamenkovic and N. M. Markovic, *Nat. Mater.*, 2012, **11**, 550–557.
37. C. K. Poh, Z. Tian, J. Gao, Z. Liu, J. Lin, Y. P. Feng and F. Su, *J. Mater. Chem.*, 2012, **22**, 13643.
38. B. Ma, J. Bai and L. Dong, *J. Solid State Electrochem.*, 2013, **17**, 2783–2788.
39. X. Sun, K. Gao, X. Pang, H. Yang and A. A. Volinsky, *J. Electrochem. Soc.*, 2015, **162**, F1540–F1548.
40. J. T. Muller, P. M. Urban and W. F. Holderich, *J. Power Sources*, 1999, **84**, 157–160.
41. L. H. Yuwen, F. Xu, B. Xue, Z. M. Luo, Q. Zhang, B. Q. Bao, S. Su, L. X. Weng, W. Huang and L. H. Wang, *Nanoscale*, 2014, **6**, 5762–5769.
42. T. Huang, S. Mao, G. Zhou, Z. Zhang, Z. Wen, X. Huang, S. Ci and J. Chen, *Nanoscale*, 2015, **7**, 1301–7.
43. Q. Jiang, L. Jiang, S. Wang, J. Qi and G. Sun, *Catal. Commun.*, 2010, **12**, 67–70.
44. C. S. Chen, F. M. Pan and H. J. Yu, *Appl. Catal. B Environ.*, 2011, **104**, 382–389.
45. X. Z. Fu, Y. Liang, S. P. Chen, J. D. Lin and D. W. Liao, *Catal. Commun.*, 2009, **10**, 1893–1897.

46. Z. Yin, M. Chi, Q. Zhu, D. Ma, J. Sun and X. Bao, *J. Mater. Chem. A*, 2013, **1**, 9157.
47. Y. Lin, S. Zhang, S. Yan and G. Liu, *Electrochimica Acta*, 2012, **66**, 1-6.
48. B. Abida, L. Chirchi, S. Baranton, T. W. Napporn, H. Kochkar, J.-M. Leger and A. Ghorbel, *Applied Catalysis B: Environmental*, 2011, **106**, 609-615.
49. J. M. Skowronski and A. Wazny, *J. Solid State Electrochem.*, 2005, **9**, 890-899.
50. W. Shi, S. Song and H. Zhang, *Chem. Soc. Rev.*, 2013, **42**, 5714-5743.
51. M. Hirano and E. Kato, *Journal of Materials Science Letters*, 1999, **18**, 403-405.
52. G. Shen, Q. Wang, Z. Wang and Y. Chen, *Materials Letters*, 2011, **65**, 1211-1214.
53. G. Wang, D. Cao, C. Yin, Y. Gao, J. Yin and L. Cheng, *Chem. Mater.*, 2009, **21**, 5112-5118.
54. Q. Wang, X. Wang, B. Liu, G. Yu, X. Hou, D. Chen and G. Shen, *J. Mater. Chem. A*, 2013, **1**, 2468-2473.
55. H. Yan, D. Zhang, J. Xu, Y. Lu, Y. Liu, K. Qiu, Y. Zhang and Y. Luo, *Nanoscale Research Letters*, 2014, **9**, 424-431.
56. Y. Xiong, I. Washio, J. Chen, H. Cai, Z.-Y. Li and Y. Xia, *Langmuir*, 2006, **22**, 8563-8570.
57. B. Wiley, T. Herricks, Y. Sun and Y. Xia, *Nano Letters*, 2004, **4**, 1733-1739.

5.5 Appendix

5.5.1 Experimental methods

5.5.1.1 Chemicals and Materials

Cerium nitrate hexahydrate ($Ce(NO_3)_3{\cdot}6H_2O$, 99.99%) was purchased from Alfa Aeser. Urea ($CO(NH_2)_2$, 99-100.%), chloroplatinic acid hydrate ($H_2PtCl_6{\cdot}H_2O$, ≥ 99.9%) and polyvinylpyrrolidone (PVP, $M_w = 55000$) were purchased from Sigma Aldrich. Methanol (CH_3OH, ≥ 99.8%) was purchased from Tedia. Sodium hydroxide (NaOH ≥ 99%) was purchased from Merck. Nickel foam (Ni ≥ 99.8%, PPI = 110, thickness = 1 mm, volumetric porosity ≥ 95%, area mass density = 300 g/m^2) was purchased from Latech Scientific Supply. All the chemicals were used without further purification.

5.5.1.2 Synthesis of Pt-CeO_2/Ni foam electrode

The Pt-CeO_2/Ni foam electrode was synthesized according to a 3-step hydrothermal-calcination-hydrothermal process. In a typical synthesis, $Ce(NO_3)_3{\cdot}6H_2O$ (0.378 g, 0.00087 mol) and urea (0.263 g, 0.0044 mol) were dissolved in 35 mL of deionized (DI) water and stirred at room temperature for 15 minutes. The molar concentration of Ce ions was kept at 0.025 M and the urea/Ce molar ratio was fixed to 5. Nickel foam (2 × 4.5 cm) was sonicated at room temperature in 3 M HCl_{aq} (10 min), ethanol (5 min), DI water (5 min) and acetone (5 min), respectively. At the end it was dried using an air gun. The mixture solution was transferred into a 45 mL Teflon-lined stainless steel autoclave and the cleaned nickel foam was immersed into the solution. The autoclave was sealed and maintained at 120°C for 13 hours inside an electric oven. After the autoclave was cooled down to room temperature naturally, the nickel foam was taken out, rinsed and sonicated in DI water for 5 minutes in order to get rid of loose particles. Then it was dried using an air gun before further processing. The hydrothermally synthesized CeO_2/Ni foam was calcined using a static oven at a selected temperature (350°C, 500°C) for 2 hours with a ramp rate of 5°C/min. Finally the Pt NPs were synthesized onto a preformed CeO_2/Ni foam piece (2 × 2.25 cm) using a modified hydrothermal process based on the work of *Ji et al.*[20] Typically, PVP (50 mg, $M_w = 55000$) was dissolved in 18 mL of $H_2PtCl_6{\cdot}H_2O$ (1 mM) aqueous solution and stirred at room temperature for 20 minutes. The $PVP_{monomer}$/Pt molar ratio was fixed to 24.6. The mixture solution was transferred into a 23 mL Teflon-lined stainless steel autoclave and the CeO_2/Ni foam was immersed into the solution. The autoclave was sealed and maintained at 160°C for 3 hours inside an electric oven. After the autoclave was cooled down to room temperature naturally, the composite electrode was taken out, rinsed with DI water and sonicated in ethanol for 2 minutes in order to remove loosely bonded Pt NPs. Finally it was dried naturally at room temperature.

5.5.1.3 Structural characterisation

The samples were characterized by X-ray diffraction (XRD), scanning electron microscopy (SEM), transmission electron microscopy (TEM) and X-ray photoelectron spectroscopy (XPS). XRD patterns were acquired with a Bruker D8 general area detector diffraction system (GADDS) using monochromatic Cu Kα radiation (1.540598 Å). The morphology of the samples was characterized using a JEOL-JSM 7200 field-emission scanning electron microscope (FE-SEM) using an acceleration voltage of 15kV. TEM imaging was carried out using a Jeol 2100 Electron Microscope at an operating voltage of 200 kV. XPS data were collected with a Thermo Fisher Scientific Theta Probe X-ray photoelectron spectrometer using monochromatic Al Kα radiation (1486.6 eV) as X-ray source. The binding energies were charge corrected using adventitious C 1s peak at 285.0 eV as reference. The weight percentage of the Pt in the electrocatalysts was measured through inductively coupled plasma optical emission spectroscopy (ICP-OES).

5.5.1.4 Electrochemical characterisation

All the electrochemical measurements were carried out in a 3-electrode configuration using silver/silver chloride (Ag/AgCl (3 M KCl)) as reference, a Pt foil as counter and the electrocatalyst as working electrode. The geometric area of the working electrode was set equal to 0.5 cm^2 for all the experiments. Cyclic voltammetry (CV) and chronoamperometric analysis (CA) were performed using a Metrohm Autolab PGSTAT101 potentiostat. The working electrode was first subjected to 20 CV scans in N_2-saturated 1 M NaOH at a scan rate of 50 mV/s from -1.0 to 0.6 V vs Ag/AgCl. The electrocatalytic activity for the methanol oxidation reaction was assessed by performing CV scans in 1 M NaOH - 0.5 M CH_3OH solution at 50 mV/s from -1.0 to 0.6 V vs Ag/AgCl. Several scans were conducted until the curves stabilized to constant values. Durability tests were performed under chronoamperometric conditions at -0.3 V vs Ag/AgCl. The electrodes after long-term chronoamperometric tests were reactivated by running several CV scans in 1 M NaOH electrolyte at 50 mV/s. Electrochemical impedance spectroscopy (EIS) was carried out using a Metrohm Autolab PGSTAT302N potentiostat in potentiostatic mode at -0.6 and -0.3 V vs Ag/AgCl, respectively, with a scanning frequency from 100 kHz to 50 mHz and an amplitude of 10 mV.

Chapter 6: Future prospects

As previously discussed, the promising performance of the three materials under study, which was revealed to be comparable to the best reported electrocatalysts in the literature (apart from WO_3/Co_3O_4 photoanode), lays the foundations for a vast program of future development. In Chapter 3 a novel highly active electrocatalyst based on a mixed cobalt-nickel sulphide supported on Ni foam was developed and described, attaining a small overpotential of 163 mV at a current density of 10 mA/cm^2 for the optimised material. As discussed, this high activity is comparable to the best electrocatalysts based on non-noble metals, and a direct comparison between some recent published works was summarised. Furthermore, the material possessed good stability, which represents an important property in terms of practical applications. In Chapter 4 an extensive investigation into the activity of a WO_3/Co_3O_4 photoanode was reported, revealing important information about the existing correlation between structure of the cocatalyst and photoelectrochemical efficiency of the composite photoanode. These findings can easily be extended to other similar systems, giving the tools for a more rationale and systematic optimisation of ever efficient photocatalysts. Based on the results obtained a potential water splitter device consisting of a photoanode for the oxygen evolution reaction and a cathode electrocatalyst for the hydrogen evolution reaction can be devised. The device will aim to lower the electrical energetic requirements for the water splitting through the partial contribution due to the photoabsorption of photons at the anode side. This work will need further optimisation of the materials and a proper design of the cell.

In Chapter 5 a highly active electrocatalyst based on ultrasmall Pt nanoparticles supported on CeO_2/Ni foam for the alkaline methanol electrooxidation was developed, attaining values of geometric current density of 202 mA/cm^2. This performance compares well with the best Pt-based electrocatalysts, and a direct comparison between some recently published works was given. The reason of such high activity was unveiled through a detailed characterisation analysis, establishing a rational structure-property relation of the material under investigation. The most striking feature of this material was due to its capacity to fully restore its original activity simply by performing cyclic voltammetry scans in fresh electrolyte. This feature has a tremendous potential in real DMFC devices, since one of the main drawbacks of these devices is represented by the poor stability of the anode electrocatalysts. A DMFC device based on this material can be devised, although further studies regarding the development of oxygen reduction electrocatalysts and anionic selective membranes are necessary.

In more general terms, all the synthesised materials presented in this work could also be tested for other important electrochemical reactions such as oxygen evolution, oxygen reduction, hydrogen oxidation and polyhydric alcohol oxidation. And last but not least the reported synthetic methodologies may be used for the generation of new materials with different and unprecedented properties in a wide range of applications.